Variable-resolution frameworks for the simulation of tropical cyclones in global atmospheric general circulation models

by

Colin Zarzycki

A dissertation submitted in partial fulfillment
of the requirements for the degree of
Doctor of Philosophy
(Atmospheric, Oceanic and Space Sciences)
in The University of Michigan
2014

Doctoral Committee:

Associate Professor Christiane Jablonowski, Chair
Assistant Professor Derek J. Posselt
Assistant Professor Brian Arbic
Mark Taylor, Sandia National Laboratories

For Mom and Dad.

ACKNOWLEDGEMENTS

I would first like to thank my thesis advisor and committee chair, Christiane Jablonowski. She has provided superb mentorship and has contributed in a significant manner to my future career as a scientist. I look forward to many years of future collaborations with her and members of her research group. I would like to thank the remainder of my committee, Brian Arbic, Derek Posselt, and Mark Taylor. I appreciate your advice and support in this endeavor.

Further thanks to Mark Taylor, Michael Levy, Peter Lauritzen, and Jose Garcia, as well as numerous others at either Sandia National Laboratories or the National Center for Atmospheric Research who assisted in various facets of working with the model that this thesis is centered around. Somehow, they all managed to put up with my pestering e-mails about why something wouldn't build and were patient enough to respond with things like "Colin, you should probably set 'aquaplanet' to true if you want to run on an aquaplanet" instead of saying "Colin, why exactly are you getting a Ph.D., again?"

Also, thank you Sandra Pytlinski, Margaret Reid, Sandee Hicks, Kristi Hansen, Barb Lupi, and Katie Abdou for keeping me insulated from the bureaucracy of being a graduate student. It undoubtedly saved me countless hours of untangling red tape.

Lastly, it would be remiss of me to not thank my friends and family. Thank you to those who resided in the Jablonowski Data Lab at some point during my tenure; Kevin, Paul, Weiye, Diana, Jared, and James. Many of the conversations were useful in developing some of the work contained in this thesis, but the occasional

unproductive moments were probably more helpful to my mental status. I also would like to thank my fellow AOSS/Red Zeppelin brethren, including Matt, Mark, Stacey, Rachael, Adam, Gina, Jacob, Steve, Dan and so many others. Finding things to do outside of the SRB (perhaps within the friendly confines of The Arena?) was important. Plus, our softball career truly was a worst-to-first story.

I would also like to extend my gratitude to the Moskow/Hanselman family, even if my waistline may not always approve. I am forever thankful for my parents who have always supported me in every decision I've made. Finally, I'd like to thank Sarah for all her love and support. And doing the dishes when I was too busy writing this to help.

PREFACE

This thesis is a compilation of the research conducted while the author was a member of Dr. Christiane Jablonowski's research group between August 2010 and May 2014. Chapter II was published in *Monthly Weather Review* (Zarzycki et al., 2014a). Chapter III was published in *Journal of Climate* (Zarzycki et al., 2014b). Michael Levy designed the grids, completed the CAM4 simulations, and performed the informal scaling study as part of his postdoctoral research at Sandia National Laboratories. Chapter IV is in preparation for submission to an undetermined journal. Peter Lauritzen provided insight and support into the topographical smoothing and Mark Taylor provided the algorithm used to smooth the orography. Diana Thatcher performed the initial analysis of the African easterly waves for a class project. Chapter V will be submitted to the *Journal of Advances in Modeling Earth Systems* following the acceptance of this thesis (Zarzycki and Jablonowski, 2014). The original cyclone tracking algorithm for Chapter V was provided by Michael Wehner and his research group. It was modified for this thesis, but the routines that handle data input/output remained largely unchanged.

TABLE OF CONTENTS

LIST OF FIGURES

Figure

LIST OF TABLES

Table

ABSTRACT

Variable-resolution frameworks for the simulation of tropical cyclones in global atmospheric general circulation models

by

Colin Zarzycki

Chair: Dr. Christiane Jablonowski

The ability of atmospheric General Circulation Models (GCMs) to resolve tropical cyclones in the climate system has traditionally been difficult. The challenges include adequately capturing storms which are small in size relative to model grids and the fact that key thermodynamic processes require a significant level of parameterization. At traditional GCM grid spacings of 50-300 km tropical cyclones are severely under-resolved, if not completely unresolved. This thesis explores a variable-resolution global model approach that allows for high spatial resolutions in areas of interest, such as low-latitude ocean basins where tropical cyclogenesis occurs. Such GCM designs with multi-resolution meshes serve to bridge the gap between globally-uniform grids and limited area models and have the potential to become a future tool for regional climate assessments.

A statically-nested, variable-resolution option has recently been introduced into the Department of Energy/National Center for Atmospheric Research (DoE/NCAR) Community Atmosphere Model's (CAM) Spectral Element (SE) dynamical core. Using an idealized tropical cyclone test, variable-resolution meshes are shown to sig-

nificantly lessen computational requirements in regional GCM studies. Furthermore, the tropical cyclone simulations are free of spurious numerical errors at the resolution interfaces. Utilizing aquaplanet simulations as an intermediate test between idealized simulations and fully-coupled climate model runs, climate statistics within refined patches are shown to be well-matched to globally-uniform simulations of the same grid spacing. Facets of the CAM version 4 (CAM4) subgrid physical parameterizations are likely too scale sensitive for variable-resolution applications, but the newer CAM5 package is vastly improved in performance at multiple grid spacings.

Multi-decadal simulations following 'Atmospheric Model Intercomparison Project' protocols have been conducted with variable-resolution grids. Climate statistics produced using ocean-centered, variable-resolution nests are almost identical to those from "unrefined" simulations using globally-uniform grids. Regional climatology is improved by refinement due to the better representation of topography. Lastly, tropical cyclone structure, intensity, and interannual variability in the Atlantic Ocean are all significantly improved with the use of variable-resolution grids. These attributes are well-matched to other modeling studies at similar horizontal resolutions while only requiring a fraction of the computational cost, highlighting the potential of using variable-resolution GCMs to simulate small-scale phenomena.

CHAPTER I

Introduction: Variable-resolution modeling and tropical cyclones

1.1 High resolution general circulation models

1.1.1 What are general circulation models?

General Circulation Models (GCMs) are the manifestation of using numerical approximations to simulate the Earth's atmosphere. They are comprised of two separate components. The dynamical core is considered the heart of GCMs, and is the component of the model tasked with solving the equations of motion governing the resolved flow of the atmosphere. The atmosphere is spatially discretized on grids covering the Earth's surface and integrated forward in time using a numerical scheme. The second component contains the subgrid physical parameterizations. These represent features not resolvable by the dynamical core and include radiation as well as processes occurring at the subgrid scale such as convection, clouds, turbulence, and surface heat fluxes, among others.

GCMs offer a multitude of utilizations, ranging from short-term weather prediction (on the order of hours to days) to long-term climate assessments (on the order of years to decades). The history of GCM evolution is a fascinating one, but well beyond the scope of this thesis. Lynch (2006) offers a comprehensive biography of Lewis Fry

Richardson, considered to be the father of numerical atmospheric modeling, as well as a general introduction to GCM theory. Reviews of more modern GCM developments can be found in Randall (2000) and Lauritzen et al. (2011).

1.1.2 What is high resolution?

The term "high resolution" as it applies to climate simulations is somewhat of a moving target. The most recent Intergovernmental Panel on Climate Change (IPCC) assessment notes that an example 87.5 kilometer (km) grid spacing is "higher resolution than most current global models" with 30 km grids being classified as "very high resolution" (Cubasch et al., 2013).

To highlight how dramatically the term has changed, we can reference global simulations carried out by Déqué and Piedelievre (1995) less than twenty years ago. They refer to T106 spectral truncation (∼125 km) as a "high resolution" option when compared to the standard T42 (∼300 km). They note that even their "high resolution" grid is "too expensive for scenario simulation" and they are only able to complete much shorter "snapshot experiments." Today this grid would be considered unsuitably coarse for many applications.

As of this writing, we judge that "high resolution" generally encompasses coupled climate simulations at or below 75 km grid spacing. We acknowledge that, like Déqué and Piedelievre (1995), this interpretation will shift, becoming more out-of-date with time.

1.1.3 Why do we need high resolution in atmospheric models?

Decreasing the distance between grid points in GCMs allows for direct resolution of features at smaller spatial scales. Better representation of processes such as precipitation, clouds, and turbulent transfer of heat, momentum, and moisture has contributed to quantifiable increases in model skill (Kalnay, 2002; Lackmann,

2011). Other atmospheric phenomena which operate at smaller spatial scales than most traditional GCMs exhibit improved representation as resolution is increased. These include tropical cyclones (ex: Manganello et al. (2012); Wehner et al. (2014)) and frontal zones (Ohfuchi et al., 2004). Aspects of the diurnal cycle of precipitation have been shown to improve with increased resolution, particularly in models which are convection-permitting (Dirmeyer et al., 2012). Increased resolution also provides a more accurate representation of mountain ranges and other topographical features. Improvements in the grid's ability to resolve topography have been shown to improve precipitation patterns (Gent et al., 2010; Boyle and Klein, 2010) and mid-latitude synoptic blocking events commonly associated with heat waves, cold snaps, and pollution outbreaks (Jung et al., 2012).

1.1.4 What are the computational issues surrounding high resolution GCMs?

The main restriction in achieving improved horizontal resolution is the processing ability and memory constraints of the computer used to run the model. As horizontal resolution is increased, the number of cells tiling the sphere also increases. Further compounding matters, the decreased grid spacing typically requires a shorter model time step (to maintain numerical stability) due to a more restrictive Courant-Friedrichs-Lewy (CFL) condition. It is clear that the computational requirements required to integrate GCMs rapidly balloon as model grids become finer. Even at large, national laboratories, running global climate simulations at $\leq$50 km remains too burdensome to be an easily-achievable operational goal. Additionally, the increasing use of multi-member ensemble simulations to improve the understanding of sources of uncertainty within a model simulation (Rougier et al., 2009; Flato et al., 2013) implies that single model runs at high horizontal resolution may not be a preferred technique for future climate assessments.

Limited area models (LAMs) (alternatively, regional climate models (RCMs)) are a potential solution to this problem. LAMs can achieve locally high resolution by only numerically simulating a specific region of the atmosphere. This eliminates the requirement to expend computational resources in portions of the global domain that are not of interest. One of the most frequently used LAMs is the Weather Research and Forecasting Model (WRF, Skamarock et al. (2008)), although there is no shortage of options available to atmospheric researchers.

By definition, LAMs require lateral boundary conditions (LBCs) at the edges of the domain in order to "force" the interior of the grid. This is done through the application of results from a global driver model. Commonly, data from a global dataset such as a reanalysis product or forecast simulation is interpolated to the boundaries of the regional model and updated at a specific frequency (ex: every 6 hours). While this technique has been used with success in the past, LBCs may not be mathematically well-posed (McDonald, 2003). They may also suffer from interpolation errors or introduce model biases induced by the parent model's dynamical core or subgrid physical parameterizations (Warner et al., 1997; Mesinger and Veljovic, 2013). In addition, since LAMs are not global in scale, generally conservation properties are ignored.

1.2 Variable-resolution models

What if we could have our cake and eat it, too? Perhaps we could selectively apply computing resources in regions we are interested in while eliminating the need for potentially numerically and physically inconsistent boundary conditions. Variable-resolution general circulation models (VRGCMs) may offer a tantalizing solution. VRGCMs employ global meshes with non-uniform grid spacing. They allow for high-resolution nests to be located in areas where fine grid spacing is required. They also maintain global connectivity, eliminating issues arising from the specification

of LBCs. VRGCMs also allow for "upscale" effects, meaning that, unlike one-way nested LAMs, features simulated in the high-resolution nest are allowed to impact the remainder of the global solution.

While VRGCMs are considered a general classification encompassing all global, atmospheric models utilizing multiple grid spacings with two-way interactions, there are primarily two techniques used to achieve variable-resolution: grid stretching and grid nesting.

1.2.1 Stretched grids

Grid stretching has historically been the more popular method of achieving variable resolution within a GCM. In these models, a globally-uniform mesh is smoothly distorted in such a fashion that a localized region can be simulated at high horizontal resolution. Stretched grids have traditionally been an attractive technique for VRGCM developers since they require only minor modifications to the numerical scheme and can still be integrated on structured grids. Until recently, the majority of VRGCMs in published literature utilized this framework.

Grid stretching itself can be broken up into two subsets, which are separated according to how the stretching is achieved. The first set is comprised of grid point models built upon a physically stretched spherical coordinate system (Staniforth and Mitchell, 1978). Environment Canada's Global Environmental Multiscale (GEM) (Côté et al., 1993; Côté et al., 1998) model utilizes a stretched grid in both latitude and longitude for short-term forecast applications over specific regions of interest. A variable-resolution option to the Goddard Earth Observing System (GEOS) was also implemented through a similar stretched coordinate system outlined in Fox-Rabinovitz et al. (1997). The Laboratoire Meteorologie Dynamique Zoom (LMDZ) model is a finite-difference GCM employing physical grid stretching (Hourdin et al., 2006, 2013) and has been used to show the representation of the Asian monsoon is

improved though the use of a telescoping mesh (Zhou and Li, 2002; Sabin et al., 2013).

The second method involves the application of the transformation first outlined in Schmidt (1977). Commonly referred to as the "Schmidt transformation," variable-resolution is achieved from a pole-symmetric dilation. Similar to a "pinching" of a uniform mesh, this provides a conformal transformation from a traditional grid to one with enhanced resolution in a specific region. These models generally contain approximately half of the grid points required for the same fine resolution as the previously discussed stretched spherical grid models, therefore costing less (McGregor, 2013), but require coarser grid spacing in the far-field region, which may cause adverse effects beyond stretching factors of approximately 7 (Caian and Geleyn, 1997).

Déqué and Piedelievre (1995) used this method to introduce variable-resolution into the Action de Recherche Petite Echelle Grande Echelle (ARPEGE) model. They found an improvement in the simulation of European temperature and precipitation compared to global models of coarser resolution. The Conformal-Cubic Atmospheric Model (CCAM) also employs this method to achieve regionally refined resolution on a cubed-sphere grid (McGregor and Dix, 2008). Tomita (2008) applied a generalization of the transformation to introduce variable-resolution into the Non-hydrostatic Icosahedral Atmospheric Model (NICAM) model. This variant has been used recently to study the predictability of tropical cyclone genesis in the Bay of Bengal (Yanase et al., 2010), Madden-Julian predictability (Nasuno, 2013), and factors controlling TC genesis from African easterly waves (Satoh et al., 2013). Harris and Lin (2013) also described a stretched-grid version of the Geophysical Fluid Dynamics Laboratory's (GFDL) Finite Volume model on a cubed-sphere grid (FV3), although the performance of the model is not significantly detailed in the literature.

Further discussion of many of these models can be found in Fox-Rabinovitz et al. (2006, 2008), who documented the Stretched Grid Model Intercomparison Project (SGMIP).

1.2.2 Nested grids

Nested grids encompass all variable-resolution techniques that physically add grid cells to a global grid to regionally refine simulations. Nested grid setups are more flexible than stretched grids since less restriction exists in the degree of the refinement and more than one region of high-resolution is possible.

While there is generally little distinction between different methods of nested VRGCMs in the literature, there are two types of setups: those which run a high-resolution and low-resolution model concurrently, passing information back and forth between the two, and those having fully-unified unstructured grids which, aside from the multiple grid spacings, are integrated exactly as a globally-uniform grid would be.

The first form can be interpreted as the equivalent of a regional model nested "on top of" a global model. Unlike a pure LAM, which only allows for a one-way transfer of information from the boundary conditions to the inner domain, these models allow for the passage of information both into and out of the high-resolution nest. They require two different model configurations for both nests, and, in some cases, are actually two separate models "stitched" together.

A simplified run sequence for these models is shown in Fig. 1.1. The global model is first run forward for a timestep (Step 1). Atmospheric conditions are then interpolated to a limited area model grid (interpolated, global-to-regional, IGTR). The regional nest is then run forward for the same length of time, likely involving multiple dynamical time steps because of the CFL constraint (Step 2). The information from the fine nest is remapped back onto the global grid (remapped, regional-to-global, RRTG) which is integrated forward for the next timestep (Step 3). Information from the global grid is then passed back to the nest as boundary conditions and so on. The process is then repeated until the desired simulation time is achieved.

Dudhia and Bresch (2002) extended the LAM Mesoscale Model 5 (MM5) to the

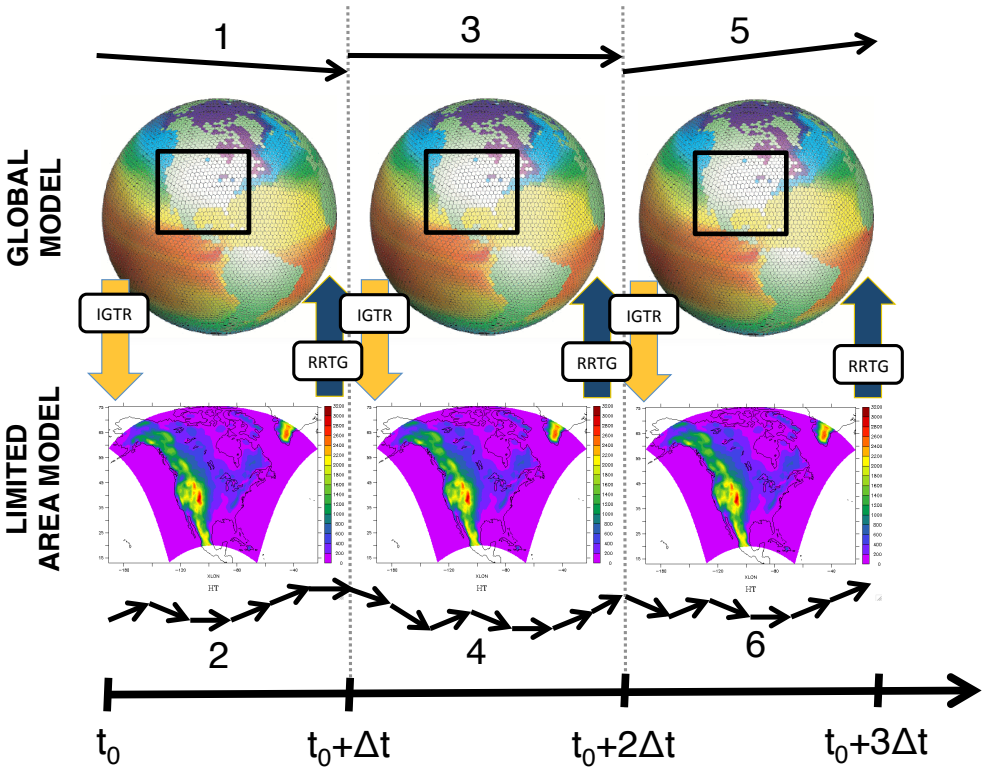

Figure 1.1: Schematic of two-way nested variable-resolution model. IGTR is the process of interpolating from the global to limited area (regional) model. RRTG is remapping from regional to global. Δt represents the subgrid physics timestep interval. Black arrows indicate dynamical timesteps. Computations are completed in numerical order (1, 2, 3, 4, etc.).

global domain through the use of two overlapping polar stereographic grids. This framework required interpolation where the grids overlapped at the equator, but allowed use of two-way nesting using the existing MM5 framework. Test short-term forecast simulations using a global 120 km mesh with an embedded 40 km nest over North America showed comparable results to simulations without the nest. They also did not observe artifacts in precipitation and sea level pressure at the grid interface. However, it appears no work exists in the published literature regarding further development of this particular setup. Two-way nesting of WRF has been recently evaluated in Hagos et al. (2013), although their outer domain only encompassed an idealized tropical channel. In addition, Williamson (2007) raised potential issues regarding the lack of conservation and extreme damping in the interface region.

Using models developed at the Max Planck Institute for Meteorology, Lorenz and Jacob (2005) nested a regional LAM with 0.5° (∼55 km) resolution inside a global spectral model at T42 (∼2.8°). They ran 10-year climate simulations with this high-resolution nest over the Maritime Continent (Indonesia) and showed improvement in regional temperature biases in the troposphere with the addition of the nest, although worse results appear in the lower stratosphere. Lesser improvements at the global scale are evident. These improvements may represent an upscale effect where the localized refinement provides more accurate information which appears in the global simulation.

Harris and Lin (2013) describe the implementation of a two-way nest setup in the aforementioned GFDL FV3 model. Unlike many previous nested model setups, the same numerical discretization and physical parameterizations are used in both the coarse and fine grid spacing. FV3 is able to achieve mass conservation, albeit by not allowing surface pressure (thereby mass) from the high-resolution nest impact the coarse grid. Therefore, FV3 only updates state variables (e.g., u-wind, v-wind, temperature, moisture) in a vorticity-conserving manner when completing the remap

from the fine to the coarse grid (the RRTG steps in Fig. 1.1). Since momentum and energy are already not fully conserved by the dynamical core, this method allows for no further degradation in conservation while avoiding potentially costly two-way, mass-conserving update methods. The nesting methodology described is currently being implemented and tested in GFDL's High Resolution Atmosphere Model (Hi-RAM) (Harris, personal communication).

The second form of nesting involves grids which span multiple resolutions within a single mesh. Finer grid cells physically replace coarser cells in the region of interest. There is no need to run a "coarse" model "underneath" the high-resolution nest, since any particular location on the sphere is associated with one and only one grid element. The numerical integration of all grid cells occur in unison, with the global timestep of the model generally restricted by the CFL constraint of the finest grid cell. This introduces an inefficiency in that the time steps in the coarse grid cells are significantly shorter than required for numerical stability. However, this technique simplifies the computational run procedure. A schematic of the model integration procedure can be seen in Fig. 1.2. It also provides more satisfactory conservation properties than the embedded LAM strategy, while also offering a more physically consistent application of subgrid parameterizations. In addition, these formulations easily lend themselves to grids with multiple patches of refinement or arbitrary refinement patterns.

One such example of this technique was implemented by Fournier et al. (2004) who assessed the performance of a spectral element method with refined grids using 2-D shallow water test cases. Baer et al. (2006) used the Spectral Element Atmospheric Model (SEAM) and CAM version 2 (CAM2) column physics to highlight the potential for refinement using spectral element methods to improve regional circulation aspects within a climate simulation. This thesis will assess an extension of this particular approach to a modern GCM as well as high horizontal spatial resolutions.

The Model for Prediction Across Scales (MPAS) is another application. Ringler

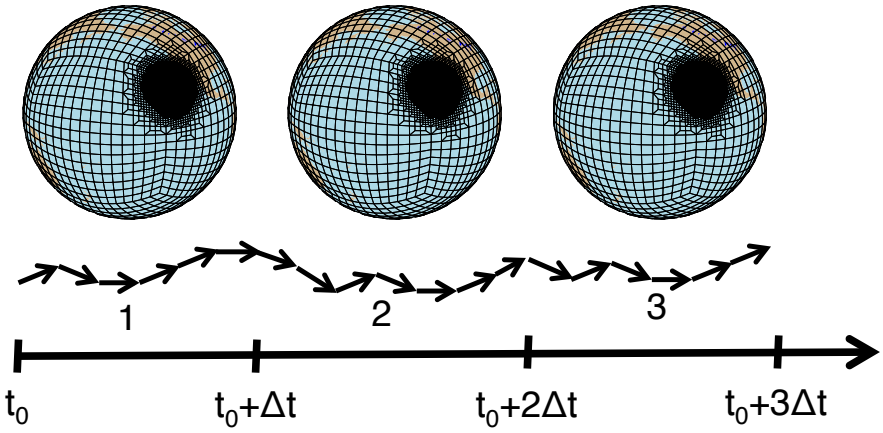

Figure 1.2: Schematic of variable-resolution model using single, unstructured grid with multiple grid spacings. Δt represents the subgrid physics timestep interval. Black arrows indicate dynamical timesteps. Computations are completed in numerical order (1, 2, 3, 4, etc.).

et al. (2008) and Skamarock et al. (2012) describe the implementation of a finite volume scheme using spherical centroidal Voronoi tessellations (SVCTs). A scalar grid density function can be applied to provide different resolutions at different locations on the sphere. Idealized aquaplanet simulations using MPAS and CAM version 4 (CAM4) physics have demonstrated promising results from a dynamical core standpoint, although the use of a multi-resolution setup highlighted potential scale-sensitivity issues with the CAM4 subgrid parameterizations (Rauscher et al., 2013; Hagos et al., 2013).

The Ocean-Land-Atmosphere Model (OLAM, Walko and Avissar (2008)) has the ability to introduce localized refinement using either hexagonal or triangular grid cells. Like MPAS, the cell shape allows for gradual transition between an area of mesh refinement and the corresponding background grid, which may assist in minimizing numerical artifacts associated with abrupt grid transitions (Walko and Avissar, 2011). OLAM has been used recently to show that increased refinement over the Americas may better resolve a signal in western United States snowpack associated with Amazon deforestation (Medvigy et al., 2013).

1.3 Tropical cyclones

1.3.1 Why simulate tropical cyclones?

Tropical cyclones (TCs) are severe storms originating in warm, tropical, ocean basins which are characterized by their strong surface winds and low pressure center. TCs also exhibit a vertically-stacked warm core temperature anomaly due to intense diabatic processes within the storm center. These thermodynamic energetics in mature storms are a natural realization of the Carnot heat engine (Emanuel, 1986). TCs are referred to regionally as tropical storms, hurricanes (Western Hemisphere) and typhoons (West Pacific). In other locales, they are also called cyclones or cyclonic storms. TCs can range anywhere from 100 km to over 4,000 km in diameter.

TCs are an important player in the climate system, moving large quantities of energy and moisture out of tropical regions and towards higher latitudes (Emanuel, 2001). Despite this, there is a relatively poor understanding of the exact mechanisms governing TC genesis and evolution. In addition, the forcing which the large-scale environment exerts on TCs appears to be regionally-dependent and, therefore, developing theory which governs activity in a climatological sense remains difficult.

Landfalling TCs produce strong winds, heavy rain, high waves, and damaging storm surge. They are currently estimated to be responsible for 19,000 fatalities per year and $26 billion/year in damages worldwide (Mendelsohn et al., 2012), making them one of the most devastating natural phenomena. Because of these impacts, future projections of tropical cyclone (TC) activity continue to be an important research question in the climate modeling community. There exists considerable discrepancy in the projected change in the number of tropical cyclones over the next decade. The majority of recent simulations project a decrease in overall tropical cyclone count over the 21st century (e.g., Bengtsson et al. (2007b); Knutson et al. (2010)) but others such as Emanuel (2013) project an increase. Improvements in the community's ability

to model these storms is of vital importance to lowering projection uncertainty and providing a more thorough picture of TCs' connection to the climate system.

1.3.2 Recent developments in high-resolution tropical cyclone modeling

Historically, GCMs have struggled simulating tropical cyclones. In particular, a significant low bias in the modeled intensity of TCs has been observed, primarily due to the relatively coarse grid-spacing of approximately 50-300 km (Bender and Ginis, 2000; Randall et al., 2007; Hamilton, 2008; Flato et al., 2013). These grid spacings are unable to sufficiently resolve the dynamics associated with the inner core of the storm.

Simulations completed in the last half decade or so have shown promising signs of improved TC representation within global models. These results are primarily tied to increases in horizontal resolution. We briefly discuss a few of the key studies here, although the frequency of sub-50 km simulations used to study TC activity is growing. Oouchi et al. (2006) used the Meteorological Research Institute (MRI)/Japan Meteorological Agency (JMA) model to complete two 10-year simulations (one present-day, one increased CO_2) at 20 km grid spacing. Their results showed improvements in storm count and intensity statistics when compared to results with coarser model results. Further improvements with the MRI-JMA model are shown in Murakami et al. (2012). Zhao et al. (2009) ran a 25-year simulation with the 50 km version of the Geophysical Fluid Dynamics Laboratory (GFDL) Atmospheric Model using historical sea surface temperature forcing. They found improved intensity statistics when compared with previous TC studies using GCMs as well as a high degree of skill in reproducing years with above or below-average TC activity in the Atlantic and Pacific Ocean basins. Simulations carried out under Project Athena (Kinter et al., 2013) showed that usage of a 10 km GCM didn't improve the spatial distribution of TC genesis and tracks compared to a 40 km run, but the representation of the most

intense TCs was greatly enhanced at finer grid spacing (Manganello et al., 2012; Satoh et al., 2012). Strachan et al. (2013) found similar sensitivities using the Hadley Centre Global Environmental Model (HadGEM) at a hierarchy of resolutions. 25 km simulations utilizing the Finite Volume (FV) option of the Community Atmosphere Model (CAM) have also demonstrated improved ability to resolve TCs when compared to the default 1° model resolution (Wehner et al., 2014; Bacmeister et al., 2014).

While published literature implies the global representation of TCs is significantly improved with finer grid spacing, simulation of Atlantic TCs has continued to be particularly difficult. While genesis and track skill among Coupled Model Intercomparison Project (CMIP) models improved with resolution, formation rates in the Atlantic were much less skillful than other ocean basins, even among the better models (Walsh et al., 2013). Strazzo et al. (2013) showed a systematic underprediction of TCs in the Caribbean and Gulf of Mexico among multiple high-resolution models. Because of this, as well as the amount of infrastructure in coastal areas which is vulnerable to landfalling storms, the Atlantic basin is a key target for future regional TC studies.

Due to their small size, intense dynamical processes, and relatively localized nature, tropical cyclones are an excellent fit for VRGCM frameworks. Modelers can introduce high resolution in regions such as low-latitude ocean basins where tropical cyclones form, as well as coastal regions where landfalling TCs may have significant impacts on human welfare as well as property. VRGCMs may prove vital in providing insight into model skill in individual basins and allow for a targeted look at how these storms impact regional climate.

1.4 Outline of thesis

In this thesis, we present our contribution to implementation and validation of a variable-resolution framework with the Community Atmosphere Model's Spectral Element dynamical core (CAM-SE). We utilize tropical cyclones to demonstrate the

benefits of this approach to the atmospheric modeling community.

This thesis is organized as follows. In Chapter II, we use idealized environments to test the fidelity of variable-resolution CAM when tropical-cyclone-like vortices are embedded in a high-resolution nest or transit between multiple grid spacings. We discuss a new test case which assesses whether a dry vortex is deformed when advected through variable-resolution transition regions. We also compare the development of a TC vortex in a variable-resolution mesh and a uniform high-resolution grid and discuss whether the results from a refined nest match that of an equivalent globally-uniform grid. We use aquaplanet simulations with a refined mesh to assess the resolution sensitivity of TC genesis and whether or not embedded nests can improve the spontaneous generations of TCs in climate models (Zarzycki et al., 2014a). Chapter III discusses the impact of variable-resolution on climate simulations. An aquaplanet framework is utilized as a simplified testbed for the climate system. We validate whether variable-resolution grids are able to reproduce climate statistics of uniform simulations corresponding to the different grid spacings in the multi-resolution setup. The scalability of certain CAM4 and CAM5 parameterizations are investigated. We also investigate whether equatorial waves transit through grid transition regions without any noticeable shift in phase speed or structure (Zarzycki et al., 2014b).

The climatological effects of introducing variable-resolution in a full-climate simulation is discussed in Chapter IV. Using Atmospheric Model Intercomparison Protocols (AMIP, Gates (1992)) we complete simulations from 1980-2002 using two different atmospheric grids; an unrefined 1° globally-uniform mesh and a refined version of the same grid with a 0.25° patch of high resolution over the North Atlantic Ocean. We assess the impact of this refinement on both the global and regional solutions from the perspective of long-term climate statistics. Finally, using the same simulations from Chapter IV, we investigate the implications of refined nests on TC representation in Chapter V. We use observational data to compare the performance of both models

in reproducing TC climatology over the North Atlantic. We perform an investigation of TC count and intensity statistics, assess the spatial distribution of simulated storms, and discuss the interseasonal and interannual variability of TC formation rates. We compare our results to other similar global high-resolution projects from other modeling centers and opine on the computation benefits of such a setup moving forward.

Chapter VI highlights the conclusions of the work, the significance and relevance to the community, collaborations fostered, as well as future work that is necessary in the VRGCM field.

CHAPTER II

Evaluating the performance of a variable-resolution general circulation model using idealized tropical cyclone experiments

2.1 Introduction

As storms which inflict significant economic harm and devastating loss of life, tropical cyclones and their role in the climate system have been an increasingly active area of interest over the last few decades. A great deal of research has been expended on potential changes in tropical cyclone counts, intensities, and tracks in a changing climate. General Circulation Models (GCMs) are the primary tool for long-term climate simulations and have increased in complexity over the last few decades (Reichler and Kim, 2008).

The most straightforward approach to simulating tropical cyclones in the climate system is to detect spontaneously generated storms through a series of objective criteria within a global GCM run. However, tropical cyclones are significantly under-resolved, if not completely unresolved, at traditional GCM grid spacings of 50-300 kilometers. Factors such as relatively small storm size and intense convective processes requiring comprehensive physical parameterizations contribute to this issue. Previous research indicates that approximately 50 kilometers or smaller horizontal

grid spacing is necessary to generate storms which appear structurally like tropical cyclones observed in the climate system (Bengtsson et al., 2007a). While advances in computing power are rapidly allowing for resolution increases, long-term climate simulations such as those used for the Intergovernmental Panel on Climate Change (IPCC) are still insufficient for comprehensive studies that allow for direct simulation of realistic tropical cyclones (Randall et al., 2007).

One solution to this problem has been high-resolution timeslice experiments, where limited area models (LAMs) are run over smaller domains for specific time periods of interest. LAMs ensure available computing time is allocated to a specific region of interest by not simulating the atmosphere beyond the domain boundaries. Since these models are not global in nature, they require the use of lateral boundary conditions (LBCs) to force the inner atmospheric nest. However, this introduces the potential for errors in the solution to be introduced through the use of a non-global domain. For example, there is debate as to the degree of well-posedness of commonly used flow-relaxation LBCs (McDonald, 2003). Additionally, LBCs are derived from a coarser global model simulation or a reanalysis data set. Therefore, LBCs allow the introduction of biases resulting from the driving model's dynamical core or physical parameterization package into the child LAM (Laprise et al., 2008). Another limitation of LAMs is the predominance of one-way nesting, which does not allow features resolved in a regional high-resolution nest to have a corresponding impact on the global driving model. This may be problematic for features like tropical cyclones which are active players in the climate system (e.g., Emanuel (2001)).

Variable-resolution GCMs (VRGCMs) are an option to help bridge the gap between LAMs and globally-uniform, high resolution models. VRGCMs allow for high spatial resolutions in areas of interest, such as low-latitude areas over ocean basins where tropical cyclones are prevalent, while maintaining a unified model hierarchy. This unification of multiple grid scales allows for targeted use of computing resources

in areas where small horizontal grid spacing is desired, similar to the LAM construct. In addition, it is straightforward for VRGCMs to conserve quantities such as mass since the numerical scheme is unified at the global scale, regardless of grid spacing. VRGCMs also maintain two-way connectivity with the global domain, eliminating the issues raised regarding one-way LBCs. VRGCMs provide a path for simulating tropical cyclones at horizontal resolutions previously only achievable through the use of axisymmetric models or LAMs.

Multiple-resolution models are not novel to the atmospheric modeling community. Stretched grids techniques (e.g., Côté et al. (1993), Courtier and Geleyn (1988), Lorant and Royer (2001), Fox-Rabinovitz et al. (2006), Abiodun et al. (2008), Tomita (2008)) increase resolution with a fixed number of degrees of freedom by clustering discretization points in a specific region while simultaneously decreasing horizontal resolution away from the refined location. This method therefore requires very little modification to the way the equations of motion are solved relative to a globally-uniform grid. Another method of achieving variable resolution in GCMs are nested grids. The majority of nested setups replace areas of cells on the background grid with patches of higher resolution, eliminating the issue of coarsened cells in stretched grids. However, they may also require modification to the dynamical calculations to account for regions where the grid transitions sharply from one resolution to another. Nested VRGCMs are becoming increasingly popular in the atmospheric community as emerging numerical techniques supporting these grids are developed (e.g., Ringler et al. (2008), Jablonowski et al. (2009), Walko and Avissar (2011), Skamarock et al. (2012), Rauscher et al. (2013), Harris and Lin (2013)). Nested models are more similar to LAMs than stretched grids because of their embedded areas of high resolution, although they also offer the appeal of fully-unified, two-way interaction at global scales. VRGCMs have yet to gain widespread use in light of the potential benefits discussed above. Some issues hindering their operational use are the lack of scale-

aware subgrid parameterizations (Arakawa et al., 2011) and potential inefficiencies in computational performance. As computing power has advanced and parameterizations have become more physically consistent, there has been a recent rejuvenation of interest in VRGCMs.

There remain questions as to whether or not variable-resolution improves the accuracy of a simulation. For example, St-Cyr et al. (2008) found in a spectral element shallow water model that small regions of refinement improve the solution in the region of interest but have negligible impact on the global error. Using a shallow water model and variable-resolution Voronoi tesselations, Ringler et al. (2011) showed that global solution error is controlled primarily by the coarsest grid spacing. However, VRGCMs offer improvements in simulation quality through the ability of regionally refined simulations to dynamically resolve features which would be sub-grid scale in a coarser uniform mesh. Here we focus on the improvement in the model's ability to be able to effectively represent regional features only possible through the use of a high-resolution mesh which would otherwise be unavailable to the global modeler. While a globally-uniform simulation (at the highest resolution) would likely offer the most accurate solution, VRGCMs may be much more computationally feasible for very long simulations or simulations with extremely fine scales.

The goal of this chapter is to showcase selected scientific characteristics of the VRGCM Community Atmosphere Model (CAM) version 5 (CAM5) with its newest Spectral Element (SE) dynamical core. CAM-SE is a hydrostatic atmospheric GCM that has been jointly developed by multiple U.S. Department of Energy (DoE) laboratories and the National Center for Atmospheric Research (NCAR) (Neale et al., 2010b). The variable-resolution aspects of the spectral element method for 2-D shallow water test cases have been described before by Fournier et al. (2004). Baer et al. (2006) used the Spectral Element Atmospheric Model (SEAM), the predecessor to CAM-SE, and CAM version 2 (CAM2) column physics to demonstrate that refine-

ment with spectral element methods improved the representation of regional features in a climate simulation. This chapter extends this discussion to the current incarnation of CAM-SE as well as high horizontal resolutions.

In particular, we focus our discussion on the potential improvements in simulating tropical cyclones within CAM-SE through the use of multi-resolution simulations. This is done via a hierarchy of increasingly complex test cases. Through these tests, we show that using nested grids in CAM-SE can improve the dynamical representation of meso-alpha scale vortices such as tropical cyclones at a regional scale without the global solution being contaminated by spurious artifacts introduced by grid nesting. The simulation of tropical cyclones is an ideal target for these models as they may play a critical role in the climate system (Emanuel, 2008). However, despite their intensity, they are severely underresolved in existing GCMs due to their small size. Completing long-term simulations at sufficiently high resolution to resolve these features requires a computational demand that is unavailable to the majority of modelers. Variable-resolution allows for a more accurate representation of cyclones for an allotted computing load and may improve the energy budget of the climate system through direct simulation of these features.

In Section 2.2 we offer a brief introduction to CAM-SE, and discuss some of the modifications required for variable-resolution simulations. In Section 2.3, we advect a small, tropical cyclone sized vortex through grid transition regions in CAM-SE nests to test the dynamical core's ability to handle the passage of a closed circulation in areas of an abrupt resolution change. These tests are completed without subgrid physical parameterizations such as surface fluxes, convection, or a boundary layer, so as to isolate the effects of the dynamical core. We then introduce a more complex test of an idealized tropical cyclone in an aquaplanet configuration in Section 2.4. We couple the CAM-SE dynamical core to the CAM5 physical parameterization package and investigate the effects of grid transition on a seeded tropical cyclone. We also evaluate

how well a tropical cyclone within a high-resolution nest embedded in a coarse global grid can reproduce the results of the same solution in a globally-uniform grid. Finally in Section 2.5 we complete a multi-year aquaplanet climate experiment to observe whether nested areas of high-resolution can lead to the increased frequency of intense tropical cyclones in low-latitude, high-sea surface temperature (SST) regions within CAM. Section 2.6 summarizes the findings and discusses future research directions for VRGCMs.

2.2 Variable resolution in CAM-SE

The Spectral Element dynamical core (Taylor et al., 1997; Taylor and Fournier, 2010; Taylor, 2011) is the newest available choice in the Community Atmosphere Model. CAM-SE is built upon a continuous Galerkin horizontal discretization and utilizes the cubed-sphere grid, eliminating the issues of converging meridians in polar regions which typically require short timesteps or polar filtering to maintain numerical stability. The polynomial degree of the basis functions on each element is selected to be three, providing fourth-order accuracy. One of the model's primary benefits is the ability to scale nearly linearly to hundreds of thousands of processors. This feature distinguishes it on massively parallel systems from less scalable dynamical cores such as global spectral transform or finite volume methods on conventional latitude-longitude grids, both of which have been shown to require large numbers of additional processors for small marginal improvements in model throughput (simulated years per day) at high processor counts (Dennis et al., 2012). As parallel computing environments continue to grow in both capability and number, CAM-SE holds significant promise in its ability to effectively utilize such architectures.

Because CAM-SE solves the primitive equations locally on individual elements, it possesses the ability to run on non-uniform grids without significant modification to the underlying numerics. The only two requirements for variable-resolution grids in

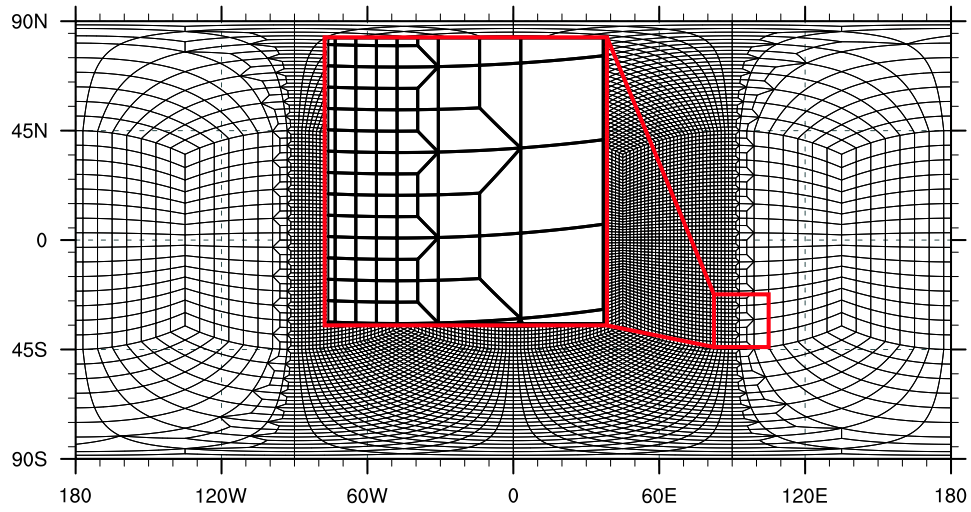

Figure 2.1: Zoom of CAM-SE transition region for variable resolution grid refined over one hemisphere.

CAM-SE are that the composing elements are quadrilateral and conforming (every element edge is shared by only two elements). The underlying grid (and therefore any refinement) is also unstructured, which eliminates the need to tile the grid in a more restrictive, ordered fashion. This allows for highly flexible refinements, including user-specified nest shapes and multiple patches of high-resolution in a single grid.

Refined grids are generated through the use of CUBIT, a software package developed at Sandia National Laboratories (Anderson et al., 2009). This software allows the user to create a globally-uniform cubed-sphere grid of a specified resolution and then refine over user-selected areas. Figure 2.1 depicts a zoom of a sample grid transition region, showing the conforming refinement structure generated by the CUBIT software package. This refinement structure is referred to as '2-refinement' where coarse cells are first divided into three elements in the transition region and then four elements in the refined area. Because it splits existing cells to increase resolution, '2-refinement' generally leaves the global structure of the grid intact while only generating a narrow region containing cells distorted by the refinement where resolution transitions.

Currently, all variable-resolution grids are static. Once the model is initialized

Table 2.1: CAM-SE resolutions of interest to this study. Grid spacing (in kilometers and degrees) correspond to the distance between collocation points within an element at the center of a cubed-sphere face. Physics and dynamics timesteps (dt) are globally constrained by the finest grid scale in an individual variable resolution model simulation, while the 4th-order diffusion coefficient $K_4\,(\Delta x)$ (hyperviscosity) is allowed to vary among individual elements.

Resolution	Grid Spacing Δx (km)	Analogous to (°)	Physics dt (s)	Dynamics dt (s)	$K_4\,(\Delta x)$ ($m^4\ s^{-1}$)
ne15	222	2°	3200	640	1.00E+16
ne30	111	1°	1600	320	1.00E+15
ne60	55	0.5°	800	160	1.00E+14
ne120	28	0.25°	400	80	1.00E+13

with a refined mesh, it remains the same throughout the model integration. The version of CAM used here is v5.1.33, and both the CAM4 (Neale et al., 2010a) and CAM5 (Neale et al., 2010b) subgrid physical parameterization packages are used. Simulations with CAM4 physics have 26 vertical levels while those using CAM5 have 30. Both physics packages utilize the Bulk Aerosol Model and prescribed aerosol fields. Resolutions are defined as the number of elements across one cubed-sphere face (ex: $n_e = 15$ is 15-by-15 elements per cubed-sphere face ($15 * 15 * 6 = 1350$ elements on the sphere)). Table 2.1 defines resolutions used in this study.

Refined patches are not required to span entire faces of the cubed-sphere but element density is defined in the same way (ex: an $n_e = 15$ grid with a patch 4-factor refinement will have a mesh density at the center of the refined patch equivalent to an $n_e = 60$ global grid). The type of refinement used is commonly referred to as h-refinement, where resolution is increased when the corresponding element size is decreased with a fixed basis function order.

The time step used in the dynamical core varies between runs but is fixed within an individual run. It is based on the finest scale in any refined mesh to maintain numerical stability. Therefore, all coarser scales are restricted to the same time step. Unlike the time step, the coefficients for the explicitly-added horizontal diffusion

(fourth-order hyperviscosity) are varied with gridscale within individual runs. The diffusion coefficient K_4 for an individual element can be calculated as

$$K_4(\Delta x) = K_4(\Delta x_{ref}) \left(\frac{\Delta x}{\Delta x_{ref}} \right)^y \tag{2.1}$$

where K_4 depends on the length of the longest axis of the element (Δx) and Δx_{ref} and $K_4(\Delta x_{ref})$ are a predetermined reference length and reference hyperviscosity coefficient to scale to. The scaling power y is defined as $\frac{log(10)}{log(2)} = 3.3219$, which results in approximately a factor of 10 decrease in $K_4(\Delta x)$ for every halving of grid spacing, and is similar to previously published tuning results for global spectral models (Boville, 1991; Takahashi et al., 2006). Diffusion is scaled such that the hyperviscosity coefficient in each region matches the default CAM-SE hyperviscosity for the uniform grid of that resolution (Levy et al., 2013). Time steps and hyperviscosity values for commonly-referenced CAM-SE resolutions are shown in Table 2.1.

2.3 Dry vortex behavior

As an initial low-complexity test, we implement a dry vortex on a non-rotating planet and advect it into and out of high-resolution nested regions. One desirable property of a VRGCM used for tropical cyclone research is satisfactory interaction of a cyclone with a grid transition region. Broad low pressure systems, which may act as tropical cyclone seeds, should be allowed to enter the high-resolution region without distortion and existing tropical cyclones should exit refined nests without reflecting waves back into the high-resolution domain. In this test, CAM-SE runs with only the dynamical core active and no physical parameterizations or other interaction with the surface turned on. This is referred to as the "adiabatic" configuration. Without moisture or surface fluxes, there is no physical mechanism for intensification. Therefore, any structural changes are controlled by the dynamical core grid's ability

to resolve the dry vortex and should provide information regarding the ability of the model's numerics to handle grid transitions.

Four grids are generated: a globally-uniform high-resolution grid ($n_e = 120$, ~0.25°), a uniform low-resolution grid ($n_e = 15$, ~2°), and two grids where two high-resolution regions of $n_e = 120$ spanning half of a cubed-sphere face are nested within a low-resolution grid of $n_e = 15$. The two refined grids are shown in Figure 2.2. One is designed so that an initial vortex originates in a low resolution region before passing into a fine region between days 2 and 3 (low-to-high or LTH, Figure 2.2a) and the other is generated such that the opposite is true (high-to-low or HTL, Figure 2.2b). For the latter two nests which are of variable-resolution, the resolution transitions over the narrowest distance which this factor of eight change can be accomplished using CUBIT's '2-refinement.' The transition region lies between approximately 85° W and 95° W in the HTL and LTH grids and therefore spans roughly 1,100 km. Using this narrow transition, any abnormal behavior of flow resulting from transitioning between resolutions should be most evident in this setup versus using a more gradual series of three transitions by a factor of two, each with small bands of intermediate ($n_e = 30$ and $n_e = 60$) resolution. The latter is likely the more logical option for actual application of variable-resolution in atmospheric modeling, since it would allow for features to adjust to the grid resolution more smoothly.

For this experiment, the initial conditions for a hydrostatically-balanced atmosphere in solid body rotation around a non-rotating Earth (angular speed $\Omega = 0\ s^{-1}$) is derived. The solid body rotation allows for advection of features embedded in the background environment at the velocity of the background wind profile. The background velocity is set to an easterly flow since this is the predominant wind direction in the tropical latitudes. Details of the derivation of the initial conditions can be found in the Appendix.

A vortex also in hydrostatic and gradient-wind balance, similar to that developed

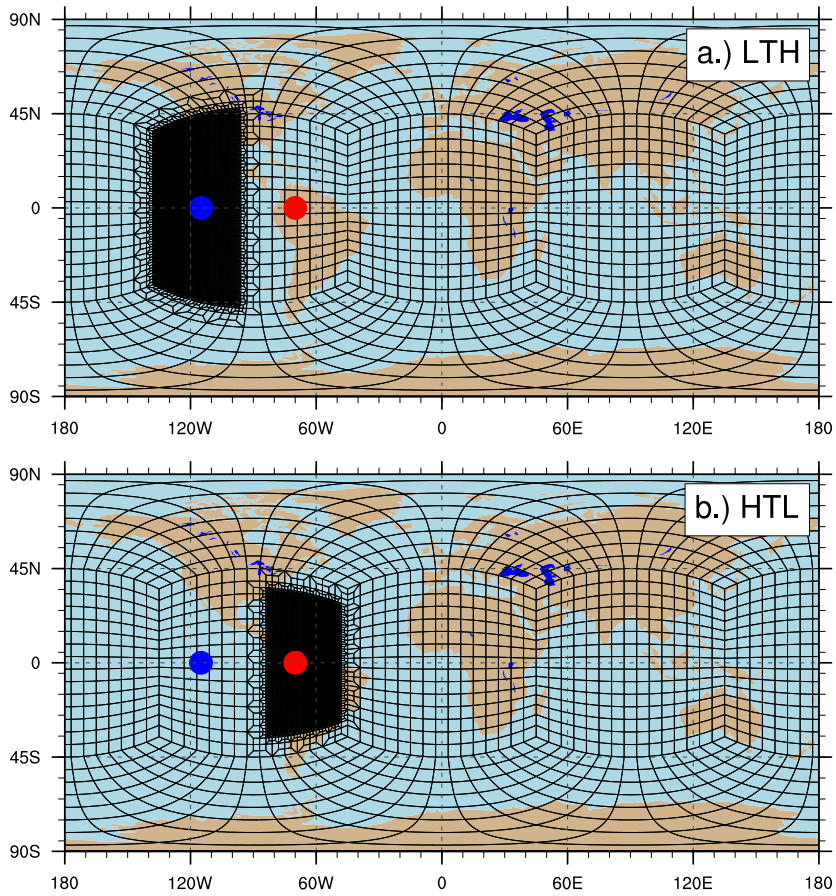

Figure 2.2: Variable-resolution low-to-high (LTH, top) and high-to-low (HTL, bottom) grids used for the dry vortex test. The red dots represent the initial location of the vortex and the blue dots are the vortex's location after 5 days of solid-body advection towards the west. The size of the dots corresponds approximately to the 20 m s^{-1} contour of the initial vortex. The continental outlines are plotted for scale only.

in Reed and Jablonowski (2011), is added to the background atmosphere. The primary differences to Reed and Jablonowski (2011) are that the vortex is developed on an irrotational sphere (therefore the Coriolis parameter f is set to 0 s^{-1}) and it is centered at 0° N, 70 W°. In addition, the vortex is dried by removing all water from the atmospheric column (specific humidity, $q = 0$) and correcting all state variables to this condition. Furthermore, the background atmospheric lapse rate (Γ) is set to 7 K km^{-1} to maintain an adiabatically stable environment. This lapse rate is continued throughout the entirety of the atmosphere up to the model top (approximately 2 hPa). The maximum amplitude of the zonal flow in solid body rotation is set to -10 m s^{-1} (easterly). From Reed and Jablonowski (2011), Δp (constant defining vortex strength) is set to 11.74 hPa and and r_p (constant defining vortex size) to 345 km. The drying of the vortex causes the resultant cyclone to be slightly stronger than it's moist counterpart, with a maximum wind speed of 23.5 m s^{-1} and radius of maximum winds equal to 315 km. The vortex is relatively shallow in its vertical extent. The wind speeds of this initial vortex seed have maximum amplitude near the surface and diminish to almost zero above 500 hPa.

The simulation is integrated for five days with a dynamics timestep of 75 seconds for all meshes. Figure 2.3 shows 850 hPa horizontal cross sections of the wind field through the center of the vortex at initialization, at day 2.5, and at day 5 on each of the four grids. In all simulations, the vortex remains symmetric before passing into a transition region. When in a transition region, the portion of the vortex in the high resolution region remains more resolved, creating small asymmetries in the wind field and providing slight distortion to the overall downstream vortex structure including small meridional deviations in the vortex track. Since the vortex is designed to be relatively well maintained in the high-resolution region while under-resolved in the coarse region, this behavior is expected.

As a measure of the cyclone's overall intensity through mesh transition regions,

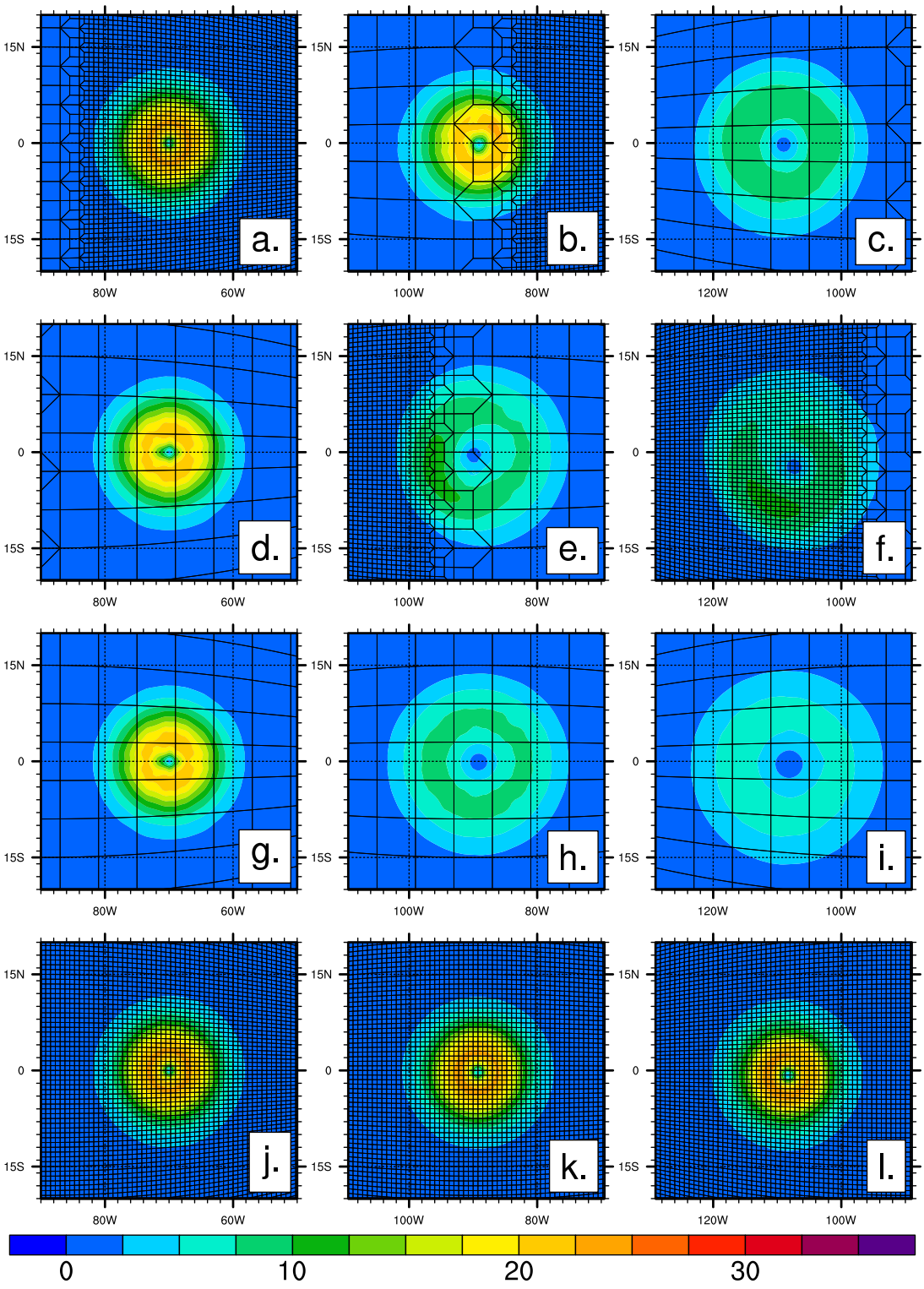

Figure 2.3: Horizontal 850 hPa wind speed (m s^{-1}) for four dry vortex test cases. (a-c) HTL, (d-f) LTH, (g-i) uniform coarse, (j-l) uniform fine. Left panels are the initialized vortex, middle panels are at 2.5 days, right panels are at 5 days.

we utilize radially integrated kinetic energy (IKE) which is calculated as follows

$$IKE = \frac{1}{2g} \int_{p_s}^{p_t} \int_{0}^{2\pi} \int_{0}^{r_\infty} (u^2 + v^2) r dr d\theta dp. \tag{2.2}$$

Here, g is gravity, p is pressure, u symbolizes the zonal wind, v stands for the meridional wind, p_s is surface pressure, and p_t is the column top (set to 500 hPa, approximately the top of the vortex). r denotes the great circle distance from the location of the surface pressure minimum ($r = 0$) which we define as the center of the vortex. r_∞ is the outer horizontal radius and is set to 1500 kilometers. θ is the angular coordinate rotated about $r = 0$. The integration limits are chosen to provide an integration cylinder large enough to completely envelop the vortex.

Figure 2.4 shows the temporal IKE evolution of the four test cases discussed above. Since the initial vortices are identical for all simulations, IKE is normalized to the time $t = 0$ value. The uniform coarse/fine simulations serve as controls, and therefore, low/high bounds on the vortex's IKE evolution. The variable-resolution HTL vortex initiated in the high resolution region is able to essentially maintain its full structure until passage into the coarse mesh (day 3) where IKE then decreases as the grid spacing becomes large and the vortex becomes underresolved. The variable-resolution LTH vortex initiated in the low resolution region follows the IKE curve of the uniform coarse solution until it transitions into the high resolution nest at around day 2.5. In this run, the energy loss levels off as the high-resolution grid is able to maintain the weakened remnants of the initial vortex.

In both of the variable-resolution cases, the slope of the IKE curve (rate of energy loss) is approximately the same as the uniform case which corresponds to the part of the mesh it is in. When either the HTL or LTH vortex is in the high-resolution region, its IKE curve is flat (near zero slope, no energy loss) since the vortex is resolved on the finer grid. When both the HTL and LTH vortices are in the coarse

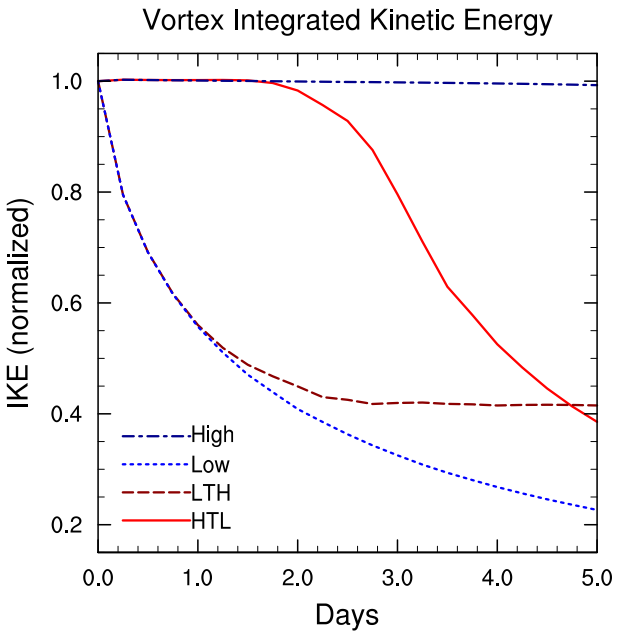

Figure 2.4: Integrated kinetic energy (IKE) for dry vortices in high and low-resolution uniform grids as well as VR grids spanning both grid spacings. Energy is normalized to initial vortex value at time $t = 0$

region, they lose energy at roughly equal rates (negative slope), and the slopes of both curves approximate the loss of energy of the control vortex in the coarse region. This indicates that the presence of a transition region is not adversely affecting any of the vortices. All changes in the dynamical structure of the vortices in both the HTL and LTH grids can be predicted and verified using the results of the test case within a standard, uniform grid.

2.4 Idealized tropical cyclones on an aquaplanet

2.4.1 Tropical cyclones and mesh transition regions with full physics

As a more complex test which is more suitable for judging the variable-resolution's ability to simulate realistic atmospheric features, CAM-SE is initialized with a warm-core vortex in axisymmetric hydrostatic and gradient-wind balance in an aquaplanet configuration (Reed and Jablonowski, 2011). Aquaplanet simulations have fixed SSTs

and no continents. Unlike the dry vortex setup, there is no background flow and Ω is set to the Earth's rotation rate of 7.292×10^{-5} s^{-1}. In addition, the planet's tilt is set to zero and the sun remains directly overhead the equator at all times resulting in a permanent equinoctial configuration.

Like the dry vortex test, this set of experiments also assesses the ability of the model numerics to propagate a bogused vortex through a grid transition region. However, the dynamical core is now coupled to a full set of physical parameterizations which add realistic feedbacks such as convection, air-sea fluxes, and boundary layer turbulence to the system. This results in the development of a warm-core tropical cyclone after 10 days.

In these simulations, a grid of $n_e = 15$ (~2°) refined to $n_e = 60$ (~0.5°) on one half of the globe (Figure 2.1) is used. This refinement is selected for three reasons. One, CAM struggles to develop tropical cyclones at 2° while capturing their general characteristics at 0.5° (Reed and Jablonowski, 2011). Two, the hemispheric refinement provides a smooth longitudinal edge at the boundary of a cubed-sphere face for the cyclone to pass through. Three, as in the dry vortex test, the transition width is designed to be as narrow as possible such that the resolution change occurs over as short of a distance as possible.

For short-term studies, the CAM5 physics package is used with the default tuning parameters. The same parameterizations and tunings are used in every column. The vortex has an initial radius of maximum winds of 250 km, and an initial intensity of 25 m s^{-1} ($\Delta p = 16.46$ hPa and $r_p = 276$ km) (Reed and Jablonowski, 2011). The vortex is centered at 10° N, 97° E which is in the coarse half of the transition region. Sea surface temperatures are set to a globally-uniform 29°C and the vortex is initialized in a quiescent environment. While there is no background steering flow, the cyclone's motion (northwesterly in Northern Hemisphere) is predictable due to the beta effect, resulting from a differential in Coriolis forces across the cyclone. This

movement allows for specification of where the initial vortex should be placed such that it transitions from the coarse mesh into the fine mesh over the ten-day simulation period. Because of this motion, the storm's core is fully contained within the high-resolution nest by approximately Day 8 of the 10-day simulation.

It is difficult to quantify to which degree the storm behaves "well" in the mesh-transition region since no reference solution exists for comparison. Unlike the previous section, changes in vortex strength and structure are the result of complicated, non-linear feedbacks in both the dynamical core's resolution of the vortex as well as the physical parameterizations. Therefore, we are required to balance both qualitative and quantitative analysis. The assessment here focuses on symmetric development of the storm, stretching or filamentation of the vortex structure during its passage from the coarse into the fine grid, and any numerical noise or wave reflection induced in the domain which does not exist when using uniform grids.

The 850 hPa wind speed and 500 hPa vorticity evolution of the storm are plotted in Figure 2.5. By the end of Day 1, the vortex seed remains closed and circular but has weakened slightly, in part due to the coarse grid's inability to resolve the core. By Day 4 the storm has moved such that it is centered in the inner half of the transition region. It remains relatively symmetric and no spurious features in the domain containing the cyclone are evident. Slight weakening due to the lack of resolution is noticeable, although the vorticity packet is still detectable at 500 hPa. By Day 6 the storm enters the fine mesh and begins intensifying as the core is better resolved. Vorticity associated with the storm's core has increased considerably. This eventually results in a recognizable tropical cyclone fully embedded in the fine mesh by Day 8, including a distinct eyewall, near-symmetric wind field, and a tight vorticity maximum collocated with the low-pressure center. The final storm structure is similar to that seen in Reed et al. (2012) which used globally-uniform CAM-SE grids to investigate tropical cyclones using the same test case but with slightly different

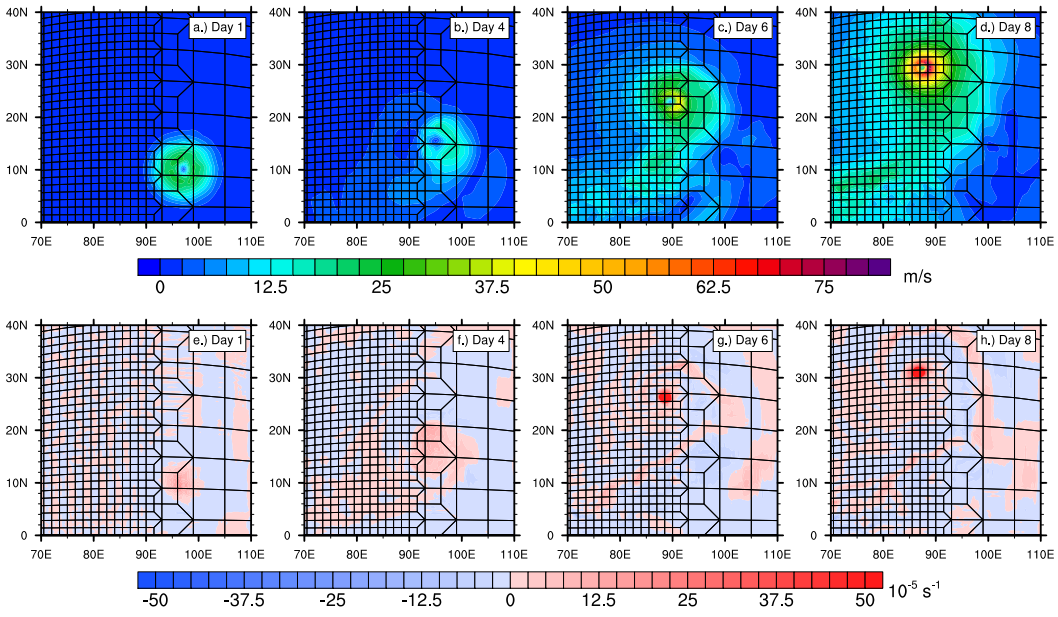

Figure 2.5: Snapshots of 850 hPa horizontal wind speed (top) and 500 hPa relative vorticity (bottom) of tropical cyclone as it moves through the grid transition region.

parameters for the initial vortex seed. No obvious numerical noise or grid imprinting is introduced in either the wind or vorticity field as the vortex moves from the coarse into the fine region. In addition, the distorted grid cells in the refinement band do not introduce any additional artifacts not associated with the storm.

To verify this result, we completed multiple simulations where the initial vortex's center longitude was shifted. This allows for the length of time it takes the vortex to enter the high resolution nest to be varied. In all cases, once the vortex enters the refinement region, it remains there for the duration of the simulation. Figure 2.6 shows the minimum surface pressure and maximum 850 hPa wind for these tests as a function of time. Circular marks denote when a storm core moves from the coarse grid into the transition region and triangular marks signify when a storm exits the transition region into the high-resolution mesh. As the storm is initialized further away (eastward) from the transition region, intensification is delayed until the vortex seed begins interacting with high-resolution cells. The overall intensity

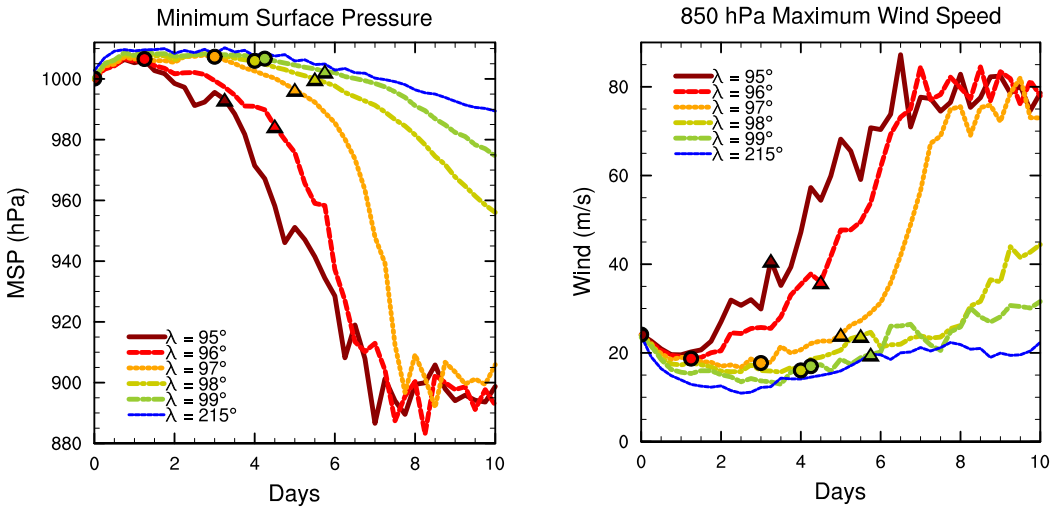

Figure 2.6: Temporal evolution of minimum surface pressure (MSP) (left) and maximum 850 hPa wind speed (right) of the cyclone test case as a function of initial longitude. Circular marks indicate storm entrance into the transition region from the coarse grid. Triangular marks denote storm exit from the transition region into the high-resolution area. The $\lambda = 215°$ curve represents a control case of a vortex that spends the entire simulation period in the coarse domain.

at Day 10 converges as the initial vortex seed is moved towards the nest (warm colored curves) since the vast majority of the cyclone lifespan is simulated at high resolution. Correspondingly, intensity curves approach the coarse simulation (blue curve) intensity as the seed is moved away.

2.4.2 Ability of refined region to match global uniform results

CAM-SE is also tested by using the same idealized cyclone seed in a globally-uniform $n_e = 60$ (~0.5°) mesh as well as in the high-resolution interior of an ne15 (~2°) mesh which is refined by a factor of four to $n_e = 60$. The latter grid is shown in Figure 2.7. The meshes have 194,402 elements (uniform) and 38,666 elements (refined) in the global domain. While the refined nest has significantly fewer elements than the uniform mesh, the grid spacing in the fine portion of the mesh is identical. Since the test case's design is specified with no background flow beyond the tropical cyclone,

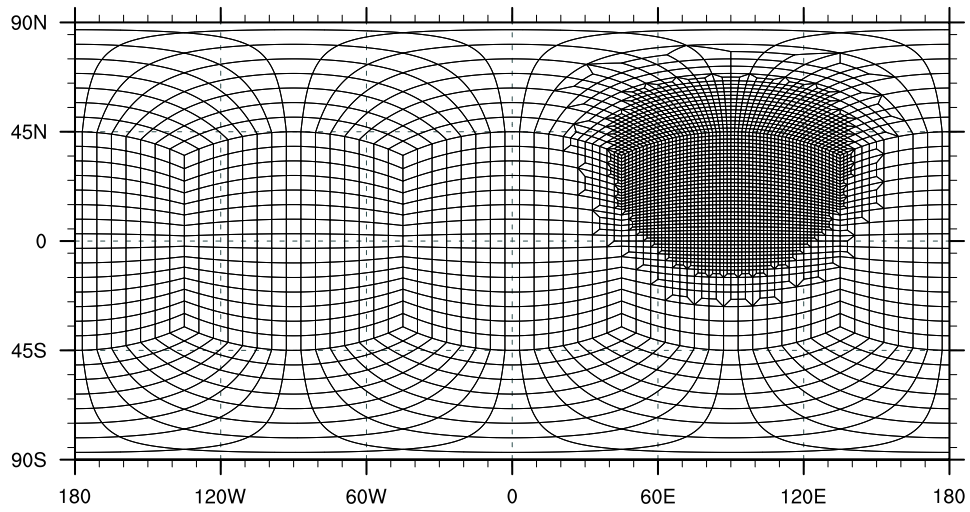

Figure 2.7: Grid used for idealized tropical cyclone comparisons. Background grid is $n_e = 15$ with a factor of four refinement to $n_e = 60$ in the high-resolution patch.

a variable resolution nest should be able to reproduce the cyclone's evolution almost identically without the need for unnecessary high resolution in the far domain.

The model is initialized with a vortex seed identical to the previous test, but now centered at 10° N and 108° E. The refined mesh is designed such that the storm is fully contained within the high-resolution region during the entire 10-day simulation. This is done to ensure that the resolution that the tropical cyclones "sees" is identical in both simulations. An ensemble of simulations is used to account for any effects of different alignments of the vortex center with respect to element edges. To accomplish this, the central position of the initial vortex is perturbed by 0.25° in both the positive and negative zonal and meridional directions. The 0.25° offset is designed such that the simulations span roughly the full width between adjacent spectral element nodes in an individual cell. Including diagonal perturbations, 18 simulations are completed including 9 with the globally-uniform $n_e = 60$ model and 9 with the $n_e = 15$ variable-resolution grid with refined $n_e = 60$ patch.

Figure 2.8 shows the temporal evolution of the minimum surface pressure and

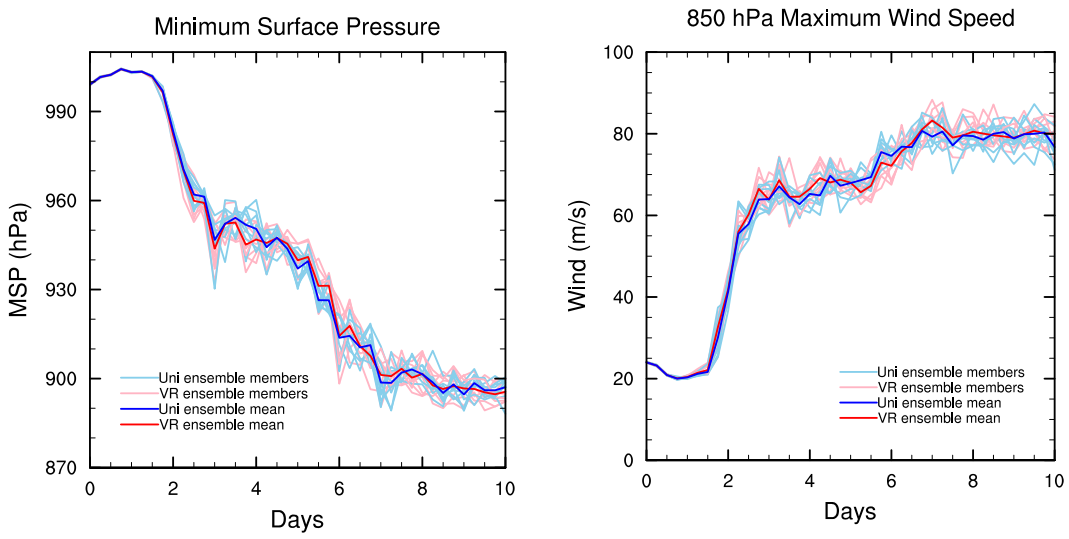

Figure 2.8: Temporal evolution of minimum surface pressure (MSP) (left) and maximum 850 hPa wind speed (right) of the cyclone test case in a globally-uniform (Uni) model (blue) and variable-resolution (VR) nest of equal grid spacing (red). Ensemble members are shown in light colors while ensemble means are denoted by darker lines.

maximum 850 hPa wind speed of the cyclones as a function of time for all 18 ensemble simulations as well as the ensemble mean for both grids. Any small differences between the two cases remain well within the ensemble envelope of storm development. Figure 2.9 shows the 850 hPa wind for four of the ensemble members (two uniform (labelled as UNI-1 and UNI-2), two variable-resolution (VR-1 and VR-2)) after 5 (top) and 10 (bottom) days. Good agreement exists in the storm's overall spatial extent, size of the eyewall, and location within the storm core of the maximum winds. Features such as an inflow band to the southeast of the storm are also well-matched in radial location and strength. These results clearly demonstrate the refined mesh's ability to match the simulation quality of the traditional uniform grid with significantly fewer degrees of freedom.

One large benefit derived from such refinement is the ability to target computing resources in regions where the modeler is most interested – in this case over the cyclone. The ratio of elements in the refined grid to those of the globally-uniform

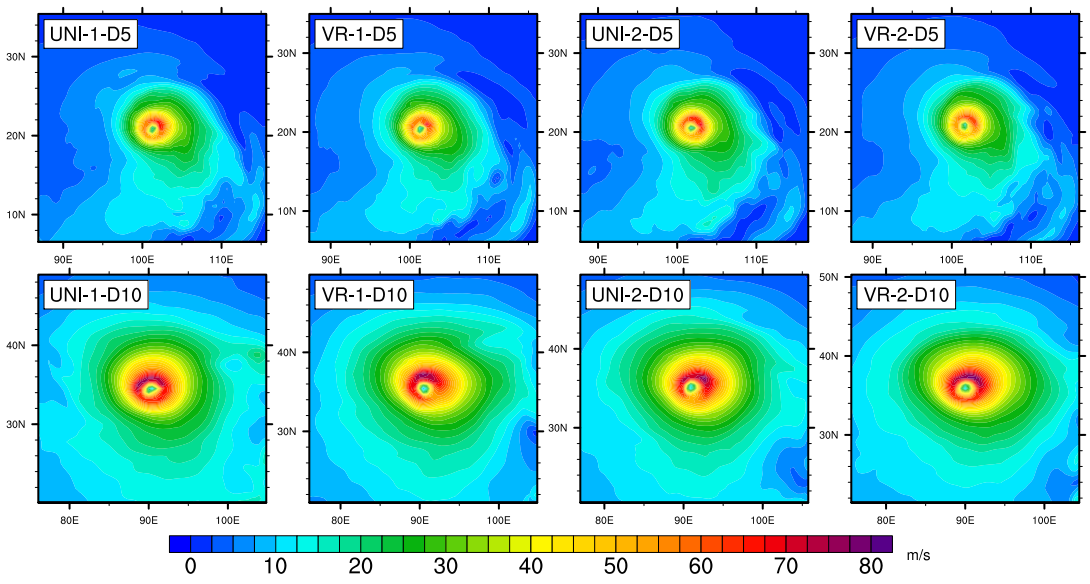

Figure 2.9: 850 hPa horizontal wind for two ensemble members of both the globally-uniform (UNI1 and UNI2) and variable-resolution (VR1 and VR2) runs in Section 2.42.4.2. The top row is cyclone winds at Day 5 (D5) and the bottom row is winds at Day 10 (D10).

grid is equal to 0.199. Figure 2.10 shows the computational runtime of each ensemble simulation on a 72 processor Linux cluster normalized to the average runtime of the uniform simulation. The model time step is identical for both grids since it is restricted to each grid's finest scale and the high-resolution patch in the refined case is of equivalent resolution to the uniform mesh. The light blue (uniform) and pink (variable-resolution) bars represent the post-initialization runtime of the model for each of the ensemble members while the dashed lines are the 'expected' runtime assuming a linear scalability of wall clock time with the number of elements in each mesh. The fact that the variable-resolution mesh produced essentially identical results to the globally uniform simulation at approximately 20 % of the computational cost highlights the potential improvements that can be made in GCM modeling of tropical cyclones by utilizing variable resolution, especially for individual case studies or projects involving regional modeling of cyclone behavior.

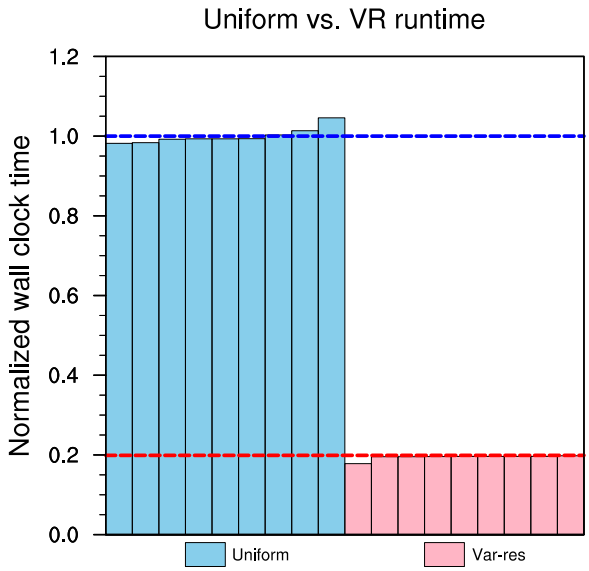

Figure 2.10: Normalized wall clock time for idealized tropical cyclone simulations in the globally-uniform mesh (light blue) and the variable-resolution grid (pink). The dashed lines indicate the theoretical scaling assuming model run time scales linearly with number of mesh elements.

2.5 Year-long aquaplanet climate experiments

As an additional level of complexity, longer simulations were completed on grids with a refined region analogous to an ocean basin in the Northern Hemisphere. The grid is similar to the grid discussed in the previous section (Figure 2.7), except the refinement patch is increased to $n_e = 120$ (~0.25° or 28 km horizontal grid spacing) and is displaced slightly southward to allow the patch to include a portion of the Southern Hemisphere. The high-resolution area is roughly the size of the north Pacific Ocean. The prescribed zonally-averaged SSTs follow the distribution:

$$SST(\varphi) = T_{max}\left(1 - sin^4\left(\frac{\pi\varphi}{2\varphi_{max}}\right)\right) \tag{2.3}$$

where T_{max} is the temperature at the equator (35°C), φ is latitude, and φ_{max} max is 60°. SSTs beyond 60° of latitude were fixed at 0°C. In order to simulate a necessary, summer-like SST distribution at latitudes with sufficient planetary vorticity

for tropical cyclogenesis in both hemispheres, T_{max} is chosen to be larger than the climatological mean and the meridional gradient is slightly flatter in mid-latitudes than observations. This results in a profile that is approximately 2°C warmer in mid-latitudes than the observed annual-mean zonal-mean SSTs. The sun is centered over the equator resulting in a state of perpetual equinox.

Over long time integration periods such aquaplanet simulations with symmetric SSTs evolve to a statistically steady state which shares similarities with the observed climate system (Neale and Hoskins, 2000). The similarities include mid-latitude westerlies with alternating high and low pressure systems as well as tropical easterlies with wave and convective features. This setup represents an intermediate-complexity test between simple, short-term, deterministic test cases such as those in Section 2.4 and more complex model setups which couple a full atmospheric model to corresponding land, ocean, or sea modules.

Simulations described here were run for 27 months, with the first three being discounted from analysis as model spin-up. Unlike Section 2.4, the CAM4 physical parameterization package was used in these studies as the effect of the new microphysics packages in CAM5 in long-term simulations with prescribed aerosol fields (required for aquaplanet simulations) is still a topic of ongoing research. We note that our time-averaged precipitation response to locally increased resolution (not shown) is similar to that seen in Rauscher et al. (2013). Refinement produces a local maximum in precipitation slightly downstream of the center of the high resolution patch. This response is not related to the dynamical core, but rather the grid scale incognizance of the CAM4 physics package. These sensitivities will be discussed in the next chapter. In general, developing new subgrid physical parameterizations for VRGCMs is an area of ongoing research.

An instantaneous sample of both the 500 and 200 hPa relative vorticity fields during the simulations is shown in Figure 2.11. The transition regions are outlined

in black, with the highest resolution ($n_e = 120$) being inside the innermost contour. There is increased resolution of small-scale features in the innermost mesh, in large part due to more intense convective processes occurring at the smaller grid scales. In the 200 hPa (lower) plot, a vorticity filament stretches from the northeast quadrant of the refined path to the western quadrant with no deformation as it spans the transition region. An extratropical low pressure center to the north of the refinement (centered at approximately 55°N, 80°E) also drags a corresponding cold front into the high-resolution area with similar results. A tropical cyclone generated by the simulation can be seen as a vorticity maximum near 25°N and 60°E.

Figure 2.12 depicts trajectories of tropical cyclones within the two-year aquaplanet simulation. Cyclones were detected using the method outlined in Vitart et al. (1997) including the updates from Knutson et al. (2007). The existence of a surface pressure minimum and collocated vorticity maximum, a warm core, and a threshold wind speed of 17 m s^{-1} near the ground are all required. The results from applying the cyclone detection algorithm are in agreement with Walsh et al. (2007) who argued that tropical cyclone detection in GCM output is strongly dependent on model resolution. Given a threshold of 17 m $^{-1}$, the coarse ($n_e = 15$) grid does an insufficient job of generating storms that meet the basic definition of a tropical cyclone. However, in the regions where the resolution is increased, the ability of the model to resolve storms which surpass the minimum criteria improves greatly. Almost all detected storms in this simulation are detected within the high-resolution domain. This relationship between resolution and cyclone detection is in good agreement with recent high-resolution tropical cyclone modeling studies (e.g. Walsh et al. (2013), Strachan et al. (2013), etc.) which have shown improved simulated cyclone intensity skill with increasing resolution.

Figure 2.13 shows the pressure-wind relationship for CAM-SE (red dots) compared to globally observed tropical cyclones (blue squares) from the IBTrACS database

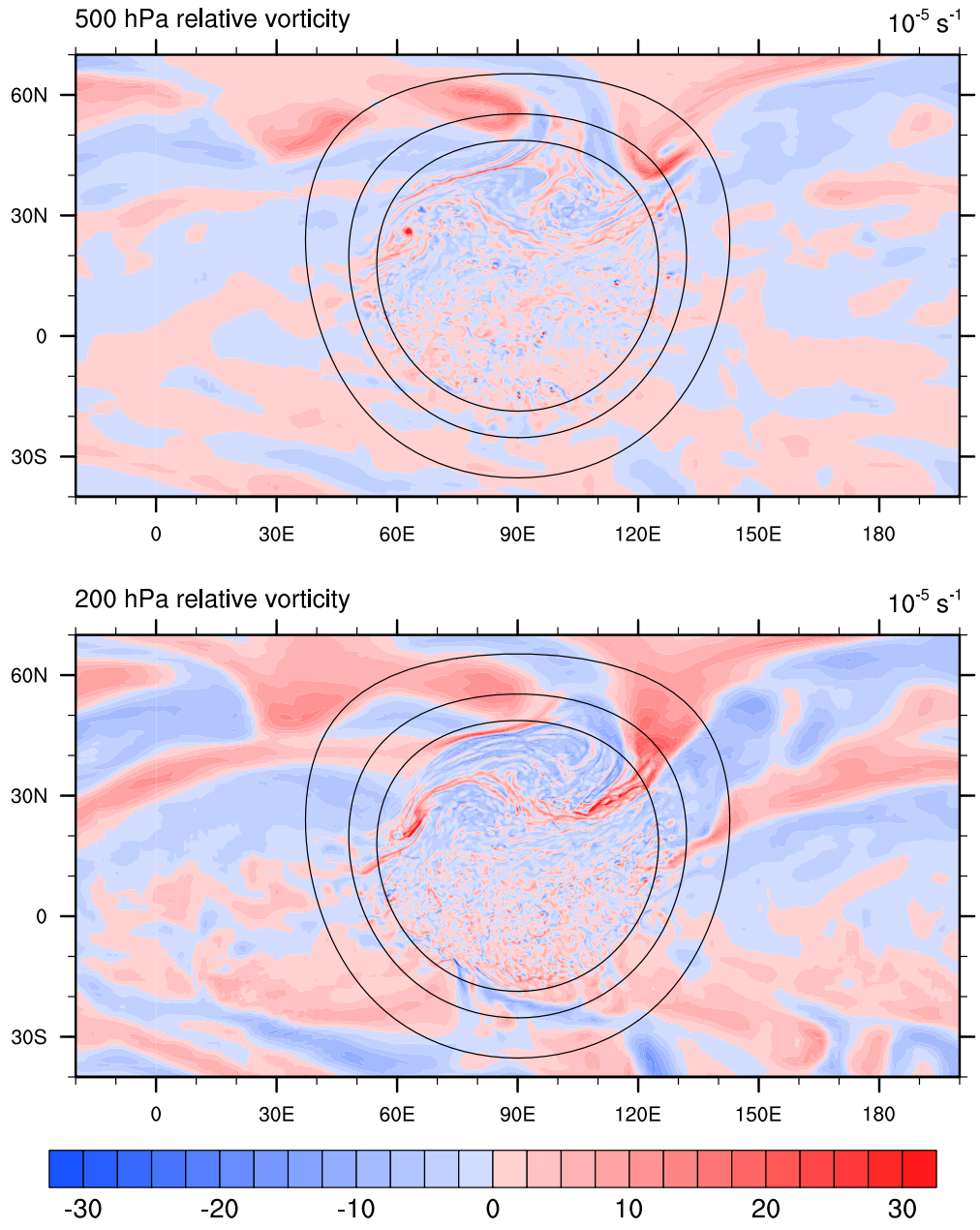

Figure 2.11: Horizontal plot of relative vorticity (10^{-5} s^{-1}) at 500 hPa (top) and 200 hPa (bottom) at Day 202 in the aquaplanet simulation. The red vorticity maximum in the top plot near 30°N and 60°E is a tropical cyclone generated by the simulation.

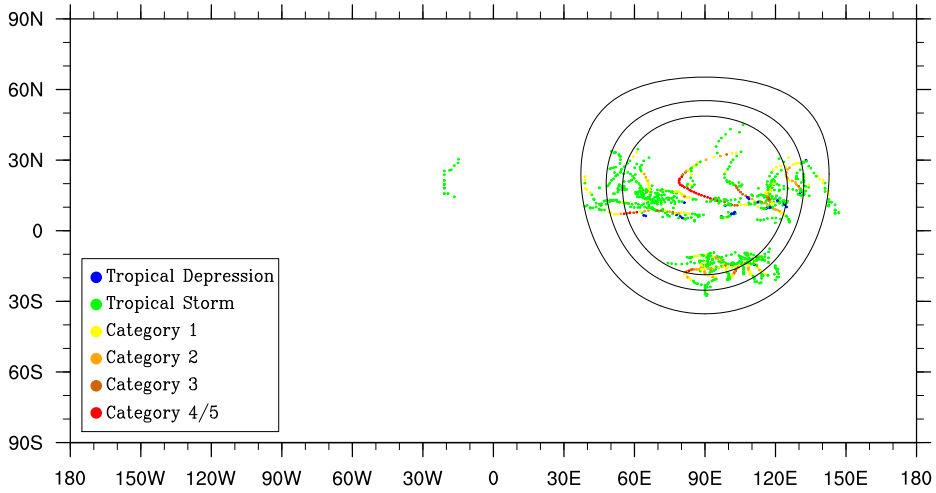

Figure 2.12: Trajectories of tropical storms in aquaplanet simulation. Colors indicate intensity on the Saffir-Simpson scale.

(Knapp et al., 2010) for the period 1981 to 2008. A quadratic least squares regression fit is shown for each distribution (solid lines). The wind is regressed from the lowest model level to 10 meters through the use of a logarithmic wind profile (Arya, 2001). We note that it is calculated instantaneously, as opposed to observations which are generally averaged over a 10-minute period. As shown in Figure 2.12, the majority of storms are found in the high-resolution region, therefore, the CAM-SE data points are generally representative of cyclones in the 0.25° (~28 km) mesh.

Even with highly favorable atmospheric conditions (ocean-covered planet, high SSTs), the simulated tropical cyclones are more clustered towards weaker intensities than the observed distribution. The slope of the CAM-SE pressure-wind curve is slightly tilted toward the left relative to observations, implying that the model does a slightly better job representing cyclone intensity by minimum surface pressure than 10-meter wind speed. This result is similar to that seen in other global experiments such as Knutson et al. (2007) and Chen and Lin (2012). However, we emphasize that these simulations are constructed to generate a highly conducive environment for tropical cyclone development and, by definition, do not include basin-dependent

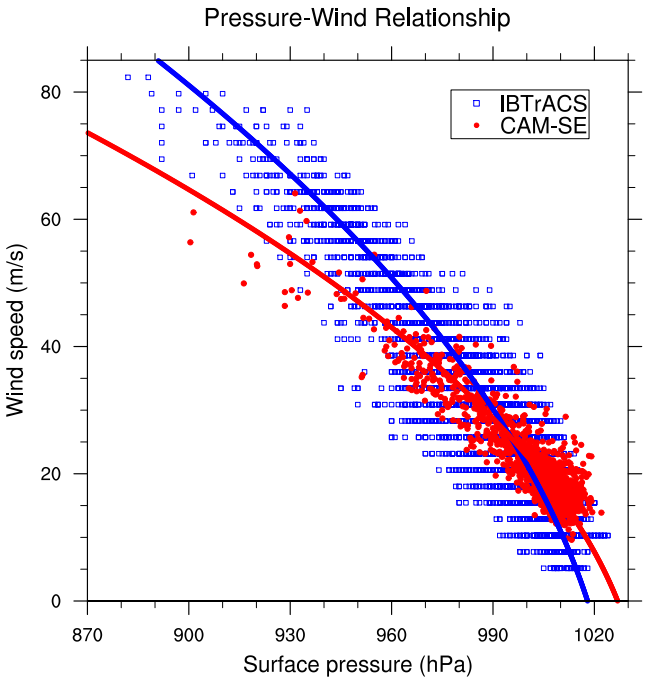

Figure 2.13: Pressure-wind relationship for CAM-SE (red dots) and IBTrACS observations (blue squares). Solid lines are quadratic least squares fit.

parameters (environmental surface pressure, land masses, etc.) that may affect the relationship between central pressure of the storm and its corresponding wind speed. More sophisticated fully-coupled climate simulations are needed to draw more definitive conclusions about the simulated intensity profiles of tropical cyclones within CAM-SE.

Figure 2.14 shows a fully developed cyclone which formed in the refined region during the first year of the simulation. A concentric wind field with an intensity maximum in the eyewall surrounding a calm eye is seen in the 850 hPa wind field (Figure 2.14a). The modeled cyclone exhibits features such as a circular precipitation maximum in the cyclone's core region as well as spiral rainbands as indicated by the simulated radar reflectivity in Figure 2.14b. In addition, the longitude-height cross section of the wind speed exposes a tilted eyewall (2.14c) and the temperature deviation from the environmental background state demonstrate that the cyclone possesses a deep warm core (2.14d). The storm reaches a minimum surface pressure of 900 hPa

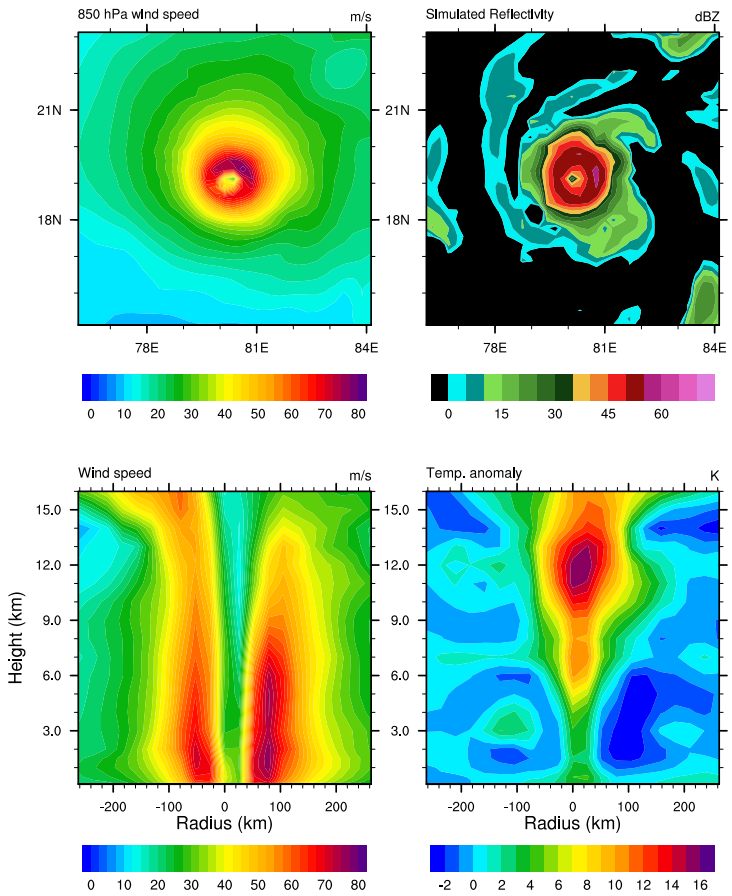

Figure 2.14: Snapshot of the strongest tropical cyclone in the aquaplanet simulation near peak intensity showing 850 hPa wind (top left), simulated radar reflectivity (top right), longitude-height cross section of the horizontal wind (bottom left) and temperature anomaly (bottom right). The radius denotes the distance to the vortex center as defined by the surface pressure minimum.

with a maximum near-surface wind speed of 75 m s^{-1} (165 mph). While the ability of CAM-SE to produce realistic cyclones at high-resolutions has been previously demonstrated, this particular refinement setup allows for an ocean-basin regional simulation of tropical activity at ~28 km with the same computational demand that would be required for a simulation of ~60-70 km without refinement.

The fact that the center of the high-resolution patch is displaced northward allows for the transition between grid scales to occur at latitudes closer to the equator in the Southern Hemisphere. This permits the generation of cyclones in the Southern

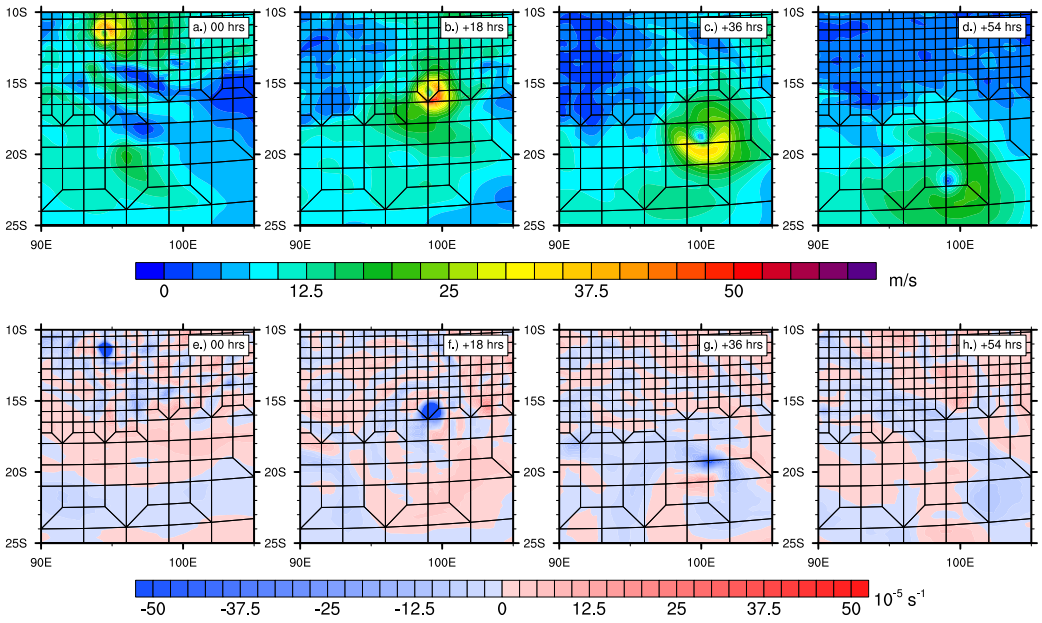

Figure 2.15: 850 hPa wind speed (top) and 500 hPa relative vorticity (bottom) evolution of a cyclone in the Southern Hemisphere which formed in the high resolution nest and passed into the coarser global nest.

Hemisphere which may exit the fine mesh as tropical cyclones. This is in contrast to the Northern Hemisphere where the mesh's spatial extent generally allows cyclones to transition to extratropical systems before leaving the refined domain. Figure 2.15 shows the temporal 850 hPa wind evolution of a cyclone passing out of the refined region as well as the corresponding relative vorticity field. As in Section 2.3, the model qualitatively maintains the closed, symmetric nature of the vortex structure without any noticeable numerical error at the boundary or wave reflection back into the refined region. The radius of maximum winds expands outwards (Figure 2.15a-d) and the 500 hPa vorticity maximum associated the storm (Figure 2.15e-h) weakens as the coarse-grid region is unable to resolve the previously intense cyclone. The storm weakens below the objective detection threshold soon after leaving the high resolution nest. No observable shifts in storm track associated with the transition region are observed with this particular system, or any of the other storms which leave the fine grid during the simulation.

2.6 Summary

This chapter investigates the potential of using variable-resolution GCMs, in particular, CAM-SE, to model tropical cyclones. Advecting dry vortices through transition regions on the sphere shows that the CAM-SE numerics behave appropriately when moving features between different grid scales, even with abrupt transition regions. Kinetic energy decay curves show that vortices in variable-resolution regimes behave identically to their globally-uniform, same-resolution counterparts. The transition between regimes appears seamless and smooth, owing to the advantages of CAM-SE's high-order numerical accuracy.

Using idealized vortex seeds, but coupling to the full CAM physics package, adds another level of complexity to the series of tests. Tropical cyclones passing into mesh transition regions are well-maintained and expected storm intensity increases/decreases are observed when cyclones move into/out of refined areas. No observable wave reflection or grid imprinting is seen in any state variable fields provided that hyperviscosity is scaled properly. These results also imply that this method is appropriate for adopting a two-way nesting setup which allows for information from the high-resolution region to "feed back" into the coarse domain, thereby allowing the fine-scale structure which develops in the refined nest to play a role in the global energy budget.

Starting with the same vortex seed, tropical cyclones in a regionally-refined mesh are nearly identical to those simulated at the corresponding (and more computationally-intensive) globally uniform resolution. This supports the dry vortex results which show that the numerics behave identically when a feature is simulated in a full globally-uniform model and that model grid's corresponding variable-resolution nest. This opens up the potential for models with variable-resolution capability (such as CAM-SE) to be used in case studies of idealized or historical tropical cyclones at high-resolutions for a much more feasible computational cost.

Finally, more complex, long-term, climate runs on an aquaplanet show that refinement supports spontaneous generation of tropical cyclones in regions of high resolution. Storm origin location corresponds directly to the high-resolution nest, underscoring the need for high-resolution to simulate cyclones in GCMs which approach observed intensities. At approximately 28 km grid spacing, these storms exhibit features common to tropical cyclones including calm eyes, tilted eyewalls, and warm cores. There is no sign of wave reflection or other numerical noise induced by the transition region when features such as horizontal wind and vorticity are plotted at any point during the simulation. The variable resolution grid used for these tests allows for the 28 km (~0.25°) nest at the same computational cost of approximately a 60-70 km globally-uniform model simulation, representing more than a factor of two increase in resolution for a specific region of interest.

These results are promising first steps in developing a framework which will allow variable-resolution GCMs to offer a new tool in modeling tropical cyclones at resolutions previously unavailable to the global modeler. Chapters III and IV will investigate the performance of existing CAM physical parameterizations in a variable-resolution model. Chapters IV and V will detail results of coupling variable-resolution CAM-SE to active land, ocean, and ice models with the Community Earth System Modeling framework (CESM).

CHAPTER III

Aquaplanet experiments using CAM's variable-resolution dynamical core

3.1 Introduction

The past few decades have seen massive improvements in the performance of global atmospheric general circulation models. One important factor behind these gains is the decrease in horizontal grid spacing, allowing for direct resolution of features at smaller spatial scales. Better representation of processes such as precipitation, clouds, and turbulent transfer of heat, momentum, and moisture has contributed to quantifiable increases in model skill (Kalnay, 2002; Lackmann, 2011). The main restriction in achieving improved horizontal resolution is the processing ability and memory constraints of the system used to run the model. As computational ability has improved, horizontal resolution has generally increased at a similar rate.

In some situations, modelers may be only concerned with a solution at a regional level. There are many reasons why this may be the case – making a local weather forecast, simulating regional climate, or comparing model output to observational statistics gathered locally. Traditionally, the use of limited area models (LAMs) (sometimes referred to as regional climate models) has allowed the achievement of these goals without expending extraneous computational resources in locations not

critical to the scientific question at hand. Assuming computational burden is approximated by the number of grid cells tiling the domain, a LAM is an effective way of eliminating "wasted" resources used to calculate a solution which is not of interest to the modeler (ex: a scientist forecasting northern hemisphere tropical cyclones may not be immediately concerned with Antarctic dynamics).

Since LAMs are not global in nature, they require external forcing via lateral boundary conditions (LBCs) to drive the domain. Typically these LBCs are derived from a coarser, global model. In many cases, these driver models use different numerical formulations or physical parameterizations compared to the LAM. This may introduce non-physical biases into the child LAM (Laprise et al., 2008). In addition, there are questions regarding the well-posedness of prevalent flow-relaxation LBCs (McDonald, 2003) and whether commonly used one-way nesting (the LAM "sees" the external boundary conditions but provides no feedback) properly allows for regional impacts of features requiring high-resolution (ex: tropical cyclones, mountain meteorology) to influence the global circulation.

Variable-resolution general circulation models (VRGCMs) may help serve to bridge the gap between global, uniform-grid GCMs and LAMs. These models are global in nature but generally use statically refined meshes to regionally increase resolution. A variable-resolution mesh that is high-resolution in a local region but significantly coarser over the rest of the globe has far fewer elements than a standard, global, high-resolution mesh. This decreases the total number of degrees of freedom in the problem, reducing the wall clock time required to complete the integration. However, since the model remains global in scope, it eliminates the need for externally-forced boundary conditions and unifies the global background circulation and the solution within the high-resolution nest. Since the same dynamical core and physics package can be used for all grid cells, biases introduced by the use of a different "driver" model can be minimized, although the magnitude of this improvement is intrinsically

conditional on the resolution sensitivity of the VRGCM's physical parameterizations.

Aside from studying regional weather or climate, VRGCMs can also be used as a key validation tool in assessing the resolution scalability of sub-grid physical parameterizations in globally-uniform simulations. Long-term climate simulations with a globally-uniform grid are typically expensive and, even with recent improvements in computer performance, generally require large blocks of wallclock time on massively parallel systems. As model resolution is increased, a thorough analysis is required to determine if the existing subgrid parameterizations perform adequately at the new horizontal grid spacings. Poorly-defined or poorly-tuned physical parameterizations can lead to a degradation of skill score and an unphysical climate. VRGCMs allow for multiple grid spacings within a single model run, meaning a suite of simulations at different resolutions used for tuning can be replaced by cheaper, single simulations. These simulations can help isolate performance changes in parameterizations that manifest themselves as changes in climate statistics with resolution and easily help researchers target specific facets of a model as areas for improvement.

A perhaps unintended side effect of introducing local refinement to global models has been a discussion on how to properly evaluate a model with non-uniform meshes. St-Cyr et al. (2008) and Ringler et al. (2011) both show that small patches of refinement improve a solution locally but have minimal effect on the global error. Ringler et al. (2011) also note that convergence studies should be based on the resolution in the coarsest region because the global error from these regions will dominate the solution. Guba et al. (2014) ran several idealized shallow water test cases from Williamson et al. (1992) on variable-resolution, spectral elements meshes resulting in the same conclusions as found in St-Cyr et al. (2008) and Ringler et al. (2011). Therefore, we choose here to focus on qualitative results of introducing variable resolution into coupled aquaplanet simulations.

In this chapter we have two primary goals. One, we aim to evaluate the per-

formance of mesh refinement in the Spectral Element option of the Community Atmosphere Model (CAM-SE) by comparing the climatology in a variable-resolution simulation with globally-uniform model runs. Two, we discuss the scale incognizence of both the CAM version 4 (CAM4, Neale et al. (2010a)) and version 5 (CAM5, Neale et al. (2010b)) physics packages using default tunings. CAM is the atmospheric component of the Community Earth System Model (CESM) that is under development by the National Center for Atmospheric Research (NCAR) and various U.S. Department of Energy (DoE) laboratories.

The chapter is structured as follows. In Section 3.2 we discuss the model setup, including special modifications required to run CAM-SE on refined grids. In Section 3.3 we present the results of aquaplanet simulations using the CAM4 physics package. In Section 3.4 we complete the same simulations using the CAM5 parameterizations and discuss differences between the packages. We also evaluate the impact of transition regions and refined cells on equatorial waves and the frequency of precipitation rates in Section 3.5. A recent update to CAM allows us to investigate the potential differences between using a bulk aerosol model and the newer modal aerosol package in CAM5 simulations which is discussed in Section 3.6. An informal discussion of the computational cost savings is found in Section 3.7. Conclusions are presented in Section 3.8.

3.2 Experimental design

3.2.1 CAM-SE

The Spectral Element (SE) dynamical core (Taylor et al. (1997), Taylor and Fournier (2010), Taylor (2011), Dennis et al. (2012)) is one of four dynamical core options available in the Community Atmosphere Model. It became the default option (superseding the finite volume core) in CAM version 5.3.

CAM-SE uses the spectral element method to discretize in the horizontal direction, a finite-difference approach in the vertical with a hybrid sigma-pressure coordinate, and a Runge-Kutta time discretization (Dennis et al., 2012). The spectral elements are based on the cubed-sphere geometry (Sadourny, 1972; Rančić et al., 1996; Ronchi et al., 1996). Cubed-sphere grids provide for quasi-uniformity over the global domain, eliminating issues with traditional grids such as converging meridians in polar regions which typically require short time steps or polar filtering to maintain numerical stability. This setup has been rigorously tested using uniform meshes both in a shallow water model (Taylor et al., 1997) and the 3D primitive equations (Fournier et al., 2004; Taylor et al., 2007). The accuracy of the model can be controlled by selecting the polynomial degree of the basis functions on each element. The default polynomial degree in CAM-SE is selected to be three (cubic polynomials), leading to fourth-order spatial accuracy.

Since the spectral element is a highly localized numerical discretization and requires minimal communication between processors on massively parallel computer systems, it is an ideal choice for future, high-resolution climate simulations. Dennis et al. (2012) and Evans et al. (2013) have shown that CAM-SE outperforms other dynamical cores in CAM at all processor counts for 0.25° resolution and finer and also scales nearly linearly up to one element per processor. As parallel computers continue to grow in size, CAM-SE is an attractive choice for high-resolution runs.

Because CAM-SE solves the primitive equations locally on individual elements, it possesses the ability to run on non-uniform grids without significant modifications to the underlying numerical scheme. The only two restrictions to running CAM-SE on non-uniform grids are that elements must be quadrilateral, and the refinement must be conforming (meaning every edge is shared by exactly two elements). Any conforming tiling of the sphere with quadrilaterals that satisfies these two criteria is acceptable.

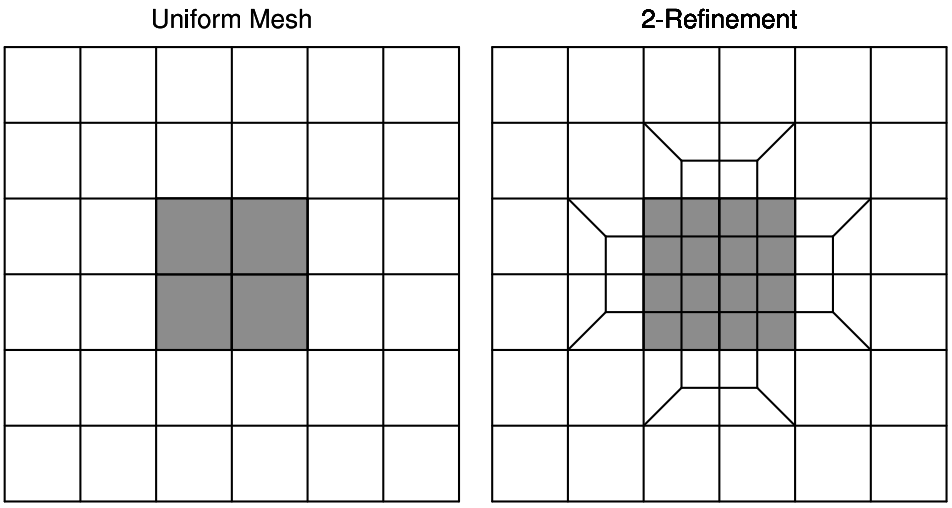

Figure 3.1: The default quadrilateral refinement in CUBIT refines the highlighted cells in the (a) uniform mesh, resulting in the (b) 2-refined mesh.

Variable-resolution meshes are generated in CUBIT[1], a geometry and mesh generation toolkit created at Sandia National Laboratories. The user selects a base resolution and subsequently refines over an arbitrary number of regions of arbitrary spatial extent. CUBIT's default quadrilateral refinement is a so-called "2-refinement." Elements in the refinement region are divided into four and those bordering the region into three (Anderson et al., 2009). This technique is shown in Fig. 3.1, and can be layered in such a way that the ratio of the edge size of the coarsest region to that of the finest region is any power of two. This technique leaves the global structure of the grid intact while only generating a narrow region containing cells distorted by the refinement where resolution transitions. This type of refinement, where resolution is increased by decreasing the area of the cubed-sphere elements while holding the basis function order fixed, is typically referred to as h-refinement.

The grid is only refined in the horizontal; each vertical column retains the same number of levels regardless of horizontal cell size. The grid is read from an external file and generated during initialization. It remains fixed for the remainder of

[1]https://cubit.sandia.gov/

the simulation. The time step used in the dynamical core is restricted by the grid's finest scale in order to satisfy the Courant-Friedrichs-Lewy stability (CFL) condition. Therefore, a globally-uniform 1° simulation will have the same dynamical time step as a 4° simulation with an area of refinement of 1°. For all cases (variable-resolution and uniform), the time step in a given run is identical for all grid cells regardless of resolution. While this means that coarse sections of variable-resolution grids are operating at shorter time steps than the CFL criteria requires, they generally constitute a small fraction of the total number of cells in a variable-resolution simulation (the majority making up the high-resolution area of interest).

Unlike the time step, the coefficients for the explicitly-added horizontal diffusion are varied with gridscale within individual runs. Fourth-order hyperviscosity is applied on individual elements for kinetic energy dissipation and numerical stability (Dennis et al., 2012). The diffusion coefficient K_4 for an individual element can be calculated as

$$K_4\left(\Delta x\right) = K_4\left(\Delta x_{ref}\right)\left(\frac{\Delta x}{\Delta x_{ref}}\right)^y \tag{3.1}$$

where K_4 depends on the length of the longest axis of the element (Δx) and Δx_{ref} and $K_4\left(\Delta x_{ref}\right)$ are a predetermined reference length and reference hyperviscosity coefficient to scale to.

The scaling power y is equal to 3.22, based on previously published tuning results for global spectral models (Boville, 1991; Takahashi et al., 2006). Therefore, $K_4\left(\Delta x\right)$ decreases by approximately an order of magnitude for every halving of grid spacing. This scaling is selected so that the hyperviscosity coefficient in each region matches the operational default CAM-SE hyperviscosity for the uniform grid of that resolution.

3.2.2 Aquaplanet experiments

The Aquaplanet Experiment (APE, Blackburn and Hoskins (2013)), and, more specifically, the setup outlined as the "control" run in Neale and Hoskins (2000), is a simplified test for atmospheric models. The model setup consists of an ocean-covered Earth, therefore eliminating the effect of topography and land on the atmospheric flow. Surface forcing comes from prescribed zonally and hemispherically-averaged sea surface temperatures that lie above the freezing level. There are no seasons, no planetary tilt, and the orbit has zero eccentricity, resulting in the model being in a state of constant equinox. Therefore, outside of the diurnal cycle in solar insolation, there is no temporal change in forcing to the climate system.

These simplifications allow for an intermediate test which is more complex than dry dynamical core experiments, but simpler than full-climate simulations which may be coupled to active land, ocean, and ice models. Even with this simplified state, aquaplanet experiments have been shown to produce realistic climate features such as transient high and low pressure systems, convectively coupled equatorial waves, and tropical cyclones.

This is an interesting experiment to run with mesh refinement because there is no 'solution' to verify against. However, since the experiment uses identical, steady-state, zonally-uniform forcing conditions; we can isolate the effects of resolution without worrying about the contribution from other model components or feedbacks. Further, the use of zonally-averaged forcing allows us to isolate zonal asymmetries which may arise from inhomogenous refinement.

Using aquaplanet experiments to test CAM is not a novel concept. Both Williamson (2008a) and Li et al. (2011) showed that precipitation extremes in aquaplanet simulations using the CAM Eulerian spectral transform dynamical core and CAM3 physics parameterization did not converge with increasing resolution and fixed physics time step. A setup utilizing the Eulerian dynamical core and CAM4 physics (T42 resolu-

Table 3.1: CAM-SE resolutions of interest to this study. Grid spacing Δx (in degrees and kilometers) correspond to the grid spacing at the center of a cubed-sphere (CS) face. Dynamics time steps (dt_{dyn}) are globally constrained by the finest grid scale in an individual variable-resolution model simulation, while the 4th-order diffusion coefficient $K_4\,(\Delta x)$ (hyperviscosity) is allowed to vary among individual elements.

Setup	CS res.	Δx (°)	Δx (km)	Cells (#)	dt_{dyn} (s)	K_4 ($m^4\ s^{-1}$)
fine	n_e120	0.25°	28	86,400	50	1.00E+13
coarse	n_e15	2°	222	1,350	600	1.00E+16
var-res	n_e15x8	varies	varies	10,609	50	varies

tion, approximately 2.8° grid spacing) was NCAR's contribution to the APE model intercomparison (Blackburn et al., 2013). Mishra et al. (2011a) used CAM4 physics and an aquaplanet to test the rainfall characteristics within an earlier version of the SE dynamical core. Rauscher et al. (2013) and Hagos et al. (2013) both used CAM4 physics to test the performance of the new Model for Prediction Across Scales (MPAS, Skamarock et al. (2012)) variable-resolution dynamical core. Aquaplanet climate simulations have also been used to investigate the representation of tropical cyclones at various resolutions in CAM (Li et al. 2013; Chapter II).

3.2.3 Model grids

Three setups are used in this study which are detailed in Table 3.1. The main difference between the three is the mesh. One run (referred to as "coarse") uses a uniform 2° (∼222 km) grid, one ("fine") uses a uniform 0.25° (∼28 km) grid, and the final simulation ("var-res") uses a grid that is 2° everywhere except for a roughly 90° × 90° patch centered on the equator that is a 0.25° mesh (with a small transition region between the two). The 90° × 90° patch is chosen so that the refinement is isolated to one face of the cubed-sphere grid. The coarse and var-res meshes are shown in Fig. 3.2. The coarse mesh contains 1,350 elements per model level, the fine grid has 86,400, and var-res has 10,609.

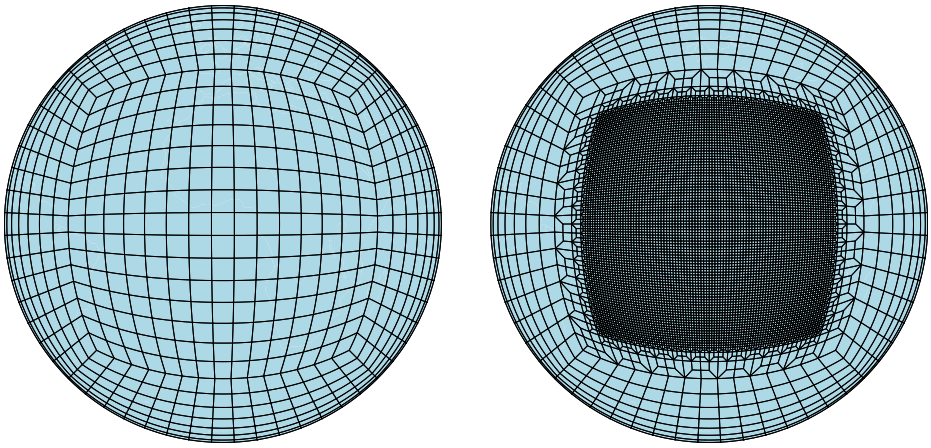

(a) (b)

Figure 3.2: The three meshes used for this study are (a) a uniform 2° resolution mesh, (not pictured) a uniform 0.25° resolution mesh, and (b) a variable-resolution mesh that ranges from 2° → 0.25°. Note that each element shown in the above plots contains additional 3×3 collocation points.

The simulations utilize the Community Atmosphere Model, version 5.1. All runs use one of two subgrid physical parameterizations packages which are options in CAM 5.1. The first set uses the CAM version 4 physics package (Neale et al., 2010a). There are 26 vertical levels and the physics routine is called every 600 seconds (10 minutes) for each simulation, regardless of horizontal resolution. The timestep is selected to match the CAM4 simulations in Williamson (2008b). These will be referred to as the CAM4 simulations. The second suite of simulations uses the CAM version 5 package (Neale et al., 2010b) with 30 levels and the physics called every 1800 seconds (30 minutes). These are the default physics time steps for each model setup at 1° (or equivalent) resolution. We have chosen to fix the physics time step because it has been shown that there is an implicit dependence of physics time step on model results (Williamson, 2013). While Williamson (2013) showed that this dependence is smaller than the change in solution from using different horizontal grid spacing, varying the physics time step would result in another degree of freedom beyond the control state of the system.

The coarse simulations are run with a 600 second dynamical time step. The fine

grid requires a smaller, 50 second dynamical time step to satisfy the CFL condition due to smaller horizontal grid spacing. The var-res simulations use the same 50 second dynamical time step since the model CFL condition is constrained by the highest resolution in the simulation. We clarify that only the dynamical time step is restricted by the CFL condition and unpublished simulations show there is very little sensitivity to different dynamical time steps.

All three simulations employ different hyperviscosity coefficients, since, as discussed in Section 3.2.1, hyperviscosity varies as a function of resolution. Where the var-res grid is identical to the coarse grid, the hyperviscosity values match, and the same is true with the fine grid. Other than those specific differences, the parameterizations are identical across all three runs. All simulations use the default physics tunings at equivalent 1° resolution in CAM, although the differences in the default tuning parameters at other grid spacings are minimal.

The two uniform mesh simulations are run for 14 months, but the first two months are considered "spin-up." Therefore, the analysis in the following sections only considers the final 12 months. The choice of two months of model spinup is supported by the findings of Williamson (2008a) who found that the model rapidly transitions to its own aquaplanet climate when starting from a closely related aquaplanet state (in our case, an equivalent spun-up APE state on a 1° uniform latitude-longitude grid interpolated to the particular CAM-SE grid of interest).

The var-res simulations are run for 50 months, with results from the last 48 months analyzed. The additional run time was given to account for the fact that, near the equator, the fine region covered just 25% of the zonal band. However, preliminary results showed little difference in climate statistics between a 14 month run and a 50 month run, implying that the simulation rapidly adjusts to grid spacing, even in the variable-resolution case.

3.3 CAM4 climatology

Two variables that have been commonly used to highlight differences between different resolutions in CAM aquaplanet simulations are cloud fraction and precipitation rate (Williamson, 2008b). We therefore pay particular attention to vertically-integrated total cloud fraction (CLDTOT) and total precipitation rate (PRECT). Unless otherwise stated, all variables presented are climatological averages over the periods discussed at the end of Section 3.2.3. Time averaging reduces variance in the results and, given the prescribed forcing, the aquaplanet climatology is zonally symmetric on a uniform mesh. Following the format of Williamson (2008a,b), we discuss global and zonal spatial averages of time-averaged data. Time-averaged contour plots are also included to highlight the effect of refinement.

The simulated global average total precipitation rates in CAM4 are 2.91 (coarse), 2.98 (var-res) and 3.09 (fine) mm day^{-1}. These values are in good agreement with the results of Mishra et al. (2011a) who produced a time-averaged, global precipitation rate of 2.95 mm day^{-1} in a 1° simulation using an earlier version of CAM-SE with CAM4 physics.

Due to the location of the refinement region, care had to be taken when determining where to average spatially to compare the var-res grid. Simple global averages disproportionately weight latitudes where the model resolution is coarse in all simulations. Figure 3.3 outlines the area of refinement and illustrates where the zonal / global averages were taken for the var-res grid. The low-resolution region of the var-res grid extends eastward from 60° E to 60° W, while the high-resolution region spans 30° W and 30° E. All averages (including the ones on the uniform grids) are taken between 25° S and 25° N so that the mid- and high-latitudes (where there is no high resolution in any of the simulations) do not affect the statistics. All spatial averages are area-weighted, despite being discussed in terms of latitude-longitude boxes.

There are two components to total precipitation in CAM; large-scale (resolved,

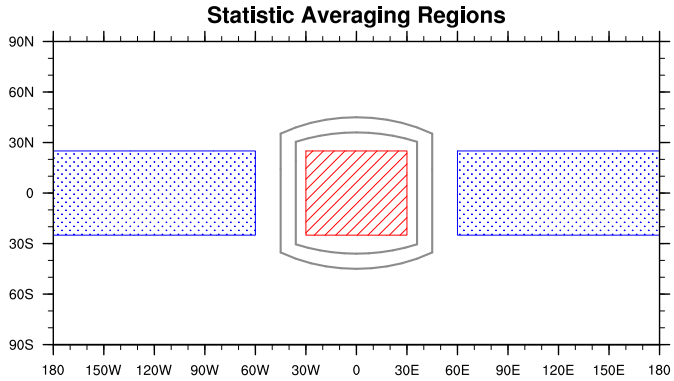

Figure 3.3: For Tables 3.2 and 3.3 and Figs. 3.4 and 3.8, the "fine" region statistics in var-res simulations come from the red (hatched) area while the "coarse" region statistics come from the blue (dotted) area. The edges of the transition region are outlined by the two black boxes.

or sometimes referred to as "stable") precipitation and unresolved precipitation resulting from the subgrid convective parameterizations. Since large-scale precipitation is the resolved component of rainfall that is removed from the supersaturation of specific humidity in a gridbox, smaller grid spacing should improve the dynamical core's ability to resolve convergent and vertical motions responsible for the production of precipitation. Therefore, if total precipitation (large-scale plus convective) is to remain scale-independent in climate models, there should be roughly a 1:1 tradeoff between any increase in large-scale precipitation and decrease in convective precipitation as resolution is increased. This trend should theoretically continue until all precipitation is fully resolved in the model, although the ability to run climate models at cloud-resolving (or finer) scales for significant lengths of time is still many years away. We will further discuss this scaling later.

Table 3.2 shows select area-weighted, time-averaged climate statistics in the equatorial band (25° N/S) for the three CAM4-SE simulations. Convective precipitation rates (PRECC) decrease as resolution is increased, whereas large-scale precipitation rates (PRECL) increase. The absolute increase in large-scale precipitation rates outweighs the decrease in convective rainfall, which can be easily verified by the increased total precipitation rate (PRECT, sum of PRECC and PRECL). The total

Table 3.2: Time-averaged statistics for CAM4 simulations in the equatorial band. Areas used for averaging are shown in Fig. 3.3. 'Var-res' is the component of the variable-resolution simulation that corresponds to the specified grid spacing. See text for explanation of acronyms.

Variable	Units	Coarse 2°	Var-res 2°	Fine 0.25°	Var-res 0.25°
PRECC	mm d^{-1}	2.18	2.25	1.23	1.14
PRECL	mm d^{-1}	1.56	1.62	3.04	2.78
PRECT	mm d^{-1}	3.75	3.87	4.27	3.91
C/L ratio		1.40	1.39	0.40	0.41
CLDTOT	frac	0.56	0.56	0.36	0.39
TPW	kg m^{-2}	33.4	33.5	32.1	31.5

precipitation rate in the low-resolution section of the var-res grid is higher than the corresponding uniform coarse grid. Conversely, it is higher in the fine grid than the matching, high-resolution section of the var-res mesh. These results imply that the precipitation does not respond to the grid immediately, but rather, the low-res grid influences the high-res component and vice versa.

The convective-to-large-scale precipitation ratio (C/L ratio) decreases with resolution (indicating higher resolution requires less adjustment from the convective scheme due to the increased amount of resolved updrafts). The C/L ratio matches across the uniform grids and the corresponding var-res region. The cloud fraction (CLDTOT) is significantly larger in the coarse mesh and the low-resolution component of the var-res grid than in either the fine grid or the refined section of the var-res mesh. Cloud fraction shows a well matched result in the coarse resolutions, but at 0.25° grid spacing, the var-res grid has a larger fraction than the fine grid. Since total cloud decreases significantly as resolution is increased in these simulations, this again implies the coarse component of the var-res grid is likely affecting the high-resolution patch. Total precipitable water (TPW) is approximately 1-1.5 kg m^{-2} higher in the coarse simulations when compared to the fine grid scale, likely due to decreased conversion to precipitation at lower resolutions.

Zonal averages for cloud fraction and total precipitation for CAM4-SE are shown

in Fig. 3.4. Figure 3.4a compares the cloud fraction in the var-res simulation to the two uniform runs globally. These results can be compared to other models in the APE in Blackburn et al. (2013) (their Fig. 12). The solution in the coarse region of the var-res mesh (green) (poleward of 30° latitude) produces very similar results to the solution of the coarse grid (blue). At all latitudes, cloud fraction decreases as resolution is increased (fine simulation, red), with the var-res simulation tending away from the coarse run and towards the fine in equatorial regions, where roughly one-quarter of the equatorial band is simulated at high resolution. The monotonic decrease of cloud fraction as horizontal resolution is increased is a troublesome, but well-known issue with both the CAM3 and CAM4 physical parameterizations (e.g., Williamson 2008a,b; Rauscher et al. 2013; Hagos et al. 2013; O'Brien et al. 2013).

Figure 3.4b only focuses on the band between 25° S and 25° N, and also divides the var-res model into its longitudinally-coarse region (60° E to 60° W) and fine region (30° W to 30° E) as shown in Fig. 3.3. Results corresponding to the coarse portion of the var-res mesh are virtually indistinguishable from those of the global coarse mesh. In contrast, the high-resolution section of the var-res grid did not match the fine grid simulation, but rather, produced slightly higher cloud fraction near the equator. This suggests that the results in the refined domain did not quite achieve the resolution of the fine-scale simulation, but remain influenced by the flow in the coarse domain.

Similarly, Fig. 3.4c shows the zonally-averaged total precipitation rates for the global domain. There is much better agreement between the three resolutions in profile shape and intensity outside of the tropics. The fine simulation has a slightly lower and more poleward peak in the mid-latitude precipitation maximum, likely associated with a small shift in extratropical storm tracks. In the equatorial band, all three simulations show a single intertropical convergence zone (ITCZ) peak centered at 0° latitude.

This absolute maximum increases with resolution and, like the cloud fraction in

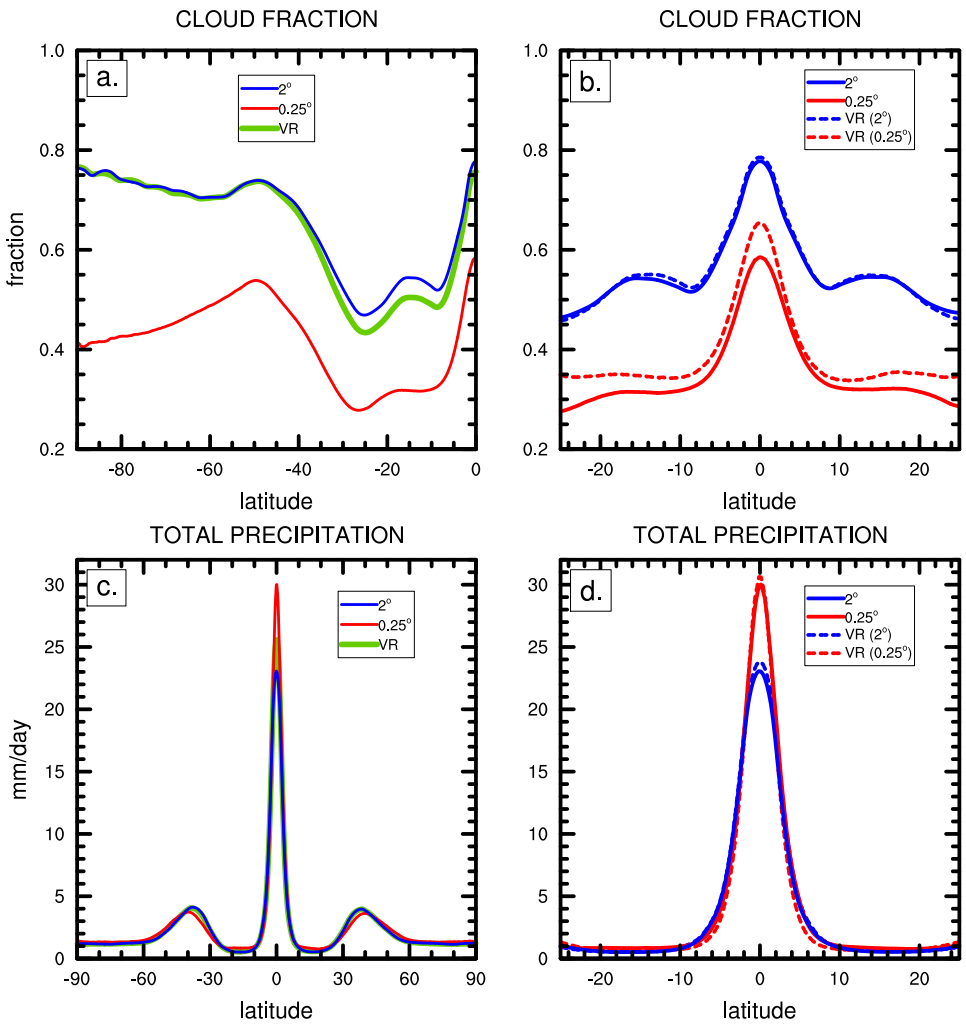

Figure 3.4: Zonal mean total cloud fraction (CLDTOT) and total precipitation rate (PRECT) using CAM4 physics. (a) Comparing CLDTOT in the uniform 2° and 0.25° meshes to variable resolution (VR). (b) Separating the fine region and the coarse region of the variable-resolution mesh near the equator. (c) and (d) are the same except for PRECT.

the equatorial band, the var-res simulation falls between the two globally-uniform simulations since its zonal average in this band is a combination of the two grid spacings. Figure 3.4d is the same as 3.4b except for total precipitation. In this case, the coarse region of the variable resolution mesh has a slightly larger average than the global coarse mesh at the equator, but is again indistinguishable outside the band of approximately 5° S to 5° N. The fine region, is well-matched with the global high resolution run at the equator, but north of 5° N and south of 5° S the global high resolution mesh produces slightly more precipitation. However, these changes are negligible at the global scale and may just be a function of the actual gridbox (discretization) locations at these latitudes.

To investigate the spatial dependence of localized refinement, we show temporally-averaged global contour plots. Figures 3.5 (cloud fraction) and 3.6 (total precipitation rate) show the simulation results for all three grids (panels a-c) in addition to the difference plots between the var-res simulation and each uniform grid counterpart (panels d-e). Figures 3.5a and 3.5c highlight the global decrease in cloud fraction with increasing resolution as seen in Figure 3.4a. The fractional decrease is relatively uniform globally, although it does maximize in the polar regions where cloud fraction decreases by nearly 50% between the coarse and fine simulations.

The extreme gridscale dependence of cloud fraction is also highlighted in the difference panels in Figs. 3.5d and 3.5e. Severe anomalies are seen associated with the region of increased resolution, both when comparing the var-res grid to the coarse and fine simulations. In addition, there also appears to be downstream impacts of the high-resolution patch as evidenced by the "tails" at approximately 25° N/S which extend eastward from the eastern periphery of the nest. This implies that, though CAM uses column physics (no knowledge of neighboring atmospheric conditions), cloud fraction does not uniformly and instantaneously assume the properties of the high-resolution nest. At the center of the latitude band where the refinement exists

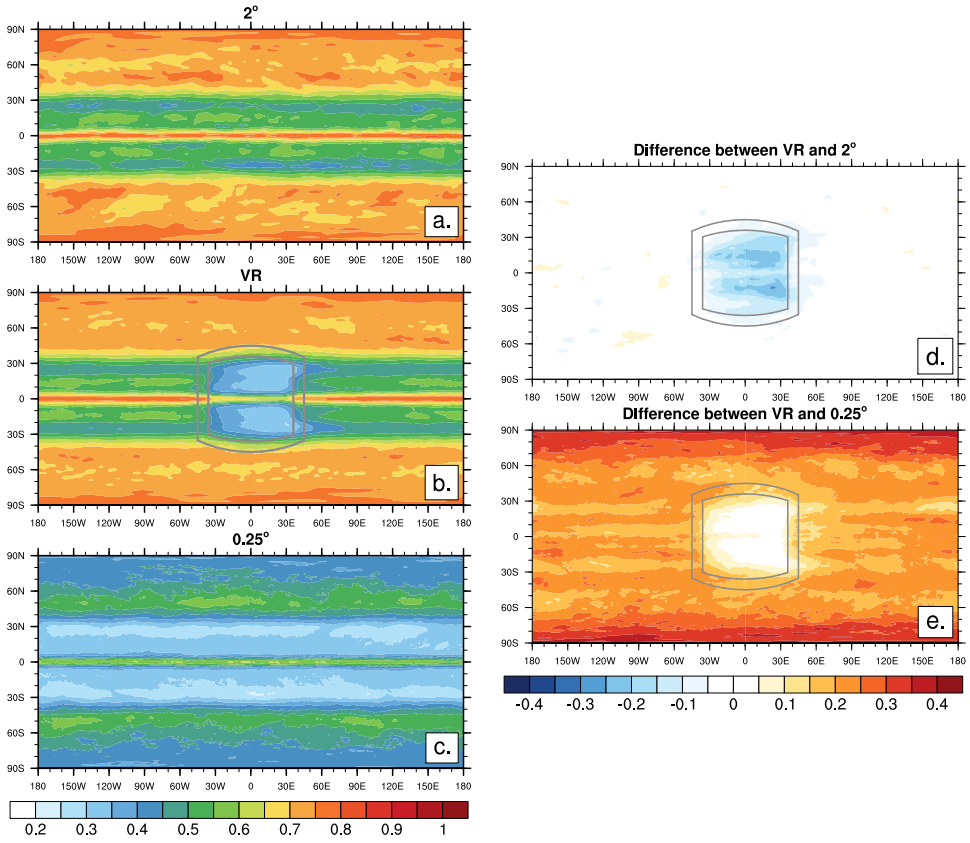

Figure 3.5: CAM4 contour plot of total cloud fraction (in percent) for (a) coarse (2°) (b) var-res (VR), and (c) fine (0.25°) simulations. The grey boxes denote the different mesh regions: inside the innermost box is the fine region, outside the outermost box is the coarse region, and between the boxes is the transition region. The difference between the var-res and coarse simulation is plotted in (d) and the var-res and fine simulation in (e).

(15° N/S), the temporally-averaged zonal flow is easterly, meaning that the majority of parcels enter the high-resolution nest from the eastern side and exit through the western boundary. However, space-time diagrams of outgoing longwave radiation (not shown) imply that these tails are associated with frontal structures which are dragged from west-to-east across the poleward side of the high-resolution patch. Parcels transiting between resolutions which are associated with these features seem to maintain "memory" of their grid spacing and require an adjustment period to acquire the physical characteristics of the new resolution upon passage through a transition area.

While the var-res contour plots exhibit an obvious signature resulting from the high-resolution patch, there is no readily apparent grid imprinting in the transition region. The fact that both the zonally-averaged and time-averaged plots show no observable spikes or other artifacts indicates the dynamical core is numerically handling the transition region appropriately. Additionally, the resolution signatures' existence shows that the var-res simulation captures the resolution signal from the globally-uniform simulations within a single model run. This is highlighted by the regions where cloud fraction matches between the var-res and uniform grids in Figs. 3.5d and 3.5e (white areas).

Figures 3.6a-c show less of a gridscale dependence when total precipitation rate is considered. All three simulations exhibit a strong equatorial peak which dominates the global average. The difference plots (Figs. 3.6d,e) show that differences poleward of approximately 10° N/S are minor, a result already implied by Fig. 3.4c. In the equatorial band, increased resolution displays a gridscale dependence, with the peak precipitation being directly proportional to the resolution of the grid. Unlike cloud fraction, precipitation appears to incur a more instantaneous adjustment to grid resolution, with positive anomalies in Fig. 3.6d associated with the increased patch of resolution spanning the entire nest end-to-end and negative anomalies spanning the

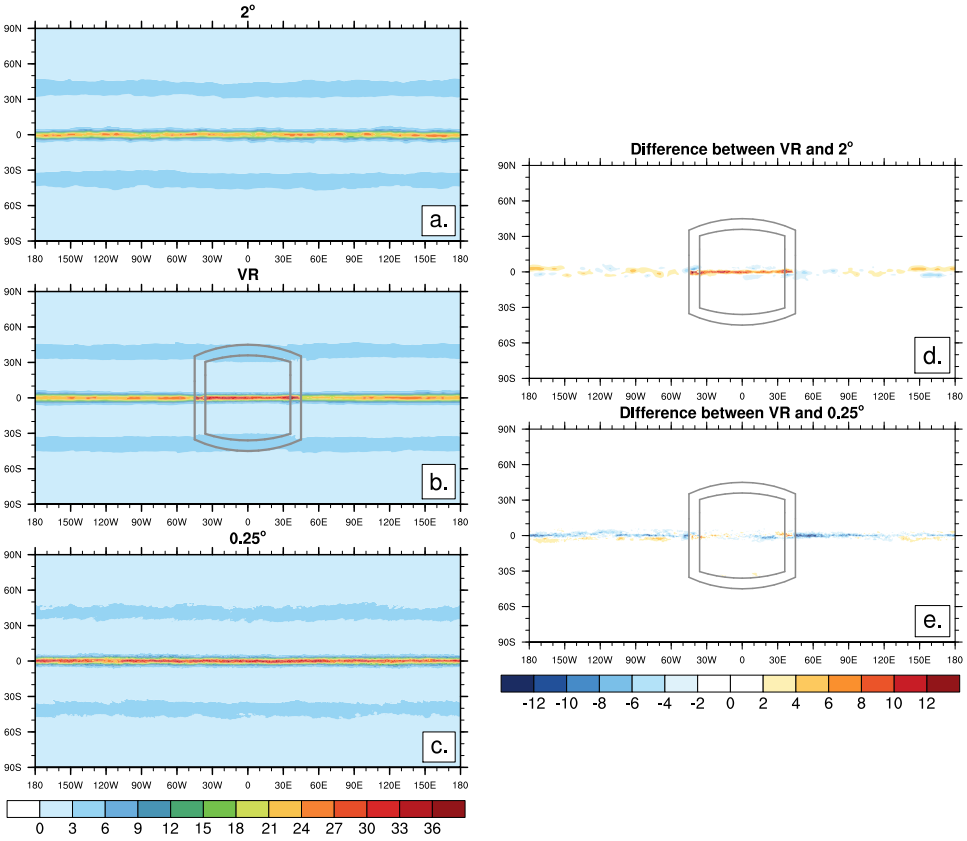

Figure 3.6: Same as Figure 3.5 except for total precipitation rate (mm day^{-1}).

entire coarse latitude band in Fig. 3.6e. This "rapid" adjustment may be because there is a much greater fraction of large-scale (resolved) precipitation (Table 3.2) in the high-resolution nest, meaning the underlying grid is the dominant driver in the bias induced by the refinement. This may be different than the cloud parameterization scheme bias which is a function of both grid spacing and the atmospheric state advected into the high-resolution region.

As first outlined in Gill (1980), zonally-asymmetric diabatic heating in equatorial regions may drive a large-scale background circulation associated with anomalous upper level divergence. In the var-res simulation, a Gill response manifests itself due to the increase in resolution; total precipitation in the high-resolution patch is increased which adds additional latent heating to the atmosphere. Variable-resolution simulations using CAM4 physics have previously been shown to suffer from this issue

(Rauscher et al., 2013). Figure 3.7a shows the zonal anomaly (deviation from the zonal mean) of the time-averaged, vertically-integrated diabatic heating. Because of the increased precipitation rate (Fig. 3.6d), condensational warming is more prevalent in the high-resolution nest. This leads to anomalous divergence, shown in color contours in Fig. 3.7b. The most significant divergence bias is on the eastern portion of the nest. This is where near-equatorial flow first encounters the high-resolution nest. Since zonally-averaged total precipitable water is higher in the coarse region (Table 3.2), this represents a rapid adjustment where moisture is quickly removed from the column by the physics routine. This release leads to additional vertical velocities, and enhanced upper-level divergence. The divergence triggers an anomalous circulation reflected in the 200 hPa eddy streamfunction (line contours, Fig. 3.7b). The anti-cyclonic (cyclonic) anomalies to the west (east) of the high-resolution patch are similar to the ones seen in Rauscher et al. (2013) (their Fig. 14a), who first highlighted the phenomenon in refined CAM4 simulations.

3.4 CAM5 climatology

Almost all published literature using aquaplanet setups in CAM have utilized the legacy CAM3 and/or CAM4 physics packages (ex: Williamson 2008a,b; Li et al. 2011; Rauscher et al. 2013, among others). Very few studies have tested the new CAM5 subgrid physical parameterization package in an aquaplanet setup. Two examples are Reed and Jablonowski (2011) and O'Brien et al. (2013). However, they focused on specific research questions (tropical cyclones, cloud scaling) as opposed to broader, general long-term statistics.

3.4.1 Differences between CAM4 and CAM5 physics

First, we highlight a few key differences between the CAM4 and CAM5 physics packages. The default number of vertical levels in CAM5 is 30 (compared to 26

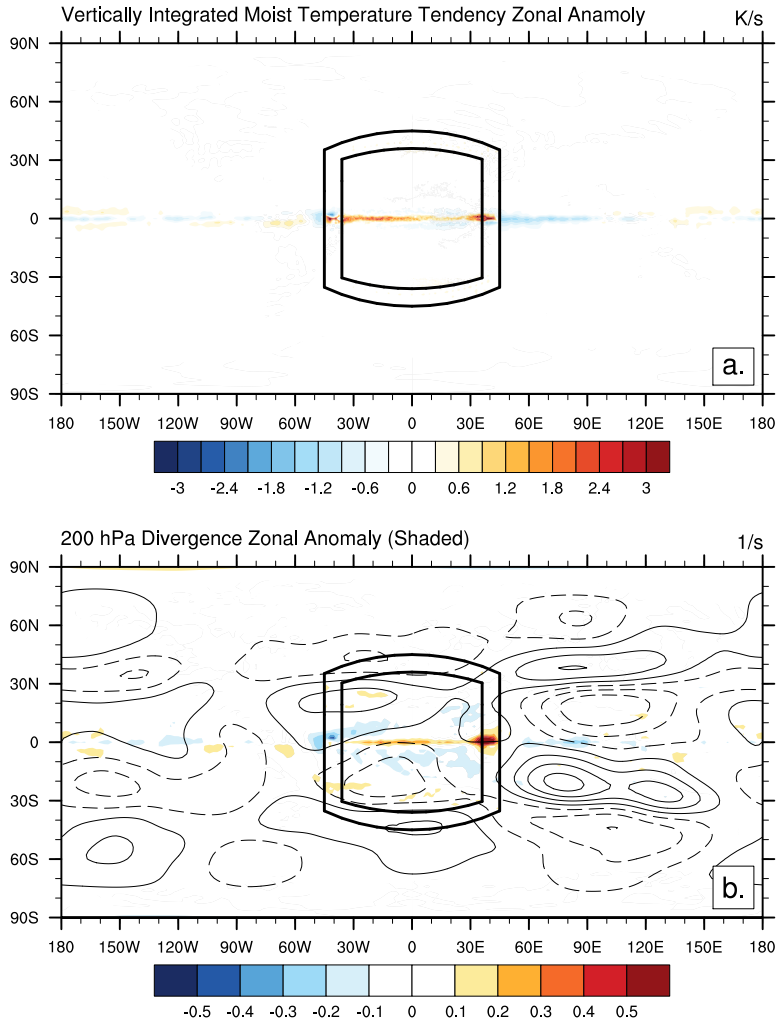

Figure 3.7: Zonal anomalies of (a) vertically integrated moist heating and (b) 200 hPa divergence (color contours) for var-res grid with CAM4 physics. In (b) the 200 hPa eddy streamfunction is contoured by 10^6 m^2 s^{-1}. Negative contours are dashed.

in CAM4). The four additional levels in CAM5 are added below 700 hPa, increasing the total number of levels below 700 hPa from 5 to 9. This resolution in the lower troposphere was added concurrently with a new planetary boundary layer and moist turbulence scheme based on diagnosed turbulent kinetic energy (Bretherton and Park, 2009). This replaced the dry turbulence scheme of Holtslag and Boville (1993) based on specified K profiles. The surface flux parameterizations and deep convective scheme (Zhang and McFarlane, 1995) remain the same between the two configurations. CAM4 uses a shallow convective parameterization outlined in Hack (1994) while CAM5 uses a newer scheme developed at the University of Washington (UW) (Park and Bretherton, 2009). Another significant change in CAM5 is the use of prognostic double moment microphysics (Morrison and Gettelman, 2008) with ice supersaturation (Gettelman et al., 2010). This is compared to prognostic single-moment microphysics (Rasch and Kristjánsson, 1998) in CAM4. A more comprehensive discussion of these and other differences between CAM4 and CAM5 physics can be found in Neale et al. (2010b).

3.4.2 CAM5 bulk aerosol model

We first run the CAM5 physics package with the prescribed aerosols within the Bulk Aerosol Model (BAM). This is the same model for aerosols used in the CAM4 simulations. The climatological dataset of aerosol mass concentrations is zonally, hemispherically, and temporally averaged to provide constant aerosol forcing which is symmetric about the equator and spatially distributed at latitudes similar to that seen in observations. This is the same setup used in Reed and Jablonowski (2011) and O'Brien et al. (2013).

Unlike CAM4, the updated CAM5 microphysics requires information about aerosols in specific modes (Morrison and Gettelman, 2008). Since the prescribed BAM does not provide that information, an internal conversion in the physics package is required

Table 3.3: Same as Table 3.2 but for CAM5 simulations.

Variable	Units	Coarse 2°	Var-res 2°	Fine 0.25°	Var-res 0.25°
PRECC	mm d^{-1}	3.66	3.59	2.25	2.68
PRECL	mm d^{-1}	0.49	0.48	1.85	1.68
PRECT	mm d^{-1}	4.15	4.08	4.10	4.36
C/L ratio		6.60	6.63	1.16	1.51
CLDTOT	frac	0.63	0.63	0.64	0.65
TPW	kg m^{-2}	32.8	32.8	31.7	31.8

to allow for mass quantities to be treated in a modal sense for each gridbox. The aerosol mass mixing ratio is first multiplied by air density to produce a mass density. This mass density is multiplied by a number-to-mass conversion and a bulk scaling factor to arrive at the number of aerosols per volume. The parameterization of Abdul-Razzak and Ghan (2000) is then used to estimate the number of activated aerosols by assuming an internal mixture within each of multiple aerosol modes. These are then passed to the relevant routines. Additional discussion detailing the use of prescribed bulk aerosols with CAM5 can be found in Bacmeister et al. (2014).

3.4.3 CAM5 results

The globally-averaged CAM5 precipitation rates are 3.15 (coarse), 3.14 (var-res) and 3.12 (fine) mm day^{-1}. These quantities represent 8%, 5%, and 1% increases over the globally-averaged CAM4 simulations, respectively. Cloud fraction also increases. All global values fall within the range of models discussed in Blackburn et al. (2013) (their Figs. 10 and 11).

Equatorial band averages for simulations using the CAM5 physics packages can be seen in Table 3.3. The convective parameterization is significantly more active in CAM5, with higher PRECC totals at all resolutions compared to CAM4. This increase outweighs the corresponding decrease in large-scale precipitation, resulting in increased total precipitation rates.

Zonal averages of cloud fraction and total precipitation are plotted in Fig. 3.8.

As shown in Fig. 3.8a, zonally-averaged cloud fraction is higher at all latitudes when compared to the CAM4 simulations (Fig. 3.4a). The distribution of cloud fraction is much less sensitive to changes in global resolution with all three distributions much closer to one another. The most dominant difference between the coarse and fine simulations is in polar regions, where there is a 5 to 10 percent decrease in cloud fraction as resolution is increased from 2° to 0.25°. In the CAM4 simulations, there is a change in the latitudinal gradient of cloud fraction poleward of approximately 60° N/S (cloud fraction increases with latitude in the coarse simulation, decreases with latitude in the fine simulation, Fig. 3.4a). This reversal still occurs in the CAM5 simulation, but is much weaker. Figure 3.8b highlights the component resolutions of the equatorial band. The peak cloud fractions near the equator are essentially identical, regardless of resolution. There are small differences in the subtropics between resolutions, but these differences are significantly smaller than seen in Fig. 3.4b (CAM4).

The equatorial peak of the precipitation rate (Figs. 3.8c) in the fine grid is approximately 17% less in CAM5 (25 mm day^{-1}) when compared to CAM4 (30 mm day^{-1}). The peak in the coarse simulation drops similarly, falling from 23 mm day^{-1} (CAM4) to 18 mm day^{-1} (CAM5). Figs. 3.8d (CAM5) shows similar results to Fig. 3.4d (CAM4) in that the fine (coarse) simulation and the high resolution (low resolution) component of the var-res grid are quite similar. This indicates that the dynamical behavior at each grid scale in the var-res simulation is similar to the corresponding uniform run.

Temporally and spatially-averaged contour plots are shown in Figs. 3.9 and 3.10. For cloud fraction in the CAM5 simulation, the plots (Fig. 3.9d-e) of the difference between the var-res grid and the corresponding uniform simulations do not show obvious grid imprinting resulting from the resolution-dependence of the parameterizations which control cloud fraction as they did with the CAM4 package (Figs. 3.5d-e). In addition to the significant decrease in scale sensitivity, the asymmetric downstream

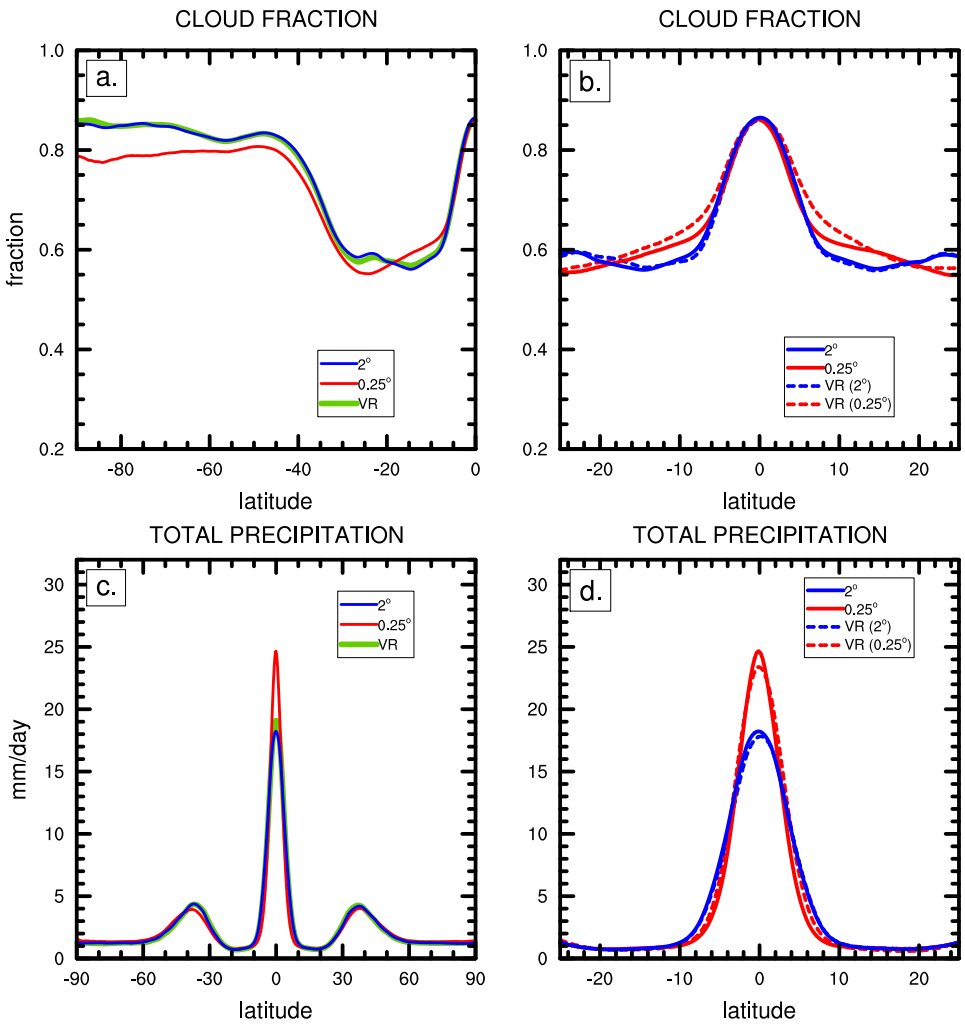

Figure 3.8: Same as Fig. 3.4 except with CAM5 physics.

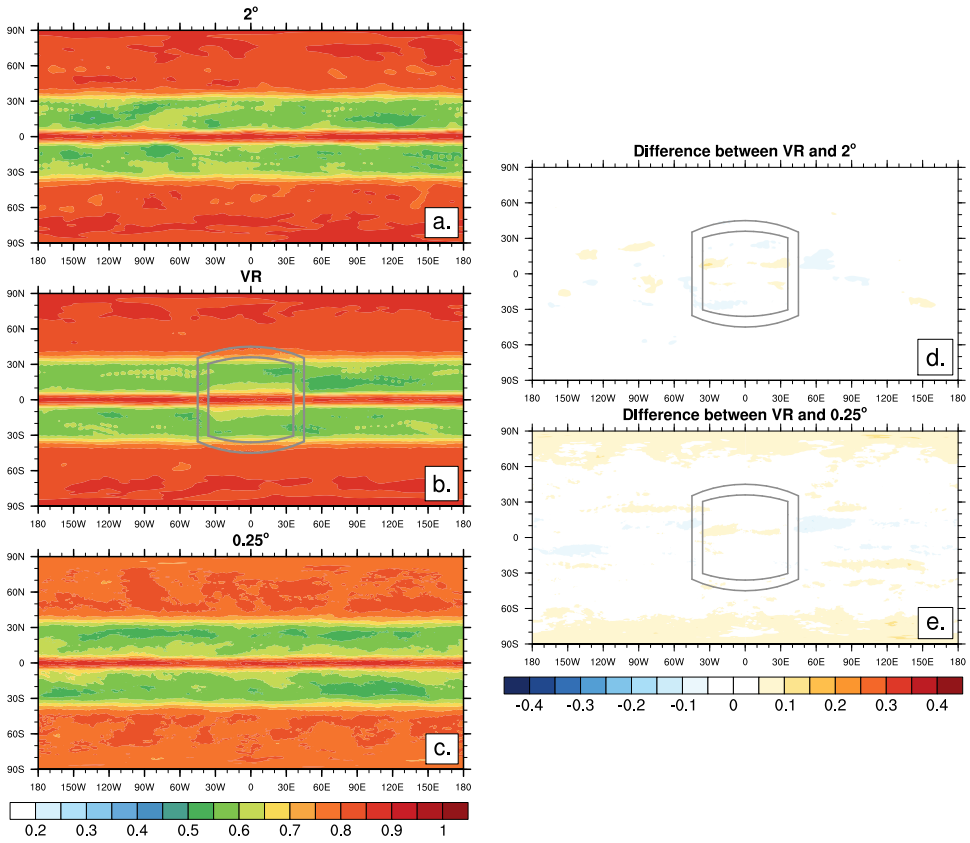

Figure 3.9: Same as Fig. 3.5 except with CAM5 physics.

effects seen in the CAM4 simulations do not appear in the CAM5 runs.

The spatial precipitation analysis (Fig. 3.10) shows that, unlike cloud fraction, the scale-dependent nature of the total precipitation rate is not significantly altered by using CAM5 physics. Like the CAM4 simulations (Fig. 3.6), the var-res simulation shows a positive zonal precipitation anomaly in the refined region when compared to the coarse grid (Fig. 3.10d). The opposite is true (outside the refinement patch) when comparing the same run to the fine simulation (Fig. 3.10e). The overall difference between the resolutions is slightly smaller in total magnitude, although this may be a result of the fact that the CAM5 simulations produce less total precipitation right at the equator (where the largest anomalies occur) in comparison to the CAM4 simulations.

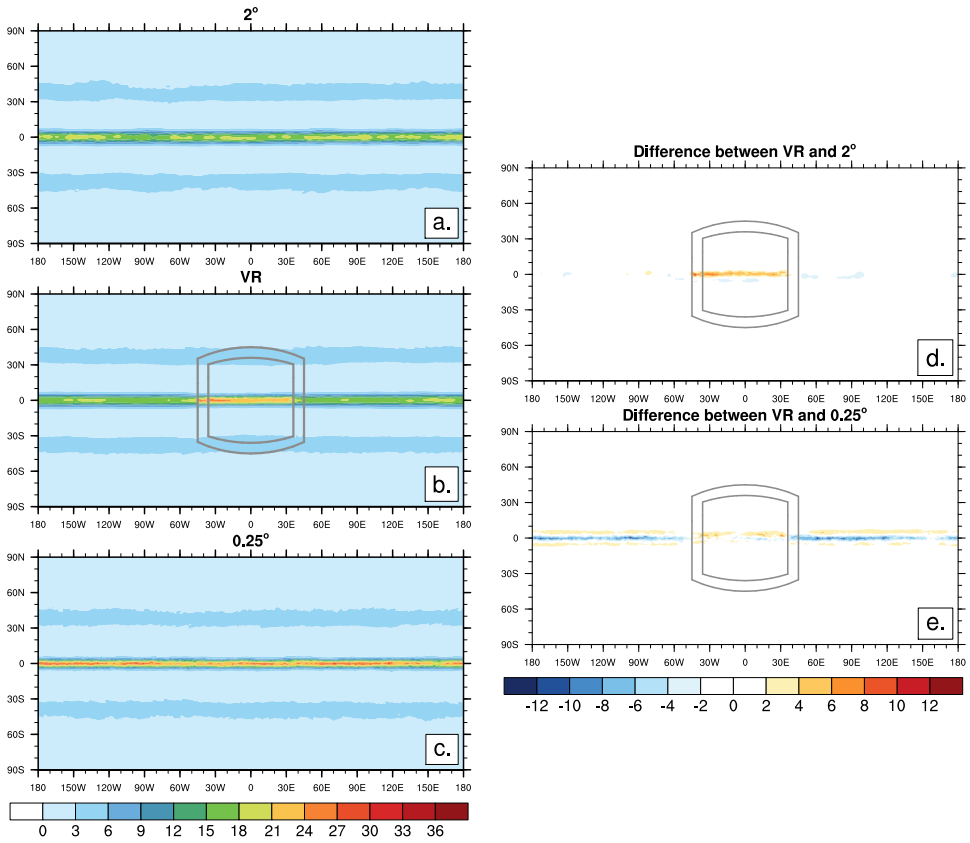

Figure 3.10: Same as Fig. 3.6 except with CAM5 physics.

Interestingly, small bands of positive anomalies appears in Fig. 3.10e that surround the negative differences at the equator. While total precipitation increases at the equator with increasing resolution in CAM5, some of this increase is balanced by a narrowing of the precipitation peak (also seen in Fig. 3.8d). To verify this is not a function of the output resolution being higher for the fine simulations, all output was remapped to the coarse grid and the same result was observed (not shown). This narrowing may be due to an increase in Hadley cell strength with resolution. This has been shown to occur in CAM and leads to enhanced vertical velocities at the equator (Rauscher et al., 2013). This therefore results in increases in large-scale precipitation, since it is sensitive to resolved motion in the atmosphere. This narrowing is also the reason why more area-weighted total precipitation is simulated with the coarse grid in the equatorial band spanning 25° N/S, as listed in Table 3.3 (PRECT). Even though the ITCZ maximum increases with resolution, the shape of the peak is sufficiently narrowed to allow the loss of spatial coverage to offset the increased maximum. Blackburn et al. (2013) also noted that compensating effects of maximum precipitation and spatial width of the ITCZ moderated tropical precipitation variance in a multi-model APE survey. The fact that integrated tropical precipitation (as in Table 3.3) is similar at multiple resolutions even with different equatorial maxima could be a manifestation of this feedback.

As seen in Fig. 3.11, the Gill-type response elicited by the high-resolution nest is still evident, but damped, when using the CAM5 physics package. A band of zonally anomalous vertically-integrated heat release can be seen in the high-resolution patch of the var-res grid in Fig. 3.11a. This is associated with the additional total precipitation induced by the increase in resolution which is shown in Fig. 3.10. This band is slightly wider, but approximately half as strong as in Fig. 3.7a (CAM4).

Interestingly, the maximum heating occurs on the western edge of the nest (where equatorial flow is preparing to exit the high resolution region). This result is opposite

to that seen in the CAM4 simulations, which had a single, strong peak in anomalous diabatic heating on the eastern (entry) edge of the nest. Since dynamical core attributes such as the grid, time step, and diffusion are all identical for the CAM4 and CAM5 simulations, it suggests that this response is a function of the physics package.

Figure 3.11b shows that the anomalous 200 hPa divergence associated with the high-resolution nest is significantly reduced. While there still is anomalous rotational flow at 200 hPa as evidenced by the eddy streamfunction contours, the pattern which matches that seen in Gill (1980) and Rauscher et al. (2013) is not as evident as in Fig. 3.7b (CAM4). While a scale-dependent aspect of total precipitation is still evident in the aquaplanet simulations, the use of CAM5 physics appears to mitigate VRGCM-induced thermal circulations.

3.5 High-frequency wave analysis

In addition to the climatological averages, 6-hourly output from the CAM5 simulations was used to analyze wave features and precipitation extremes produced. The main point of interest is whether these were significantly affected by the variable resolution, and in particular, the transition regions. Our CAM4 simulations did not produce output at a high enough temporal frequency for the following analyses. However, the results of Williamson (2008a) and Rauscher et al. (2013), as well as cursory analysis of the temporally-coarser CAM4 data (not shown), indicate the wave analysis results as they pertain to variable-resolution would be similar to the CAM5 simulations.

3.5.0.1 Equatorial wave activity

Wavenumber-frequency diagrams, following the spectral analysis methodology of Wheeler and Kiladis (1999), are shown in Fig. 3.12. Following Williamson (2008a) and Blackburn et al. (2013), we plot the full power in Figs. 3.12a-f without normal-

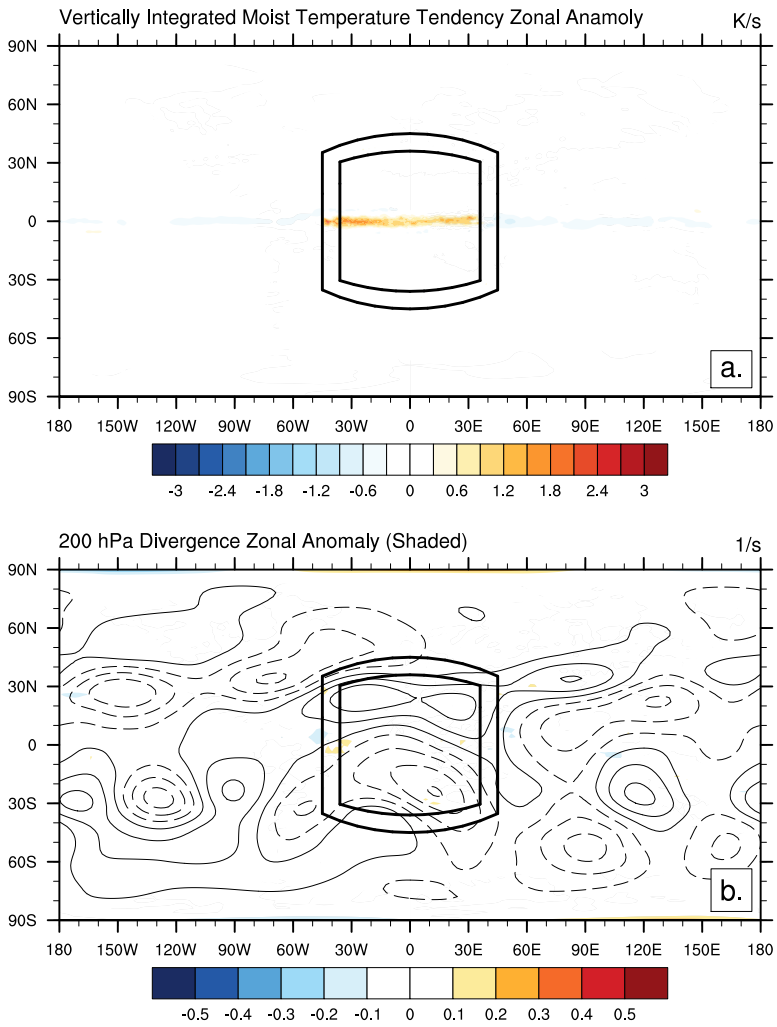

Figure 3.11: Same as Fig. 3.7 but with CAM5 physics.

izing by the background spectrum. Normalization is typically performed because it helps isolate spectral peaks with specific modes. However, it also removes the resolution dependence contained in the background spectrum. Figures 3.12a and 3.12c show this unnormalized anti-symmetric component of the spectra of 6-hourly outgoing longwave radiation (OLR) averaged between 10° N/S for the coarse (2°) and fine (0.25°) grids, respectively. As resolution is increased, total power in high-frequency (greater than 0.4 cycles per day (cpd)) eastward waves decreases, while the opposite is true for high-frequency westward waves. Figures 3.12d and 3.12f are the same for the symmetric component. The variable-resolution results are shown in Fig. 3.12b (anti-symmetric) and Fig. 3.12e (symmetric).

The normalized symmetric power spectra for the three simulations are shown in Figs. 3.12g-i. Little significant wave activity was seen in the normalized anti-symmetric component (not shown). Eastward propagating Kelvin waves are the dominant feature in the simulation. These waves are centered on the h=25 m equivalent depth curve at frequencies below 0.17 cpd (corresponding to 6 days and longer) for all model simulations, but shift to higher equivalent depths, and therefore higher phase speeds, with increasing wavenumber. This result is in agreement with previous CAM aquaplanet simulations (Mishra et al., 2011b; Rauscher et al., 2013).

In all cases, variable resolution does not significantly alter the solution. There are no obvious peaks that can be attributed to spurious wave interaction with resolution changes resulting in parasitic modes. The results are very similar to both the fine and coarse panels. In many cases, the variable-resolution simulation appears to represent a "transition" between the two simulations, sharing signatures that are evident in the analysis of both corresponding uniform grid spacings. An example of this would be the decrease in high-frequency (greater than 0.35 cpd) Kelvin-type waves (symmetric panels, Figs. 3.12d-i). The power decreases in this spectral region from the coarse to the var-res simulation and then the var-res to the fine simulation. The exact reasoning

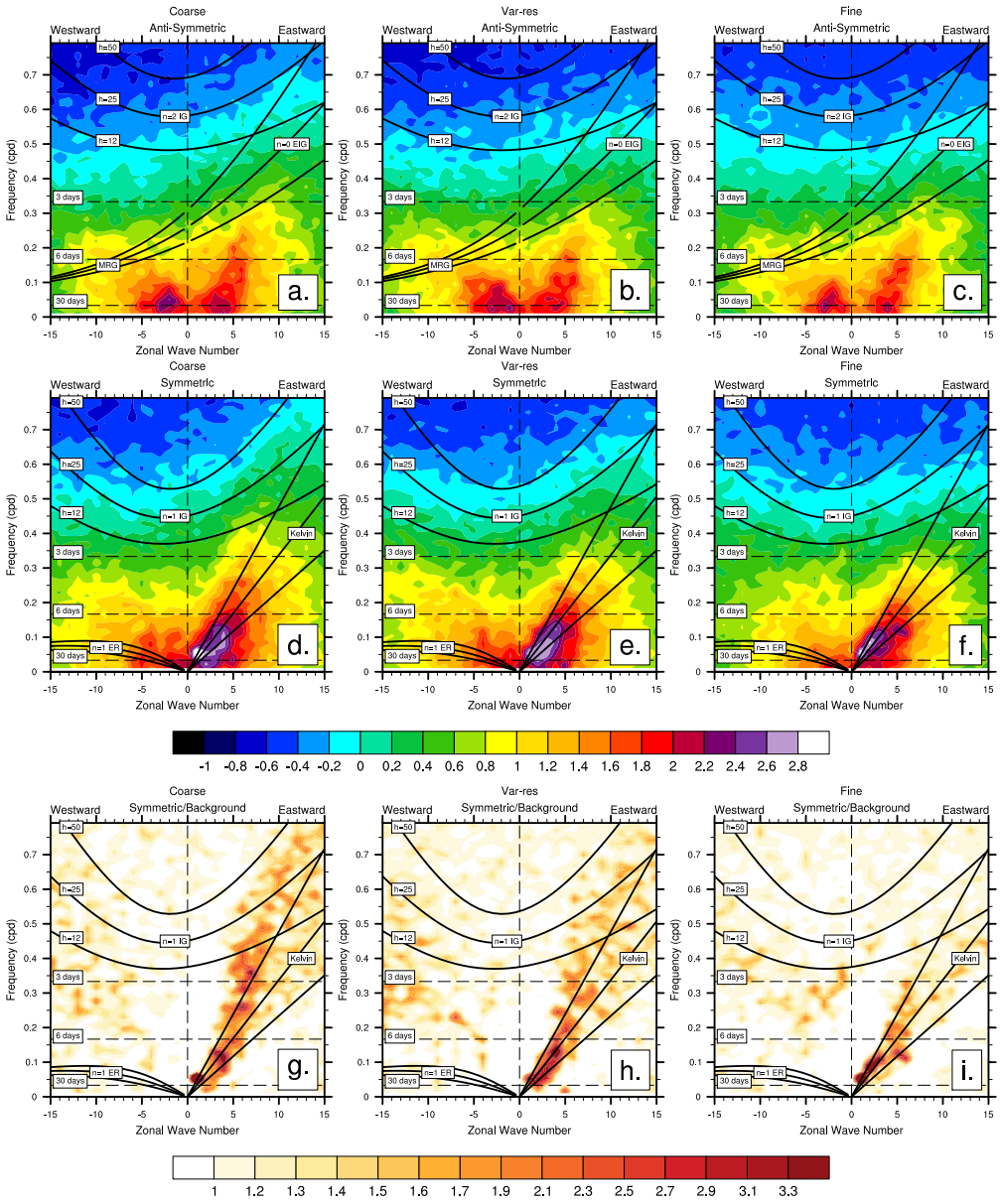

Figure 3.12: Wavenumber-frequency diagrams of outgoing longwave radiation averaged between 10° N/S. Unnormalized anti-symmetric (a-c), unnormalized symmetric (d-f), and normalized symmetric (g-i) components of the logarithm of the power are shown for the coarse (a,d,g), var-res (b,e,h), and fine (c,f,i) simulations. Dispersion curves from linear shallow-water theory for a zero wind basic state with equivalent depths h=12, 25 and 50 m are overlaid as in Wheeler and Kiladis (1999). Inertio-gravity (IG), equatorial Rossby (ER), equatorial inertio-gravity (EIR), and Kelvin waves are marked with their meridional mode numbers n.

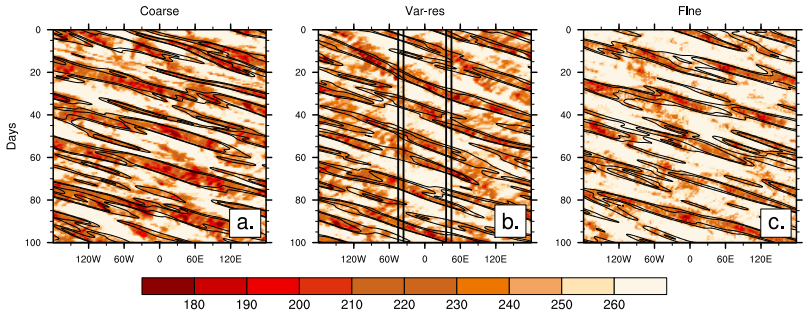

Figure 3.13: Hovmöller diagram of 100 days of outgoing longwave radiation (W m^{-2}) for each of the three grid types averaged between 10° N/S. A band-pass filter of wavenumbers 1 to 14 and periods between 2.5 and 20 days is contoured in black.

behind this difference is unclear. Given the fact that parameterized convective activity is higher in the coarse runs (see Table 3.3), this may be a high-frequency signal heavily influenced by the convective scheme operating on near-diurnal scales.

Figure 3.13 shows 100-day Hovmöller diagrams of OLR for each of the grid types in the CAM5 simulations. OLR is averaged between 10° N/S. In the var-res grid (Fig. 3.13b), the longitudes of the transition regions are demarcated using black vertical lines. The solid black contours are band-pass filtered values of OLR corresponding to Kelvin wave activity. There is a slight decrease in background OLR when resolution is increased from the coarse to the fine grid. The var-res grid reflects this with lower OLR values during non-Kelvin wave events in the high-resolution region.

In the var-res simulation, there is no discernable change in slope or kinking of the contours, which would represent a change in the phase speed of the wave activity upon interaction with a transition region. This is similar to the findings in Chapter II, where cyclonic vortices interacting with mesh transition regions in similar setups of CAM-SE did not exhibit artificial wave reflection or distortion.

3.5.0.2 Precipitation frequency

Histograms of precipitation rate frequency in the three CAM5 simulations are shown in Fig. 3.14. Statistics are calculated in a band extending 10° N/S from the

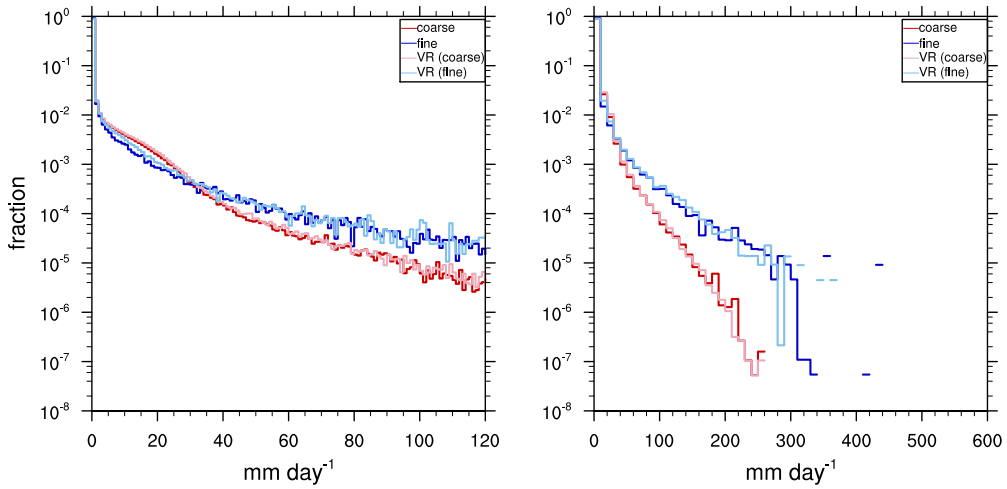

Figure 3.14: Precipitation histogram representing fraction (logarithmic scale) of instances where 6-hourly instantaneous precipitation rates were in specific intensity bins for CAM5 simulations. Statistics are averaged between 10° N/S. Variable-resolution simulation is broken into component resolutions using the areas depicted in Figure 3.3. Bin sizes are 1 mm day^{-1} in the left panel and 10 mm day^{-1} on the right.

equator using 6-hourly instantaneous total precipitation rate output. The variable-resolution analysis is seperated by grid spacing, using the boundaries shown in Fig. 3.3. Output is conservatively remapped to a uniform 2° grid based on the recommendations of Chen and Knutson (2008). Both Figs. 3.14a and 3.14b show the same data, with Fig. 3.14a only focusing on precipitation values less than 120 mm day^{-1}.

Even after remapping, both panels show an increase in the frequency of extreme events with higher resolution. The coarse grid and low-resolution component of the var-res grid both have a higher frequency of low precipitation events. For this model setup, the equilibrium point where the two simulations cross (are at equal frequencies) is approximately 32 mm day^{-1}. The histograms for the coarse and fine grids match their corresponding var-res resolution well. This is another indication that dynamically, the model behaves as expected in each regime. We note that the globally-uniform fine grid has a slightly longer tail than the high-resolution patch in the var-res run (Fig. 3.14b). There appears to be a small upscaling/downscaling effect where parcels at the edge of the sampling area (red hatch, Fig. 3.3) have not fully

adapted to the high-resolution nest yet. This is confirmed by shrinking the area of analysis by 5° in the latitudinal direction, which shows better agreement for extreme events (not shown). This may have implications on the "buffer" area required for regional climate-type simulations as well as whether or not wider transition regions are needed to allow for the flow to adjust to the grid spacing. Given CAM-SE's high-order numerics, dynamical features are resolved well, even with fairly abrupt transitions. However, the solution may be improved in coupled climate systems by broadening this transition given current column-based subgrid parameterizations.

3.6 CAM5 modal aerosols

While completing the previously discussed simulations with the Spectral Element version of CAM 5.1, CAM version 5.3 was released, providing support for prescribed modal aerosols in the Modal Aerosol Model (MAM). The release provides a climatological dataset containing information about modeled aerosol species. This dataset is used as an input to the model with the active chemistry package turned off. This is similar to the bulk aerosol model discussed earlier, however, the model now supports variation in aerosol concentration within species-specific modes. In contrast, BAM with CAM5 provides only bulk mass concentrations for a specific species, which are empirically converted to modes within the model physics.

We follow the same steps discussed earlier to generate an aquaplanet-type aerosol distribution. The data set was first time-averaged to provide temporally-homogenous fields. In this case, each aerosol mode was averaged separately, allowing for latitudinal variation in ratio of modes (such as fine-to-coarse, etc.). Our model results so far indicate that solutions at particular grid spacings within variable-resolution simulations do a satisfactory job matching their uniform counterpart. Therefore, we have only completed var-res simulations.

Figure 3.15 displays the zonally-averaged cloud fraction and total precipitation

for CAM5 coupled to both aerosol packages with the var-res configuration. Figures 3.15a and 3.15c show the global zonal averages for cloud and precipitation while Figs. 3.15b and 3.15d differentiate between the fine and coarse grid spacings in the equatorial band. Global cloud fraction is largely unchanged between the two aerosol packages. The largest difference exists in the ITCZ where MAM produces about 4% less cloud fraction than BAM. MAM appears to be slightly more scale-selective as shown in Fig. 3.15b. Like cloud fraction, precipitation is largely matched between the two simulations outside of the latitudes in the immediate vicinity of the equator. Simulations utilizing the MAM produce slightly less precipitation in both the fine and coarse components of the grid.

This result, while generally qualitative in nature, may have implications for climate studies using different types of prescribed aerosols. Using prescribed aerosols greatly reduces the computing requirements for the CAM5 physics package and may allow users with limited resources to use the new CAM5 physics over a less expensive, but older, set of subgrid parameterizations. While global quantities of cloud and precipitation are similar, differences are not necessarily insignificant at the equator in these simplified simulations. This may translate to a bias in tropical clouds and precipitation in coupled runs using prescribed aerosols, although a more rigorous analysis is necessary to confirm whether or not this is the case. However, the difference in simulation results from using the two different techniques for prescribing aerosols in CAM5 is smaller than the differences between various resolutions in CAM4. This serves to confirm that the CAM5 physics does not suffer from as much scale sensitivity as CAM4, since it retains consistent results across scales, even with two different aerosol forcing packages.

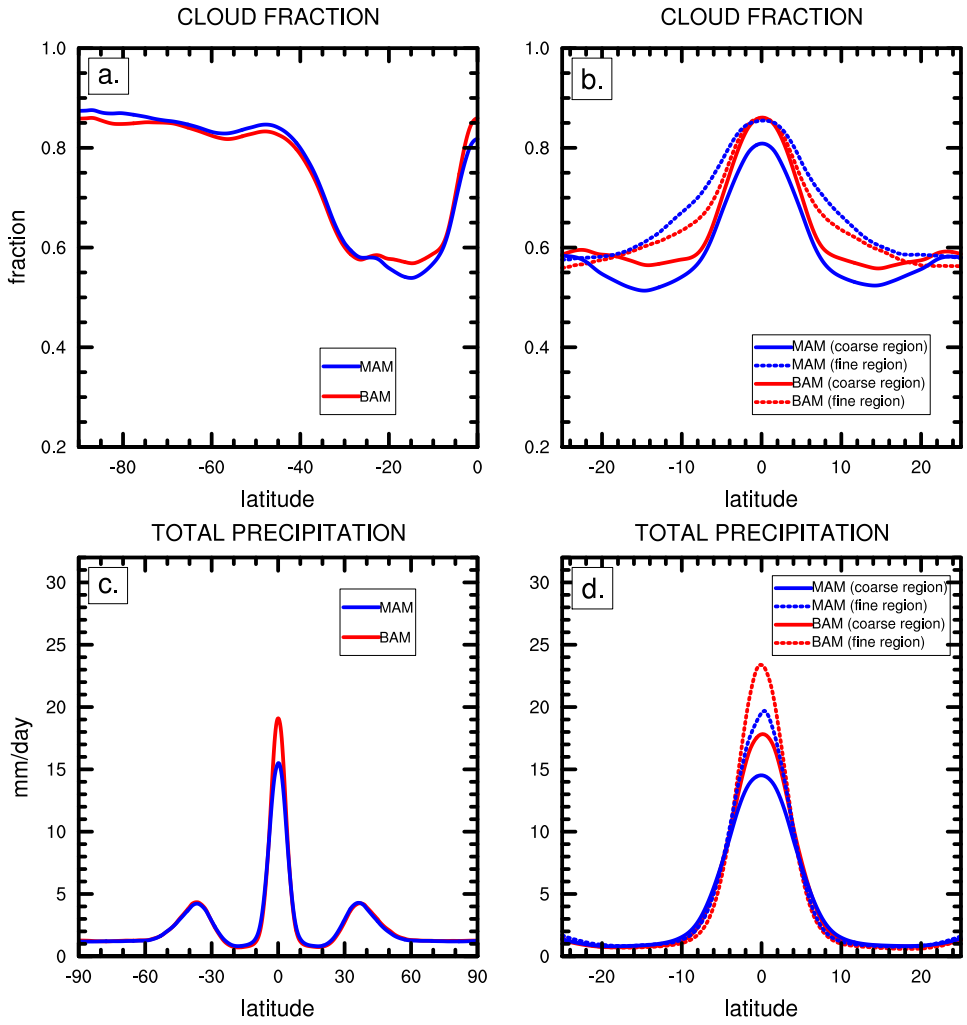

Figure 3.15: Zonal mean total cloud fraction (CLDTOT) and total precipitation rate (PRECT) using CAM5 physics package with modal (MAM) aerosols and bulk (BAM) aerosols. All simulations use the var-res grid. (a) Comparing the two aerosol packages in the var-res grid (CLDTOT). (b) Separating the fine region and the coarse region of the var-res mesh near the equator. (c) and (d) are the same except for PRECT.

3.7 Performance and timing

Since the focus of this study is a comparison of the climate predicted by variable-resolution meshes rather than collecting more formal timing results, a detailed study was not performed. However, some meaningful data was collected. Here, we only discuss the CAM4 simulations. Since the CAM5 physical parameterizations are also column-based, the scaling results for those runs should be essentially identical, and preliminary results (not shown) imply that this is the case.

All CAM4 simulations were run on the same computing hardware (Red Sky at Sandia National Laboratories), although not necessarily on the same nodes. Since the var-res simulation and the fine grid simulation use the same time step, the only variation in timing is expected to come from the number of elements in the mesh.

As mentioned in Section 3.2 and shown in Table 3.1, the uniform 0.25° grid contains approximately eight times more elements than the refined var-res setup, so it is expected to run about 8 times slower. The variable-resolution simulation achieved 3.84 simulated years per day (SYPD) on 400 cores, while the high-resolution simulation ran at 1.35 SYPD on 1,280 cores. Assuming linear scalability, that translates into 0.42 SYPD on 400 cores, more than 9 times slower than var-res.

For completeness, the coarse simulation ran at 42.5 SYPD on 160 cores, equivalent to 106 SYPD on 400 cores, which is just over 250 times faster than the fine run. This is expected because there is a factor of 64 fewer elements and the dynamics time step is 12 times larger. As mentioned earlier, the physics time step was held constant across all runs.

Since there was no significant effort to control these factors for a formal timing study, these results should be taken as an aside. The primary goal of our study is the analysis of the model statistics in coupled, aquaplanet simulations. Small deviations from perfect scaling are inevitable due to factors such as initialization cost, latency bottlenecks, input/output constraints and noise introduced by random node selection.

However, the fact that model runtime was close to predicted values given linear scaling is promising.

3.8 Conclusions

The spectral element dynamical core in the Community Atmosphere Model supports mesh refinement based on quadrilateral, conforming grid elements. Using a refined mesh provides a method to collect high resolution climate statistics in a particular area of interest while producing a low resolution simulation outside the region, reducing the computational cost of running CAM. The effectiveness of variable resolution meshes in CAM-SE was shown by running the aquaplanet control test from Neale and Hoskins (2000) and analyzing the global and zonal averages of quantities such as total cloud fraction and precipitation. Both CAM4 and CAM5 physics were tested to investigate the scale-sensitivity of the physics parameterizations and test the dynamical core as an option for use in climate simulations. Model throughput was improved tremendously with variable resolution due to the lower number of grid cells and, therefore, decreased computational cost. All simulations show that a high-resolution nest embedded within a coarse global grid generally matches climate statistics produced by a corresponding uniform high-resolution grid.

Variable-resolution simulations with CAM4 physics show a significant resolution signature in both integrated cloud fraction and total precipitation rate, with these signatures focused in or near the region of refinement. The statistics in the refined patch match results from globally-uniform simulations with the same model, indicating these issues are a deficiency in the model physics not being scale-aware as opposed to an issue in the variable-resolution implementation in the CAM-SE dynamical core.

Simulated total cloud fraction in CAM5 is increased over CAM4. This increase occurs at all latitudes, and, while most pronounced at the poles, is not dominated regionally. Both cloud fractions fall well within the range of model performance in

the Aquaplanet Experiment (Blackburn et al., 2013). Convection is significantly more active in CAM5 than CAM4, which is an interesting result since both versions of the model use the same deep convective scheme. One likely source of this discrepancy is CAM5's updated microphysics. Even though the convection routine is called first in the moist physics calling sequence, a less active microphysics scheme (in terms of large-scale precipitation removed from the atmosphere) leaves more water available to the convective scheme at subsequent time steps. Another possible cause might be that CAM5's updated boundary layer scheme moistens the lower portion of the troposphere more effectively thus providing more favorable conditions for convection. Unfortunately, given the strong interdependency of physics packages in current climate models, it is extremely difficult to disentangle the individual impact one factor might have on a specific process in these simulations.

We note that recent work such as Williamson (2008a) and O'Brien et al. (2013) argue that assessing the convective/large-scale precipitation ratio may not be the correct way to approach resolution dependence in this framework. True convective precipitation generally occurs at less than 10 km grid scales, and therefore should remain equally parameterized at spacings above this threshold. However, Reed and Jablonowski (2012) showed in simplified simulations at 55 and 28 km grid spacing that only a large-scale condensation routine was necessary to produce realistic precipitation in a convectively-dominated system (tropical cyclones). These results suggest that additional clarity is needed in denoting exactly how precipitation is partitioned at hydrostatic resolutions.

In addition, the overt grid scale dependence of total cloud fraction seen in CAM4 simulations appears to be significantly improved with the CAM5 physics package. The fact that no visible grid imprinting is seen in Fig. 3.9c is a good indicator that physical parameterizations involved in cloud formation behave well in a variable-resolution framework. They adjust 'rapidly' to the underlying grid resolution within

a single simulation without the need for variable tuning between the different sized elements. This improved cloud scaling is also observed in O'Brien et al. (2013), who postulate that this improvement is a function of the new Morrison-Gettlemen microphysics package. This implies that the Rasch-Kristjansson microphysics scheme in CAM4 might significantly contribute to the resolution dependence in the CAM4 simulations.

An increase in precipitation with resolution is seen with both physics packages, although the magnitude of this sensitivity is higher for CAM4. Given the addition of a refined patch, this sensitivity excites a diabatic heating anomaly in the zonal direction. This heating forces an anomalous circulation which exists due to the high-resolution nest. The CAM4 simulations show an obvious response to the heating, similar to that seen in Rauscher et al. (2013). The diabatic heating anomaly, while still existent, is weaker in CAM5. This leads to less upper level divergence and a weaker circulation response. However, it is unknown whether either anomaly would have a significant impact on climate statistics in a fully-coupled VRGCM simulation.

Interestingly, the peak zonally-anomalous divergence in the tropics in the CAM4 simulations occurs at the nest entrance (eastern edge) while this peak occurs near the nest exit (western edge) in CAM5. This implies that the moist physics/gridscale feedback is altered in CAM5. This may be due to the modified microphysics scheme. The Morrison-Gettlemen microphysics (CAM5) may not respond as "harshly" to abrupt grid resolution changes which allow the equatorial flow in the ITCZ to more slowly adapt to the high-resolution nest. The CAM5 result (diabatic heating anomaly near nest exit) is actually more similar to the results seen in Rauscher et al. (2013), although they used CAM4 physics. Since their grid transition region is much more gradual, it also suggests a strong gridscale feedback is inherent in the CAM4 physics.

Equatorial waves in the CAM5 simulations show that CAM-SE's numerics perform well when atmospheric features transit through a resolution discontinuity into

a high-resolution nest. No anomalous variance is seen in Wheeler-Kiladis diagrams. The variable-resolution qualitatively appears to bridge fine and coarse simulations. Temporal analysis also qualitatively shows that Kelvin wave features do not incur phase speed shifts upon entry and exit of the high-resolution patch. Additionally, individual precipitation events show similar frequency at specified grid spacings, further confirming that the flow in the high-resolution nest within the var-res grid behaves in the same fashion as a globally-uniform fine grid.

Computational cost is saved by reducing the number of elements in the grid. Dennis et al. (2012) and Evans et al. (2013) both show that CAM-SE scales nearly linearly, so reducing the number of elements also reduces the number of cores needed to maintain throughput. The decreased computational demands make it significantly faster to generate an ensemble of runs, which will greatly speed up the process of tuning the model or testing new physical parameterizations.

The next chapters will involve testing variable-resolution in CAM-SE in more complex climate simulations. While the CAM5 physics package would appear to be a superior choice in variable-resolution simulations due to the improved cloud fraction scaling, other processes, such as precipitation, still exhibit a resolution signature. Both Chapter II and Guba et al. (2014) showed that any numerical errors arising from grid refinement within the dry CAM-SE dynamical core are small. This suggests that the resolution signatures seen in this study are the result of the physics packages.

Further work may be necessary to modify existing parameterizations such that they behave in a more scale-independent manner. This may include the introduction of cell-specific tuning parameters for each cell size, which would allow the same physical parameterization to be tuned for multiple grid spacings within a single, multi-resolution run. In addition, more widespread adoption of variable-resolution models in weather forecasting or climate assessments may push for a paradigm shift in sub-grid parameterization development, requiring novel fully scale-aware approaches for

truly seamless prediction.

CHAPTER IV

Assessing the model climatology of variable-resolution GCM simulations

4.1 Introduction

It has been shown that the use of high horizontal resolution (less than 75 km grid spacing) improves climate simulation in many ways. Phenomena operating at spatial scales too small for traditional General Circulation Models (GCMs) become better resolved with finer grid spacing. These include tropical cyclones (ex: Manganello et al. 2012; Wehner et al. 2014) and frontal zones (Ohfuchi et al., 2004). The diurnal cycle of precipitation is better simulated with increased resolution, particularly in models which are convection-permitting (Dirmeyer et al., 2012). Additionally, increased resolution provides a more accurate topographical boundary condition. Better orographic representation has been shown to improve precipitation patterns (Gent et al., 2010; Boyle and Klein, 2010) and mid-latitude blocking events (Jung et al., 2012).

However, integrating for long periods of time (multiple decades) at these grid spacings is not feasible, even at large national centers dedicated to atmospheric modeling. Additionally, multi-member ensemble simulations provide additional insight into sources of uncertainty within a model simulation (Rougier et al., 2009; Flato et al., 2013). This information is unattainable given a single model run at fine hori-

zontal grid spacing, which may make exhausting all resources on a lone simulation a less-than-ideal option.

Variable-resolution general circulation models (VRGCMs) hold the potential to significantly improve regional climate simulations by alleviating some of these issues. VRGCMs employ grid stretching (ex: Côté et al. 1993; Déqué and Piedelievre 1995; Fox-Rabinovitz et al. 1997; Lorant and Royer 2001; Tomita 2008) or grid refinement (ex: Ringler et al. 2008; Jablonowski et al. 2009; Walko and Avissar 2011; Skamarock et al. 2012; Rauscher et al. 2013; Harris and Lin 2013, 2014; Chapter II) to only simulate a portion of the global domain at high-resolution. This focuses available computing resources in high-resolution areas while lessening the cost required to simulate the global circulation over the remainder of the (coarser) domain. This decrease in computational burden, while still allowing regionally-high resolutions within a global framework, may support improvements such as longer simulations and additional members within ensembles. VRGCMs can be considered a bridge between more computationally expensive traditional GCMs with uniform grid spacing, and limited area models (LAMs) which require forcing from lateral boundary conditions. These boundary conditions may be poorly interpolated, mathematically ill-posed, or physically inconsistent (Warner et al., 1997; McDonald, 2003; Laprise et al., 2008; Mesinger and Veljovic, 2013).

Recently, a variable-resolution option has been implemented within the Community Atmosphere Model's (CAM) Spectral Element (SE) dynamical core (Neale et al., 2010b). CAM is jointly developed by the National Center for Atmospheric Research (NCAR) and various Department of Energy (DoE) laboratories. Variable-resolution CAM-SE has shown promise in allowing for high-resolution simulation of tropical cyclones (Chapter II). In addition, related aquaplanet simulations with CAM-SE exemplify that refined nests can accurately reproduce the regional climatology of a uniform high-resolution run at a fraction of the computational expense (Chapter III).

In this chapter, we increase the complexity of our variable-resolution CAM-SE assessments and report on two 23-year simulations that follow the Atmospheric Model Intercomparison Project (AMIP) protocol (Gates, 1992). CAM is forced with prescribed sea surface temperatures (SSTs) and ice coverage in an attempt to recreate the observed climatology of the last three decades. One simulation utilizes a globally-uniform 1° (∼111 km) grid, analogous to resolutions used in recent climate assessments. The other simulation uses the same grid with an embedded 0.25° (∼28 km) nest over the Atlantic Ocean. The reason for this refinement was to investigate the performance of CAM-SE at simulating tropical cyclones using multi-resolution nests. Those results are contained within Chapter V.

This chapter discusses the long-term climatological state of both simulations. We pay particular attention to changes in regional climate arising from the addition of a high-resolution nest. We also investigate the scale sensitivity of the CAM version 5 physical parameterization package and whether the addition of refinement degrades large-scale circulation patterns or climate statistics. The chapter is structured as follows. In section 4.2 we briefly discuss CAM-SE and the special considerations for variable-resolution, including the development of a multi-resolution topographical dataset. Section 4.3 discusses the climatological averages and the spatial effects of an embedded nest on long-term means. Section 4.4 discusses equatorial waves, particularly African easterly waves, and the impact of refinement on their representation in the model. Section 4.5 outlines a few examples regional climate improvements which arise from the use of variable-resolution. Section 4.6 summarizes the results and discusses the potential implications of this work as well as future research directions.

4.2 Model description and experimental setup

4.2.1 CAM-SE

The SE dynamical core is the default dynamical core in CAM as of version 5.3, superseding the Finite Volume (CAM-FV) option. CAM-SE is based upon a continuous Galerkin spectral finite-element method applied on a cubed-sphere grid (Taylor et al., 1997; Taylor and Fournier, 2010; Dennis et al., 2012). The use of the quasi-uniform, cubed-sphere mesh eliminates problems arising from converging meridians on standard latitude-longitude grids. CAM-SE locally conserves mass and tracer mass to machine precision, as well as moist total energy to the level of time truncation error (Taylor, 2011). The primitive equations governing atmospheric motion are solved locally on individual elements, reducing the amount of interprocessor communication required with other numerical schemes. This gives CAM-SE attractive scaling properties; the model has been shown to scale nearly linearly to hundreds of thousands of cores (Dennis et al., 2012; Evans et al., 2013). These characteristics make CAM-SE a compelling option for future high-resolution climate simulations on massively parallel systems.

Because the discretization is localized on individual elements, variable-resolution can be introduced through refined meshes provided the elements tiling the sphere are conforming quadrilaterals. This setup allows variable-resolution grids to maintain the key conservation and scalability aspects that make CAM-SE a desirable model choice for climate simulations.

There are only a few modifications required to utilize CAM-SE in conjunction with variable-resolution grids. CAM-SE applies explicit fourth-order hyper-diffusion both for numerical stability and to simulate a realistic kinetic energy spectrum (Dennis et al., 2012). This fourth-order hyper-diffusion must be scaled with resolution such that the proper damping is applied at the coarse grid scales without harming

dynamically-resolved features in the high-resolution nest. The fourth-order diffusion coefficient is scaled according to the grid spacing of each element with higher (lower) values in larger (smaller) gridboxes. Further discussion of the scaling of the hyper-diffusion can be found in Chapters II and III.

4.2.2 Experimental setup

This chapter utilizes version 1.1.17 of the Community Earth System Model (CESM). CESM is a coupled climate system model combining CAM with other model components such as land and ocean.

We run two simulations with two different CAM grids. One is a globally-uniform 1° (∼111 km) CAM-SE grid. We refer to this as the 'coarse' simulation. This is the default model grid for CAM simulations as of version 5.3. The other is a refined mesh that uses the same 1° grid but a patch of 0.25° (∼28 km) refinement is embedded over the Atlantic Ocean. A small transition band of 0.5° (∼55 km) grid spacing separates the inner nest from the coarser, background grid. This is referred to as the 'variable-resolution' (VR), or 'var-res' mesh. Both grids can be seen in Fig. 4.1. The shape of the high-resolution patch was determined by historical tropical cyclone activity in the North Atlantic Ocean basin. The grid generation procedure and refinement structure is detailed in Chapter III.

The default polynomial degree in CAM-SE is chosen to be three, which is the operational default in CAM. This selection leads to fourth-order spatial accuracy. We utilize a finite difference approach in the vertical with a hybrid sigma-pressure coordinate as well as a Runge-Kutta time discretization. The dynamical timestep (Δt_{dyn}) of the model is restricted by the finest grid spacing in order to satisfy the Courant-Friedrich-Lewy constraint. For the 1° simulation, Δt_{dyn} is set to 360 seconds, while set to a shorter 100 seconds in the variable-resolution mesh. The physics time step, Δt_{phys}, is set to 1800 seconds for both simulations. This is the CAM default

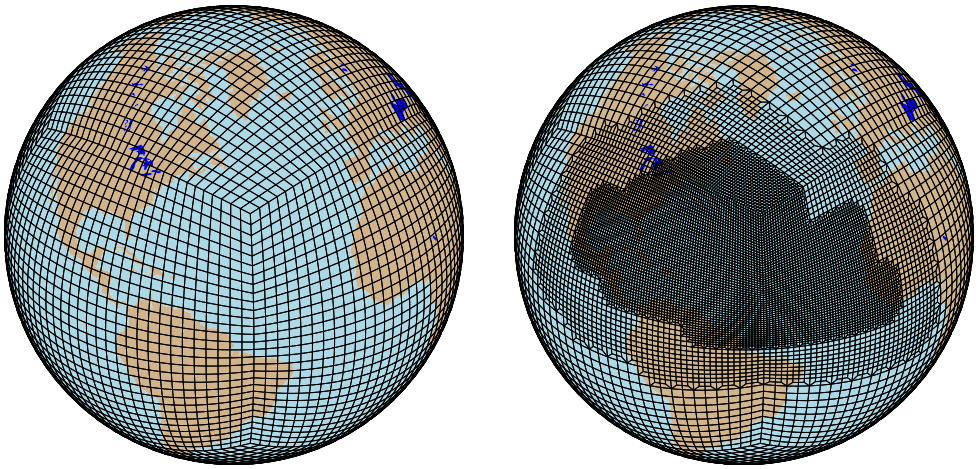

(a) (b)

Figure 4.1: The two meshes used for this study are (a) a uniform 1° resolution mesh and (b) a variable resolution mesh that ranges from 1° → 0.25°. Note that each element shown in the above plots contains additional 3 × 3 collocation points.

for 1° grids but four times longer than the 0.25° default of 450 seconds. Williamson (2013) showed that CAM's deep convective scheme performed poorly at smaller values of Δt_{phys} (such as 450 seconds) due to hard-coded relaxation timescales in the parameterization which are tuned to be used in conjunction with a Δt_{phys} of 1800 seconds. We seek to minimize sources of difference in the model results beyond the application of a high-resolution nest, so the selection of a uniform value of Δt_{phys} for both simulations is a natural one.

We utilize the CAM version 5 (CAM5) subgrid physics package (Neale et al., 2010b). CAM5 is the newest set of physical parameterizations available within CESM and has been shown to be the superior choice within CAM for variable-resolution simulations due to improved scaling of cloud fraction and precipitation at multiple resolutions when compared to prior versions (Chapter III). To minimize computational cost incurred by the addition of the new 3-moment interactive modal aerosol model (MAM, Liu et al. (2012)) in CAM5, we utilize a prescribed aerosol configuration similar to the bulk aerosol model (BAM, Kiehl et al. (2000)) used in previous

versions of CAM. A more detailed description regarding the prescribed BAM aerosol setup in CAM5 can be found in Bacmeister et al. (2014).

Cold ice and rain water autoconversion coefficients were set to match the defaults for high-resolution (0.25°) CAM simulations using the Finite Volume (FV) dynamical core. All other physical parameterization tuning parameters are non-resolution-specific CAM defaults which are derived from 1° CAM-FV simulations. These tuning parameters are identical to recent simulations using CAM-FV at 0.25° resolution (Bacmeister et al., 2014; Wehner et al., 2014), and the adoption of CAM-FV tuning parameters for CAM-SE has been used with success in past studies (Evans et al. 2013; Chapter III).

The simulations follow the AMIP protocols first outlined in Gates (1992). SSTs and ice coverage are applied through the 1° Hadley Centre Sea Ice and Sea Surface Temperature dataset (HadISST, Hurrell et al. (2008)). Greenhouse gas concentrations and aerosol climatology are prescribed based on past observations. The atmospheric grid is coupled to ocean/ice and land models through the CPL7 tri-grid coupler (Craig et al., 2012), which allows fluxes passed between the atmosphere and other model components to be conservatively remapped to the different grids. We utilize the Community Land Model (CLM) version 4.0 which is run on a 0.9 by 1.25° latitude-longitude grid. The land model is not prescribed and freely adjusts with the climate system.

Both simulations are initialized in September of 1979, although the first four months are discarded for model spinup. Both runs continued through the middle of 2003, although only fully-simulated calendar years (1980 through 2002) are analyzed. The variable-resolution simulation was completed on NCAR's Bluefire machine in late 2012 and averaged ∼0.42 simulated years per day (SYPD) on 384 processors. The globally-uniform 1° simulation was run on the Agri computing cluster at the University of California, Davis in mid-2013 with a model throughput of about 2.5

SYPD on 384 processors. We note that a direct scaling analysis between the two runs is not possible due to the different hardware architectures of the two systems.

4.2.3 Variable-resolution topography

One particular challenge which arises from the use of VRGCMs is the representation of topography. CAM-SE, which uses terrain-following coordinates, requires smoother topography at coarser resolutions to maintain numerical stability and prevent numerical artifacts such as Gibbs ringing. In addition, topography that is too rough has been shown to produce spurious vertical velocities within CAM-SE (Evans et al., 2013).

To generate surface topography data for variable-resolution CAM-SE, the CAM-FV default topography at 0.23°x0.31° is regridded to the unstructured CAM-SE grid using bilinear interpolation. This is the highest resolution data set packaged with CAM. Cursory tests showed that there is no appreciable difference between using bilinear interpolation and an alternative high-order remapping scheme. Interpolating from 0.23°x0.31° data is an acceptable option because CAM-SE requires slightly smoother topography fields than CAM-FV (Evans et al., 2013). It is worth noting that we have recently updated the topography generation routine to use the National Geophysical Data Center (NGDC) 2-minute (∼3.5 km) Gridded Global Relief Dataset (ETOPO2v2). The use of a higher-resolution dataset will provide more user control over the degree of smoothing in future model simulations at resolutions finer than 0.25°.

The regridded surface geopotential is smoothed iteratively using the following formulation:

$$\Phi_{VR} = \Phi_U + cK_o \left(\Delta x\right) \nabla^o \Phi_U \tag{4.1}$$

where Φ_{VR} is the variable-resolution surface geopotential, Φ_U is the unsmoothed,

regridded high-resolution topography, $K_o(\Delta x)$ is the hyperviscosity coefficient, o is the hyperviscosity order (equal to 2 for Laplacian), and c is a tunable constant (equivalent to a numerical timestep) which controls the intensity of the smoothing. The hyperviscosity order (o) controls the horizontal extent of the smoothing, with higher orders resulting in heavier, but more localized, smoothing. By using the grid-dependent coefficient $K_o(\Delta x)$, this method can provide for more (less) smoothing over areas tiled with larger (smaller) elements. Therefore, the smoothing is scaled approximately by element area as in the hyperviscosity formulation (Taylor, personal communication).

The variable-resolution topography is smoothed for 32 iterations with o equal to 2 and c equal to 120 s. $K_2(\Delta x)$ is equal to 1.0 x 10^5 m^2 s^{-1} in the 0.25° grid and increased/decreased by an order of magnitude for each doubling/halving of grid spacing.

A comparison of the topography at different grid spacings for the two simulations is shown in Fig. 4.2. More fine scale structure in surface geopotential is apparent in the high-resolution nest of the variable-resolution simulation (Fig. 4.2a) due to the scaling of $K_2(\Delta x)$ in Eqn. 4.1. We note that because the topography for the variable-resolution simulation is smoothed from a 0.23°x0.31° FV grid, the default 1° CAM-SE topography smoothness was not identically reproduced in the coarse region.

These parameters produce a slightly smoother result in the high-resolution region than the default CAM-SE topography data sets supplied with CESM at 0.25° resolution. However, default CAM-SE at 0.25° resolution applies 2.5 times stronger divergent component of the explicit diffusion to allow for rougher topography (Lauritzen, personal communication). Recent work has indicated that features such as tropical cyclones in climate models may be significantly affected by modifications of the explicitly applied diffusion (Zhao et al., 2012), and, in particular, divergence damping. Therefore, we have opted to use smoother topography to avoid this increased diffusion

Table 4.1: Variables used to evaluate CAM model performance for both grids and the corresponding observational dataset (and period) used as a reference baseline.

Variable	Abbreviation	Dataset	Obs. Period
Cloud cover	CLDTOT	ISCCP (Rossow and Schiffer, 1999)	1984 – 2009
Precipitable water	TMQ	MERRA (Rienecker et al., 2011)	1980 – 2002
Total precip. rate	PRECT	GPCP (Adler et al., 2003)	1981 – 2010
U-wind	U	NCEP (Kalnay et al., 1996)	1981 – 2010
V-wind	V	NCEP	1981 – 2010
Relative humidity	RELHUM	NCEP	1981 – 2010
Temperature	T	NCEP	1981 – 2010
Surface pressure	PS	NCEP	1981 – 2010

of the divergent motion in an attempt to use as consistent a diffusion formulation as possible.

A globally-uniform high-resolution data set is mapped to the grid of the smoothed data to provide conservatively mapped values for subgrid variability of topography used in the parameterization of turbulent mountain stress, subgrid orographic drag, and momentum flux deposition due to gravity waves (Lauritzen et al., 2012).

4.2.4 Observational datasets

As a reference baseline to compare the model solutions, we use a variety of observational and reanalysis products. These are shown in Table 4.1. We acknowledge that caution must be exercised when using reanalysis products (ex: Bosilovich et al. (2011)) as "truth." However, in this case we are less concerned with the accuracy of these products, but rather, using them as quasi-realistic proxies constrained to some extent by observations which allow for a comparison of the model results. The main uses of these datasets are for normalization and subjective discussion of relative differences between the two model simulations.

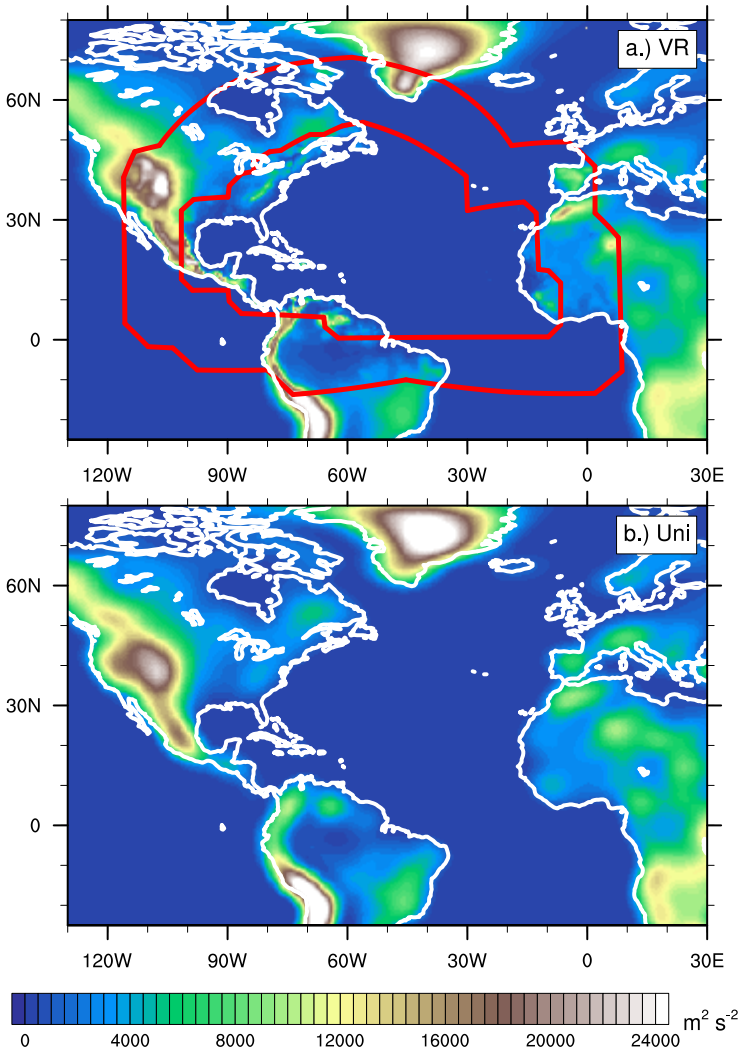

Figure 4.2: Surface geopotential of the topography over the location of the high-resolution nest (North Atlantic) in the (a.) variable-resolution simulation and (b.) uniform 1° simulation. In (a.), the innermost red contour encompasses the 0.25° grid spacing, the outermost contour bounds the 0.5° transition region, and 1° grid spacing lies outside the outermost contour.

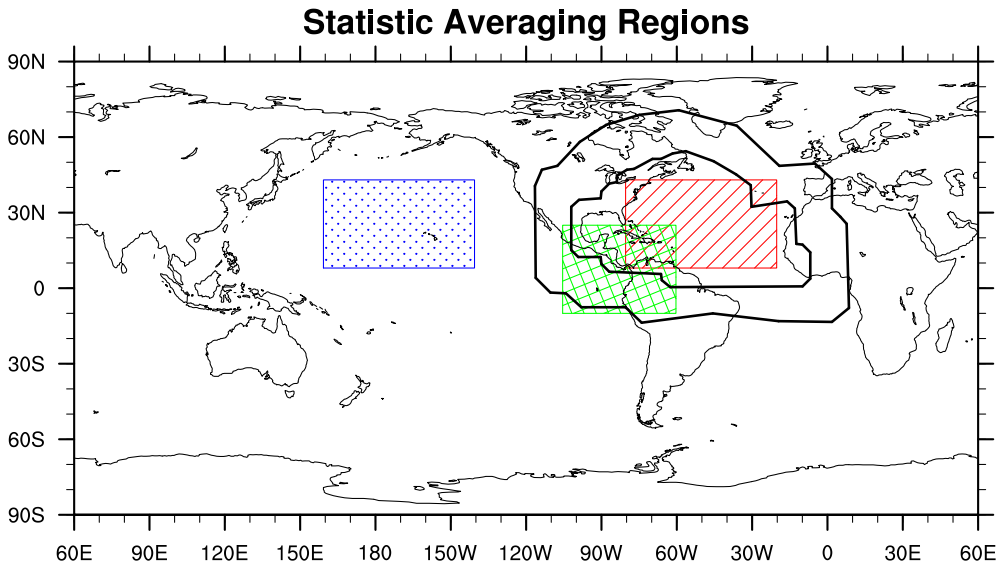

Figure 4.3: Averaging regions used in this study.

4.3 Climatological averages

To assess whether or not the refinement has any significant impact on the model climatology, we investigate four spatial regions. These areas are plotted in Fig. 4.3. The first area is simply the entire global domain. We also subselect regions of equal area over both the North Atlantic (red, diagonal hatch) and North Pacific Oceans (blue, stippled). These areas represent locations where the grid spacing is different between the two simulations (Atlantic) and where it is the same (Pacific). For topographically-modified flow, we also look at a fourth region centered over Central and northern South America (green, crossed hatch) which contains the largest differences in topographical structure between the two models (as seen in Fig. 4.2).

4.3.1 Global averages

Global annual averages (for the full 23-year simulation period) for select parameters between both the uniform 1° and variable-resolution simulations are listed in Table 4.2. In addition to the averages, the absolute difference between the two model

runs as well as the percent difference (normalized to the 1°) are also listed. We note that the global average total precipitation (PRECT) rate of 3.11 mm day^{-1} in both simulations is in good agreement with previously published CAM5-FV results of 3.04–3.18 mm day^{-1} (Bacmeister et al., 2014). All parameters other than the convective (PRECC) and large-scale precipitation rates (PRECL) do not differ between the simulations by more than 1.5%, with all analyzed variables other than total cloud fraction and surface sensible heat flux having relative differences of 0.1% or less. It is clear that the addition of the high-resolution nest in this study contributes very little in the way of significant changes in model averages at the global level.

Averages for just the Atlantic basin are shown in Table 4.3. The largest discrepancy between the two models runs is in the breakdown of convective and large-scale (stratiform) precipitation. The resolution-dependence of both components of the parameterized precipitation is a known behavior of CAM (e.g.: Duffy et al. 2003; Williamson 2008a; Boyle and Klein 2010; Li et al. 2011; O'Brien et al. 2013; Chapter III). As refinement is introduced, convective precipitation decreases by 11.2% while large-scale precipitation correspondingly increases by 79.9%. The strength and frequency of resolved dynamical updrafts increase with resolution, leading to increased activation of the large-scale microphysics routine, therefore resulting in more precipitation from that model component at finer grid spacing.

The difference in total precipitation (the sum of both the convective and large-scale precipitation components) is significantly smaller than either of the components when considered separately. In the Atlantic region, the additional precipitation from the large-scale routine in the variable-resolution simulation is offset by a decrease in activity from the convective precipitation parameterizations. The total precipitation is slightly higher in the fine grid simulation which agrees with previous simulations investigating the scale-sensitivity of precipitation in CAM (e.g. Williamson 2008a; Rauscher et al. 2013; Bacmeister et al. 2014; Wehner et al. 2014; Chapter III).

Table 4.2: Global statistics averaged over the 23-year simulation period for various climate metrics in both the uniform 1° and the variable-resolution (V-R) simulation. VAR is the variable abbreviation, ΔVAR is the absolute difference between the two simulations and ΔVAR (%) is the percentage difference normalized to the 1° run.

	VAR	units	Uni. 1°	V-R	ΔVAR	ΔVAR (%)
Total cloud fraction	CLDTOT	fraction	0.63	0.64	0.01	1.3%
Outgoing longwave rad.	FLUT	W m^{-2}	240.96	240.87	-0.09	-3.9E-2%
Sfc. latent heat flux	LHFLX	W m^{-2}	89.96	89.86	-0.09	-0.1%
Convective precip. rate	PRECC	m s^{-1}	2.46E-08	2.40E-08	-6.39E-10	-2.6%
Large-scale precip. rate	PRECL	m s^{-1}	1.15E-08	1.21E-08	6.07E-10	5.3%
Total precip. rate	PRECT	m s^{-1}	3.60E-08	3.60E-08	-3.24E-11	-0.1%
Surface pressure	PS	Pa	98465.8	98534.9	69.1	0.1%
Sfc. sensible heat flux	SHFLX	W m^{-2}	19.03	19.26	0.23	1.2%
500 mb temperature	T500	K	257.49	257.40	-0.09	-3.5E-2%
850 mb temperature	T850	K	279.92	279.81	-0.11	-3.8E-2%
Total precipitable water	TMQ	kg m^{-2}	24.97	24.98	0.01	-3.3E-2%
2-m temperature	TREFHT	K	287.19	287.07	-0.13	-4.4E-2%

Table 4.3: Same as Table 4.2 except only averaging over the Atlantic region outlined in Figure 4.3.

VAR	units	Uni. 1°	V-R	ΔVAR	ΔVAR (%)
CLDTOT	fraction	0.56	0.59	0.03	6.2%
FLUT	W m^{-2}	260.55	260.75	0.20	0.1%
LHFLX	W m^{-2}	144.71	145.01	0.30	0.2%
PRECC	m/s	2.94E-08	2.61E-08	-3.28E-09	-11.2%
PRECL	m/s	5.42E-09	9.74E-09	4.33E-09	79.9%
PRECT	m/s	3.48E-08	3.58E-08	1.05E-09	3.0%
PS	Pa	101530	101598	68	0.1%
SHFLX	W m^{-2}	16.93	18.02	1.09	6.4%
T500	K	262.52	262.40	-0.12	-4.5E-2%
T850	K	285.86	286.04	0.17	0.1%
TMQ	kg m^{-2}	31.93	31.73	-0.20	-0.6%
TREFHT	K	295.88	295.73	-0.15	-0.1%

The magnitudes of both cloud fraction and surface sensible heat flux also show slight (less than 7%) increases in the variable-resolution nest. The sensible heat flux increase may be due to an increase in the frequency of extreme low-level wind speeds within the high-resolution nest (not shown). This increases the surface stress on the ocean surface and increases the heat transfer to the lowest levels of the atmosphere. Both simulations utilize the same SST boundary data and have highly similar 850 hPa temperature (T850) and 2-meter temperature (TREFHT) climatology, implying that the temperature gradient between the ocean surface and low atmosphere is not the driver. Interestingly, the latent heat flux also increases, but much less than the sensible heat flux. This may be due to the additional non-linearity of moisture introduced in the formulation of the latent heat flux. A study investigating the model resolution sensitivity of the boundary layer and surface flux schemes is a target for future research.

Statistics for the Pacific basin are shown in Table 4.4. Since both simulations have identical grid spacing over this region, significant differences would be the result of potential upstream or downstream effects of the Atlantic refinement. All metrics

Table 4.4: Same as Table 4.2 except only averaging over the Pacific region outlined in Figure 4.3.

VAR	units	Uni. 1°	V-R	ΔVAR	ΔVAR (%)
CLDTOT	fraction	0.59	0.60	0.01	2.1%
FLUT	W m^{-2}	257.31	256.13	-1.18	-0.5%
LHFLX	W m^{-2}	144.29	141.16	-3.13	-2.2%
PRECC	m s^{-1}	3.23E-08	3.26E-08	3.06E-10	0.9%
PRECL	m s^{-1}	1.07E-08	1.04E-08	-2.78E-10	-2.6%
PRECT	m s^{-1}	4.30E-08	4.30E-08	2.82E-11	0.1%
PS	Pa	101662.0	101725.0	63.0	0.1%
SHFLX	W m^{-2}	14.43	14.14	-0.29	-2.0%
T500	K	262.60	262.47	-0.12	-4.5E-2%
T850	K	284.53	284.51	-0.02	-7.4E-3%
TMQ	kg m^{-2}	32.99	33.21	0.22	0.7%
TREFHT	K	295.11	295.08	-0.03	-4.4E-2%

exhibit less than a 3% difference in climatology between the simulations. This near-identical match of the climatology supports the conclusion that model behavior at the 1° grid spacing in the variable-resolution is well matched to the corresponding globally-uniform run.

4.3.2 Spatial differences

The global, annual-averaged plot of 200 hPa zonal wind (U200) is shown in Fig. 4.4. Figures 4.4a-b show the results from the two model runs. The top two panels are virtually indistinguishable from one another, particularly over the refinement region which is outlined in black (Fig. 4.4a). The absolute difference between the two simulations is plotted in Fig 4.4c, which further shows the similarity between the simulations. The largest differences are in the midlatitude eastern Pacific but the maximum discrepancy between the two runs at any spatial location is less than 5%. The U200 NCEP reanalysis product is shown in Fig. 4.4d. Both model solutions appear to overestimate the mid-latitude jet stream in the southern hemisphere. The differences between either model simulation and NCEP are much larger than the

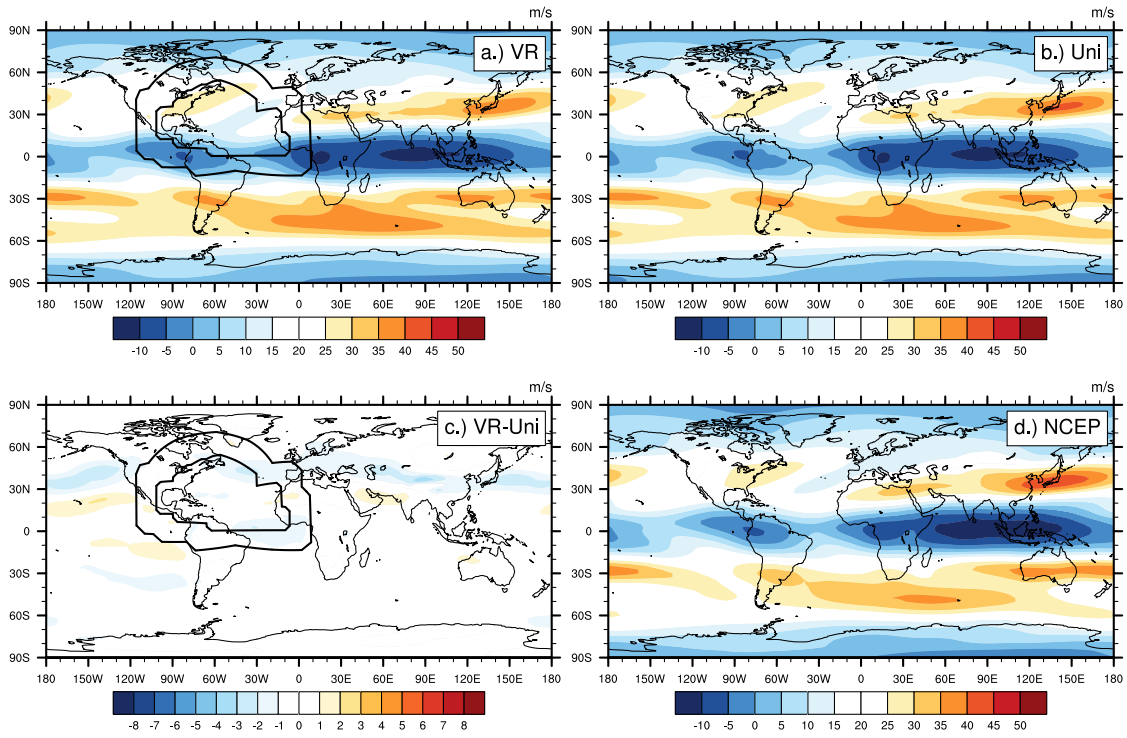

Figure 4.4: Plot of annually-averaged 200 hPa zonal wind (U200, m s^{-1}) for the (a) variable-resolution (VR) and (b) uniform 1° simulations. The difference between the two panels is shown in (c) and U200 from the NCEP reanalysis is shown in (d).

differences between the individual model simulations themselves.

To quantify this, we calculate the global root-mean square error (RMSE). The RMSE for U200 between both CAM-SE configurations is 0.77 m s^{-1}. In contrast, it is 2.34 m s^{-1} and 2.32 m s^{-1} when the NCEP reanalysis is compared to the var-res and uniform 1° CAM-SE simulations, respectively. This confirms that the differences between simulations using the two grids are extremely small relative to their discrepancy with respect to NCEP. The RMSE for either simulation compared to NCEP is also slightly smaller than the 2.87 m s^{-1} RMSE calculated in Evans et al. (2013) who use the same uniform 1° CAM-SE grid with CAM version 4 (CAM4, Neale et al. (2010a)) physics.

A latitude-height cross-section of the same time-mean zonal wind is plotted in Fig. 4.5. Here, the analysis is constrained to the high-resolution nest. The longitudinal

subset used for averaging (20°W to 80°W) is restricted to the Atlantic (red) gridbox from Fig. 4.3. Black lines on Figs. 4.5a,c denote the approximate latitudes of the grid transition region. Both Fig. 4.5a and Fig. 4.5b are very similar. The uniform 1° model has a slightly stronger and taller jet stream core (peaking at approximately 225 hPa, 47°N), although as seen in Fig. 4.5c, this difference is less than 7% (region above 200 hPa). As in Fig. 4.4, the differences between the two model simulations are much smaller than the difference between either simulation and the NCEP dataset (Fig. 4.5d). The jet stream in the var-res simulation is more similar to the NCEP data, although it is unclear whether this is a physical result due to the addition of resolution.

The spatial distributions of annually-averaged column total precipitable water (TMQ) for both models are plotted in Figs. 4.6a-b. The absolute difference between the two simulations is plotted in Fig. 4.6c with the average from the MERRA reanalysis over the 1980-2002 time period posted in Fig. 4.6d. TMQ is an interesting metric to examine because it is a rather smooth field but larger mountain ranges have significant regional impact on the spatial structure of the field in their immediate vicinity (Tuller, 1968). Because we seek to emphasize the topographical enhancement provided by variable resolution, we have chosen to use MERRA due to it's increased horizontal resolution (0.5°x0.666° (∼55-70 km) compared to NCEP's T62 (∼210 km) resolution). Analysis using NCEP's total precipitable water product showed that the resolution was too coarse to allow topography to impact regional TMQ structure in a meaningful way.

Figs. 4.6a-b show multiple key differences between the var-res and uniform 1° TMQ fields. Structure associated with the Appalachian Mountain range (near 40°N, 80°W) is noticeable over eastern North America in Fig. 4.6a, along with a local minimum in TMQ over the island of Hispaniola. In addition, the topographical signature of mountainous areas of Mexico, Central America, and northern South

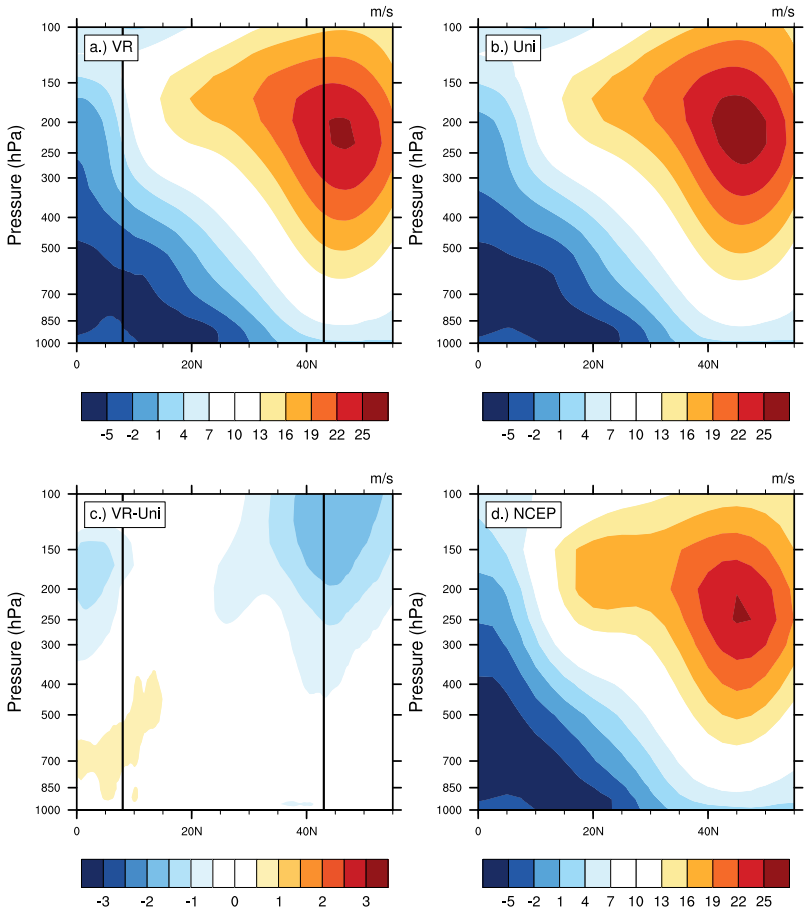

Figure 4.5: Pressure latitude cross-section of average zonal wind for (a.) variable-resolution simulation, (b.) uniform 1° simulation, and (d.) NCEP. The difference between the two model simulations is shown in (c.). The zonal average is taken between 80° W and 20° W, which corresponds to the longitude bounds of the Atlantic refinement in Fig. 4.3. Black lines denote the latitude bounds of the averaging area.

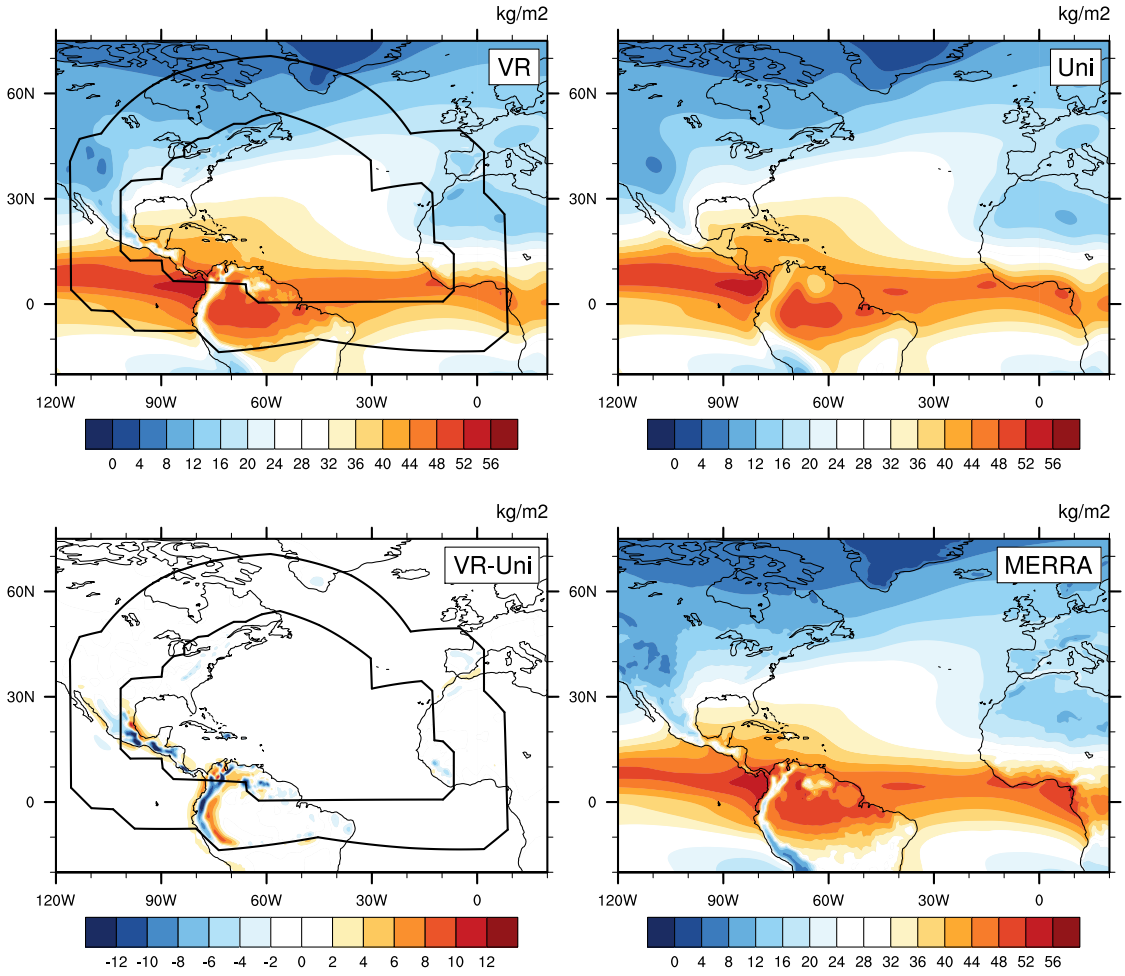

Figure 4.6: Plot of annually-averaged total precipitable water (TMQ, kg m^{-2}) for the (a) variable-resolution and (b) uniform 1° simulations. The difference between the two panels is shown in (c) and the TMQ from the MERRA data set is shown in (d).

America are much more structured in the var-res simulation with the relative TMQ deficit being more significant than in the coarse, uniform 1° model run.

Unlike Figs. 4.4 and 4.5, the difference panel (Fig. 4.6c) shows significantly more spatial difference between the two models. The vast majority of the differences are constrained to regions where the topography has been more (less) smoothed in the uniform 1° (variable-resolution) simulation (Fig. 4.2). Conversely, there is very little notable difference across the different grid scales themselves. For example, there is essentially no anomaly seen in Fig. 4.6c over the central Atlantic Ocean (the center of the refined nest). This is in contrast to grid-imprinting induced by highly-scale sensitive parameterization schemes (see Fig. 3.5 in Chapter III for an example of grid imprinting in CAM4 cloud fraction). This result implies that the majority of the climatological impact of refinement on average TMQ is not directly due to the grid spacing but indirectly due to the rougher topography allowed by the use of variable-resolution. The lack of observable difference over the Atlantic Ocean shows that localized refinement does not affect the large-scale TMQ distribution.

It is clear that the MERRA product (Fig. 4.6d) much more closely resembles the variable-resolution simulation (Figure 4.6a), especially in areas of the refined patch where the topographical representation is improved (Central America and northern South America). This implies that the refined resolution produces more topographically realistic flow.

We also show similar analysis for total cloud fraction, total precipitation rate, and outgoing longwave radiation (OLR) in Fig. 4.7. All fields agree with the conclusions from investigating the TMQ climatology. The largest discrepancy resulting from the addition of the refined patch appears to be constrained in areas where the topography is better represented due to the increased horizontal resolution. There are almost no distinguishable artifacts in the long-term means that appear as a result of variable-resolution, either as artifacts in/near transition regions due to the numer-

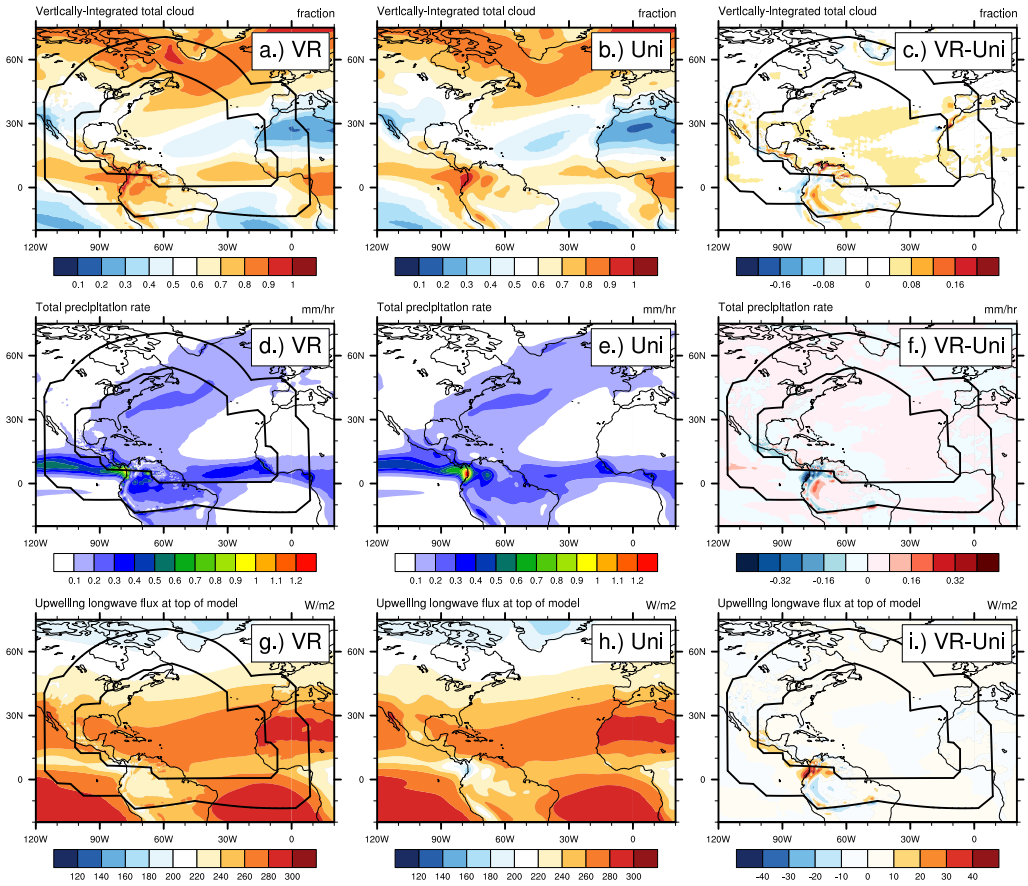

Figure 4.7: Plots of annually-averaged (a-c) vertically-integrated cloud fraction, (d-e) total precipitation rate, and (f-h) outgoing longwave radiation for the (left) variable-resolution and (center) uniform 1° simulations. The difference between the two panels is shown on the right.

ical discretization or as an induced climate bias appearing over the central Atlantic due to the physical parameterizations behaving significantly differently in the refined nest. The fact that the spatial patterns match well is a positive result for the implementation of variable-resolution CAM-SE as a tool for regional climate studies, but also confirms the results of Bacmeister et al. (2014) who concluded that substantial climate biases at large scales will likely not be improved through merely increasing resolution in CAM5.

Note that there is a degree of grid imprinting that appears at the southern interface between the intermediate 0.5° grid spacing and the global 1° grid (solid line stretching

from Peru to Bolivia over the Amazon). This is primarily evident in the precipitation field (Fig. 4.7), but also discernible in both OLR and cloud fraction. For example, the variable-resolution simulation produces slightly less precipitation to the north and slightly more precipitation to the south of this grid transition region than the global 1° simulation.

This imprinting was not evident until the run was completed and long-term means were calculated since it is not overtly discernible in instantaneous output. It is curious that these artifacts only appear over South America and not around other portions of the grid transition region which contain the same grid refinement structure. In an attempt to determine the source of these artifacts, we completed a two-year simulation using the release version of CESM version 1.2.0 coupled to the same version of CAM-SE used for this study. All user-defined model settings such as time step, model tunings, and topography are identical to the full simulation. A zoom of the 1999-2000 average precipitation is shown in Fig. 4.8. Upgrading from the CESM 1.1.17, which was a developmental version, to the release candidate of CESM 1.2.0 has mitigated these problems, indicating the issue was not with the variable-resolution aspect of the dynamical core but another model component. Unfortunately, since CESM is a combination of multiple model components being developed in parallel, it is difficult to isolate the specific cause of the artifacts. The elimination of these artifacts when using the release version implies the routine responsible for these features may have had a bug corrected or another improvement. Future simulations will utilize CESM version 1.2.0 or higher.

4.3.3 Taylor statistics

Taylor diagrams are an effective way of depicting how well-matched a spatial pattern produced by a model simulation is to observations (Taylor, 2001). The models are compared to the observational datasets found in Table 4.1. For the majority of this

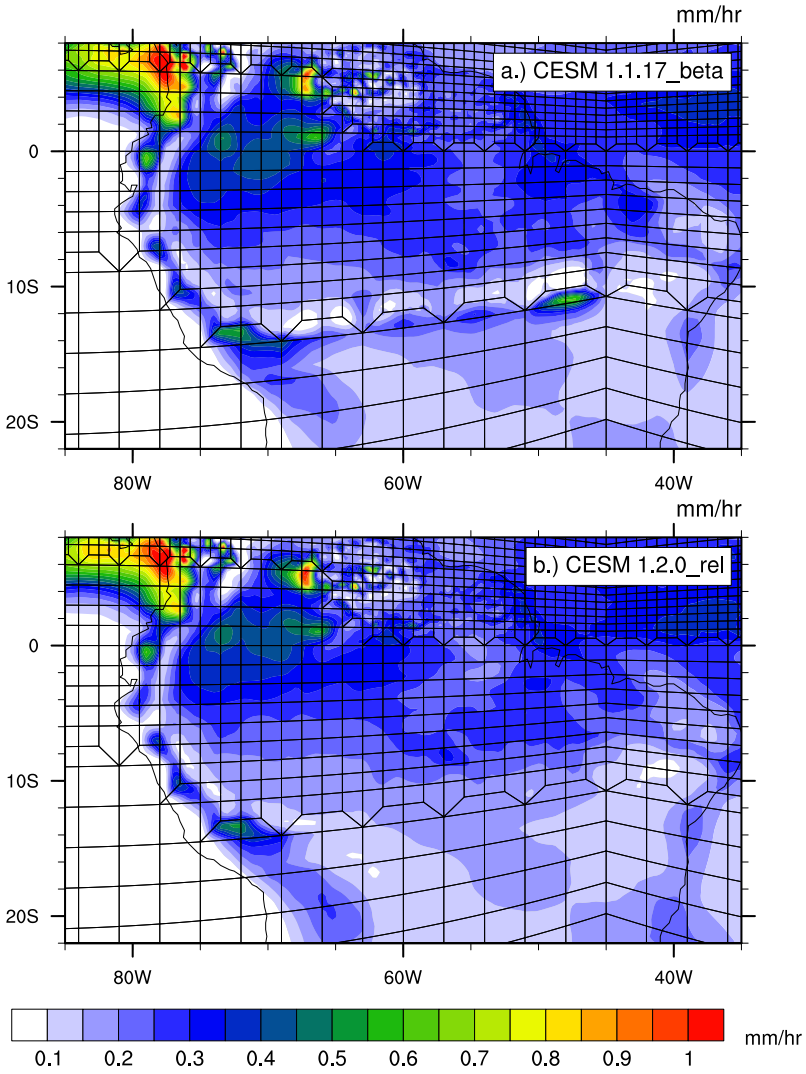

Figure 4.8: Comparison of annually-averaged precipitation rate for 1999-2000 between var-res simulation using (a) the CESM 1.1.17 developmental release and (b) CESM 1.2.0.

analysis we are more concerned with the relative difference between the two models and whether or not the skill of the model is significantly altered by the addition of refinement. A thorough analysis understanding why certain parameters are modeled with their particular degree of skill is beyond the scope of this thesis.

Taylor statistics for 23-year-mean global-mean quantities for sea-level pressure (PSL), total cloud fraction (CLDTOT), total precipitable water (TMQ), total precipitation rate (PRECT), 200 hPa zonal wind (U200), 850 hPa zonal wind (U850), 600 hPa relative humidity (RH600) and 500 hPa temperature (T500) are shown in Fig. 4.9. The absolute distance from the origin represents the normalized root-mean-square (RMS) difference while the spatial correlation is plotted as the radial angle between the model marker and the origin. Perfect agreement between model and observations would result in a marker being plotted at 1.0 correlation and at the "REF" location on the x-axis. Red dots indicate the variable-resolution simulation skill while blue crossed circles are from the uniform 1° simulation. As in Table 4.2, the model shows good agreement between the two simulations in terms of long-term climatology. The fact that the majority of the corresponding variable score pairs either overlay one another or are very close show that the spatial distribution and magnitude of these variables on both grids are essentially identical to one another.

Figure 4.10 shows the seasonal (December-January-Februrary (DJF) and June-July-August (JJA)) statistics broken out into the three shaded regions from Fig. 4.3. There is more separation in some of the point pairs, indicating potentially different solutions at the regional scale. Figures 4.10a-b show Taylor statistics in only the North Atlantic region marked in Fig. 4.3. Refinement appears to have little quantifiable effect on TMQ, PRECT, U850, and T500 when the analysis is restricted to the high-resolution part of the Atlantic basin. PSL is slightly harmed in DJF while improved in JJA when refinement is added. Little change is noted in CLDTOT during winter months. The uniform 1° simulation has higher CLDTOT skill in summer, although

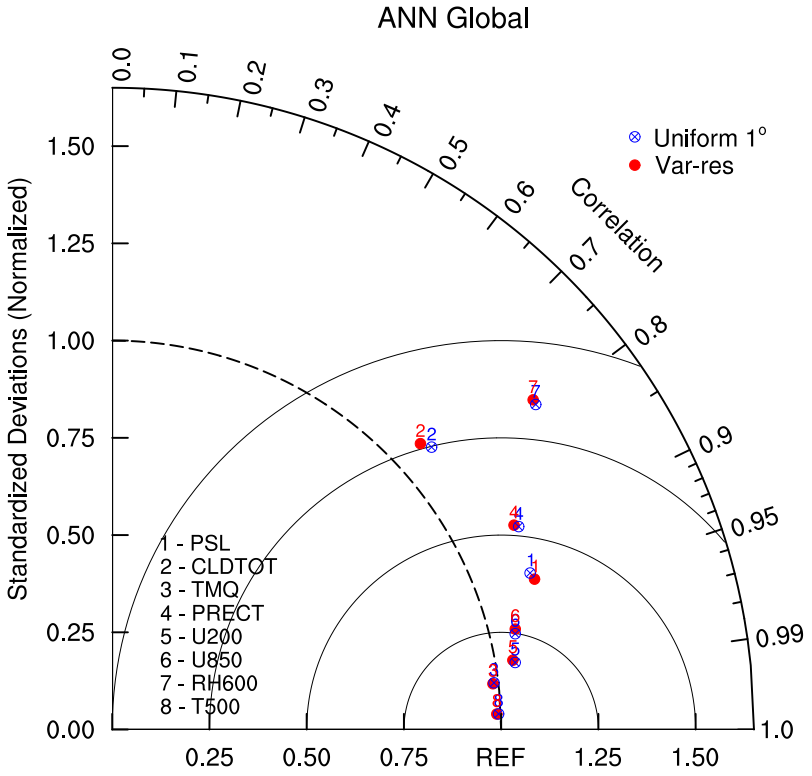

Figure 4.9: Taylor diagram for globally and annually-averaged climate statistics. Blue, crossed circles represent the uniform 1° simulation while red, filled circles represent the variable-resolution run. Data sets used as observations are listed in Table 4.1. See text for description of the diagram and explanation of acronyms.

this quantity is poorly simulated in both model runs during this season. U850 and RH600 improve slightly in both seasons with the addition of resolution.

Figure 4.10c-d shows the same analysis except for the North Pacific. In these plots, particularly the summer, corresponding pairs are not separated by significant distance, implying the model solution in both runs is highly similar. Interestingly, PSL is significantly degraded in the winter in the var-res simulation, while PRECT has a slightly lower correlation, but improved RMS difference. It is unclear if these represent upscale effects, especially since wintertime differences in the North Atlantic were relatively small (Fig. 4.10a) and very high agreement is shown between the two model simulations during the Pacific summer (Fig. 4.10d). It is possible some of this difference may stem from slightly different Himalayan topography which was alluded to in Section 4.2.3. These small differences may have a minor impact on certain patterns in the North Pacific.

The most interesting analysis is in Figs. 4.10e-f, which highlight Taylor statistics over the Central American region (Fig. 4.3, green crosshatch). This is the region where the largest differences between the simulations was seen, and may be attributable to the improved topographical representation in the variable-resolution simulation. Winter-time PRECT and TMQ are dramatically improved in the var-res simulation, with a smaller improvement in CLDTOT. All three of these features would be expected to have a strong relationship with the model topography since topography exerts direct control on vertical motion. In the summer, TMQ is similarly improved with resolution, while PRECT shows a more modest improvement. CLDTOT correlation decreases slightly but the magnitude of the RMS error is slightly smaller than in the uniform 1° run.

PSL shows a decrease in skill as measured by both quantities in both seasons. This result is similar to that seen in Bacmeister et al. (2014) who found a decrease in performance with higher resolution in aspects of CAM5, such as surface pressure,

that may be related to the model's "turbulent mountain stress" (TMS). TMS in CAM5 is intended to add surface stress due to unresolved subgrid orography (Richter et al., 2010). Bacmeister et al. (2014) postulate that the TMS tunings (which are tuned for $\sim 1^\circ$ simulations) may result in negative effects with increased resolution. RH600 also shows a slight decrease in both skill measurements with resolution during the summer, although it is unclear if this is related to the TMS parameterization or another mechanism which influences mid-level moisture or temperature. All other quantities in both seasons appear to have unremarkable differences between the two simulations, even in this smaller region with highly disparate topography.

4.4 Equatorial waves

One common method for detecting atmospheric waves is to generate wavenumber-frequency diagrams following the methodology of Wheeler and Kiladis (1999). Figure 4.11 shows the wavenumber-frequency diagrams for both the uniform 1° simulation (left) and the var-res simulation (right). The spectral analysis here uses 3-hourly total precipitation rates averaged between +/- 10°, which produce similar results to the more commonly used outgoing longwave radiation (not shown). Both the anti-symmetric (Figs. 4.11a-b) and symmetric components (Figs. 4.11c-d) of the power spectra are normalized by the background component to show the most active waves.

The diagrams are generated using 96-day segments with 60 days of overlap. Precipitation between 15°S and 15°N from 1992 to 2001 is used. Following Wheeler and Kiladis (1999), dispersion curves at equivalents depths of h = 12, 25, and 50 m for $n = 0$ eastward inertio-gravity waves (n=0 EIG), $n = 2$ inertio-gravity waves (n=2 IG), and mixed Rossby-gravity waves (MRG) are shown in the antisymmetric panels (top) with the same curves for $n = 1$ equatorial Rossby waves (n=1 ER), $n = 1$ inertio-gravity waves (n=1 IG), and Kelvin waves shown on the symmetric panel (bottom).

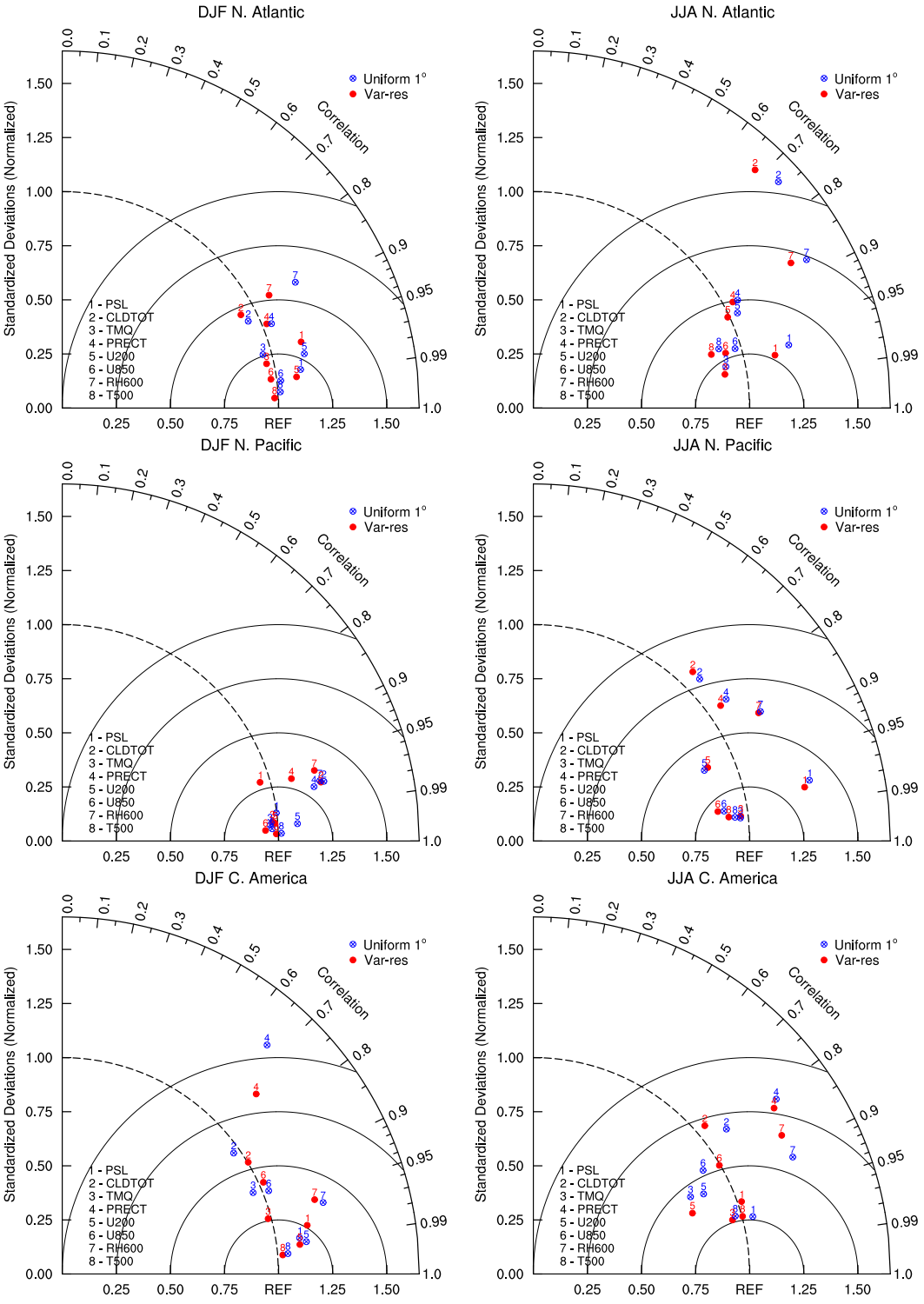

Figure 4.10: Same as Fig. 4.9 except broken down by season and basin. DJF statistics are on the left and JJA averages are on the right. Basins are defined in Fig. 4.3. North Atlantic averages are on top, North Pacific in the middle, and Central/South America on the bottom.

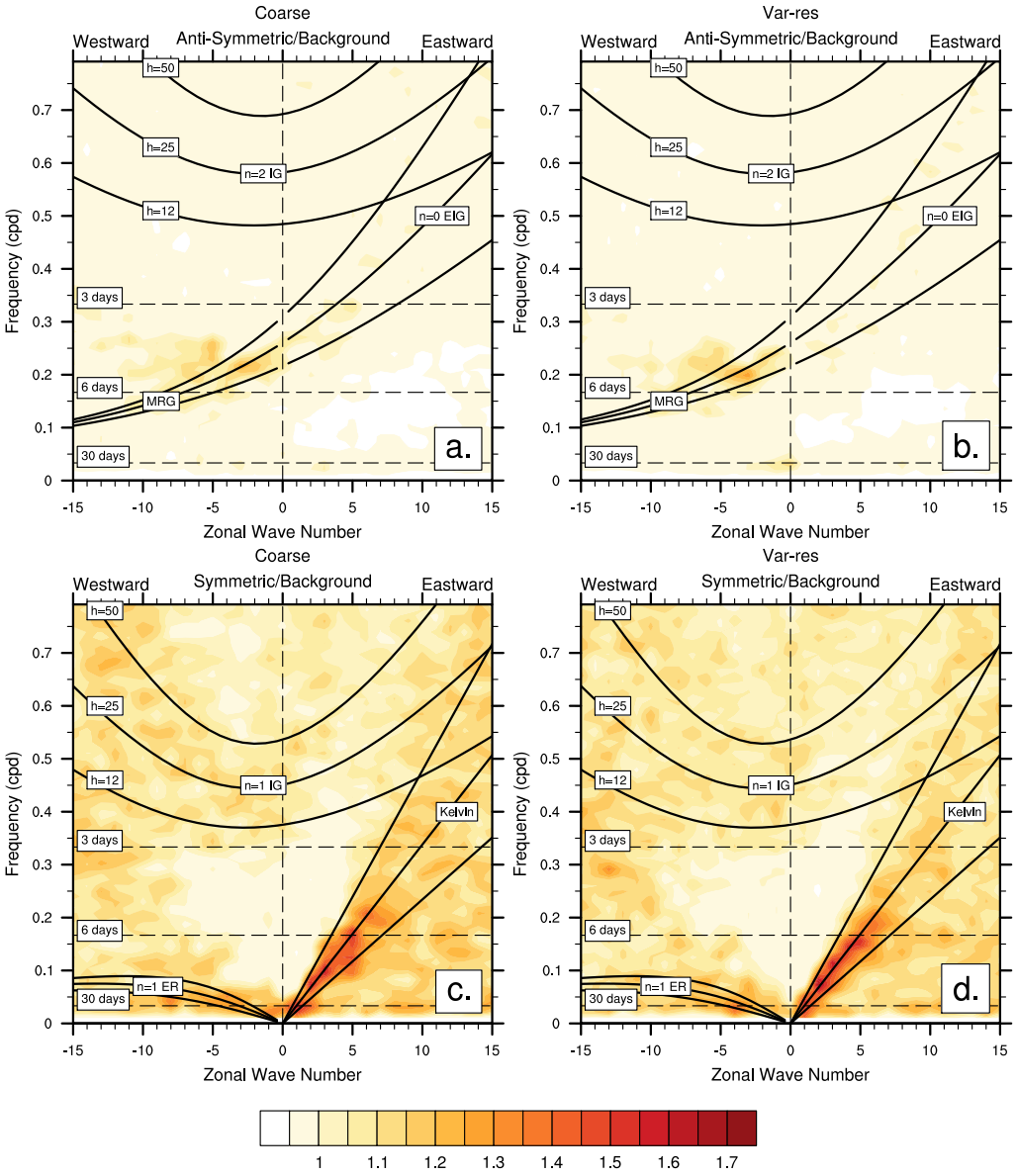

Figure 4.11: Wavenumber-frequency diagrams of total precipitation rate averaged between 10° N/S. Normalized anti-symmetric (a-b) and normalized symmetric (c-d) components of the logarithm of the power are shown for the coarse (a,c) and var-res (b,d) simulations. Dispersion curves from linear shallow-water theory for a zero wind basic state with equivalent depths h=12, 25 and 50 m are overlaid as in Wheeler and Kiladis (1999). Inertio-gravity (IG), equatorial Rossby (ER), equatorial inertio-gravity (EIR), and Kelvin waves are marked with their meridional mode numbers n. The uniform 1° simulation is shown on the left and variable-resolution on the right.

Figures 4.11a-b show low wave activity in the anti-symmetric power spectra. The highest peak occurs in westward propagating waves with frequencies between 0.15 and 0.25 cycles per day. This peak is associated with MRG waves. In Figs. 4.11c-d, low-frequency Kelvin waves are prominent, with the most variance located between the 25 and 50 m equivalent depth curves at longer periods (lower frequency). n=1 ER waves are also present, albeit weaker, and there is no significant n=1 IG wave activity.

These results are in good agreement with previous work using CAM-SE to perform AMIP simulations (Evans et al., 2013). Using CAM4 physics and a uniform 1° grid, their results also showed a robust Kelvin wave signature at lower wavenumbers that decreases with frequency. ER waves were also simulated with reasonable skill, but the model failed to produce peaks corresponding to westward propagating IG waves as well as MRG waves outside of the wavenumber band seen in this study. Additional comparison of wave features in the SE dynamical core using aquaplanet simulations can be found in Mishra et al. (2011a).

Most relevant for this study, Fig. 4.11 indicates good agreement between the two simulations. The high-resolution patch covers approximately 35% of the equatorial region north of the equator. However, this refinement does not adversely affect waves already resolved in the 1° simulation. Both simulations produce the same wave activity without any shift in phase speed or power. In addition, there does not appear to be spurious wave reflection or distortion induced by the grid transition region which would be denoted by the appearance of an anomalous power peak in either Fig. 4.11b or Fig. 4.11d.

4.4.1 African easterly waves

African Easterly Waves (AEWs) are dynamical features originating over North Africa. These waves are related to the African Easterly Jet present in the mid-

troposphere, south of the Saharan desert. The source region for AEWs is between 32°E and 15°E and centered at around 16°N (Holton, 2004). AEWs occur in the lower troposphere, near 700 hPa, during the summer months with a periodicity of about 3-5 days (Burpee, 1972). The meridional wind has a maximum amplitude of 1-2 m/s. The waves travel across the Atlantic Ocean, occasionally reaching the eastern Pacific Ocean, and play a key role in the generation of tropical cyclones in the tropical Atlantic (Frank, 1970).

In the variable-resolution simulation, the area most strongly associated with AEW genesis straddles the transition region as seen in Figure 4.1. Given this and the impact of AEWs on tropical cyclogenesis, they are an interesting case study for assessing the performance of the model from both a physical and dynamical standpoint. Figure 4.12 shows the vertical cross-section of the zonal wind between 20°S and 40°N (averaged between 15°W and 15°E) for the 1° coarse simulation (left) and variable-resolution simulation (right). Winds are averaged over the northern hemisphere summer (JJAS) seasons from 1990-2000. The jet associated with westerly monsoon winds is located at 5°N extending from the surface to around 850 hPa. The African Easterly Jet (AEJ) is centered around 13° and 650 hPa with the Tropical Easterly Jet (TEJ) located around 6°N and 200 hPa. Note that the longitudinal span cuts directly through the transition region between the high-resolution nest and the background 1° grid. No material difference is seen between the two simulations. The strengths of both the TEJ and AEJ are essentially identical and the shape and location of these two features are the same in both simulations. Both jets span at least 10° in latitude and are well-resolved at the various grid spacings in the simulations. Their impressive similarity indicates that the resolved flow can transit through transition regions and adapt to multiple grid spacings in a physically-consistent manner.

AEWs are detected by analyzing the meridional wind speed at 700 hPa. The area of interest, 20°S to 40°N and 50°W to 40°E, covers West Africa and the eastern

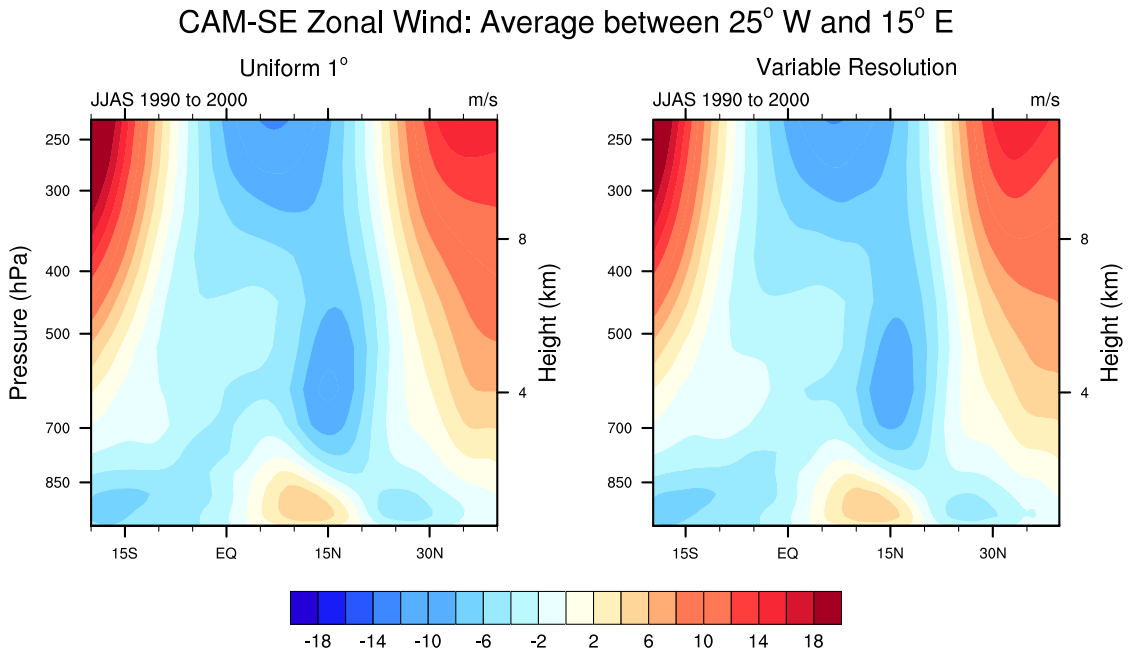

Figure 4.12: CAM-SE average zonal wind during JJAS for the uniform 1° simulation (left) and the variable-resolution simulation (right). Data is averaged between 15°W and 15°E over the time period 1990-2000.

portion of the Atlantic Ocean. The meridional wind data is averaged daily and bandpass filtered to isolate the activity with a frequency of 2-6 days during the JJAS summer months for each year. The variance is computed and then averaged over 20 years (1981-2000) to produce a measure of the typical AEW activity over West Africa.

Figure 4.13 shows the AEW activity in both model runs. In Fig. 4.13a, the solid black lines mark the outline of the transition region in the variable-resolution mesh. The overall structure is comparable with the uniform 1° results and there is no discernible grid imprinting, even along the lines which indicate the region where the grid resolution changes. This again indicates the transition regions are being well-handled by the model and suggests that tropical cyclone simulations using a multi-resolution grid within CAM-SE may not require that the high resolution region extend over the entire continent of Africa to properly resolve wave precursors to cyclone genesis in the Atlantic Ocean.

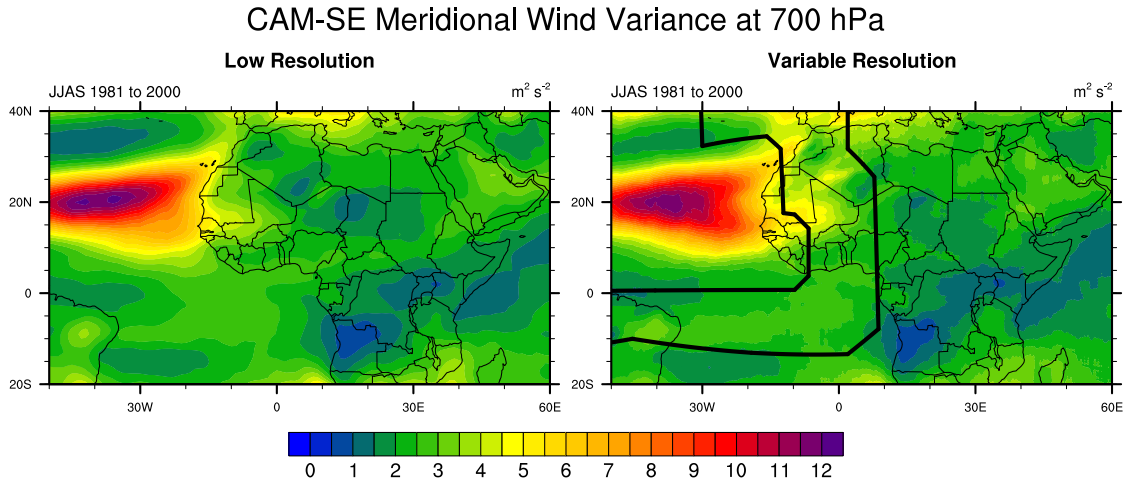

Figure 4.13: Variance of 700 hPa meridional wind for the uniform 1° simulation (left) and the variable-resolution simulation (right). Data is 2-6 day bandpass filtered and averaged over JJAS for the period 1981-2000.

It is worth noting that when compared to the ERA-40 reanalysis data (not shown), the magnitudes of the CAM-SE wind variance are much higher (using either grid), suggesting that the model may produce unrealistically high AEW activity. However, wave activity in CAM-SE falls well within the multi-model results described in Skinner and Diffenbaugh (2013), implying CAM performs similarly to other comparable models. The total spread in model results from Skinner and Diffenbaugh (2013) is an order of magnitude greater than than the differences seen between the coarse uniform and variable-resolution simulations in Fig. 4.13, further showing that the model produces a highly similar solution with or without the presence of a high-resolution nest.

4.5 Regional climatology improvements

4.5.1 Precipitation extremes

The frequency of high-intensity precipitation events has been shown to increase with resolution in both earlier versions of CAM (Williamson, 2008a; Li et al., 2011) as well as CAM5 (Chapter III; Wehner et al. 2014). As implied by the results in

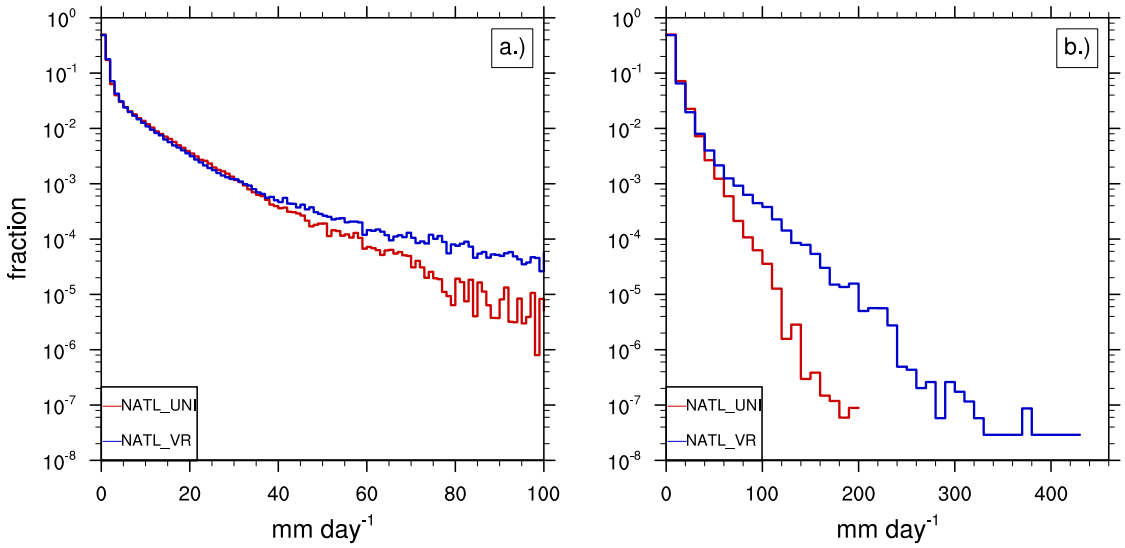

Figure 4.14: Precipitation histogram representing fraction (logarithmic scale) of instances where 3-hourly instantaneous precipitation rates were in specific intensity bins for AMIP simulations. Statistics are averaged over North Atlantic (NATL) region from Fig. 4.3. The uniform 1° simulation (UNI) is plotted in red and the var-res (VR) simulation in blue. Bin sizes are 1 mm day^{-1} in the left panel and 10 mm day^{-1} on the right.

Table 4.3, finer resolution leads to stronger resolved updrafts and an increase in large-scale precipitation which is not fully compensated by a corresponding decrease in convective precipitation rate. Figures 4.14 and 4.15 show precipitation histograms for the Atlantic and Pacific statistical regions, respectively. Statistics are calculated using 3-hourly total precipitation rate. Precipitation rates are first conservatively remapped to a uniform 2° grid based on the recommendations of Chen and Knutson (2008). Both panels in the figures show the same data, with the left panel only focusing on precipitation values less than 100 mm day^{-1}.

The 0.25° nest over the Atlantic produces an obvious divergence in precipitation frequency from the 1° grid spacing beyond 32 mm day^{-1}, with the variable resolution simulation producing a much higher frequency of more intense events. Over the central Atlantic basin, the 1° simulation only produces a maximum precipitation rate of approximately 200 mm day^{-1}, while the variable-resolution simulation produces events greater than 400 mm day^{-1}, even after remapping. Fig. 4.14a shows that

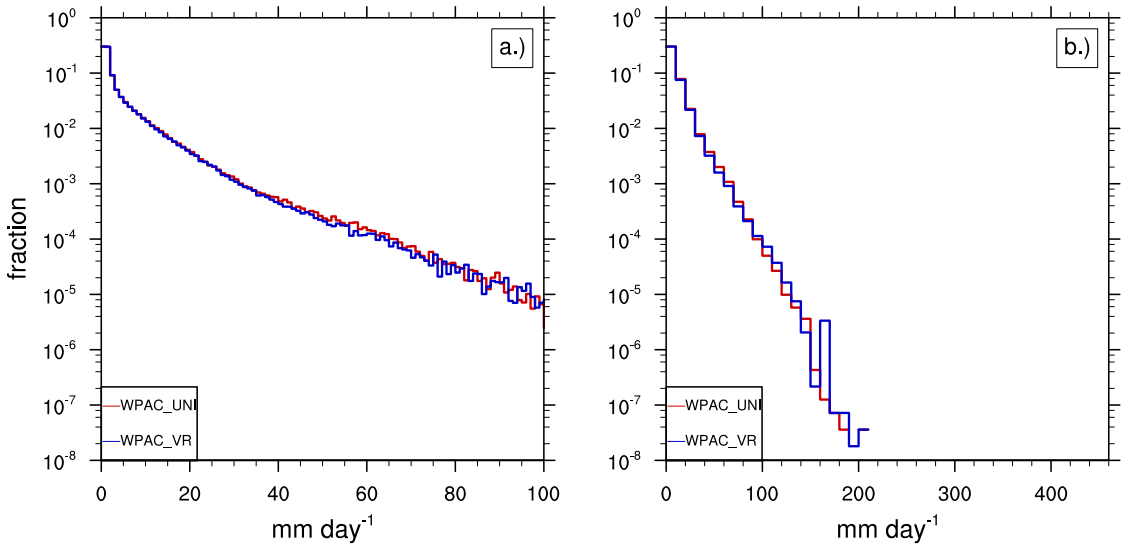

Figure 4.15: Same as Fig. 4.14 except for North Pacific averaging region.

for precipitation rates less than approximately 32 mm day^{-1}, the frequency of light precipitation events is higher in the coarse grid. While Table 4.3 lists a small (3%) increase in precipitation in the high-resolution nest compared to the 1° simulation, it is clear that the increase in high-intensity events is at least partially offset by a decrease in high-frequency, low-intensity, "drizzle" events at the finer grid spacing. Figure 4.15 displays nearly identical frequency profiles, which suggests that the dynamical behavior in the 1° portion of the var-res grid is the same as in the globally-uniform 1° simulation.

4.5.1.1 South American precipitation

While the direct simulation of transient small-scale features such as tropical cyclones, squall lines, and other extreme mesoscale features are popular targets for regional refinement, orographically-influenced climatology is another area which may be improved through the use of multi-resolution grids.

In Figs. 4.16a-c we plot the mean climatology of total precipitation rates over Central America and the nearby bodies of water for both model simulations as well as observations. The observations are climatology averages from the Tropical Rainfall

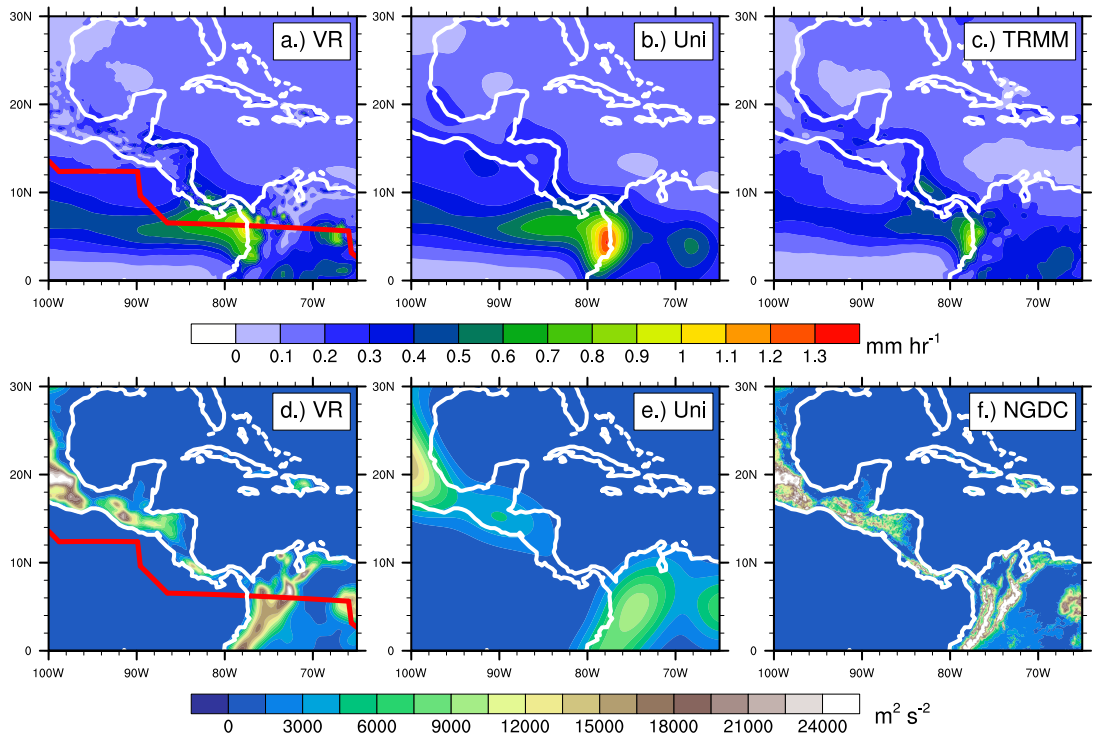

Figure 4.16: Annual average total precipitation rate in the variable-resolution (a.) and uniform 1° (b.) simulations as well as TRMM observations (c.). Topography for the same regions is shown for both models (d. and e.) as well as the NGDC dataset (f.). The transition boundary between 0.25° and 0.5° in the variable-resolution grid is highlighted in red in (a.) and (d.).

Measuring Mission (TRMM) 3B43 product (Huffman et al., 2007). This dataset has a higher resolution than GPCP product but only spans the equatorial regions, making it more useful for regional analysis. Model topography for the corresponding region is plotted in Figs. 4.16d-e. The NGDC ETOPO2v2 topography is shown in Fig. 4.16f.

The precipitation fields within the variable-resolution simulation (Fig. 4.16a) are noisy. However, more structure is apparent when compared to the unrefined 1° simulation (Fig. 4.16b). In particular, local maxima in precipitation are seen over various islands in the Caribbean Sea. This is also present in the TRMM observations (Fig. 4.16c). These results are similar in nature to the TMQ analysis in Fig. 4.6.

There is a high bias in the local maximum in precipitation off the western coast of Colombia. This anomaly also appears in previous 1° CAM4 AMIP simulations using

both the SE and FV dynamical cores (Neale et al., 2013; Evans et al., 2013). This bias is greatly reduced in the variable-resolution simulation. We hypothesize that this improvement stems from the fact that less smoothing of the western slopes of the Andes is required in the variable-resolution simulation. Smoothing of orography in the 1° simulation has pushed the mountains 200-300 km into the Pacific Ocean (Fig. 4.16e). This leads to anomalously-forced upslope flow over model grid boxes still masked as ocean cells, leading to dramatically increased precipitation. Neale et al. (2013) also showed that the bias (at 1° resolution) was somewhat reduced through coupling to an active ocean model.

This improved orography also simulates rain shadowing on the eastern side of the Andes mountains (manifested as a narrow strip of suppressed precipitation oriented from north-northeast to south-southwest across northwestern South America) which is not seen in the uniform 1° simulation.

4.5.1.2 Mountain-gap winds

A mountain-gap wind which passes southward through the Sierra Madre range is prevalent during boreal fall, winter, and spring. This feature is due to an increased pressure gradient between the Gulf of Mexico and the tropical Pacific during cold air outbreaks over North America. The pressure gradient results in a cross-isthmus wind that is funneled into a gap just north of the Gulf of Tehuantepec creating a low-level jet strong enough to appear in the mean climatology (Chelton et al., 2000). These features are shown to be associated with tropical cyclogenesis in the eastern Pacific (Holbach and Bourassa, 2014) and therefore their representation within the model may be critical to producing realistic storm climatology.

Figure 4.17 shows the lowest model level January meridional wind (v-wind) for the two models (a,b), and observations (c) from the NOAA Blended Sea Wind dataset (Zhang et al., 2006). Topography is again shown in the lower panels (Figs. 4.17d-

f). Note that the scales for Figs. 4.17a-b and Fig. 4.17c are not the same since the observed winds are surface winds (as opposed to the lowest model level, which is approximately 992 hPa in CAM) and also are a blend of various products which have different effective averaging times. The jet associated with the aforementioned phenomenon is seen as the southward maximum in wind located at approximately 15°N and 95°W. This feature is significantly more robust and localized in the variable-resolution simulation (Fig. 4.17a) when compared to the coarse 1° run (Fig. 4.17b). It is apparent that the improved topographical representation in the variable-resolution simulation (Fig. 4.17d) leads to improved local dynamics in this region. Better simulations of features such as these will lead to improved local climate representation in areas that are strongly influenced by orographic features at spatial scales below the typical resolution of most global climate models.

4.6 Discussion and conclusions

We have presented climatological results comparing a global simulation with a refined nest to an identically-forced simulation without the nest. Using CAM-SE with the latest CAM5 physics package, it is found that the addition of a high-resolution refinement over the Atlantic ocean (approximately 1/10th of the global domain) does not have any noticeable impact on the global circulation. Global averages are well matched to the previously published CAM5 results from Bacmeister et al. (2014) and Wehner et al. (2014).

When just the Atlantic is isolated, an expected increase (decrease) in large-scale (convective) precipitation is observed with the variable-resolution mesh. These effects partially compensate each other with regards to the total modeled precipitation, although total precipitation still increases slightly in the high-resolution nest. The only other parameterized variable showing >5% difference in its long-term mean between the refined and unrefined simulations is the sensible heat flux. We hypothesize

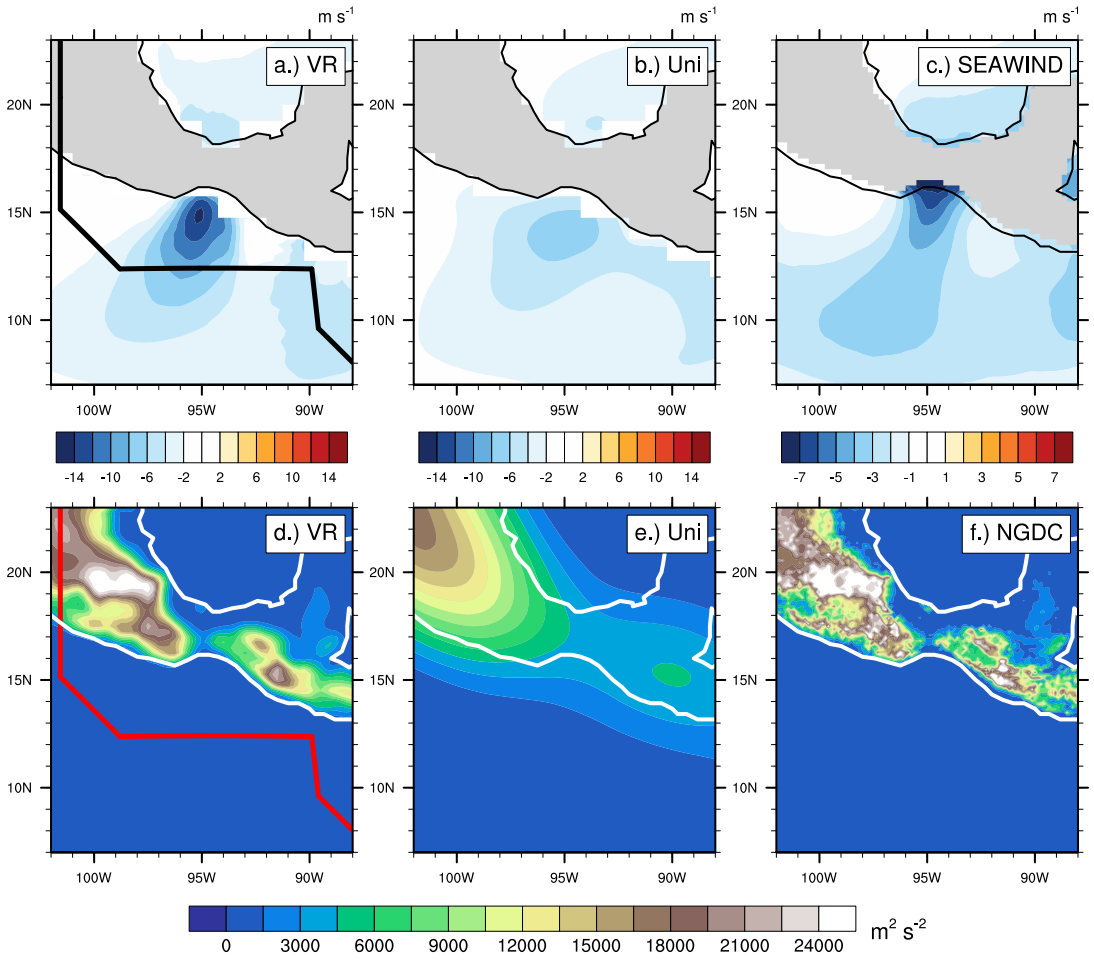

Figure 4.17: Average January meridional wind near the Gulf of Tehuantepec for the lowest model level in the variable-resolution (a.) and uniform 1° (b.) simulations as well as at the surface from SEAWIND observations (c.). Topography for the same regions is shown for both models (d. and e.) as well as the NGDC dataset (f.). The transition boundary between 0.25° and 0.5° in the variable-resolution grid is highlighted in black and red in (a.) and (d.)

this may be a manifestation of the increased resolved wind speeds with horizontal refinement, although future work is necessary to isolate this mechanism.

Minor statistical differences are seen between the far-field portion of the grid (region over the North Pacific with identical grid spacing). Minor differences (<3%) are apparent in cloud fraction and surface fluxes. It is unclear whether these are physical differences due to the grid or a result of the smaller spatial averaging region (compared to the global domain). Chapter V shows the high-resolution nest may provide some upscale effect to the global domain via extratropical transition of better resolved tropical cyclones, which may have an impact on the downstream atmosphere, although further analysis is necessary to understand the magnitude of these effects.

Features such as equatorial waves and zonal jets over the west coast of Africa are not disturbed by the addition of refinement, implying atmospheric flow passes through transition regions without developing significant errors in phase speed or other wave reflection/distortion. The frequency of precipitation extremes are increased in the high-resolution nest, which agrees with previous research with CAM (Chapter III; Wehner et al. 2014).

Variable resolution allows for a better representation of topography in the high-resolution nest. Improvement is seen in quantities which are spatially correlated with topographical signatures. We highlight improvements in the simulation of precipitation in the vicinity of mountains and mountain-gap winds using variable-resolution grids. Other topographically-affected flow may be better represented in global models through this framework.

This study shows that, while the overall spatial pattern of precipitation is improved with increased resolution, possible noise may occur in the precipitation field in the presence of the sharper topography within the refined nest. While not extensively investigated, this phenomenon is likely induced by approximate discontinuities in the surface boundary condition (orography) and may be analogous to Gibbs ringing

seen in global spectral models near sharp gradients. Preliminary work has shown that increasing the divergent component of the explicit diffusion (hyperviscosity) within the model's dynamical core improves some of this noise in the vicinity of rougher topography (Lauritzen, personal communication). In addition, improved smoothing techniques may also provide better results. These will be areas of future testing and development with variable-resolution CAM.

In addition, while the scalar hyperviscosity described in Chapter II and used here handles explicit diffusion in transition regions adequately, a new tensor-based hyperviscosity has been shown to improve results of variable-resolution grids using shallow-water test cases (Guba et al., 2014). This formulation allows for a more consistent treatment of dissipation in highly distorted elements and will be tested as an update to the treatment of hyperviscosity in future simulations using CAM. In addition, new techniques for grid generation are in development (Guba et al., 2014) which would provide less distorted transition regions in future variable-resolution CAM-SE applications.

CHAPTER V

A multidecadal simulation of Atlantic tropical cyclones using a variable-resolution global atmospheric general circulation model

5.1 Introduction

With tropical cyclones currently estimated to be responsible for 19,000 fatalities/year and $26 billion/year in damages worldwide (Mendelsohn et al., 2012), future projections of tropical cyclone (TC) activity continue to be an important research question in the climate modeling community. Simulating TCs in global atmospheric general circulation models (GCMs) is extremely difficult because they operate on small spatial scales. Fine horizontal grid spacing and, subsequently, significant computational resources is required. Global models used for recent climate assessments exhibited tropical cyclone intensity statistics which were biased low since models cannot adequately resolve the dynamics of these features (Hamilton, 2008; Flato et al., 2013). Improvements in the community's ability to model these storms is of vital importance to lowering projection uncertainty and providing a more thorough picture of tropical cyclones' connection to the climate system.

Recent advances in computational ability have allowed for global simulations at relatively high (sub-50 kilometer) horizontal resolution. This increased resolution has

shown to produce significantly more realistic storm counts when compared to models with coarser grid spacing (Oouchi et al., 2006; Bengtsson et al., 2007a; Zhao et al., 2009; Murakami et al., 2012; Manganello et al., 2012; Satoh et al., 2012; Strachan et al., 2013; Wehner et al., 2014). However, even with improved counts at the global scale, simulation of Atlantic TCs has continued to be particularly difficult, with overall climatology being represented more poorly than other ocean basins, even in models utilizing higher resolution (Walsh et al., 2013).

The development of variable-resolution grids in conjunction with next-generation models can allow for the selective application of high resolution in specific geographic regions, thereby improving both short-term predictions and long-term projections of tropical cyclones on parallel computing architectures. Variable-resolution general circulation models (VRGCMs) are similar to regional climate or limited area models (LAMs) in that they nest high resolution over a specific area of interest, saving computational time which would have otherwise been used to simulate the remainder of the globe at high resolution. However, LAMs require lateral boundary conditions, which may be formulated using inconsistent models, may suffer from interpolation error, and may be mathematically inconsistent, among other issues (Warner et al., 1997; Mesinger and Veljovic, 2013). VRGCMs avoid these inconsistencies.

VRGCMs possess the ability to simulate the atmosphere at multiple resolutions and can serve as the intermediary tool between fixed-resolution GCMs and LAMs. Such variable-resolution models span multiple scales in a single simulation, focus their computational (high resolution) efforts on a specific region while establishing two-way interactions in a numerically and physically consistent way. While grid stretching techniques exist (e.g., Côté et al. (1993); Abiodun et al. (2008); Tomita (2008), among others), the majority of VRGCMs make use of locally refined grids to embed the high resolution domain. The past few years has seen a proliferation of new models capable of spanning multiple resolutions in a single simulations (e.g.,

Ringler et al. 2008; Walko and Avissar 2011; Skamarock et al. 2012; Harris and Lin 2013; Chapter II; Chapter III) which utilize recent advancements in both computing power and subgrid parameterizations. Tropical cyclones are an excellent target for these variable-resolution frameworks given their resolution dependence and the fact that storms are localized to individual ocean basins. However, VRGCMs have only been used by Chauvin et al. (2006) and Caron et al. (2011) for long-term studies of regional tropical cyclone climatology.

In this chapter we explore climate simulations using a variable-resolution implementation of the Community Atmosphere Model's (CAM) with a Spectral Element (SE) dynamical core (Neale et al., 2010b). This model has been jointly developed by the National Center for Atmospheric Research (NCAR) and U.S. Department of Energy (DoE) laboratories. A high-resolution nest is embedded over the Atlantic Ocean. We discuss the implications of this refinement on tropical cyclone statistics in a multi-decadal climate simulation using prescribed sea surface temperatures (SST) and sea ice. This experiment follows protocols outlined in the Atmospheric Model Intercomparison Project (AMIP) (Gates, 1992). We seek to determine whether refinement provides a substantial increase in model skill in simulating tropical cyclones at the regional level, while not requiring the computing resources of a globally-uniform, high-resolution grid. We also compare the performance of a refined grid to an unrefined grid to determine if tropical cyclones generated outside of the nest are impacted by the addition of the high-resolution patch.

Section 5.2 offers an introduction to CAM-SE and its variable-resolution option as well as details regarding the climate simulation. Section 5.3 outlines the method used to detect tropical cyclones in model data. Section 5.4 explores the results of the simulations by investigating spatial climatology, count statistics, intensity profiles, and model variability of cyclone activity at the seasonal and interannual time scales. The findings of the study are discussed in Section 5.5 and future areas of research

pertaining to tropical cyclones and VRGCMs are suggested.

5.2 Model description

5.2.1 CAM-SE

The atmospheric model used for this study is the NCAR/DoE Community Earth System Model (CESM) version 1.1. CESM is a fully-coupled, community model allowing for various configurations of four separate models (atmosphere, ocean, land, sea ice) to simulate global climate.

The atmospheric component within CESM is CAM. In particular, we utilize the CAM version 5 subgrid physical parameterization package (Neale et al., 2010b) and the spectral element dynamical core (Taylor et al., 1997; Taylor, 2011; Dennis et al., 2012). The SE dynamical core is the newest of the four dynamical cores available in CAM and replaced the Finite Volume (FV) option as the model default as of version 5.3, released in 2013. The spectral element scheme's mathematical compatibility allows for exact local conservation of mass, energy and 2-D potential vorticity (Taylor and Fournier, 2010).

CAM-SE uses the spectral element method on a cubed-sphere grid to discretize in the horizontal direction (Dennis et al., 2012). Cubed-sphere grids provide for quasi-uniform mesh spacing over the entire surface of the globe. This eliminates issues that arise from the use of traditional latitude-longitude grids such as the convergence of meridians in polar regions which requires either extremely short time steps or polar filtering to satisfy numerical stability constraints. The accuracy of the model can be controlled by selecting the polynomial degree of the basis functions on each quadrilateral element. The default polynomial degree in CAM-SE is selected to be three (cubic polynomials), leading to fourth-order spatial accuracy. We utilize a finite-difference approach in the vertical with a hybrid sigma-pressure coordinate,

and a Runge-Kutta time discretization.

Spectral elements are highly localized numerical discretizations and therefore require minimal communication between processors on massively parallel computer systems. Therefore, it is an optimal choice for future, high-resolution climate simulations. Dennis et al. (2012) and Evans et al. (2013) have shown that CAM-SE outperforms other dynamical cores in CAM at all processor counts for 0.25° (∼28 km) resolution and finer and also scales nearly linearly up to one element per processor. As parallel computers continue to grow in size, CAM-SE is an attractive choice for high-resolution runs.

5.2.2 Variable resolution in CAM-SE

Because CAM-SE solves the hydrostatic primitive equations locally on individual elements, it possesses the ability to run on non-uniform grids without significant modifications to the underlying numerical scheme. The only two restrictions to running CAM-SE on non-uniform grids are that elements must be quadrilateral and the refinement must be conforming (meaning every edge is shared by exactly two elements). Any conforming tiling of the sphere with quadrilaterals that satisfies these two criteria is acceptable, and allows CAM-SE to maintain key conservation properties on highly distorted grids.

To perform integrated climate simulations, CAM-SE is coupled to both an ocean/ice and land model through the CPL7 tri-grid coupler within the CESM framework (Craig et al., 2012). The coupler utilizes conservative remaps between model components to allow the atmosphere to run in conjunction with more standard ocean and land grids. Prescribed SSTs and sea ice concentrations are provided on a gx1v6 tripole grid. The land model is the Community Land Model (CLM) version 4.0 run on a 0.9 by 1.25° latitude-longitude grid. Unlike the ocean/ice, the land model is not prescribed and is allowed to freely adjust.

We perform two identical simulations using two different atmospheric grids. The first is a globally-uniform 1° (∼111 km) grid, seen in Fig. 5.1a. This is also referred to as the "coarse" grid. The second is a grid with a global base resolution of 1° with a refined patch of 0.25° (∼28 km) grid cells centered over the North Atlantic Ocean (Fig. 5.1b). This is referred to as the variable-resolution or "var-res" (VR) setup. Note that Fig. 5.1 shows the elements which tile the sphere; each element contains an additional 3-by-3 grid of cells defined by the spectral element method's collocation points which is used to define the effective horizontal resolution. In the variable-resolution model runs, there is a transition region of 0.5° between the global background grid and the main refinement area. The irregular shape of the high-resolution nest was selected to approximate the region where North Atlantic tropical cyclones occur in the historical record. A '2-refinement' structure is used to transition between resolutions, where a halving of grid spacing is achieved by dividing each cubed-sphere element into four equal elements with a one-element transition region in between (Anderson et al., 2009).

The variable-resolution grid in Fig. 5.1b contains approximately 1/6th of the number of grid cells as a globally-uniform 0.25° mesh. Past work has shown CAM-SE performance scales linearly with the number of grid elements (Dennis et al. 2012; Evans et al. 2013; Chapter III) up to very large processor counts, so the variable-resolution mesh should allow for a factor of 6 times runtime improvement over a globally-uniform grid high-resolution grid. Short, informal timing studies comparing a uniform 0.25° grid with the variable-resolution mesh show that this is a valid assumption, although components of CESM which are less scalable than CAM-SE result in a slight degradation of the linear speedup.

A comparison of the two model grids and their configuration is shown in Table 5.1. Explicit fourth-order hyper-diffusion is applied in each element and the diffusion coefficient is scaled according to grid spacing. A more detailed discussion about the

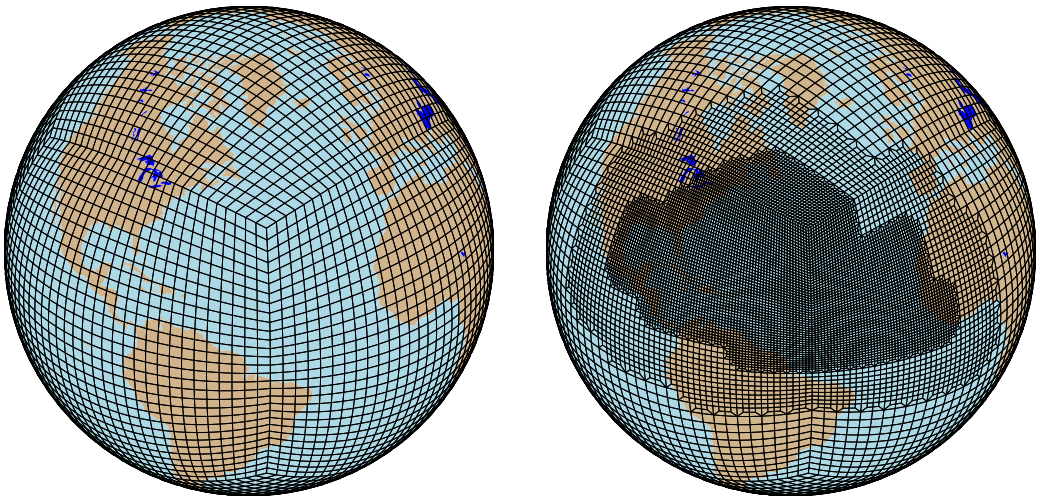

(a) (b)

Figure 5.1: The two meshes used for this study are (a) a uniform 1° resolution mesh and (b) a variable resolution mesh that ranges from 1° → 0.25°. Note that each element shown in the above plots contains additional 3 × 3 collocation points.

hyper-diffusion can be found in Chapter II. The number of vertical levels is 30. The physics time step is set to 1800 seconds instead of the 0.25° default of 450 seconds. Williamson (2013) showed that CAM's deep convective scheme performed poorly at short physics time steps due to inherent relaxation timescales in the parameterization. Reed et al. (2012) suggested that using an 1800 second time step produced more realistic tropical cyclone intensities by providing more reasonable partitioning between the large-scale and convective precipitation in CAM. Cold ice and rain water autoconversion coefficients were set to match the defaults for high-resolution (0.25°) CAM-FV runs. All other physical parameterization tuning parameters are CAM defaults which are derived from 1° CAM-FV simulations.

In the variable-resolution simulation, topography is differentially smoothed by starting with an initial high-resolution data set and applying a Laplacian smoother over the global domain. The smoothing is scaled approximately by element area as in the hyper-diffusion formulation, providing more (less) smoothing over areas tiled with

Table 5.1: CAM-SE resolutions of interest to this study. Grid spacing Δx (in kilometers and degrees) correspond to the grid spacing at the center of a cubed-sphere (CS) face. Dynamics time steps (Δt_{dyn}) are globally constrained by the finest grid scale in an individual variable resolution model simulation, while the 4th-order diffusion coefficient $K_4\,(\Delta x)$ (hyper-diffusion) is allowed to vary among individual elements.

Setup	CS res.	Δx (°)	Δx (km)	Elements (#)	Δt_{dyn} (s)	K_4 ($m^4\ s^{-1}$)
Uniform	n_e30	1°	111	5,400	360	1E+15
Var-res	n_e30x4	1° → 0.25°	111 → 28	13,340	100	1E+15 → 1E+13

larger (smaller) elements. The newly smoothed data is used to provide conservatively mapped values for subgrid variability of topography needed for the parameterization of turbulent mountain stress, subgrid orographic drag, and momentum flux deposition due to gravity waves (Lauritzen et al., 2012). The overall magnitude of smoothing is constrained such that it closely matches the profile of the operational default topography data used for uniform-resolution simulations in CESM. To lessen atmospheric noise with rougher topography at higher resolution, an additional divergence damping is applied to the momentum equations in 0.25° simulations utilizing the SE dycore (Lauritzen et al., 2014). However, given the findings of Zhao et al. (2012) which showed potentially significant sensitivity of GCM-simulated TCs to explicit diffusion, we have chosen to utilize a slightly smoother topography profile in the high-resolution nest such that numerical noise near topographical peaks is eliminated without this additional damping.

The simulations follow AMIP protocols. SSTs are specified by the Hadley Centre Sea Ice and Sea Surface Temperature dataset (HadISST, Hurrell et al. (2008)). Greenhouse gas concentrations and aerosol climatology are also prescribed in an attempt to reproduce past observations. Both simulations are initialized in September of 1979, although the first four months are discarded for model spinup. Both models are integrated through the middle of 2003, although only the years 1980 through

2002 (inclusive) are analyzed in this chapter. The variable-resolution model run was conducted on NCAR's Bluefire machine and averaged ∼0.42 simulated years per day on 384 cores. The 1° simulation was completed on the Agri computing cluster at the University of California, Davis. Due to the coarse grid having fewer elements and a longer stable timestep, model throughput was ∼2.5 simulated years per day on 384 processors, although a direct comparison of simulations across different hardware platforms is difficult.

5.3 Tropical cyclone detection algorithm

Objective detection of tropical cyclones within the climate dataset was performed using a method similar to that described in Vitart et al. (1997) and Knutson et al. (2007). Candidate cyclones were detected in 6-hourly model output as follows:

1. All local 850 hPa vorticity maxima greater than 1.0 x 10^{-4} s^{-1} at 850 mb were found between the latitudes of 45° S and 45° N.

2. For each maximum, the nearest collocated sea level pressure (SLP) minimum was defined as the storm center. This minimum must occur within 4° of the vorticity maximum.

3. The nearest local maximum of 500-200 hPa average temperature is defined as the center of the warm core. This cannot be offset from the storm center by more than 2° of latitude. From the center of the warm core, the temperature must decrease by at least 0.8 K out to 5° in all directions.

An allowable 4° offset (compared to 2° in Knutson et al. (2007)) was found to provide fewer "misses" of weaker or broader storms which sometimes contained multiple vorticity peaks or elongated pressure minima within the circulation. It also assisted

in alleviating the occasional double counting of broken trajectories as discussed in Camargo and Zebiak (2002).

The 850 hPa vorticity field is calculated from the zonal and meridional wind components using spherical harmonics. A 9-point filter was used to apply localized smoothing and damp grid-scale maxima that may influence the tracking algorithm, especially when tropical cyclones are near areas of steep topography (ex: Bay of Campeche, Yucatan Basin). Unlike past studies using lower resolution data (e.g., Vitart et al. (1997)), splines were not used to interpolate between grid cells so as to not introduce overshoots or undershoots beyond the model resolution's capability. Simple tests comparing splined and non-splined fields showed negligible difference in detected storms and this also greatly sped up the tracker's computational runtime.

Once candidate tropical cyclones are collected using the above criteria, trajectories are computed as follows:

1. Search for storms that occur within 400 km the following 6-hour period (this translates to an average forward velocity of 18.5 m s^{-1} or 41.4 mph).

2. If no storms exist with the above criteria, the trajectory of a detected storm is considered terminated. If only one storm is detected within 400 km, it is considered to be the same storm. If multiple storms occur within the 400 km region, first preference is given to storms in the northwest quadrant (Northern Hemisphere) or southwestern quadrant (Southern Hemisphere) and the closest storm is chosen as belonging to the same trajectory as the initial storm from the previous 6-hour period.

3. To be considered a full trajectory, the storm must persist for at least 2 days. These days do not have to be consecutive. The maximum surface wind velocity within 4° of the storm center must be greater than 17 m s^{-1}.

This setup allows for the candidate cyclone algorithm to be embarrassingly parallel on parallel computing architectures. The model data can be broken up into an arbitrary number of subsets and candidate cyclones are detected in parallel. Following the completion of this process, the list of possible cyclones is sorted and merged before trajectories are determined.

Surface wind is calculated by taking the wind at the center of the model's lowest level (approximately 60 meters) and correcting it to 10 meters using a logarithmic law with an open sea roughness coefficient (Garratt, 1992; Wieringa, 1992). Logarithmic profiles have been shown to approximate below-maximum winds in tropical cyclones (Giammanco et al., 2012). This correction results in approximately a 15% reduction between the lowest model level and 10 meters.

We compare the model results to observational data. For historical tropical cyclone climatology, we use the IBTrACS database (Knapp et al., 2010). All observed wind speeds are corrected to 1-minute averages using the methodology outlined in Harper et al. (2010). This is done to homogenize wind speed observations, although no correction is required for the Atlantic and East Pacific, where the National Hurricane Center is the primary source of cyclone data. The Saffir-Simpson scale (Simpson, 1974) is used to simplify intensity analysis although we note that the model winds are defined as instantaneous as opposed to 1-minute averages. The categories within the Saffir-Simpson scale are outlined in Table 5.2 along with corresponding surface wind speed thresholds. Since our focus is primarily on the North Atlantic basin, we use the term "hurricane" to represent any storm with wind speeds greater than 33 m s^{-1}. The term "major hurricane" signifies a storm that equals or exceeds Category 3 on the Saffir-Simpson scale ($\geq$ 50 m s^{-1}). For all other analysis of the large-scale environment, we use the NCEP/NCAR Reanalysis (Kalnay et al., 1996).

Table 5.2: Saffir-Simpson (S-S) intensity scale.

S-S Category	Wind speed			
	m s^{-1}	knots	mph	km h^{-1}
Tropical Depression	< 17	< 34	< 38	< 62
Tropical Storm	18-32	35-63	39-73	63-118
Category 1	33-42	64-82	74-95	119-153
Category 2	43-49	83-95	96-110	154-177
Category 3	50-58	96-112	111-129	178-208
Category 4	58-70	113-136	130-156	209-251
Category 5	$\geq$70	$\geq$137	$\geq$157	$\geq$252

5.4 Results

5.4.1 Spatial patterns of storm origins and trajectories

Figure 5.2a displays the trajectories of all tropical cyclones in the simulation with the globally-uniform 1° mesh. The climatology of all 23 years is shown. When compared to observations (Fig. 5.2c), the model does an adequate job of producing TCs in climatalogically active locations. However, the low resolution of the model precludes simulation of the correct spatial pattern and density of storms in all ocean basins. In particular, TC development is deficient in the North Atlantic, East Pacific, and West Pacific, with the model simulating only a fraction of observed TCs.

Figure 5.2b plots TC trajectories in the variable-resolution simulation. The high resolution patch lies within the innermost black outline. The transition band (0.5°) lies between the two black grid outlines. The resolution outside the outermost black contour matches the coarse 1° simulation in Fig. 5.2a. In the North Atlantic, TC density increases greatly and becomes much more similar to observations. In addition to the increased number of storms, more intense storms, represented by warmer colors, are better represented. Where the coarse simulation could only support the occasional tropical cyclone which reached Category 1 strength, the variable-resolution run contained multiple storms which would be classified as "major storms" (Category

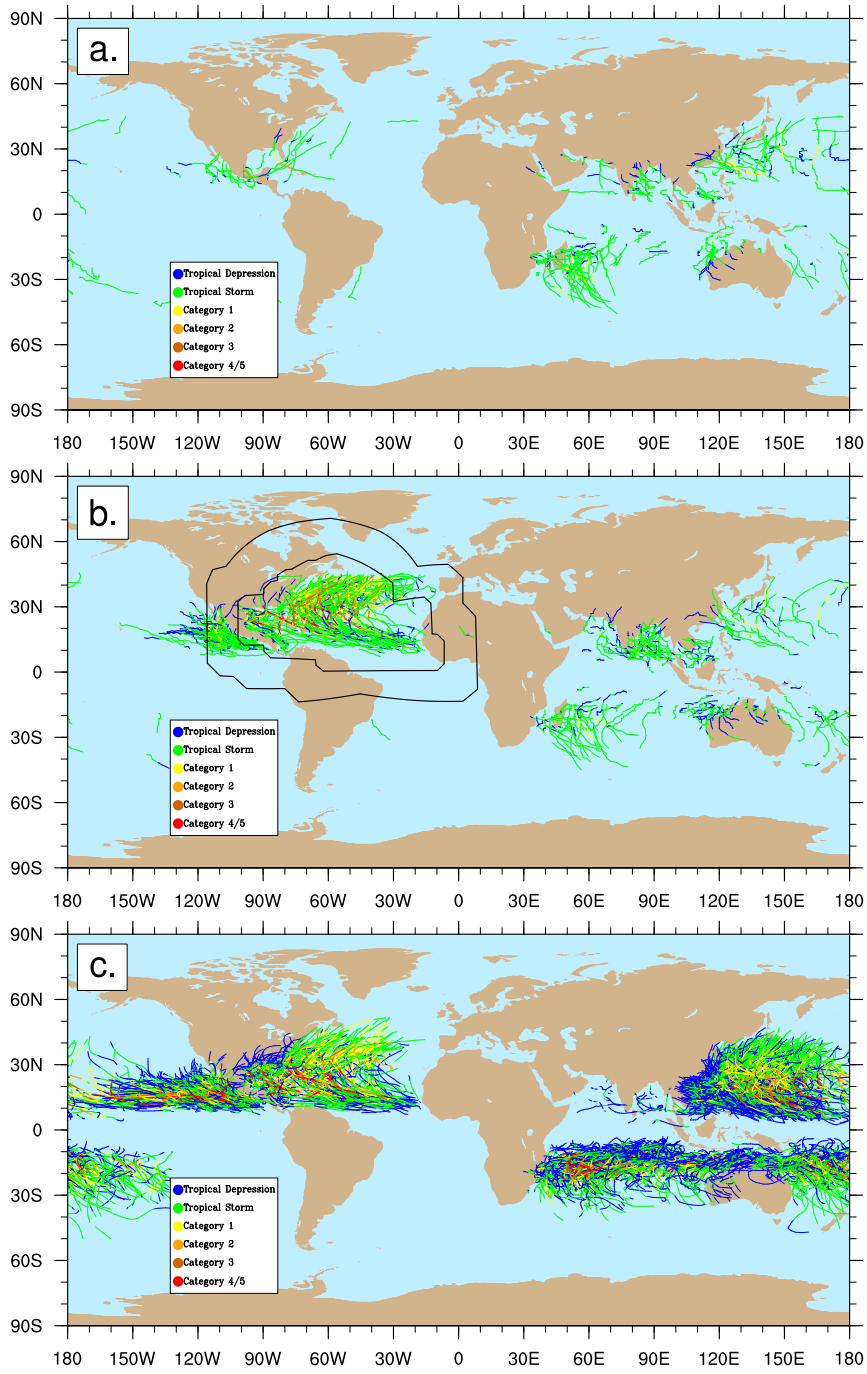

Figure 5.2: Global distribution of storm trajectories from 1980-2002 in the (a.) global 1° simulation, (b.) variable-resolution simulation, and (c.) IBTrACS observational dataset. Storm paths are color-coded by intensity at each location in their trajectory. The outline of the high-resolution nest is shown in black in (b.).

3 and higher) on the Saffir-Simpson scale.

An increase in storm count is seen in the East Pacific within the variable-resolution simulation as well. This is attributable to the 0.5° transition region added between the 0.25° nest over the Atlantic and the remainder of the global domain. It is worth noting that the number of storms increased, but the intensity remained relatively weak, implying that while 0.5° in CAM is more amenable to TC genesis, it remains unsuitable for simulating particularly intense cyclones. The remainder of the global basins, such as the Western Pacific, Southern Pacific, and Indian Oceans appear very similar when Figs. 5.2a and 5.2b are compared. This highlights that the TC deficiency due to the 1° grid spacing exists regardless of which simulation is analyzed.

Storm origin locations in the North Atlantic basin are shown in Fig. 5.3 for both CAM-SE simulations as well as observations. Fig. 5.3a again shows that very few storms are supported by the 1° grid spacing, with the majority forming over the western half of the basin. A much more realistic distribution of genesis locations is seen in the variable-resolution run (Fig. 5.3b) when compared to observations (Fig. 5.3c). In particular, genesis occurs further east, with storms forming just off the African coast and across the Main Development Region (MDR), the area of the Atlantic bounded by 10-20° N and 20-85° W. The var-res simulation is able to adequately capture genesis of Cape Verde storms. Also, the majority of the simulation's intense (Category 3 or greater) storms form in this region, similar to observed data. The model also reproduces the local minimum in TC genesis over the eastern Caribbean Sea as well as the local maximum over the Gulf of Honduras and the southwestern Caribbean. Over the Gulf of Mexico, the model only produces approximately 50% of the observed TC formation rate, and those storms that form are weaker. While the majority of Gulf of Mexico storms in the IBTrACS data also only attain tropical storm status, occasional storms intensify into hurricanes or major hurricanes, a feature not simulated by CAM-SE. Additionally, the model generates too many weak storms north of

35°N. This may be a result of the objective tracking algorithm and is discussed more in-depth in Section 5.4.5.

Figures 5.4a-c shows the Atlantic track densities for all TCs during the 1980-2002 time period for both model simulations (a,b) and observations (c). Each 6-hour latitude-longitude pair for tracked tropical cyclones between 1980 and 2002 is binned into 4°x4° gridboxes. Again, it is evident that the coarse simulation (Fig. 5.4a) is highly deficient in simulating TCs. TCs that do form do not follow a coherent pattern of tracks that mimic observations (Fig. 5.4c). The var-res simulation (Fig. 5.4b), however, exhibits a pattern of cyclone tracks that is much more correlated with observations. Cape Verde trajectories originating in the eastern half of the basin are apparent as well as the general recurvature pattern that occurs with the majority of Atlantic TCs. In addition, the var-res simulation simulates the dual peaks in the center of the ocean basin, with one lying just off the coast of the southeastern United States and the other in the central Atlantic.

Figures 5.4d-f show the same analysis with only storms of hurricane-strength or higher considered. The global 1° simulation (Fig. 5.4d) is nearly devoid of all hurricane formation whereas the var-res simulation (Fig. 5.4e) produces a more robust signature similar to observations (Fig. 5.4f). The var-res simulation continues to show the double peak in the track densities over the central Atlantic, but is biased low over the entire basin. As implied from the cyclone origins, this bias is especially prevalent over the Gulf of Mexico. This underprediction of storms in the Caribbean and Gulf of Mexico has been observed in other high-resolution climate models (Strazzo et al., 2013), and may impact regional analysis of landfalling TCs in the southeastern United States. In addition, the var-res simulation has lower track densities over the eastern Atlantic. When assessed together with Fig. 5.4b, the var-res simulation produces a realistic count of Cape Verde storms, but these storms strengthen to hurricanes more slowly than their observed counterparts, leading to this low bias in hurricane density

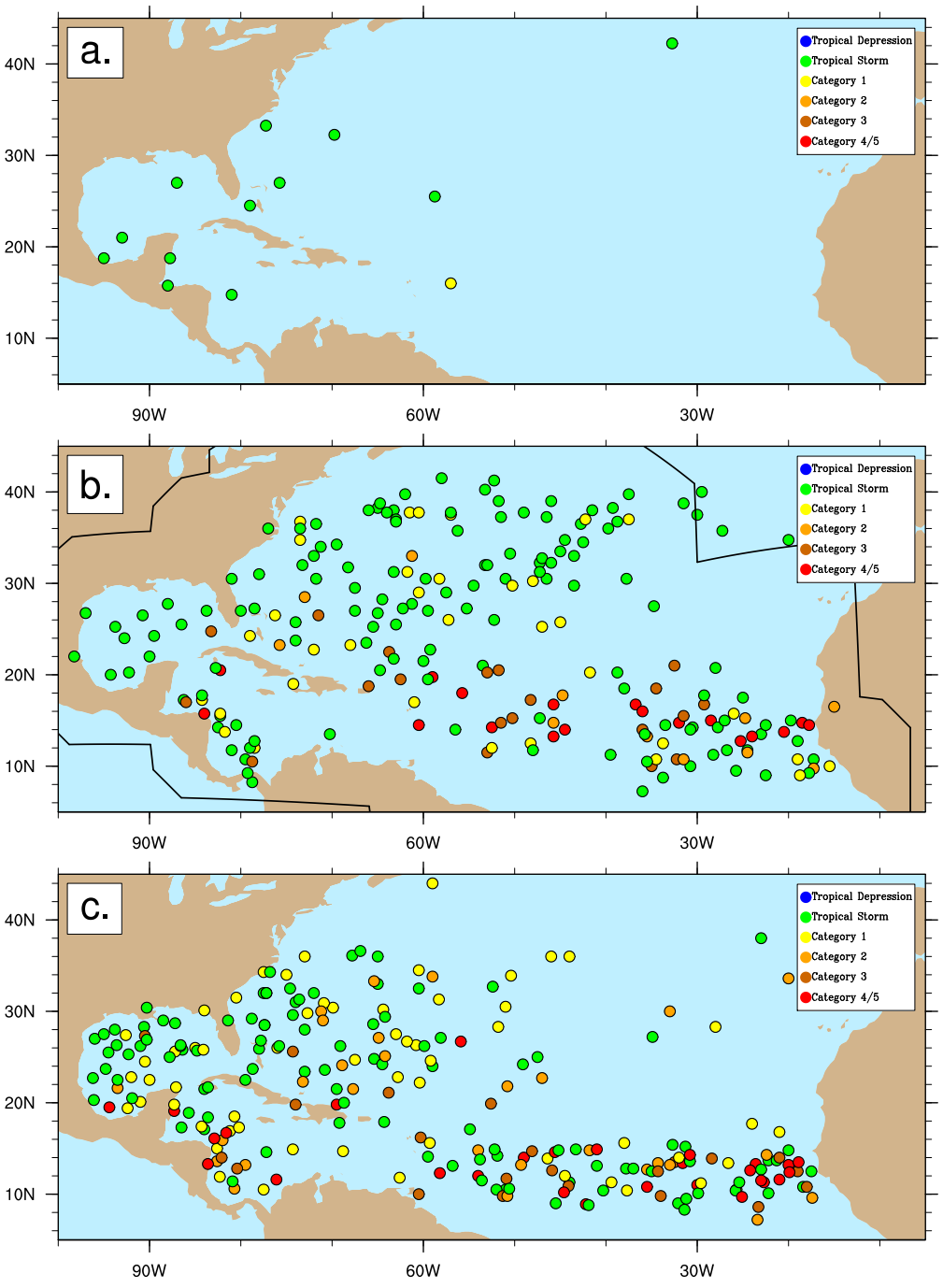

Figure 5.3: TC genesis locations in the (a.) global 1° simulation, (b.) variable-resolution simulation, and (c.) IBTrACS observational dataset. Storms are color-coded by peak intensity during their lifetime. The outline of the high-resolution nest is shown in black in (b.).

stretching over much of the low-latitude Atlantic.

5.4.2 Annual average statistics

Annual cyclone statistics (counts) averaged over the 1980-2002 period are shown in Table 5.3. Results are shown for the 1° coarse run (left), variable-resolution simulation (center), and observations (right). Each model is broken out into three spatial subsets shown in Figure 5.5. These subregions (North Atlantic (NATL), East Pacific (EPAC), "rest of globe" (GLOB)) represent the three different resolutions (0.25°, 0.5°, 1°) in the variable-resolution simulation. We use the standard deviation of the statistical timeseries as a proxy for the measure of interannual variability (in parentheses).

When compared to the coarse grid, the number of TCs generated by the variable-resolution simulation in the North Atlantic (9.7 per year) is very similar to IBTrACS observations (10.7 per year). While the model simulation only simulates 60% of the observed hurricane count, it produces 1.6 major hurricanes per year (Category 3 strength or higher), compared to 2.2 in observations. TC, hurricane, and major hurricane days (cumulative summation of the lifetimes of all storms during a given calendar year) all show similar results when comparing the North Atlantic in the var-res simulation to observations. The fact that storm counts and storm days share the same proportional biases shows that lifetimes of individual storms are well-represented in the model.

Accumulated Cyclone Energy (ACE) is an integrated measure of TC activity which combines intensity and duration (Bell et al., 2000). ACE is defined as:

$$\mathrm{ACE} = 10^{-4} \sum v_{max}^2 \tag{5.1}$$

where v_{max} is the maximum surface wind (in knots) for the TC and the sum is taken in 6-hourly increments. The simulated ACE is ∼79% of the observed annual mean due to the low bias in the number of hurricane-strength TCs. The standard

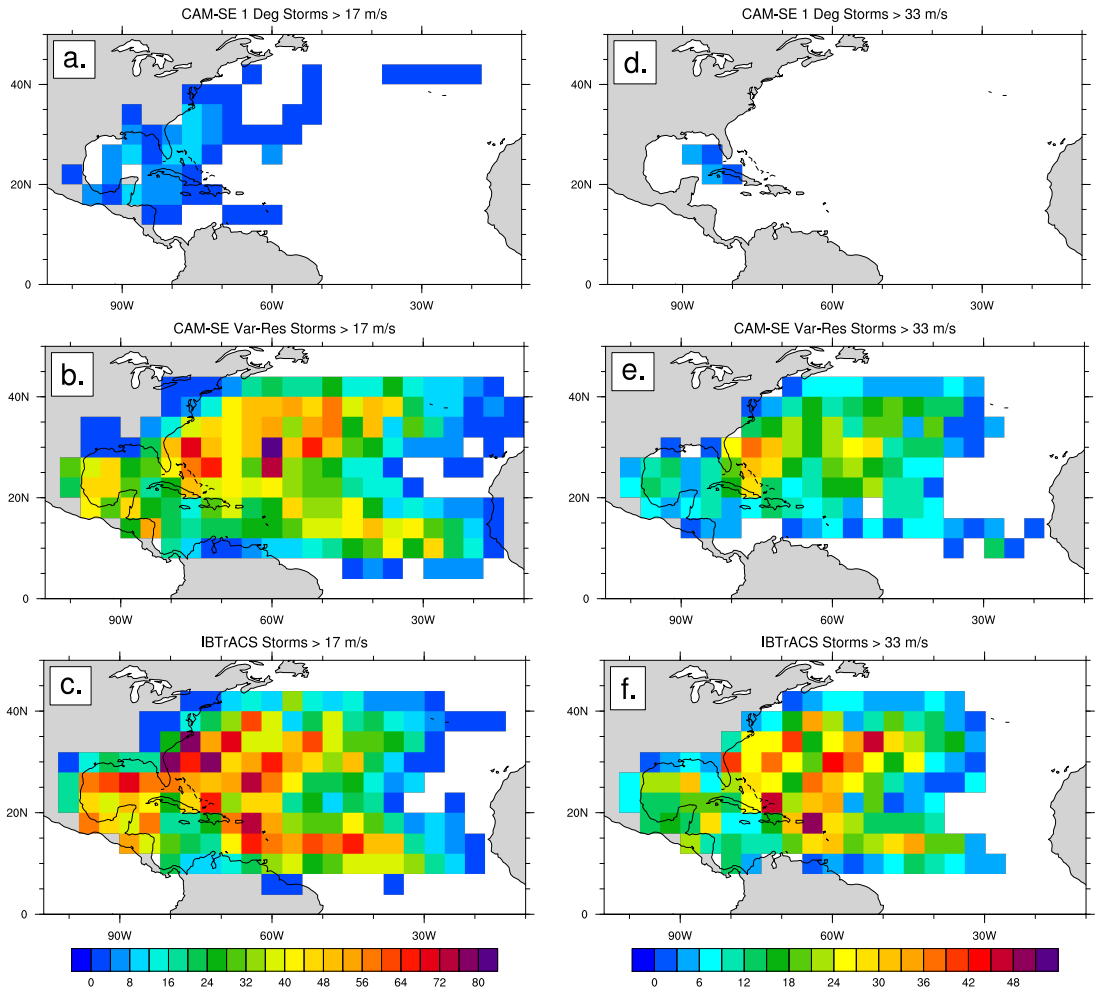

Figure 5.4: Track density plots for North Atlantic (left) all tropical cyclones (>17 m s^{-1}) and (right) hurricanes (>33m s^{-1}) in global coarse (1°) and variable-resolution (0.25°) simulations as well as observations. Units are cumulative six-hourly storm position frequency per 4°x4° gridbox for period 1980-2002.

Table 5.3: TC statistics (counts) for coarse 1° simulation (left), var-res simulation (center), and IBTrACS observations (right). Categories are TCs (all storms tropical storm strength or greater), Hurrs (only hurricanes), MHs (only major hurricanes), and accumulated cyclone energy (ACE). The standard deviation is denoted in parentheses.

	1°			Var-res			Obs		
	NATL	EPAC	GLOB	NATL	EPAC	GLOB	NATL	EPAC	GLOB
Resolution	1°	1°	1°	0.25°	0.5°	1°	-	-	-
TCs	0.6 (0.6)	0.7 (0.8)	7.4 (3.8)	9.7 (3.4)	4.9 (2.0)	8.0 (2.9)	10.7 (3.6)	16.0 (4.1)	77.3 (8.1)
Hurr	0.0 (0.2)	0.0 (0.0)	1.0 (1.0)	3.6 (2.5)	1.1 (0.8)	0.8 (0.8)	6.0 (2.6)	9.2 (2.8)	32.4 (4.9)
MH	0.0 (0.0)	0.0 (0.0)	0.0 (0.0)	1.6 (1.6)	0.1 (0.3)	0.0 (0.0)	2.2 (1.6)	4.6 (2.3)	14.3 (4.1)
TC Days	1.8 (2.3)	1.7 (2.6)	25.1 (12.2)	48.4 (24.2)	18.3 (7.8)	27.3 (11.6)	51.8 (26.0)	75.1 (26.9)	308.2 (56.4)
Hurr Days	0.1 (0.5)	0.0 (0.0)	1.2 (2.2)	13.4 (11.1)	1.8 (2.3)	1.2 (1.4)	22.6 (15.9)	32.2 (13.6)	116.0 (31.7)
MH Days	0.0 (0.0)	0.0 (0.0)	0.0 (0.0)	3.7 (4.0)	0.0 (0.1)	0.0 (0.0)	4.6 (4.5)	9.8 (5.8)	27.8 (11.9)
ACE	1.7 (2.6)	1.3 (2.2)	21.7 (12.1)	72.1 (48.1)	16.5 (9.0)	22.0 (10.6)	91.3 (58.3)	139.3 (59.1)	525.1 (125.8)

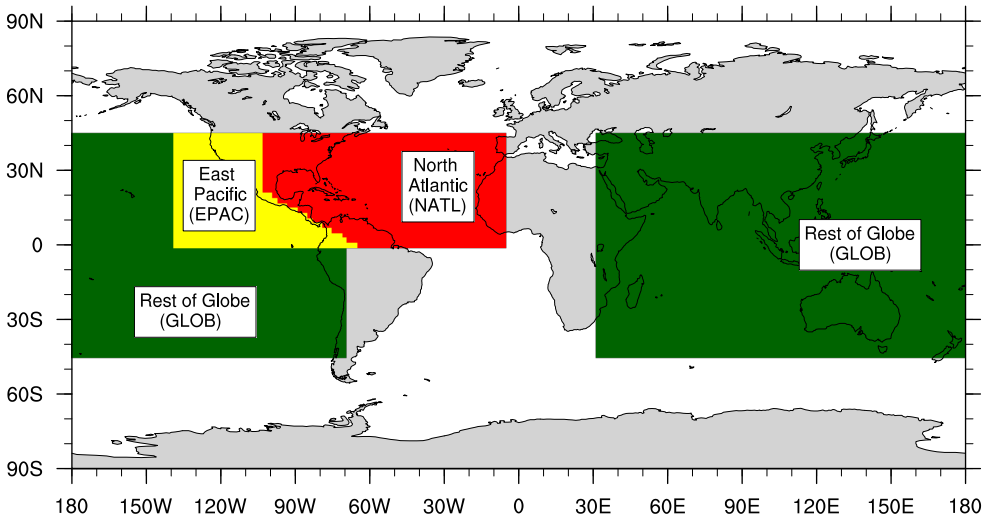

Figure 5.5: Basin mask definitions used for calculating TC statistics.

deviations of all statistics are also in good agreement with observations which shows that year-to-year variability in storm genesis is well-simulated.

Storm counts are biased low in the Eastern Pacific within the variable-resolution simulation. With the basin lying in the transition region between the high-resolution North Atlantic nest and the global 1° base mesh, it produces TC statistics that lie between the coarse, uniform 1 ° simulation and observations. The var-res model produces 4.9 TCs/year, ∼30% of the observed count. It only produces ∼12% of the observed hurricanes, however (1.1 hurricanes/year compared to 2.9), further indication that the 0.5° spacing struggles to sustain more intense cyclones. This is further highlighted by the fact that the simulated ACE in the East Pacific of the var-res simulation is also only ∼12% of the observed average.

In all ocean basins, the coarse simulation produces very few TCs and only approximately one storm of hurricane strength or greater per year at the global scale. No storms with intensity greater than Category 3 develop and simulated ACE is between 1-4% of the observed value. These results emphasize the inadequacy of coarser model grid spacings to generate and sustain realistic tropical cyclones within a long-term climate simulation.

A positive result is that the "rest of globe" statistics are nearly identical between the coarse 1° simulation and the variable-resolution run. These storms are simulated at the same grid resolution, so their similar statistics is a good indication that the model result in the 1° portion of the variable-resolution simulation closely matches the climatology of the globally-uniform 1° simulation without refinement.

5.4.3 Resolution impact on intensity

Figure 5.6 shows the average number of TCs per year which reached each Saffir-Simpson category for the variable-resolution simulation (Figs. 5.6a-c) and in observations (Figs. 5.6d-f) during the 1980-2002 period. Note that the total count is scaled individually for the Figs. 5.6c,f. In the Atlantic basin (Fig. 5.6a), we see that the majority of storms tracked in the simulation are tropical storms. This is similar to the observed distribution (Fig. 5.6d) although the total number of storms only reaching tropical storm strength is higher in the model (6 per year) than observations (4.7 per year). The overall shape of the modeled distribution is similar to observation. The modeled intensities are biased low, with the relative fraction of hurricanes greater than Category 1 intensity being lower than observed. However, the model still generates between 1 and 2 major hurricanes (Category 3 or higher) per year.

In the Eastern Pacific the negative intensity bias in the model (Fig 5.6b) is more apparent, and evidenced by a shift in the distribution towards weaker storms. This is due to the fact that the majority of the Eastern Pacific basin is simulated at 0.5° equivalent grid spacing. When compared to observed intensities (Fig 5.6e), very few cyclones greater that Category 1 intensity occur, although there is one instance of a Category 4 strength cyclone. However, while the intensity is biased low, the absolute count of modeled tropical storms remains on the same order of magnitude as observations. All storms in basins other than the Atlantic and Eastern Pacific ("rest of globe") are shown in Fig 5.6c (var-res model) and 5.6f (observations). At 1° grid

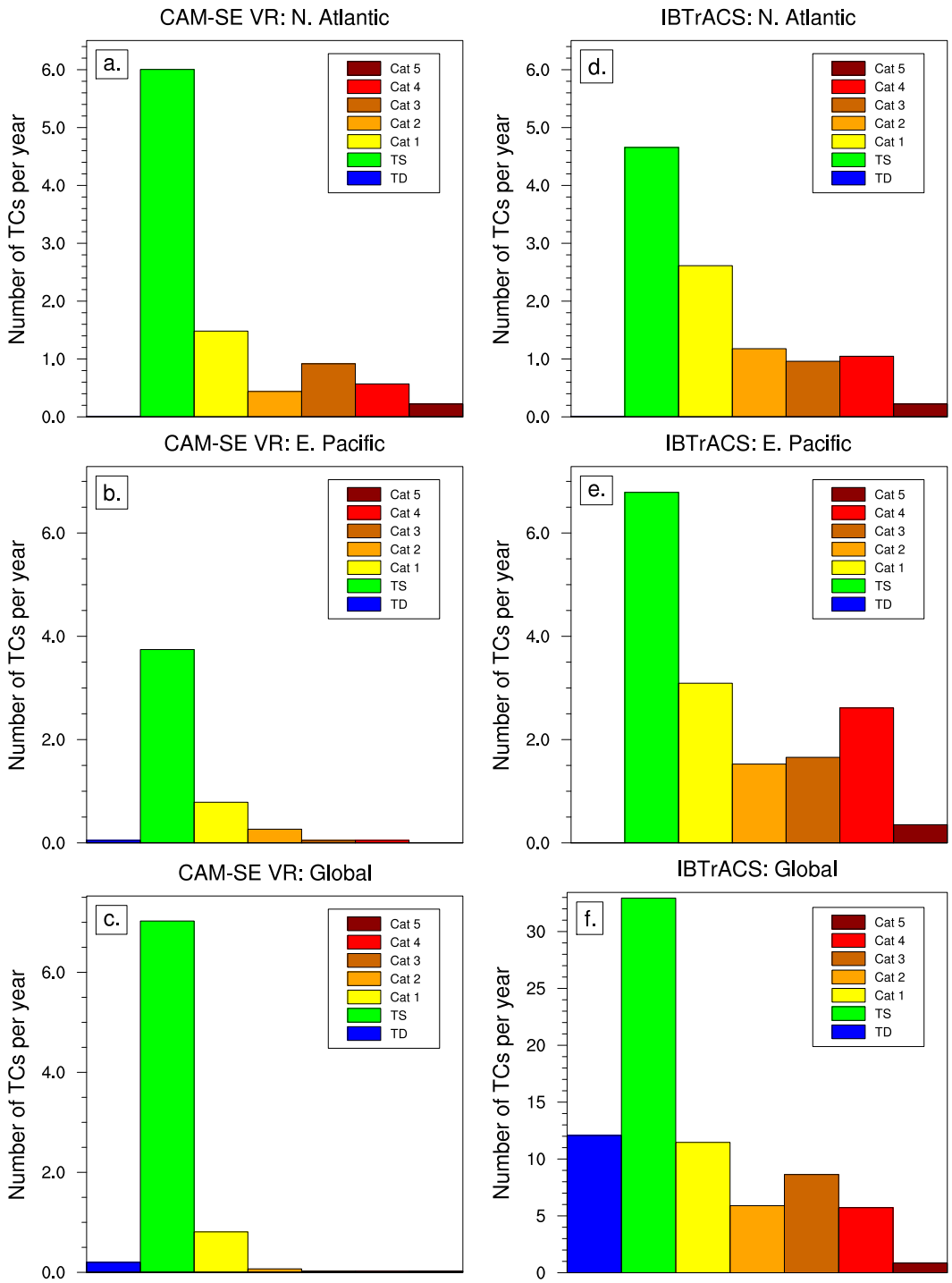

Figure 5.6: Annual storm count (averaged over 23 years) binned by maximum Saffir-Simpson intensity for the variable-resolution simulation (left) and observations (right). The equivalent model resolution for the (top) North Atlantic basin is 0.25°, (middle) East Pacific is 0.5°, and (bottom) rest of the globe 1°). Note the difference in the y-axis in raw storm count between the bottom two panels.

spacing, the model struggles to simulate any storms beyond tropical storm strength. The scale of the y-axis is approximately an order of magnitude less than that used for the observations, underscoring the model's ability to only resolve approximately 10% of the annual number of TCs in the 1° mesh.

The pressure-wind curve for the Atlantic Basin is plotted in Figure 5.7 and follows the analysis of Atkinson and Holliday (1977). Each individual 6-hourly pressure-wind pair is plotted for the variable-resolution simulation (red), the coarse simulation (green), and observations (blue). A quadratic fit is regressed to the data and overlaid as a solid line. The fit for the coarse simulation is truncated at 50 m s^{-1} due to the non-existence of stronger storms in the data. The coarse simulation pressure-wind pairs fall within the envelope of that from the var-res model, implying that the CAM5 physical parameterizations governing the intensity relationships within weaker tropical cyclones behave similarly at both 0.25° and 1°. The 0.25° North Atlantic grid is well-matched to observations in terms of spread and extent of the pressure-wind relationship. The model is able to produce multiple storms with minimum central pressures deeper than 930 hPa and maximum surface winds greater than 60 knots. These results are well matched to a similar analysis of storms in a 0.25° CAM-FV simulation using identical prescribed SST and ice data (Wehner et al., 2014).

There is a downward bias in the best fit curve relative to wind speed. While the model adequately produces the overall spread seen in observations, extreme (low) surface pressures do not produce wind speeds high enough to match observations. This is especially prevalent at surface pressures lower than 960 hPa. This is a similar result to previously published model-derived pressure-wind curves (Oouchi et al., 2006; Knutson et al., 2007; Manganello et al., 2012; Satoh et al., 2012). Manganello et al. (2012) proposes that this deficiency may arise due to the lack of explicitly resolved convection as well as unrealistic surface roughness parameterizations in the most intense storms. It is worth noting that inconsistencies in the historical record

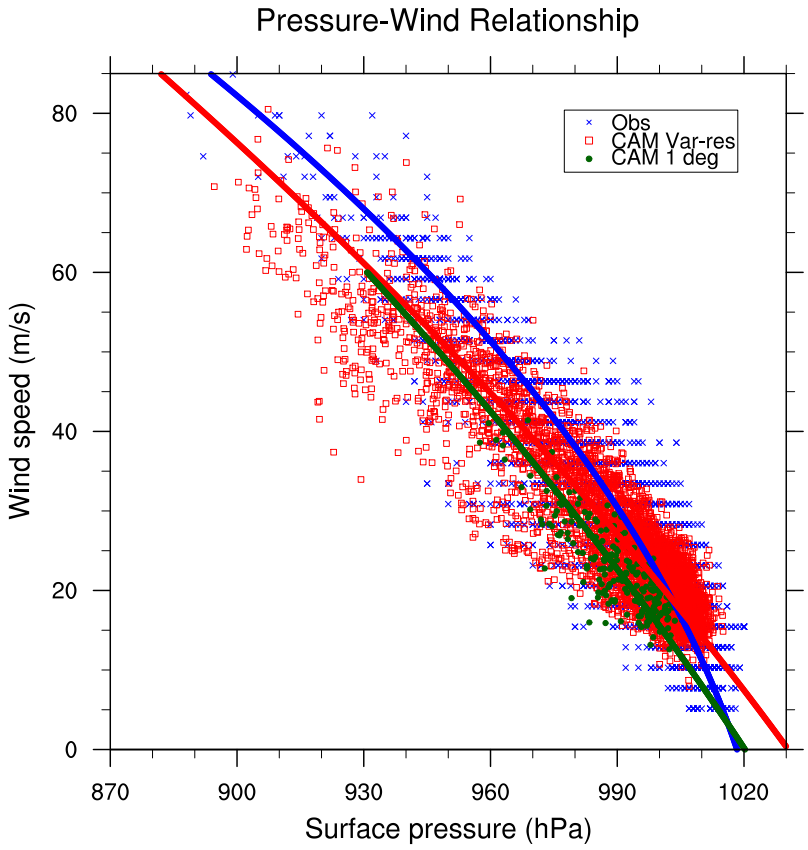

Figure 5.7: Pressure-wind pairs for each 6-hourly TC measurement for (green) global 1° simulation, (red) variable-resolution simulation, and (blue) observations. A quadratic regression is fit to each distribution of pressure-wind pairs.

have been highlighted recently (Knaff and Zehr, 2007). In addition, the pressure-wind relationship is highly sensitive to the manner in which surface winds are derived in model output, so future work standardizing how tropical cyclone intensity is assessed within climate models may be useful in addressing some of these issues.

5.4.4 Resolution impact on storm structure

Figure 5.8 is a four-panel snapshot of the most intense storm generated in the var-res simulation. The storm formed in the high resolution nest over the Atlantic Ocean in August 1985. It developed in the MDR before tracking north of the Caribbean and into the Gulf of Mexico. The storm reached a maximum surface wind intensity of 80

m s^{-1} (minimum surface pressure of 895 hPa). Figure 5.8a shows the instantaneous horizontal 850 hPa wind at the storm's peak intensity. The storm exhibits a classical, intense tropical cyclone structure (Frank, 1977). This includes a calm eye, maximum winds located in a tight eyewall, and a local wind maximum in the northeast quadrant due to the storm's northwesterly motion. Figure 5.8b plots the simulated radar reflectivity at the same instant. Spiral rainbands are evident, as well as an intense area of precipitation under the central dense overcast (CDO). A minimum in precipitation in the area of the storm's eye is also apparent. Figures 5.8c-d show the longitude-height cross sections of the wind speed and temperature anomaly, respectively. The temperature anomaly is calculated by subtracting an environmental reference temperature profile taken from approximately 350 km from the cyclone center along the same latitude. The cyclone exhibits a calm eye at all levels and a low-level wind maximum. An outward slope in the wind contours with height matches observations of intense TCs (Hazelton and Hart, 2012). In addition, a strong warm core associated with diabatic heat release is located between 9 and 12 kilometers above the cyclone center.

Figure 5.9 is the same as Figure 5.8 except for one of the most intense storms that developed in the North Atlantic in the coarse simulation (1°). The storm also formed in the MDR in August 1989. It reached a maximum wind speed of 31 m s^{-1} and a minimum pressure of 973 hPa. When compared to the Atlantic storm depicted in Fig. 5.8, the coarse grid storm shows a much broader and weaker wind field (Fig. 5.9a). There are no inflow bands in Fig. 5.9b. In addition, while the CDO is evident, it is weaker and does not have a readily apparent eye, even though a local wind maximum is discernible at the center of the cyclone. Figures 5.9c and 5.9d show that the coarse grid storm is much weaker and less similar to intense tropical cyclones seen in observations. The storm exhibits a broader, shallower wind field as well as a lower, much more diffuse warm core. While only snapshots of individual storms within the

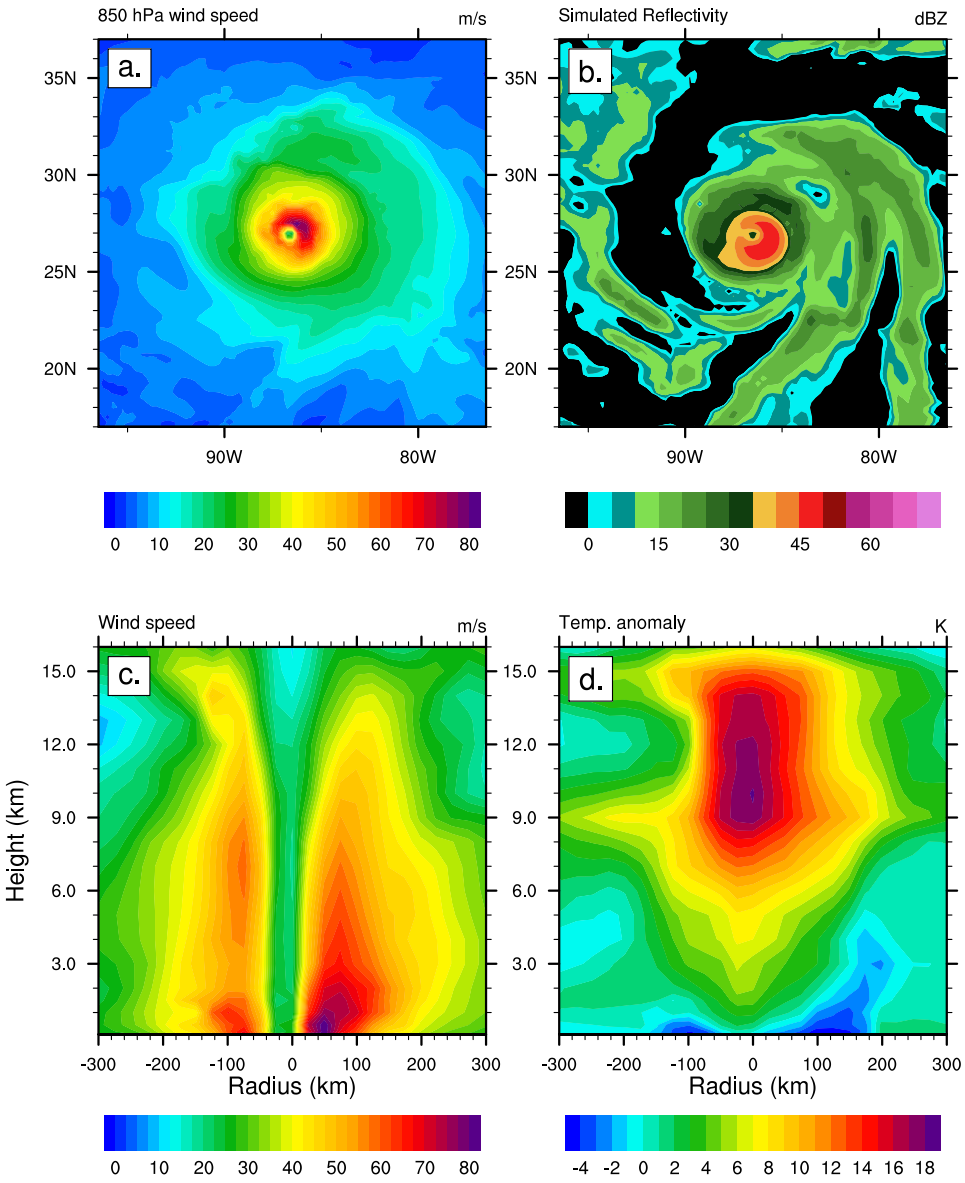

Figure 5.8: (a.) 850 hPa horizontal wind, (b.) simulated radar reflectivity, (c.) and longitude-height cross sections of the horizontal wind speed and (d.) temperature anomaly for the most intense storm generated in 0.25° (North Atlantic) mesh. The radius measures distance to the center of the storm as defined by the surface pressure minimum.

model simulation, these results highlight the differences in dynamical storm structure between the two grid spacings.

5.4.5 Reproducibility of seasonal cycle

The seasonal cycle of TC genesis in the North Atlantic is plotted in Fig. 5.10. TC count by month is plotted in Figs. 5.10a-c for the var-res simulation and observations. Note that these use different y-axis scales to emphasize the overall shape of the distribution. The model (red) reproduces the correct observed (blue) peak for all TCs (Fig. 5.10a) with September being the most active month, followed by August, and then October. When only storms of hurricane strength or stronger are considered (Fig. 5.10b), the model's peak is shifted one month early relative to observations. The same trend holds true for major TCs (Fig. 5.10c). Figures 5.10d-f display the counts for all TCs, hurricanes, and major hurricanes in the Atlantic on the same scale. The 1° simulation is shown in green. We see that the var-res model slightly underpredicts the peak number of storms at all intensity scales, in agreement with the results from Section 5.4.2. The 1° simulation shows approximately the correct peak in activity from a temporal standpoint, but produces fewer than one TC per year.

We note that the tracker detects a handful of weaker storms during months outside of the Atlantic hurricane season (January-May) (Figs. 5.10a,d). Subtropical storms (cyclones with hybrid tropical and extratropical characteristics) remain a gray area between purely warm or purely cold-core systems, with questions as to how well they are demarcated from tropical cyclones in models, the historical record, or even current observations (Guishard et al., 2009). A cursory analysis of some of the detected storms indicate that approximately one or two storms per ocean basin per year may be a subtropical or warm-seclusion extratropical cyclone. These storms generally occur off-season and occur at higher latitude. Knutson et al. (2007) found likewise biased

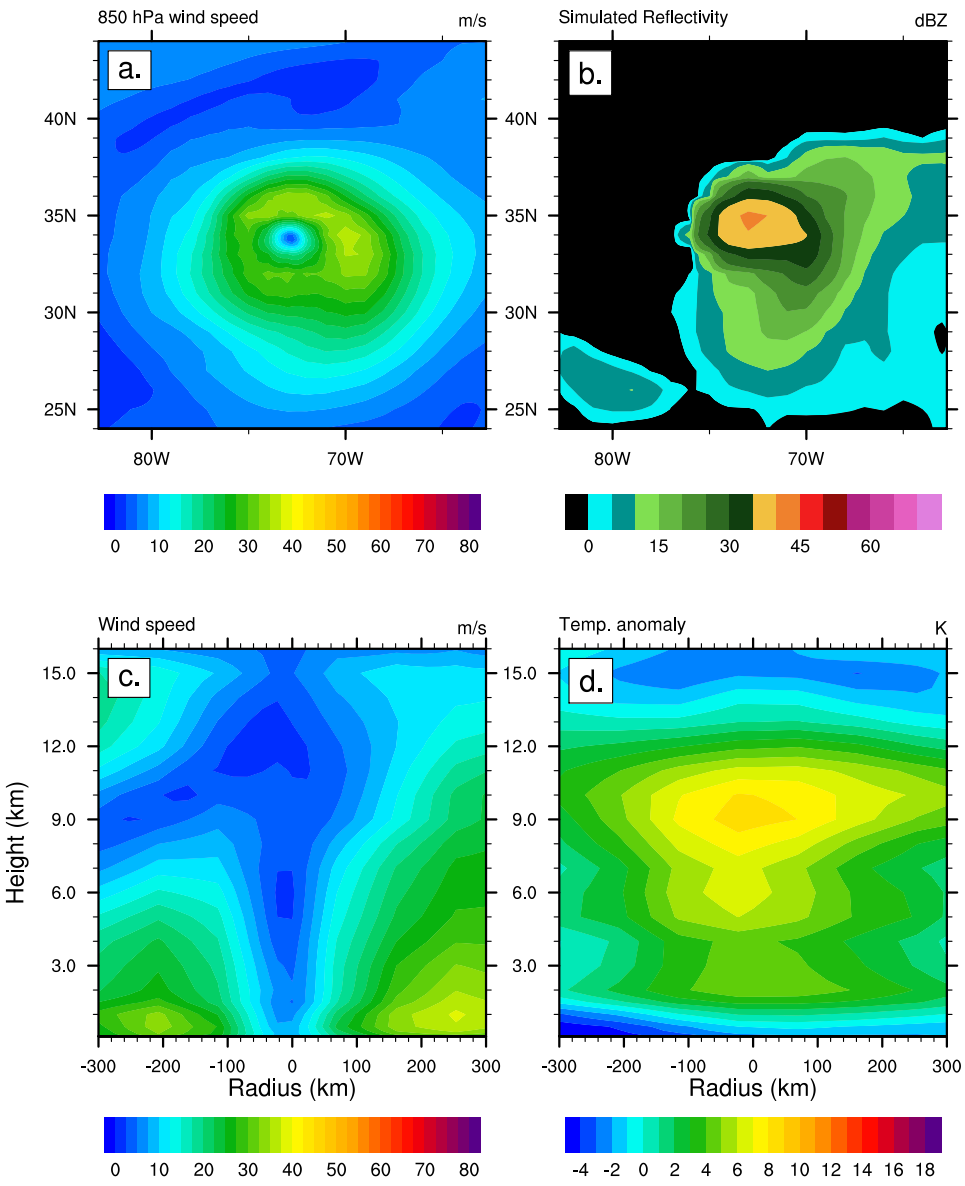

Figure 5.9: Same as Fig. 5.8 but for a North Atlantic storm generated in 1° simulation.

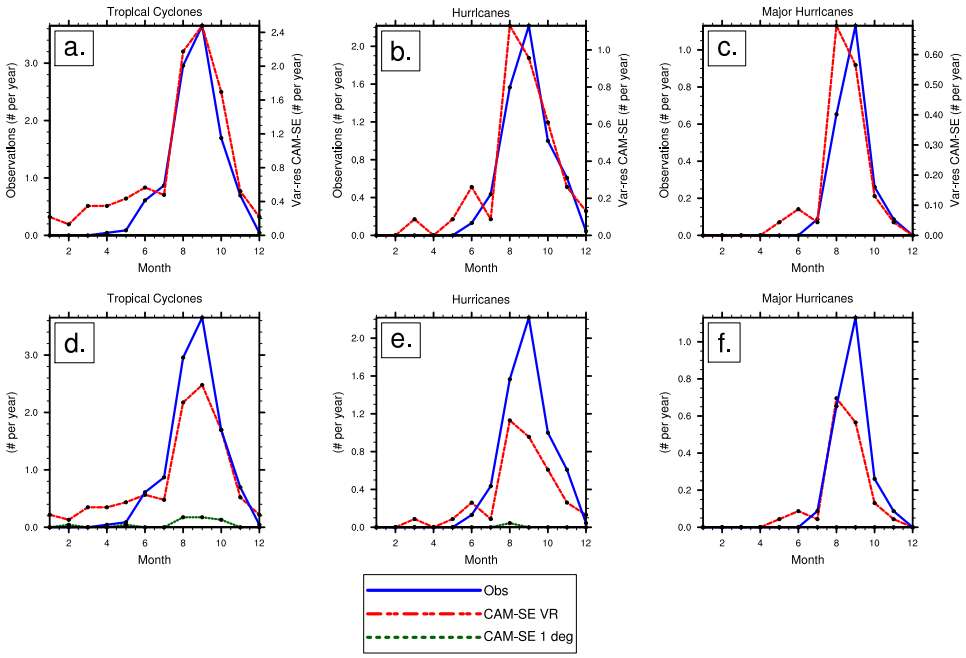

Figure 5.10: Average annual cycle of (left) TC, (center) hurricane, and (right) major hurricane formation rates. (a-c) show comparison between the var-res model (red, right y-axis) and observations (blue, left y-axis) and are normalized using separate y-axis labels. (d-f) show storm formation rates on the same scale and also include the 1° coarse simulation (dark green).

storm counts in the northern North Atlantic using a very similar tracking method. However, these biases are relatively low compared to overall TC count. A manual classification of all tracked storms is beyond the scope of this chapter.

5.4.6 Interannual variability

5.4.6.1 Interannual storm activity

Simulated TCs as a function of calendar year are plotted in Fig. 5.11. Figure 5.11a shows all storms tracked throughout the model integration for both the variable-resolution simulation (red) and the global coarse simulation (green). Observations are shown in blue. The model does not reproduce the slight increase in cyclone counts over the 1980-2002 time period, and, in fact, exhibits a slight decrease. Certain features, such as the local maximum in TC activity in 1984-1985 as well as the decline in storm counts from 1990-1994 are well matched between var-res simulation and observations. However, other aspects, like the 1983 minimum in activity and spike in 1995 are not captured. The 1° simulation appears to approximate "active" or "not active" seasons, but fails to generate more than 2 storms in any given season. The number of storms which reach hurricane strength is plotted in Fig. 5.11b, with similar results to those seen in Fig. 5.11a.

To quantify the ability of CAM-SE to reproduce to proper change in sign in overall cyclone activity between seasons, both the historical and CAM timeseries are first detrended. There remains question as to whether the upward trend in cyclone count between the 1980's and the mid-2000's was, in part, due to advent of new observing techniques such as wind scatterometers and better satellite measurements (Landsea et al., 2009). The correlation between model and observations for the detrended yearly TC counts in the N. Atlantic is 0.25 and 0.23 for ACE. The correlation for TCs is similar to that found in single-simulation studies such as Bengtsson et al. (2007a), Murakami et al. (2012) and Wehner et al. (2014) but lower than the ensemble

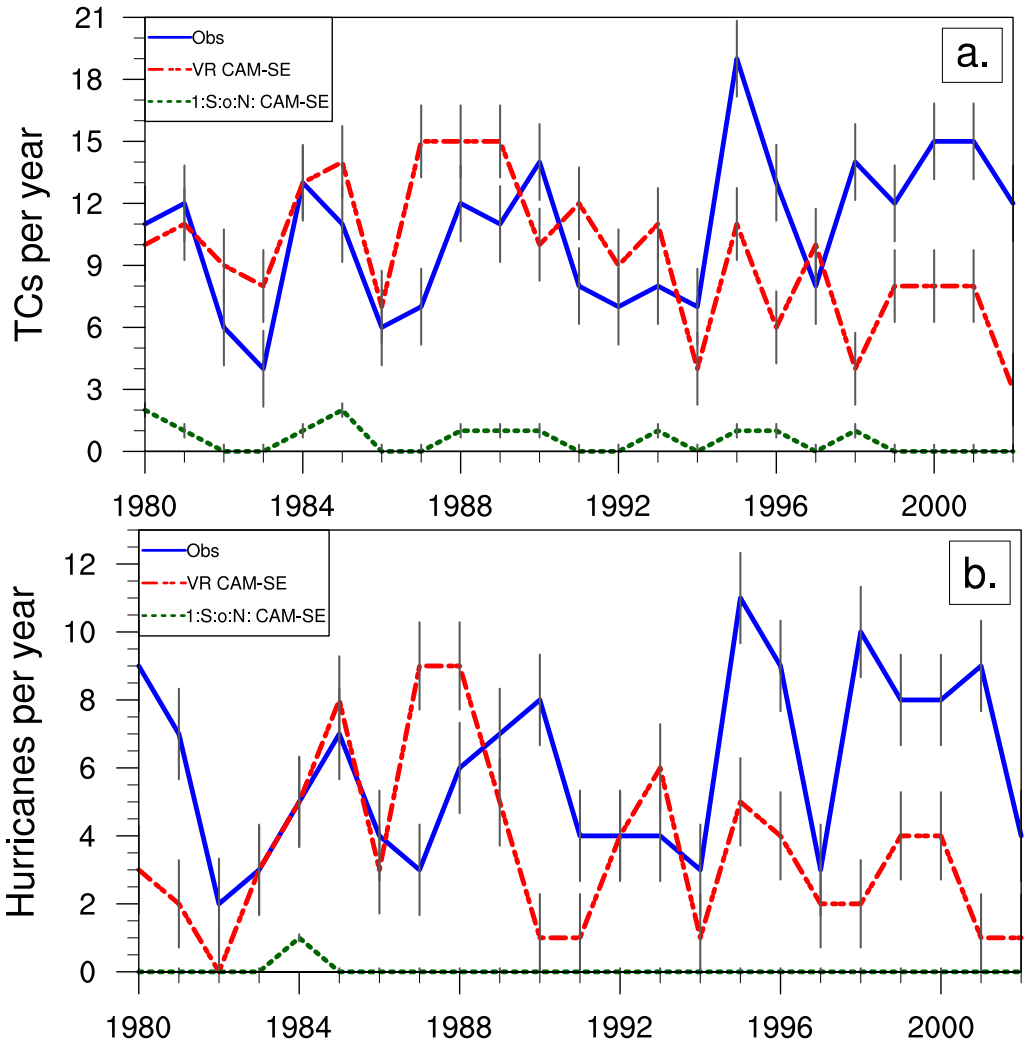

Figure 5.11: Number of (a) tropical cyclones and (b) storms which reach hurricane strength as a function of calendar year for the var-res (red) and global 1° models (green) as well as observations (blue). Grey, vertical lines show standard deviations of interannual storm counts.

simulations of LaRow et al. (2008), Zhao et al. (2009), and Strachan et al. (2013). This result may highlight the need for ensemble simulations to increase confidence in modeled TC statistics, especially given the relatively low frequency and chaotic nature of TC genesis over short time periods.

Correlation coefficients for hurricanes, tropical cyclone days, and hurricane days are also all positive (between 0.10 and 0.25), indicating some potential skill, but the correlation fails to achieve statistical significance. Interestingly, the statistic with the highest correlation is annual major hurricane days (0.36, significant at 90%). Along with further confirmation of CAM-SE's ability to generate intense TCs at 0.25° resolution, it may also imply that strong storms have a stronger interannual signal in climate models at these grid spacings. This may be a future research question of interest as high-resolution global simulations become more prevalent in the climate community over the coming decade.

5.4.6.2 ENSO

It is well-known that Atlantic tropical cyclone storm counts are intrinsically tied to the El Niño-Southern Oscillation (ENSO) (Gray, 1984). In particular, El Niño (La Niña) events lead to strong (weaker) westerly winds and therefore stronger (weaker) vertical wind shear over much of the Atlantic basin, leading to suppressed (increased) TC activity.

Figure 5.12 shows the average number of Atlantic TCs (top) and hurricanes (bottom) that form in the warm (El Niño), neutral, and cold (La Niña) phases of ENSO for the var-res simulation (left) and observations (right). The observed relationship between ENSO phase and TC activity (Fig. 5.12b) is well-simulated by the var-res model run (Fig. 5.12a), with overall magnitudes as well as bias from neutral years being approximately equal to those seen in observations. When TCs that do not attain hurricane strength are removed (Figs. 5.12c-d), the same trends are apparent,

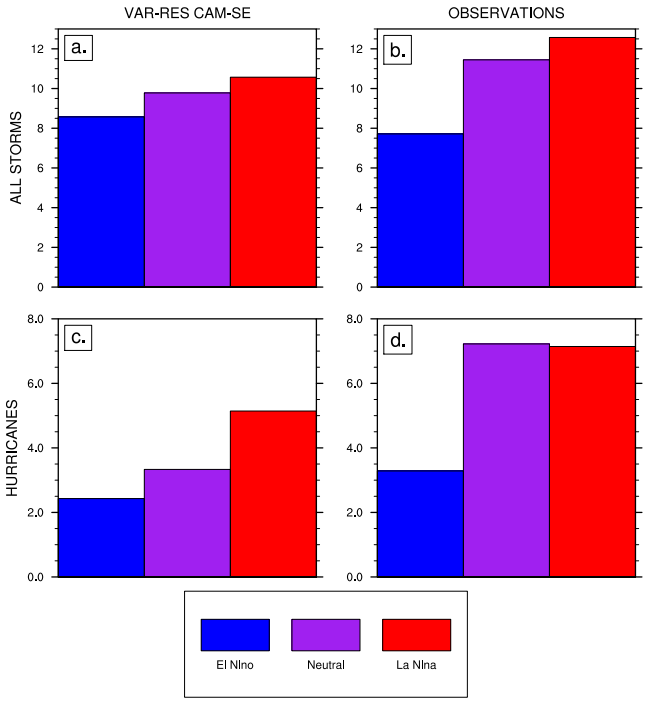

Figure 5.12: Bar chart showing the average number of storms (per year) that form in both El Nino and La Nina ENSO phases, as well as neutral years. Var-res CAM-SE results are on the left (a,c) with observations on the right (b,d). All TCs are shown in top (a,b) with only hurricanes on the bottom (c,d).

although the model shows a stronger signal between neutral and La Niña years than observed. The low bias in Atlantic hurricane activity is also evident, with the raw average totals in each ENSO phase from the model simulation being lower than the corresponding phase in the observational dataset.

5.4.6.3 Synoptic scale variability

To assess the synoptical scale setup in the models we utilize the Genesis Potential Index (GPI). The version of GPI used is described in Emanuel and Nolan (2004). GPI has shown to be a good predictor of the seasonal cyclone of tropical cyclone activity in individual ocean basins (Camargo et al., 2007). It includes four criteria which are determined to be important to cyclogenesis and is calculated as follows:

Table 5.4: Correlation between GPI calculated from NCEP Reanalysis and var-res simulation for both the North Atlantic (NATL) and East Pacific (EPAC) basins. Correlations statistically significant at the 99% level (**) and 95% (*) using one-sided Student's t-test are marked.

Basin	**Monthly**	**Ann. Avg.**	**TC Season**
NATL	0.85**	0.41*	0.57**
EPAC	0.82**	0.50*	0.42*

$$GPI = |10^5\eta|^{\frac{3}{2}} \left(\frac{RH_{600}}{50}\right)^3 \left(\frac{V_{pot}}{70}\right)^3 (1 + 0.1|V_{shear}|)^{-2} \tag{5.2}$$

Here, η is the 850 hPa vorticity, RH_{600} is the 600 hPa relative humidity in percent, V_{pot} is the potential intensity, and $|V_{shear}|$ is the magnitude of the deep-layer vertical wind shear between 850 to 200 hPa in m s^{-1}. V_{pot} is defined using the formulation from DeMaria and Kaplan (1994).

GPI is calculated over the entirety of each individual ocean basin. Bruyère et al. (2012) showed that the GPI over more localized regions (such as the Atlantic MDR) is more closely correlated with TC activity, but we only seek to quantify the broad synoptic patterns over the whole basin. Table 5.4 shows time-series correlation coefficients between the var-res simulation and NCEP Reanalysis I for both the North Atlantic and East Pacific (basins affected by refinement). Each basin has three correlation coefficients. The first is the full monthly time series (276 data points). The second and third are the annual calendar average and tropical cyclone season average, respectively (23 points). The tropical cyclone season statistic only averages over months considered to have potential tropical cyclone activity (June through December in the North Atlantic, etc.).

Both the North Atlantic (NATL) and the East Pacific (EPAC) show high correlation between the var-res simulation and observational data. These areas are climatologically active, but also are likely to be more data-rich, lending to a more accurate reanalysis as well as better SST fields given to CAM. Other ocean basins (not shown)

Table 5.5: Same as Table 5.4 except showing correlation between the var-res simulation and global 1° coarse simulation.

Basin	Monthly	Ann. Avg.	TC Season
NATL	0.97**	0.93**	0.93**
EPAC	0.92**	0.84**	0.72**

showed positive but slightly weaker correlation (in some cases not significant at 95%). This may be due to these basins being more data-sparse.

Table 5.5 shows the same analysis as Table 5.4 except the var-res simulation is correlated to the globally-uniform 1 degree coarse simulation instead of reanalysis data. Since the two AMIP simulations are forced with identical SSTs and also vary in atmospheric grid and topography roughness, highly correlated values indicate that the addition of high-resolution in the var-res simulation does not significantly alter the large-scale synoptic environment. Both basins are well-correlated at the 99% confidence level for all three time series. This result shows that the refined nest does not significantly impact the already resolved scales from the coarse model. In addition, the majority of correlations are higher in Table 5.5 than Table 5.4, showing the model is more highly correlated to another version of itself rather than reanalysis data.

5.4.7 Extratropical transition and upscale effects

Better resolution of tropical cyclones in VRGCMs may also allow for these TCs to impact the global circulation through the meridional transport of momentum, heat, and moisture. Coarse global models which do not resolve high-intensity TCs and one-way nested LAMs are unable to allow for this feedback. Hart (2006) found that seasons with low numbers of Atlantic TCs which recurve to the east in mid-latitudes have anomalously high values of meridional heat flux in mid-latitudes during the following winter, implying recurving TCs play an important role in the poleward

redistribution of energy. Recent work has also implied recurving TCs have significant downstream impacts which may span multiple ocean basins (Harr, 2010, and references therein).

It is clear from Figs. 5.2a-b that there are essentially no recurving TCs of significant intensity in the uniform 1° simulation whereas there are numerous intense recurvatures in the variable-resolution simulation. Additionally, the magnitudes of meridional transient eddy transport of both zonal and meridional momentum are smallest during boreal summer due to the reduced temperature gradient between the tropics and polar region (Holopainen, 1967). Therefore, it is plausible that the signature of recurving TCs may be significant enough to appear when comparing simulated northward transport between the two model simulations during the Atlantic hurricane season (August-September-October, ASO).

Table 5.6 summarizes the spatially-averaged ASO meridional fluxes for momentum, heat, and moisture at 500 hPa due to transient eddies. Values are calculated using the method outlined in Peixoto and Oort (1992). Averages are taken over the region spanning the area from 40°N to 60°N and 70°W to 10°W. The area was selected because it is at the boundary of the high-resolution nest and spans an area where extratropical transition of TCs occurs. All transient fluxes show higher values in the variable-resolution simulation. Cursory tests of the same analysis over the Western North Pacific (where the model is at the same resolution in both cases) shows much smaller differences which do not share a consistent sign (not shown), lending credence to the notion that the increased transport of these quantities is due to the presence of the high-resolution nest.

Figure 5.13 shows the spatial pattern of the difference (variable-resolution minus uniform 1°) of the ASO meridional transient eddy fluxes in Table 5.6. An overlay of the variable-resolution TC tracks are shown in black. Trajectories extend further northward than those in Fig. 5.2b because vorticity maxima are tracked beyond 45°

Table 5.6: Spatially averaged transient meridional eddy fluxes during ASO period. Averages are taken between 40°N to 60°N and 70°W to 10°W. Δ_{VR-Uni} is the difference between the two simulations.

Variable	Units	Var-res	Uniform	Δ_{VR-Uni}
$\overline{V'V'}$	$m^2\ s^{-2}$	102.5	97.2	5.3
$\overline{V'U'}$	$m^2\ s^{-2}$	7.5	4.7	2.8
$\overline{V'T'}$	$K\ m\ s^{-1}$	3.1	2.2	0.9
$\overline{V'Q'}$	$kg\ m\ kg^{-1}\ s^{-1}$	1.92E-3	1.90E-3	2.0E-5

latitude to better capture storms during and just after extratropical transition. Only TCs from the first half of the 23-year simulation period are plotted to make the plot readable.

For the northward flux of both zonal and meridional momentum (Figs. 5.13a-b) the differences over the North Atlantic are positive and are centered in the area where recurving tropical cyclones are prevalent. This indicates that these storms may be playing a key role in depositing momentum and energy northward. The spatial signal is not quite as strong in either transient meridional eddy transport of temperature or moisture during ASO (Figs. 5.13c-d) and negative differences appear on the western side of the basin. However, both show an area-averaged positive anomaly over the center of the basin.

The results here taken in combination with Fig. 5.2 (which shows a high density of strong, recurving TCs into the mid-latitudes and out of the high-resolution nest) would seem to imply that variable-resolution grids may help provide "upscale" effects to the global circulation not achievable through one-way LAM nesting or coarser climate model simulations. This is physically consistent with the idea that extratropical TCs can be significant contributors to the transport of momentum, heat, and moisture from the tropics to mid and high-latitudes. Given the simplicity of this analysis it is unclear as to the exact contribution of TCs to these budgets in these models. While this cursory investigation is interesting, further work is necessary to determine

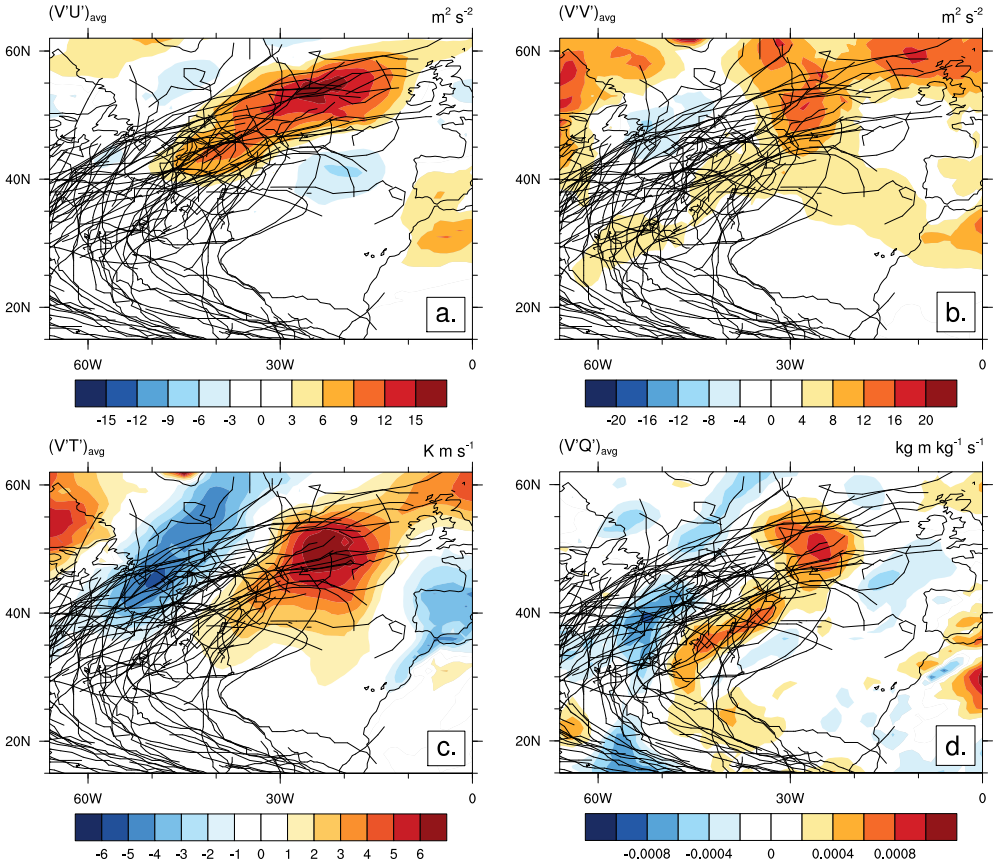

Figure 5.13: Differences in ASO transient meridional (northward) eddy fluxes of (a) zonal momentum, (b) meridional momentum, (c) temperature and (d) moisture between the variable-resolution and uniform 1° solutions. Difference is calculated as variable-resolution minus uniform 1°. Extended TC tracks from the variable-resolution simulation are marked in black to demonstrate recurvature region.

if these effects are significant and if their impact on the global budget of momentum, heat, and moisture is significant.

5.5 Discussion and conclusions

This chapter presents a global climate simulation using the variable-resolution option of the Community Atmosphere Model's Spectral Element dynamical core. The addition of a refined nest over the North Atlantic basin adds increased skill to simulated tropical cyclone climatology at the regional scale. Additionally, the use of variable-resolution significantly decreases the computational cost required to complete a simulation. In the high-resolution nest, average storm climatology is dramatically improved when compared to the use of a global coarse grid. The average TC count closely matches observations while the high-resolution nest allows for the direct simulation of intense cyclones with maximum wind speeds up to approximately 80 m s^{-1}.

While this study was not directly compared to a globally uniform high-resolution run due to the large computational expense that would be required for such a simulation, Chapter III showed that localized refinement patches closely matched the climatology from those regions within a globally-uniform high-resolution run in aqua-planet simulations. Wehner et al. (2014) and Bacmeister et al. (2014) also show similar TC results with globally-uniform 0.25° CAM-FV simulations. These results in aggregate indicate that the high-resolution patch within the variable-resolution simulation outlined in this chapter does a sufficient job reproducing the climatology of a 0.25° globally-uniform grid over the Atlantic basin.

These results also underscore the critical necessity for high resolution (less than 50 kilometer horizontal grid spacing) to properly resolve the dynamical structure of TCs. However, it is interesting that CAM simulates an extremely realistic distribution of TC intensities at 0.25° grid spacing. While this resolution is considered very high

for climate simulations, it remains well above the resolutions required for studying more fine-scale aspects of tropical cyclone dynamics such as eyewall asymmetries (Persing et al., 2013). Cursory simulations using a similar variable-resolution CAM setup with 0.125° grid spacing show that some tropical cyclones in the Atlantic reach minimum surface pressures below 890 hPa. Reed et al. (2012) also found that at higher resolutions, CAM-FV with CAM5 physics produced storms which exceeded their maximum potential intensity. This result may mean further tuning or modification of physical parameterizations is necessary for long-term, high-resolution simulations within CAM. It also emphasizes the critical feedback on TC development between the dynamical core and subgrid parameterizations such as convection and surface fluxes. Future work will continue to investigate the performance of these parameterizations at high resolutions and suggest potential modifications required for further improvement in TC representation as model resolutions push lower.

These intensities may also result from the specification of fixed SSTs. Tropical storms remove heat from the ocean surface through flux extraction and turbulent mixing of the upper ocean which draws cooler water upward (Price, 1981; Emanuel, 2001). This cooling reduces sensible and latent heat available to the TC and thereby provides a negative feedback on its intensity. As this cooling increases with increased surface stress (faster wind speed), this governing mechanism is stronger for higher intensity storms. With climate models now able to produce Category 4 and higher intensities (e.g., this study, Manganello et al. (2012); Satoh et al. (2012); Wehner et al. (2014)) it is likely the practice of using prescribed SSTs needs to be re-evaluated for high-resolution climate simulations.

As shown in Section 5.4.6, while the variable-resolution simulation does an adequate job simulating average TC statistics, it struggles to produce high correlation statistics when individual years within the model are compared to observations. These difficulties are interesting given the fact that past work with global models at lower

resolutions (50–100 km) found very high correlations (>0.7) between modeled TCs and observations in the Atlantic basin without internally nudging synoptic scales (e.g. LaRow et al. (2008); Zhao et al. (2009)). This result is unlikely to indicate a deficiency in the variable-resolution setup. For example, Wehner et al. (2014) and Bacmeister et al. (2014) also found similarly poor correlations between modeled cyclone count and observations when using AMIP protocols and CAM-FV with CAM5 physics. The model is able to reproduce the Atlantic cyclone teleconnection to ENSO events, implying that some component of the prescribed SST signal affects Atlantic TC formation. Therefore it is unknown whether this is an inherent issue with the flow of information from the ocean surface to the atmosphere which is specific to CAM or merely the result of using a single simulation as compared to an ensemble. One advantage to developing a variable-resolution global model is the decrease in computational assets required for a single simulation that focuses on a regional phenomenon. This provides obvious potential for VRGCMs to be used for multi-model ensemble studies instead of single, globally-uniform, high resolution model runs. Therefore, future work will include developing an ensemble of AMIP simulations with variable-resolution meshes to see if skill in reproducing interannual variation in cyclone counts and intensity over the historical time period is improved.

We emphasize that these improvements are due to the increased model throughput when compared to climate simulations on globally-uniform grids which allow for a) finer grid spacing, b) longer integration times, or c) additional ensemble members. As shown in this chapter, VRGCMs such as CAM-SE should approach the same regional climatology as their uniform-resolution counterparts. With models are rapidly approaching resolutions an order of magnitude or more finer than their subgrid parameterizations were designed for, new parameterizations which can improve skill at these grid spacings remain an urgent need in the community. The implementation of VRGCMs as climate tools which span multiple grid spacings within a single

simulation will only serve to push this initiative.

CHAPTER VI

Conclusions

While the horizontal resolution of global general circulation models has improved greatly over the past decade, many atmospheric phenomena remain severely under-resolved at operational grid spacings. These include tropical cyclones, mesoscale convective clusters, and orographically-forced precipitation. The advent of massively parallel computing systems and methods allowing for non-uniform grid spacing on the sphere will provide scientists and policymakers access to data that resolves phenomena which previously required the use of limited area models or heavy subgrid parameterization. Variable-resolution general circulation models (VRGCMs) have the potential to greatly improve regional climate assessments and will serve as vital tools in bridging the gap between weather and climate simulations as the community moves towards systems of seamless prediction.

6.1 Summary

The work contained in this thesis documents validation of variable-resolution in the Community Atmosphere Model (CAM). We demonstrate that VRGCMs have the potential to be useful tools in the assessment of regional climatology within global models. In particular, variable-resolution CAM-SE exhibits positive results when mesh refinement is introduced in conjunction with the CAM5 physics package, pro-

viding improved tropical cyclone representation without deleterious effects on the global climatology. This can be achieved with a fraction of the computational cost of a globally-uniform high-resolution model.

In Chapter II, we outline simplified tests to test the fidelity of mesh refinement in CAM-SE. In particular, we develop a novel dry vortex test case which can be advected through mesh transition regions via a balanced background state in solid body rotation. We show that the behavior of this vortex is predictable and variable-resolution simulations are constrained by their corresponding unrefined grid spacings. We also utilize the idealized vortex described in Reed and Jablonowski (2011) to show that tropical cyclones (TCs) are well-simulated in transition regions without distortion or wave reflection. Deterministic simulations using the idealized vortex also show that a refined nest can reproduce results from a globally-uniform grid at a greatly reduced computational cost. Using a multi-year aquaplanet simulation, horizontal resolution is shown to be crucial to TC genesis. Variable-resolution meshes are shown to have the capability of dramatically improving the count and structural realism of TCs at the regional scale.

Chapter III assesses the performance of running variable-resolution (var-res) simulations on an aquaplanet. Model climatology using a variable-resolution grid with a refined patch centered at the equator is compared to that from globally-uniform runs of corresponding resolution. This work demonstrates a significant resolution dependence exists when using the CAM4 subgrid physical parameterization package across scales. Global cloud fraction decreases and equatorial precipitation increases with finer horizontal resolution, resulting in drastically different climates between the different uniform grid runs and a physics-induced grid imprinting in the var-res simulation. CAM5 physics significantly improves cloud fraction scaling at different grid resolutions. In addition, the equilibrium solution at each grid spacing within the var-res simulations captures the majority of the resolution signal of the corre-

sponding globally-uniform grids. We also demonstrate that wave propagation is not adversely affected by refinement, particularly in equatorial regions where the grid nest is located.

Chapters IV and V present the results of a multi-decadal, coupled climate simulation using a refined nest over the Atlantic Ocean. In Chapter IV, it is concluded that minimal differences in global climatology exist between unrefined (globally uniform 1°) and refined (1° grid with the addition of 0.25° nest) simulations. The frequency of extreme precipitation events is increased within the high-resolution nest. Certain aspects of long-term regional climatology including precipitation, cloud fraction, and precipitable water are improved. This occurs because these quantities are generally significantly influenced by topography and variable-resolution grids allow for a better representation of orography than globally-coarse meshes. They include precipitation statistics in the vicinity of mountain ranges as well as topographically-induced low-level wind features. Chapter V shows that North Atlantic TC representation in CAM-SE is significantly improved with the addition of a refined nest (0.25°, ∼28 km) over the Atlantic basin. Tropical cyclone statistics more closely match observations and demonstrate the critical need for resolution to accurately portray TCs in the climate system. As in Chapter IV, we demonstrate that the "coarse" portion of the variable-resolution mesh matches the globally-uniform 1° run from a TC statistics standpoint. In addition, we postulate that variable-resolution may allow for intense TCs to feed back into the global climate system, a mechanism not allowed by traditional one-way limited area model nesting. We conclude that variable-resolution simulations with CAM5 physics hold strong promise in improving the representation of TCs at the regional level without having a negative impact on the global climate solution.

6.2 Accomplishments

6.2.1 Significance and relevance

This dissertation has demonstrated the fidelity of using highly-scalable VRGCMs, in particular CAM-SE, as future tools for weather and climate research. The idealized tests developed in this dissertation will be used to validate the performance of future VRGCMs. With the implementation of variable-resolution being a key goal for the next major release of the Community Earth System Model (CESM), the simulations presented here will also provide a roadmap for future multi-scale simulations utilizing CAM-SE. These results will also provide a crucial point of comparison for other global modeling centers. It has been demonstrated that VRGCM approaches are suitable for regional tropical cyclone studies, which may aid in pushing localized horizontal resolution in global simulations beyond those currently utilized. These simulations will also serve as an impetus for the development of non-hydrostatic dynamical cores which are required for extending this framework to grid spacings below those acceptable for hydrostatic modeling.

6.2.2 Collaboration

This research has built collaborations between the University of Michigan (UMich) and several other entities, including the Computation, Computers, Information and Mathematics Center at the Department of Energy (DoE), Sandia National Laboratories (SNL), the Institute for Mathematics Applied to Geosciences (IMAGe) and Climate and Global Dynamics Division (CGD) at the National Center for Atmospheric Research (NCAR), Lawrence Berkeley National Laboratory (LBNL) as well as research groups from the University of Colorado and the University of California, Davis (UCDavis). In particular, direct contributors to the research contained in this thesis have included Christiane Jablonowski (UMich), Mark Taylor (SNL), Michael

Levy (NCAR) and Paul Ullrich (UCDavis).

6.3 Future work

Statically-refined dynamical core development. Further efforts are required in implementing, validating, and improving VRGCMs. As discussed in this thesis, model-applied diffusion must be scale-selective such that the model does not over-filter in areas of fine grid spacing (thereby removing resolved phenomena) or under-filter in areas of coarse grid spacing (which may lead to grid-scale noise and instabilities). Exploration of the effects of these filtering strategies on model solutions by using idealized tests such as those outlined in the Dynamical Core Model Intercomparison Project (DCMIP) would be useful.

Additionally, CAM-SE is a hydrostatic dynamical core. This restricts the horizontal grid spacing in CAM-SE to approximately 10 km, below which, the hydrostatic assumption breaks down. For VRGCMs to be a practical tool for simulations on the order of 1 km (or less), development of non-hydrostatic options within the CAM framework is a necessity.

Scale-aware subgrid physics parameterizations for general circulation models. Multi-resolution models will only be as effective as the subgrid physical parameterizations used to simulate phenomena such as turbulence, radiation, clouds, and precipitation. As the horizontal resolution in VRGCM simulations pushes below 10 km, modelers enter a gray area where features such as convection become partially resolved and may not require subgrid parameterization. Implementation of scale-dependent tuning, where each individual atmospheric column has unique parameterization tuning variables determined by cell area may help alleviate some of the issues arising from the use of variable-resolution. Future work may involve general modification of existing schemes or the implementation of innovative scale-aware strategies.

Unstructured grids for non-atmospheric model components. This thesis has utilized a version of the CESM that has simulated the atmosphere with variable-resolution meshes but maintained traditional grids for other model components. This requires the use of a model coupler and leads to decreased throughput because of the frequent, and possibly computationally cumbersome, remapping that is required to pass information between different grids. Further developing the ability to run other models on the same unstructured, variable-resolution grids as CAM-SE would not only lead to a vertically-stacked refinement approach where all corresponding model components have localized high resolution, but would also eliminate the need for computationally-expensive remapping required when information is exchanged between the atmosphere and the surface.

Tropical cyclone climatology simulations. This thesis has demonstrated the capability of variable-resolution CAM-SE to produce realistic tropical cyclone genesis, track, and intensity statistics with a regionally-refined nest. Future work should exploit the massively parallel capability of CAM-SE to use variable-resolution grids to further increase regional resolution beyond current operational grid spacings. Refined grids will also offer the capability for longer integration periods or the use of multi-member ensembles. All of these avenues will help provide more realistic simulations for scientists and policymakers.

APPENDICES

APPENDIX A

Initial conditions for hydrostatically-balanced atmosphere in solid-body rotation

For the dry vortex test in Section 2.3 we have developed an analytical steady-state solution in hydrostatic and gradient wind balance for a sphere in solid-body rotation. The initial conditions are derived in a general framework that includes the Earth's angular velocity Ω. Note that the initial conditions slightly simplify on an irrotational Earth with $\Omega = 0$ s^{-1} as used in Section 2.3 of this thesis.

We have set the equatorial surface pressure p_{eq} to 1015 hPa and equatorial surface temperature T_{eq} to 302.15 K to match the settings of the tropical cyclone test case described in Reed and Jablonowski (2011). We select a zonal background wind amplitude u_0 of -10 m s^{-1} to advect the vortex through the transition region.

The initial zonal, meridional and vertical wind speeds are

$$u(\lambda, \varphi, z) = u_0 \cos(\varphi), \tag{A.1}$$

$$v(\lambda, \varphi, z) = 0, \tag{A.2}$$

$$w(\lambda, \varphi, z) = 0. \tag{A.3}$$

where λ is longitude, φ is latitude, and z is vertical height. The corresponding

pressure velocity is similarly set to zero everywhere, $\omega(\lambda, \varphi, z) = 0$. We assume that no surface topography is present ($z_s = 0$ m), so that the surface geopotential satisfies $\Phi_s = \Phi(z = z_s) = 0$ m^2 s^{-2}.

Since the model is run without subgrid physical parameterizations the specific humidity field q is set to zero. We specify a constant lapse rate ($\Gamma = 7$ K km^{-1}) throughout the whole atmosphere. The surface temperature at $z_s = 0$ m is given by

$$T_s(\lambda, \varphi) = T_{eq} - \frac{(u_0 + 2\Omega a)u_0\Gamma}{2g} \sin^2(\varphi). \tag{A.4}$$

where g is gravity and a is the radius of the Earth. The surface temperature equation is used in the definition of the 3D environmental background temperature

$$T_b(\lambda, \varphi, z) = T_s(\lambda, \varphi) - \Gamma z \tag{A.5}$$

$$T_b(\lambda, \varphi, p) = T_s(\lambda, \varphi) \left(\frac{p}{p_s(\lambda, \varphi)} \right)^{\frac{R_d\Gamma}{g}} \tag{A.6}$$

for both height and pressure coordinates, respectively. R_d is the gas constant for dry air. The surface pressure is given by

$$p_s(\lambda, \varphi) = p_{eq} \left(\frac{T_s(\lambda, \varphi)}{T_{eq}} \right)^{\frac{g}{R_d\Gamma}} \tag{A.7}$$

which follows from the definition of the 3D environmental pressure field

$$p(\lambda, \varphi, z) = p_{eq} \left(\frac{T_s(\lambda, \varphi) - \Gamma z}{T_{eq}} \right)^{\frac{g}{R_d\Gamma}}, \tag{A.8}$$

evaluated at the surface level $z_s = 0$ m. Note that Eq. (A.8) can also be reformulated to yield a pressure-based expression for the height z

$$z(\lambda, \varphi, p) = \frac{T_s(\lambda, \varphi)}{\Gamma} \left[1 - \left(\frac{p}{p_s(\lambda, \varphi)} \right)^{\frac{R_d\Gamma}{g}} \right] \tag{A.9}$$

which was utilized to convert the height-based temperature (Eq. (A.5)) into the pressure-based temperature (Eq. (A.6)).

BIBLIOGRAPHY

BIBLIOGRAPHY

Abdul-Razzak, H. and S. J. Ghan, 2000: A parameterization of aerosol activation: 2. Multiple aerosol types. *Journal of Geophysical Research: Atmospheres*, **105 (D5)**, 6837–6844, doi:10.1029/1999JD901161.

Abiodun, B. J., J. M. Prusa, and W. J. Gutowski, 2008: Implementation of a non-hydrostatic, adaptive-grid dynamics core in CAM3. Part I: comparison of dynamics cores in aqua-planet simulations. *Climate Dynamics*, **31 (7-8)**, 795–810.

Adler, R., et al., 2003: The version-2 global precipitation climatology project (GPCP) monthly precipitation analysis (1979-present). *Journal of Hydrometeorology*, **4 (6)**, 1147–1167, doi:10.1175/1525-7541(2003)004<1147:TVGPCP>2.0.CO;2.

Anderson, B. D., S. E. Benzley, and S. J. Owen, 2009: Automatic all quadrilateral mesh adaption through refinement and coarsening. *Proceedings of the 18th International Meshing Roundtable*, B. W. Clark, Ed., Springer Berlin Heidelberg, 557–574.

Arakawa, A., J.-H. Jung, and C.-M. Wu, 2011: Toward unification of the multiscale modeling of the atmosphere. *Atmospheric Chemistry and Physics*, **11 (8)**, 3731–3742, doi:10.5194/acp-11-3731-2011.

Arya, S., 2001: *Introduction to Micrometeorology*. International Geophysics Series, Academic Press, 420 pp.

Atkinson, G. D. and C. R. Holliday, 1977: Tropical cyclone minimum sea level pressure/maximum sustained wind relationship for the western North Pacific. *Monthly Weather Review*, **105 (4)**, 421–427.

Bacmeister, J. T., M. F. Wehner, R. B. Neale, A. Gettelman, C. Hannay, P. H. Lauritzen, J. M. Caron, and J. E. Truesdale, 2014: Exploratory high-resolution climate simulations using the Community Atmosphere Model (CAM). *Journal of Climate*, **27 (9)**, 3073—3099, doi:10.1175/JCLI-D-13-00387.1.

Baer, F., H. Wang, J. J. Tribbia, and A. Fournier, 2006: Climate modeling with spectral elements. *Monthly Weather Review*, **134 (12)**, 3610–3624, doi:10.1175/MWR3360.1.

Bell, G. D., et al., 2000: Climate assessment for 1999. *Bulletin of the American Meteorological Society*, **81**, 1328–1328, doi:10.1175/1520-0477(2000)081<1328:CAF>2.3.CO;2.

Bender, M. A. and I. Ginis, 2000: Real-case simulations of hurricane–ocean interaction using a high-resolution coupled model: Effects on hurricane intensity. *Monthly Weather Review*, **128 (4)**, 917–946, doi:10.1175/1520-0493(2000)128<0917:RCSOHO>2.0.CO;2.

Bengtsson, L., K. I. Hodges, and M. Esch, 2007a: Tropical cyclones in a T159 resolution global climate model: comparison with observations and re-analyses. *Tellus A*, **59 (4)**, 396–416, doi:10.1111/j.1600-0870.2007.00236.x.

Bengtsson, L., K. I. Hodges, M. Esch, N. Keenlyside, L. Kornblueh, J. J. Luo, and T. Yamagata, 2007b: How may tropical cyclones change in a warmer climate? *Tellus Series A-Dynamic Meteorology and Oceanography*, **59 (4)**, 539–561.

Blackburn, M. and B. J. Hoskins, 2013: Context and aims of the Aqua Planet Experiment. *Journal of the Meteorological Society of Japan*, **91A**, 1–15, doi:10.2151/jmsj.2013-A01.

Blackburn, M., et al., 2013: The Aqua-Planet Experiment (APE): Control SST simulation. *Journal of the Meteorological Society of Japan*, **91A**, 17–56, doi:10.2151/jmsj.2013-A02.

Bosilovich, M. G., F. R. Robertson, and J. Chen, 2011: Global energy and water budgets in MERRA. *Journal of Climate*, **24 (22)**, 5721–5739, doi:10.1175/2011JCLI4175.1.

Boville, B. A., 1991: Sensitivity of simulated climate to model resolution. *Journal of Climate*, **4 (5)**, 469–485.

Boyle, J. and S. A. Klein, 2010: Impact of horizontal resolution on climate model forecasts of tropical precipitation and diabatic heating for the twp-ice period. *Journal of Geophysical Research: Atmospheres*, **115 (D23)**, doi:10.1029/2010JD014262.

Bretherton, C. S. and S. Park, 2009: A new moist turbulence parameterization in the Community Atmosphere Model. *Journal of Climate*, **22 (12)**, 3422–3448, doi:10.1175/2008JCLI2556.1.

Bruyère, C. L., G. J. Holland, and E. Towler, 2012: Investigating the use of a genesis potential index for tropical cyclones in the north atlantic basin. *Journal of Climate*, **25 (24)**, 8611–8626, doi:10.1175/JCLI-D-11-00619.1.

Burpee, R. W., 1972: The origin and structure of easterly waves in the lower troposphere of North Africa. *Journal of the Atmospheric Sciences*, **29 (1)**, 77–90.

Caian, M. and J.-F. Geleyn, 1997: Some limits to the variable-mesh solution and comparison with the nested-LAM solution. *Quarterly Journal of the Royal Meteorological Society*, **123 (539)**, 743–766, doi:10.1002/qj.49712353911.

Camargo, S., A. Sobel, A. Barnston, and K. Emanuel, 2007: Tropical cyclone genesis potential index in climate models. *Tellus A*, **59 (4)**.

Camargo, S. J. and S. E. Zebiak, 2002: Improving the detection and tracking of tropical cyclones in atmospheric general circulation models. *Weather and Forecasting*, **17 (6)**, 1152–1162.

Caron, L.-P., C. G. Jones, and K. Winger, 2011: Impact of resolution and downscaling technique in simulating recent atlantic tropical cylone activity. *Climate Dynamics*, **37 (5-6)**, 869–892, doi:10.1007/s00382-010-0846-7.

Chauvin, F., J.-F. Royer, and M. Déqué, 2006: Response of hurricane-type vortices to global warming as simulated by arpege-climat at high resolution. *Climate Dynamics*, **27 (4)**, 377–399, doi:10.1007/s00382-006-0135-7.

Chelton, D. B., M. H. Freilich, and S. K. Esbensen, 2000: Satellite observations of the wind jets off the pacific coast of central america. part i: Case studies and statistical characteristics. *Monthly Weather Review*, **128 (7)**, 1993–2018, doi:10.1175/1520-0493(2000)128<1993:SOOTWJ>2.0.CO;2.

Chen, C.-T. and T. Knutson, 2008: On the verification and comparison of extreme rainfall indices from climate models. *Journal of Climate*, **21 (7)**, 1605–1621, doi: 10.1175/2007JCLI1494.1.

Chen, J.-H. and S.-J. Lin, 2012: Seasonal predictions of tropical cyclones using a 25-km-resolution general circulation model. *Journal of Climate*, **26 (2)**, 380–398, doi:10.1175/JCLI-D-12-00061.1.

Côté, J., S. Gravel, A. Méthot, A. Patoine, M. Roch, and A. Staniforth, 1998: The operational CMC-MRB Global Environmental Multiscale (GEM) model. Part I: Design considerations and formulation. *Monthly Weather Review*, **126 (6)**, 1373–1395.

Côté, J., M. Roch, A. Staniforth, and L. Fillion, 1993: A variable-resolution semi-Lagrangian finite-element global-model of the shallow-water equations. *Monthly Weather Review*, **121 (1)**, 231–243.

Courtier, P. and J. F. Geleyn, 1988: A global numerical weather prediction model with variable resolution: Application to the shallow water equations. *Quarterly Journal of the Royal Meteorological Society*, **114**, 1321–1346.

Craig, A. P., M. Vertenstein, and R. Jacob, 2012: A new flexible coupler for earth system modeling developed for CCSM4 and CESM1. *International Journal of High Performance Computing Applications*, **26 (1)**, 31–42, doi: 10.1177/1094342011428141.

Cubasch, U., D. Wuebbles, D. Chen, M. Facchini, D. Frame, N. Mahowald, and J.-G. Winther, 2013: Introduction. *Climate Change 2013: The Physical Science Basis. Contribution of Working Group I to the Fifth Assessment Report of the Intergovernmental Panel on Climate Change*, T. Stocker, D. Qin, G.-K. Plattner, M. Tignor, S. Allen, J. Boschung, A. Nauels, Y. Xia, V. Bex, and P. Midgley,

Eds., Cambridge University Press, Cambridge, United Kingdom and New York, NY, USA, 119–158.

DeMaria, M. and J. Kaplan, 1994: Sea surface temperature and the maximum intensity of atlantic tropical cyclones. *Journal of Climate*, **7 (9)**, 1324–1334, doi: 10.1175/1520-0442(1994)007<1324:SSTATM>2.0.CO;2.

Dennis, J. M., et al., 2012: CAM-SE: A scalable spectral element dynamical core for the Community Atmosphere Model. *International Journal of High Performance Computing Applications*, **26 (1)**, 74–89, doi:10.1177/1094342011428142.

Déqué, M. and J. Piedelievre, 1995: High resolution climate simulation over europe. *Climate Dynamics*, **11 (6)**, 321–339, doi:10.1007/BF00215735.

Dirmeyer, P. A., et al., 2012: Simulating the diurnal cycle of rainfall in global climate models: resolution versus parameterization. *Climate Dynamics*, **39 (1-2)**, 399–418, doi:10.1007/s00382-011-1127-9.

Dudhia, J. and J. F. Bresch, 2002: A global version of the PSU–NCAR mesoscale model. *Monthly Weather Review*, **130 (12)**, 2989–3007, doi:10.1175/1520-0493(2002)130<2989:AGVOTP>2.0.CO;2.

Duffy, P., B. Govindasamy, J. Iorio, J. Milovich, K. Sperber, K. Taylor, M. Wehner, and S. Thompson, 2003: High-resolution simulations of global climate, part 1: present climate. *Climate Dynamics*, **21 (5-6)**, 371–390, doi:10.1007/s00382-003-0339-z.

Emanuel, K., 2001: Contribution of tropical cyclones to meridional heat transport by the oceans. *Journal of Geophysical Research: Atmospheres*, **106 (D14)**, 14 771–14 781.

Emanuel, K., 2008: The hurricane—climate connection. *Bulletin of the American Meteorological Society*, **89 (5)**, ES10–ES20.

Emanuel, K. and D. S. Nolan, 2004: Tropical cyclone activity and the global climate system. *Preprints, 26th Conf. on Hurricanes and Tropical Meteorology*, American Meteorological Society, 240–241.

Emanuel, K. A., 1986: An air-sea interaction theory for tropical cyclones. Part I: Steady-state maintenance. *Journal of Atmospheric Sciences*, **43**, 585–605, doi: 10.1175/1520-0469(1986)043<0585:AASITF>2.0.CO;2.

Emanuel, K. A., 2013: Downscaling cmip5 climate models shows increased tropical cyclone activity over the 21st century. *Proceedings of the National Academy of Sciences*, **110 (30)**, 12 219–12 224.

Evans, K. J., P. H. Lauritzen, S. K. Mishra, R. B. Neale, M. A. Taylor, and J. J. Tribbia, 2013: AMIP simulation with the CAM4 spectral element dynamical core. *Journal of Climate*, **26 (3)**, 689–709, doi:10.1175/JCLI-D-11-00448.1.

Flato, G., et al., 2013: Evaluation of climate models. *Climate Change 2013: The Physical Science Basis. Contribution of Working Group I to the Fifth Assessment Report of the Intergovernmental Panel on Climate Change*, T. Stocker, D. Qin, G.-K. Plattner, M. Tignor, S. Allen, J. Boschung, A. Nauels, Y. Xia, V. Bex, and P. Midgley, Eds., Cambridge University Press, Cambridge, United Kingdom and New York, NY, USA, 741–866.

Fournier, A., M. A. Taylor, and J. J. Tribbia, 2004: The spectral element atmospheric model: High-resolution parallel computation and response to regional forcing. *Monthly Weather Review*, **132**, 726–748.

Fox-Rabinovitz, M., J. Cote, B. Dugas, M. Deque, J. L. McGregor, and A. Belochitski, 2008: Stretched-grid Model Intercomparison Project: decadal regional climate simulations with enhanced variable and uniform-resolution GCMs. *Meteorology and Atmospheric Physics*, **100 (1-4)**, 159–178, doi:10.1007/s00703-008-0301-z.

Fox-Rabinovitz, M. S., J. Côté, B. Dugas, M. Déqué, and J. L. McGregor, 2006: Variable-resolution GCMs: stretched-grid model intercomparison project SGMIP. *Journal of Geophysical Research: Atmospheres*, **111**, D16 104.

Fox-Rabinovitz, M. S., G. L. Stenchikov, M. J. Suarez, and L. L. Takacs, 1997: A finite-difference GCM dynamical core with a variable-resolution stretched grid. *Monthly Weather Review*, **125**, 2943–2968.

Frank, N. L., 1970: Atlantic tropical systems of 1969. *Monthly Weather Review*, **98 (4)**, 307–314.

Frank, W. M., 1977: The structure and energetics of the tropical cyclone I. storm structure. *Monthly Weather Review*, **105 (9)**, 1119–1135.

Garratt, J. R., 1992: *The Atmospheric Boundary Layer*. Cambridge University Press, 316 pp.

Gates, W. L., 1992: AMIP: The Atmospheric Model Intercomparison Project. *Bulletin of the American Meteorological Society*, **73**, 1962–1970.

Gent, P. R., S. G. Yeager, R. B. Neale, S. Levis, and D. A. Bailey, 2010: Improvements in a half degree atmosphere/land version of the ccsm. *Climate Dynamics*, **34 (6)**, 819–833, doi:10.1007/s00382-009-0614-8.

Gettelman, A., et al., 2010: Global simulations of ice nucleation and ice supersaturation with an improved cloud scheme in the Community Atmosphere Model. *Journal of Geophysical Research: Atmospheres*, **115 (D18)**, doi:10.1029/2009JD013797.

Giammanco, I. M., J. L. Schroeder, and M. D. Powell, 2012: Observed characteristics of tropical cyclone vertical wind profiles. *Journal of Wind and Structures*, **15**, 1–22.

Gill, A. E., 1980: Some simple solutions for heat-induced tropical circulation. *Quarterly Journal of the Royal Meteorological Society*, **106 (449)**, 447–462, doi: 10.1002/qj.49710644905.

Gray, W. M., 1984: Atlantic seasonal hurricane frequency. Part I: El Niño and 30 mb Quasi-Biennial Oscillation influences. *Monthly Weather Review*, **112 (9)**, 1649–1668, doi:10.1175/1520-0493(1984)112<1649:ASHFPI>2.0.CO;2.

Guba, O., J. R. Overfelt, M. A. Taylor, M. N. Levy, and P. A. Ullrich, 2014: The spectral element method on variable resolution grids: Evaluating grid sensitivity and resolution-aware numerical viscosity. Technical Note 2014-4110J, Sandia National Laboratories.

Guishard, M. P., J. L. Evans, and R. E. Hart, 2009: Atlantic subtropical storms. Part II: Climatology. *Journal of Climate*, **22 (13)**, 3574–3594.

Hack, J. J., 1994: Parameterization of moist convection in the National Center for Atmospheric Research Community Climate Model (CCM2). *Journal of Geophysical Research: Atmospheres*, **99**, 5551–5568, doi:10.1029/93JD03478.

Hagos, S., R. Leung, S. A. Rauscher, and T. Ringler, 2013: Errors characteristics of two grid refinement approaches in aqua-planet simulations: MPAS-A and WRF. *Monthly Weather Review*, **141**, 3022–3036, doi:10.1175/MWR-D-12-00338.1.

Hamilton, K., 2008: Numerical resolution and modeling of the global atmospheric circulation: A review of our current understanding and outstanding issues. *High Resolution Numerical Modelling of the Atmosphere and Ocean*, K. Hamilton and W. Ohfuchi, Eds., Springer New York, 7–27, doi:10.1007/978-0-387-49791-4_1.

Harper, B. A., J. D. Kepert, and J. D. Ginger, 2010: Guidelines for converting between various wind averaging periods in tropical cyclone conditions. Tech. Rep. WMO/TD-1555, World Meteorological Organization, 54 pp.

Harr, P. A., 2010: The extratropical transition of tropical cyclones: Structural characteristics, downstream impacts, and forecast challenges. *Global Perspectives on Tropical Cyclones: From Science to Mitigation*, J. C. L. Chan and J. D. Kepert, Eds., World Scientific, Vol. 4, 436.

Harris, L. M. and S.-J. Lin, 2013: A two-way nested global-regional dynamical core on the cubed-sphere grid. *Monthly Weather Review*, **141 (1)**, 283–306.

Harris, L. M. and S.-J. Lin, 2014: Global-to-regional nested-grid climate simulations in the GFDL high resolution atmosphere model. *Journal of Climate*, doi: 10.1175/JCLI-D-13-00596.1.

Hart, R. E., 2006: Global temperature redistribution by recurving tropical cyclones: A wildcard in midlatitude winter forecasting. *Preprints, 27th Conf. on Hurricanes and Tropical Meteorology, Monterey, CA, Amer. Meteor. Soc. A*, Vol. 3.

Hazelton, A. T. and R. E. Hart, 2012: Hurricane eyewall slope as determined from airborne radar reflectivity data: Composites and case studies. *Weather and Forecasting*, **28 (2)**, 368–386, doi:10.1175/WAF-D-12-00037.1.

Holbach, H. M. and M. A. Bourassa, 2014: The effects of gap-wind-induced vorticity, the monsoon trough, and the ITCZ on East Pacific tropical cyclogenesis. *Monthly Weather Review*, **142 (3)**, 1312–1325, doi:10.1175/MWR-D-13-00218.1.

Holopainen, E. O., 1967: On the mean meridional circulation and the flux of angular momentum over the northern hemisphere. *Tellus*, **19 (1)**, 1–13, doi:10.1111/j.2153-3490.1967.tb01453.x.

Holton, J. R., 2004: *An Introduction to Dynamic Meteorology*. 4th ed., Elsevier Acadamic Press, ISBN 0123540151, 535 pp.

Holtslag, A. A. M. and B. A. Boville, 1993: Local versus nonlocal boundary-layer diffusion in a global climate model. *Journal of Climate*, **6**, 1825–1842.

Hourdin, F., et al., 2006: The LMDZ4 general circulation model: climate performance and sensitivity to parametrized physics with emphasis on tropical convection. *Climate Dynamics*, **27 (7-8)**, 787–813.

Hourdin, F., et al., 2013: LMDZ5B: the atmospheric component of the IPSL climate model with revisited parameterizations for clouds and convection. *Climate Dynamics*, **40 (9-10)**, 2193–2222.

Huffman, G. J., et al., 2007: The TRMM Multisatellite Precipitation Analysis (TMPA): Quasi-global, multiyear, combined-sensor precipitation estimates at fine scales. *Journal of Hydrometeorology*, **8 (1)**.

Hurrell, J. W., J. J. Hack, D. Shea, J. M. Caron, and J. Rosinski, 2008: A New Sea Surface Temperature and Sea Ice Boundary Dataset for the Community Atmosphere Model. *Journal of Climate*, **21 (19)**, 5145–5153, doi: 10.1175/2008JCLI2292.1.

Jablonowski, C., R. C. Oehmke, and Q. F. Stout, 2009: Block-structured adaptive meshes and reduced grids for atmospheric general circulation models. *Philosophical Transactions of the Royal Society A*, **367**, 4497–4522.

Jung, T., et al., 2012: High-resolution global climate simulations with the ECMWF model in Project Athena: Experimental design, model climate, and seasonal forecast skill. *Journal of Climate*, **25 (9)**, 3155–3172, doi:10.1175/JCLI-D-11-00265.1.

Kalnay, E., 2002: *Atmospheric Modeling, Data Assimilation, and Predictability*. Cambridge University Press, 364 pp.

Kalnay, E., et al., 1996: The NCEP/NCAR 40-year reanalysis project. *Bulletin of the American Meteorological Society*, **77 (3)**, 437–471, doi:10.1175/1520-0477(1996)077<0437:TNYRP>2.0.CO;2.

Kiehl, J. T., T. L. Schneider, P. J. Rasch, M. C. Barth, and J. Wong, 2000: Radiative forcing due to sulfate aerosols from simulations with the National Center for Atmospheric Research Community Climate Model, version 3. *Journal of Geophysical Research: Atmospheres*, **105 (D1)**, 1441–1457, doi:10.1029/1999JD900495.

Kinter, J. L., et al., 2013: Revolutionizing climate modeling with Project Athena. *Bulletin of the American Meteorological Society*, **94 (2)**.

Knaff, J. A. and R. M. Zehr, 2007: Reexamination of tropical cyclone wind-pressure relationships. *Weather and Forecasting*, **22 (1)**, 71–88, doi:10.1175/WAF965.1.

Knapp, K. R., M. C. Kruk, D. H. Levinson, H. J. Diamond, and C. J. Neumann, 2010: The international best track archive for climate stewardship (IBTrACS). *Bulletin of the American Meteorological Society*, **91 (3)**, 363–376, doi:10.1175/2009BAMS2755.1.

Knutson, T. R., J. J. Sirutis, S. T. Garner, I. M. Held, and R. E. Tuleya, 2007: Simulation of the recent multidecadal increase of Atlantic hurricane activity using an 18-km-grid regional model. *Bulletin of the American Meteorological Society*, **88**, 1549, doi:10.1175/BAMS-88-10-1549.

Knutson, T. R., et al., 2010: Tropical cyclones and climate change. *Nature Geoscience*, **3 (3)**, 157–163.

Lackmann, G., 2011: *Midlatitude synoptic meteorology: dynamics, analysis, and forecasting*. American Meteorological Society, Boston, Mass., 345 pp.

Landsea, C. W., G. A. Vecchi, L. Bengtsson, and T. R. Knutson, 2009: Impact of duration thresholds on atlantic tropical cyclone counts. *Journal of Climate*, **23 (10)**, 2508–2519, doi:10.1175/2009JCLI3034.1.

Laprise, R., et al., 2008: Challenging some tenets of regional climate modelling. *Meteorology and Atmospheric Physics*, **100 (1-4)**, 3–22, doi:10.1007/s00703-008-0292-9.

LaRow, T. E., Y.-K. Lim, D. W. Shin, E. P. Chassignet, and S. Cocke, 2008: Atlantic basin seasonal hurricane simulations. *Journal of Climate*, **21 (13)**, 3191–3206, doi:10.1175/2007JCLI2036.1.

Lauritzen, P. H., J. Bacmeister, M. A. Taylor, and R. B. Neale, 2012: New CAM (NSF-DOE Community Atmosphere Model) topography generation software: CAM5.2. Abstract A53C-0157 presented at 2012 Fall Meeting, AGU, San Francisco, Calif., 3-7 Dec.

Lauritzen, P. H., J. T. Bacmeister, T. Dubos, S. Lebonnois, and M. A. Taylor, 2014: Held-Suarez simulations with the Community Atmosphere Model Spectral Element (CAM-SE) dynamical core: A global axial angular momentum analysis using Eulerian and floating Lagrangian vertical coordinates. *Journal of Advances in Modeling Earth Systems*, doi:10.1002/2013MS000268.

Lauritzen, P. H., C. Jablonowski, M. A. Taylor, and R. D. Nair, 2011: *Numerical Techniques for Global Atmospheric Models*, Lecture Notes in Computational Science and Engineering, Vol. 80. Springer, 556 pp.

Levy, M., J. Overfelt, and M. A. Taylor, 2013: A variable resolution spectral element dynamical core in the Community Atmosphere Model. Technical Note 2013-0697J, Sandia National Laboratories.

Li, F., W. D. Collins, M. F. Wehner, and L. R. Leung, 2013: Hurricanes in an aquaplanet world: Implications of the impacts of external forcing and model horizontal resolution. *Journal of Advances in Modeling Earth Systems*, **5 (2)**, 134–145, doi: 10.1002/jame.20020.

Li, F., W. D. Collins, M. F. Wehner, D. L. Williamson, J. G. Olson, and C. Algieri, 2011: Impact of horizontal resolution on simulation of precipitation extremes in an aqua-planet version of Community Atmospheric Model (CAM3). *Tellus Series A*, **63**, 884–892, doi:10.1111/j.1600-0870.2011.00544.x.

Liu, X., et al., 2012: Toward a minimal representation of aerosols in climate models: description and evaluation in the Community Atmosphere Model CAM5. *Geoscientific Model Development*, **5 (3)**, 709–739, doi:10.5194/gmd-5-709-2012.

Lorant, V. and J. Royer, 2001: Sensitivity of equatorial convection to horizontal resolution in aquaplanet simulations with a variable-resolution GCM. *Monthly Weather Review*, **129**, 2730–2745, doi:10.1175/1520-0493(2001)129<2730:SOECTH>2.0.CO;2.

Lorenz, P. and D. Jacob, 2005: Influence of regional scale information on the global circulation: A two-way nesting climate simulation. *Geophysical Research Letters*, **32 (18)**, doi:10.1029/2005GL023351.

Lynch, P., 2006: *The emergence of numerical weather prediction: Richardson's dream*. Cambridge University Press, 290 pp.

Manganello, J. V., et al., 2012: Tropical cyclone climatology in a 10-km global atmospheric GCM: Toward weather-resolving climate modeling. *Journal of Climate*, **25 (11)**, 3867–3893, doi:10.1175/JCLI-D-11-00346.1.

McDonald, A., 2003: Transparent boundary conditions for the shallow-water equations: Testing in a nested environment. *Monthly Weather Review*, **131 (4)**, 698–705.

McGregor, J. L., 2013: Recent developments in variable-resolution global climate modelling. *Climatic Change*, 1–12.

McGregor, J. L. and M. R. Dix, 2008: An updated description of the Conformal-Cubic Atmospheric Model. *High resolution numerical modelling of the atmosphere and ocean*, K. Hamilton and W. Ohfuchi, Eds., Springer, 51–75.

Medvigy, D., R. L. Walko, M. J. Otte, and R. Avissar, 2013: Simulated changes in northwest u.s. climate in response to amazon deforestation*. *Journal of Climate*, **26 (22)**, 9115–9136, doi:10.1175/JCLI-D-12-00775.1.

Mendelsohn, R., K. Emanuel, S. Chonabayashi, and L. Bakkensen, 2012: The impact of climate change on global tropical cyclone damage. *Nature Climate Change*, **2 (3)**, 205–209.

Mesinger, F. and K. Veljovic, 2013: Limited area NWP and regional climate modeling: a test of the relaxation vs Eta lateral boundary conditions. *Meteorology and Atmospheric Physics*, **119 (1-2)**, 1–16, doi:10.1007/s00703-012-0217-5.

Mishra, S. K., M. A. Taylor, R. D. Nair, P. H. Lauritzen, H. M. Tufo, and J. J. Tribbia, 2011a: Evaluation of the HOMME dynamical core in the aquaplanet configuration of NCAR CAM4: Rainfall. *Journal of Climate*, **24**, 4037–4055, doi: 10.1175/2011JCLI3860.1.

Mishra, S. K., M. A. Taylor, R. D. Nair, H. M. Tufo, and J. J. Tribbia, 2011b: Performance of the HOMME dynamical core in the aqua-planet configuration of NCAR CAM4: equatorial waves. *Annales Geophysicae*, **29 (2)**, 221–227, doi: 10.5194/angeo-29-221-2011.

Morrison, H. and A. Gettelman, 2008: A new two-moment bulk stratiform cloud microphysics scheme in the Community Atmosphere Model, version 3 (CAM3). Part I: Description and numerical tests. *Journal of Climate*, **21 (15)**, 3642–3659, doi:10.1175/2008JCLI2105.1.

Murakami, H., et al., 2012: Future changes in tropical cyclone activity projected by the new high-resolution MRI-AGCM. *Journal of Climate*, **25 (9)**, 3237–3260, doi:10.1175/JCLI-D-11-00415.1.

Nasuno, T., 2013: Forecast skill of Madden-Julian Oscillation events in a global nonhydrostatic model during the CINDY2011/DYNAMO observation period. *SOLA*, **9 (0)**, 69–73.

Neale, R. B. and B. J. Hoskins, 2000: A standard test for AGCMs including their physical parametrizations: I: The proposal. *Atmospheric Science Letters*, **1 (2)**, 101–107.

Neale, R. B., J. Richter, S. Park, P. H. Lauritzen, S. J. Vavrus, P. J. Rasch, and M. Zhang, 2013: The mean climate of the Community Atmosphere Model (CAM4) in forced SST and fully coupled experiments. *Journal of Climate*, **26 (14)**, 5150–5168, doi:10.1175/JCLI-D-12-00236.1.

Neale, R. B., et al., 2010a: Description of the NCAR Community Atmosphere Model (CAM 4.0). NCAR Technical Note NCAR/TN-485+STR, National Center for Atmospheric Research, 212 pp., Boulder, Colorado.

Neale, R. B., et al., 2010b: Description of the NCAR Community Atmosphere Model (CAM 5.0). NCAR Technical Note NCAR/TN-486+STR, National Center for Atmospheric Research, 268 pp., Boulder, Colorado.

O'Brien, T. A., F. Li, W. D. Collins, S. A. Rauscher, T. D. Ringler, M. A. Taylor, S. M. Hagos, and R. L. Leung, 2013: Observed scaling in clouds and precipitation and scale incognizance in regional to global atmospheric models. *Journal of Climate*, **26**, 9313–9333, doi:10.1175/JCLI-D-13-00005.1.

Ohfuchi, W., et al., 2004: 10-km mesh meso-scale resolving simulations of the global atmosphere on the earth simulator – preliminary outcomes of AFES (AGCM for the Earth Simulator). *Journal of the Earth Simulator*, **1**, 8–34.

Oouchi, K., J. Yoshimura, H. Yoshimura, R. Mizuta, S. Kusunoki, and A. Noda, 2006: Tropical cyclone climatology in a global-warming climate as simulated in a 20 km-mesh global atmospheric model: Frequency and wind intensity analyses. *Journal of the Meteorological Society of Japan*, **84 (2)**, 259–276.

Park, S. and C. S. Bretherton, 2009: The University of Washington shallow convection and moist turbulence schemes and their impact on climate simulations with the Community Atmosphere Model. *Journal of Climate*, **22 (12)**, 3449–3469, doi: 10.1175/2008JCLI2557.1.

Peixoto, J. P. and A. H. Oort, 1992: *Physics of Climate*. American Institute of Physics, New York, 520 pp.

Persing, J., M. T. Montgomery, J. C. McWilliams, and R. K. Smith, 2013: Asymmetric and axisymmetric dynamics of tropical cyclones. *Atmospheric Chemistry and Physics Discussions*, **13 (5)**, 13 323–13 438, doi:10.5194/acpd-13-13323-2013.

Price, J. F., 1981: Upper ocean response to a hurricane. *Journal of Physical Oceanography*, **11 (2)**, 153–175.

Rančić, M., R. J. Purser, and F. Mesinger, 1996: A global shallow-water model using an expanded spherical cube: Gnomonic versus conformal coordinates. *Quarterly Journal of the Royal Meteorological Society*, **122 (532)**, 959–982, doi: 10.1002/qj.49712253209.

Randall, D. A., 2000: *General Circulation Model development: Past, present, and future*. Academic Press, 807 pp.

Randall, D. A., et al., 2007: Climate models and their evaluation. *Climate Change 2007: The Physical Science Basis. Contribution of Working Group I to the Fourth Assessment Report of the Intergovernmental Panel on Climate Change*, S. Solomon, D. Qin, M. Manning, Z. Chen, M. Marquis, K. B. Averyt, M. Tignor, and H. L. Miller, Eds., Cambridge University Press, Cambridge, United Kingdom and New York, NY, USA, 589–662.

Rasch, P. J. and J. E. Kristjánsson, 1998: A comparison of the CCM3 model climate using diagnosed and predicted condensate parameterizations. *Journal of Climate*, **11 (7)**, 1587–1614.

Rauscher, S. A., T. D. Ringler, W. C. Skamarock, and A. A. Mirin, 2013: Exploring a global multiresolution modeling approach using aquaplanet simulations. *Journal of Climate*, **26 (8)**, 2432–2452, doi:10.1175/JCLI-D-12-00154.1.

Reed, K. A. and C. Jablonowski, 2011: An analytic vortex initialization technique for idealized tropical cyclone studies in AGCMs. *Monthly Weather Review*, **139 (2)**, 689–710, doi:10.1175/2010MWR3488.1.

Reed, K. A. and C. Jablonowski, 2012: Idealized tropical cyclone simulations of intermediate complexity: A test case for AGCMs. *Journal of Advances in Modeling Earth Systems*, **4**, M04 001, doi:10.1029/2011MS000099.

Reed, K. A., C. Jablonowski, and M. A. Taylor, 2012: Tropical cyclones in the spectral element configuration of the Community Atmosphere Model. *Atmospheric Science Letters*, **13 (4)**, 303–310.

Reichler, T. and J. Kim, 2008: How well do coupled models simulate today's climate? *Bulletin of the American Meteorological Society*, **89 (3)**, 303–311.

Richter, J. H., F. Sassi, and R. R. Garcia, 2010: Toward a physically based gravity wave source parameterization in a general circulation model. *Journal of the Atmospheric Sciences*, **67 (1)**, 136–156, doi:10.1175/2009JAS3112.1.

Rienecker, M. M., et al., 2011: MERRA: NASA's Modern-Era Retrospective Analysis for Research and applications. *Journal of Climate*, **24 (14)**, 3624–3648, doi:10.1175/JCLI-D-11-00015.1.

Ringler, T., L. Ju, and M. Gunzburger, 2008: A multiresolution method for climate system modeling: Application of spherical centroidal Voronoi tessellations. *Ocean Dynamics*, **58**, 475–498.

Ringler, T. D., D. Jacobsen, M. Gunzburger, L. Ju, M. Duda, and W. Skamarock, 2011: Exploring a multiresolution modeling approach within the shallow-water equations. *Monthly Weather Review*, **139 (11)**, 3348–3368, doi:10.1175/MWR-D-10-05049.1.

Ronchi, C., R. Iacono, and P. Paolucci, 1996: The "cubed sphere": A new method for the solution of partial differential equations in spherical geometry. *Journal of Computational Physics*, **124 (1)**, 93 – 114, doi:10.1006/jcph.1996.0047.

Rossow, W. B. and R. A. Schiffer, 1999: Advances in understanding clouds from ISCCP. *Bulletin of the American Meteorological Society*, **80 (11)**, 2261–2287.

Rougier, J., D. M. H. Sexton, J. M. Murphy, and D. Stainforth, 2009: Analyzing the climate sensitivity of the HadSM3 climate model using ensembles from different but related experiments. *Journal of Climate*, **22 (13)**, 3540–3557, doi: 10.1175/2008JCLI2533.1.

Sabin, T., R. Krishnan, J. Ghattas, S. Denvil, J.-L. Dufresne, F. Hourdin, and T. Pascal, 2013: High resolution simulation of the South Asian monsoon using a variable resolution global climate model. *Climate Dynamics*, **41 (1)**, 173–194.

Sadourny, R., 1972: Conservative finite-difference approximations of the primitive equations on quasi-uniform spherical grids. *Monthly Weather Review*, **100**, 136–144.

Satoh, M., R. Nihonmatsu, and H. Kubokawa, 2013: Environmental conditions for tropical cyclogenesis associated with African easterly waves. *SOLA*, **9 (0)**, 120–124.

Satoh, M., et al., 2012: The intra-seasonal oscillation and its control of tropical cyclones simulated by high-resolution global atmospheric models. *Climate Dynamics*, **39 (9-10)**, 2185–2206, doi:10.1007/s00382-011-1235-6.

Schmidt, F., 1977: Variable fine mesh in a spectral global model. *Beitr. Phys. Atmos.*, **50**, 211–217.

Simpson, R. H., 1974: The hurricane disaster – potential scale. *Weatherwise*, **27 (4)**, 169–186, doi:10.1080/00431672.1974.9931702.

Skamarock, W. C., J. B. Klemp, M. G. Duda, L. D. Fowler, S.-H. Park, and T. D. Ringler, 2012: A multiscale nonhydrostatic atmospheric model using centroidal Voronoi tesselations and C-grid staggering. *Monthly Weather Review*, **140 (9)**, 3090–3105, doi:10.1175/MWR-D-11-00215.1.

Skamarock, W. C., et al., 2008: A description of the Advanced Research WRF Version 3. NCAR Tech. Note NCAR/TN-475+STR, National Center for Atmospheric Research, Boulder, Colorado. 113 pp., available from http://www.ucar.edu/library/collections/technotes/technotes.jsp.

Skinner, C. B. and N. S. Diffenbaugh, 2013: The contribution of African easterly waves to monsoon precipitation in the CMIP3 ensemble. *Journal of Geophysical Research: Atmospheres*.

St-Cyr, A., C. Jablonowski, J. M. Dennis, H. M. Tufo, and S. J. Thomas, 2008: A comparison of two shallow-water models with nonconforming adaptive grids. *Monthly Weather Review*, **136 (6)**, 1898–1922, doi:10.1175/2007MWR2108.1.

Staniforth, A. N. and H. L. Mitchell, 1978: A variable-resolution finite-element technique for regional forecasting with the primitive equations. *Monthly Weather Review*, **106**, 439–447.

Strachan, J., P. L. Vidale, K. Hodges, M. Roberts, and M.-E. Demory, 2013: Investigating global tropical cyclone activity with a hierarchy of AGCMs: The role of model resolution. *Journal of Climate*, **26 (1)**, 133–152, doi:10.1175/JCLI-D-12-00012.1.

Strazzo, S., J. B. Elsner, T. LaRow, D. J. Halperin, and M. Zhao, 2013: Observed versus GCM-generated local tropical cyclone frequency: Comparisons using a spatial lattice. *Journal of Climate*, **26 (21)**, 8257–8268, doi:10.1175/JCLI-D-12-00808.1.

Takahashi, Y. O., K. Hamilton, and W. Ohfuchi, 2006: Explicit global simulation of the mesoscale spectrum of atmospheric motions. *Geophysical Research Letters*, **33**, L12 812, doi:10.1029/2006GL026429.

Taylor, K. E., 2001: Summarizing multiple aspects of model performance in a single diagram. *Journal of Geophysical Research: Atmospheres*, **106 (D7)**, 7183–7192, doi:10.1029/2000JD900719.

Taylor, M., J. Tribbia, and M. Iskandarani, 1997: The spectral element method for the shallow water equations on the sphere. *Journal of Computational Physics*, **130**, 92–108.

Taylor, M. A., 2011: Conservation of mass and energy for the moist atmospheric primitive equations on unstructured grids. *Numerical Techniques for Global Atmospheric Models*, P. H. Lauritzen, C. Jablonowski, M. A. Taylor, and R. D. Nair, Eds., Springer, Lecture Notes in Computational Science and Engineering, Vol. 80, 357–380.

Taylor, M. A., J. Edwards, S. Thomas, and R. D. Nair, 2007: A mass and energy conserving spectral element atmospheric dynamical core on the cubed-sphere grid. *Journal of Physics: Conference Series*, **78**, 012 074.

Taylor, M. A. and A. Fournier, 2010: A compatible and conservative spectral element method on unstructured grids. *Journal of Computational Physics*, **229 (17)**, 5879–5895.

Tomita, H., 2008: A stretched icosahedral grid by a new grid transformation. *Journal of the Meteorological Society of Japan*, **86 (0)**, 107–119.

Tuller, S. E., 1968: World distribution of mean monthly and annual precipitable water1. *Monthly Weather Review*, **96 (11)**, 785–797.

Vitart, F., J. L. Anderson, and W. F. Stern, 1997: Simulation of interannual variability of tropical storm frequency in an ensemble of GCM integrations. *Journal of Climate*, **10 (4)**, 745–760.

Walko, R. L. and R. Avissar, 2008: The Ocean-Land-Atmosphere Model (OLAM). Part I: Shallow-water tests. *Monthly Weather Review*, **136 (11)**, 4033–4044.

Walko, R. L. and R. Avissar, 2011: A direct method for constructing refined regions in unstructured conforming triangular–hexagonal computational grids: Application to OLAM. *Monthly Weather Review*, **139 (12)**, 3923–3937, doi:10.1175/MWR-D-11-00021.1.

Walsh, K., S. Lavender, E. Scoccimarro, and H. Murakami, 2013: Resolution dependence of tropical cyclone formation in CMIP3 and finer resolution models. *Climate Dynamics*, **40 (3-4)**, 585–599, doi:10.1007/s00382-012-1298-z.

Walsh, K. J. E., M. Fiorino, C. W. Landsea, and K. L. McInnes, 2007: Objectively determined resolution-dependent threshold criteria for the detection of tropical cyclones in climate models and reanalyses. *Journal of Climate*, **20 (10)**, 2307–2314.

Warner, T. T., R. A. Peterson, and R. E. Treadon, 1997: A tutorial on lateral boundary conditions as a basic and potentially serious limitation to regional numerical weather prediction. *Bulletin of the American Meteorological Society*, **78 (11)**, 2599–2617.

Wehner, M. F., et al., 2014: The effect of horizontal resolution on simulation quality in the Community Atmospheric Model, CAM5.1. *Journal of Advances in Modeling the Earth System*, in review.

Wheeler, M. and G. N. Kiladis, 1999: Convectively coupled equatorial waves: Analysis of clouds and temperature in the wavenumber–frequency domain. *Journal of the Atmospheric Sciences*, **56 (3)**, 374–399.

Wieringa, J., 1992: Updating the Davenport roughness classification. *Journal of Wind Engineering and Industrial Aerodynamics*, **41 (1-3)**, 357 – 368, doi:10.1016/0167-6105(92)90434-C.

Williamson, D. L., 2007: The evolution of dynamical cores for global atmospheric models. *Journal of the Meteorological Society of Japan*, **85B**, 241–269, doi:10.2151/jmsj.85B.241.

Williamson, D. L., 2008a: Convergence of aqua-planet simulations with increasing resolution in the Community Atmospheric Model, Version3. *Tellus*, **60A**, 848–862.

Williamson, D. L., 2008b: Equivalent finite volume and Eulerian spectral transform horizontal resolutions established from aqua-planet simulations. *Tellus*, **60A**, 839–847.

Williamson, D. L., 2013: The effect of time steps and time-scales on parametrization suites. *Quarterly Journal of the Royal Meteorological Society*, **139 (671)**, 548–560, doi:10.1002/qj.1992.

Williamson, D. L., J. B. Drake, J. J. Hack, R. Jakob, and P. N. Swarztrauber, 1992: A standard test set for numerical approximations to the shallow water equations in spherical geometry. *Journal of Computational Physics*, **102**, 211–224.

Yanase, W., H. Taniguchi, and M. Satoh, 2010: The genesis of tropical Cyclone Nargis (2008): Environmental modulation and numerical predictability. *Journal of the Meteorological Society of Japan*, **88**, 497–519.

Zarzycki, C. M. and C. Jablonowski, 2014: A multidecadal simulation of Atlantic tropical cyclones using a variable-resolution global atmospheric general circulation model. *Journal of Advances in Modeling Earth Systems*, in prep.

Zarzycki, C. M., C. Jablonowski, and M. A. Taylor, 2014a: Using variable resolution meshes to model tropical cyclones in the Community Atmosphere Model. *Monthly Weather Review*, **142 (3)**, 1221—1239, doi:10.1175/MWR-D-13-00179.1.

Zarzycki, C. M., M. N. Levy, C. Jablonowski, J. R. Overfelt, M. A. Taylor, and P. A. Ullrich, 2014b: Aquaplanet experiments using CAM's variable resolution dynamical core. *Journal of Climate*, doi:10.1175/JCLI-D-14-00004.1, in press.

Zhang, G. J. and N. A. McFarlane, 1995: Sensitivity of climate simulations to the parameterization of cumulus convection in the Canadian Climate Centre General Circulation Model. *Atmos.–Ocean*, **33**, 407–446.

Zhang, H.-M., J. J. Bates, and R. W. Reynolds, 2006: Assessment of composite global sampling: Sea surface wind speed. *Geophysical Research Letters*, **33 (17)**, doi:10.1029/2006GL027086.

Zhao, M., I. M. Held, and S.-J. Lin, 2012: Some counterintuitive dependencies of tropical cyclone frequency on parameters in a GCM. *Journal of the Atmospheric Sciences*, **69 (7)**, 2272–2283, doi:10.1175/JAS-D-11-0238.1.

Zhao, M., I. M. Held, S. J. Lin, and G. A. Vecchi, 2009: Simulations of global hurricane climatology, interannual variability, and response to global warming using a 50-km resolution GCM. *Journal of Climate*, **22 (24)**, 6653–6678.

Zhou, T. and Z. Li, 2002: Simulation of the East Asian summer monsoon using a variable resolution atmospheric GCM. *Climate Dynamics*, **19 (2)**, 167–180.